Important Notice

UNIVERSITY OF CALGARY

Anelastic attenuation in seismic data: modeling, measurement, and correction

by

Peng Cheng

A THESIS

SUBMITTED TO THE FACULTY OF GRADUATE STUDIES

IN PARTIAL FULFILMENT OF THE REQUIREMENTS FOR THE

DEGREE OF DOCTOR OF PHILOSOPHY

DEPARTMENT OF GEOSCIENCE

CALGARY, ALBERTA

AUGUST, 2013

UNIVERSITY OF CALGARY

FACULTY OF GRADUATE STUDIES

The undersigned certify that they have read, and recommend to the Faculty of Graduate Studies for acceptance, a thesis entitled “Anelastic attenuation in seismic data: modeling, measurement, and correction” submitted by Peng Cheng in partial fulfilment of the requirements for the degree of Doctor of Philosophy.

_____

Supervisor, Dr. Gary F. Margrave, Department of Geoscience

_____

Dr. Laurence R. Lines, Department of Geoscience

_____

Dr. Robert J. Ferguson, Department of Geoscience

_____

Dr. Jörn Davidsen, Department of Physics and Astronomy

_____

External Examiner, Dr. Mauricio D. Sacchi, Department of Physics, University of Alberta

_____

Date

Abstract

Various aspects of the anelastic attenuation of seismic data are investigated in this thesis, including modeling, measurement, and correction using Gabor deconvolution.

For the modeling of seismic attenuation, a nonstationary convolution model, the reflectivity method, and a finite-difference technique for viscoelastic seismic modeling are described. For the implementation of the nonstationary convolution model, two approaches are proposed to incorporate the impulse response representing attenuation process accurately. The reflectivity method is implemented for stratified anelastic media, and the implementation is validated in terms of producing correct events and amplitudes, accurate incorporation of Q attenuation, and the flexibility to give total and partial response of the media. For the finite-difference method of viscoelastic seismic modeling, results obtained from commercial software are evaluated.

For the estimation of seismic attenuation, three new methods are presented, including complex spectral-ratio method, interpretive spectral-ratio method, and match-filter method. The proposed methods have connections with the classic spectral-ratio method, the spectrum-modeling method and the match-technique method which are also described. The performances of these methods are evaluated in terms of robustness to noise and capacity of estimating Q from reflection data, using synthetic VSP data, real VSP data and synthetic 1D reflection data. The effects of spectral smoothing, frequency band, and stationary deconvolution on Q estimation are investigated. For the complex spectral ratio-method, the issue of inaccurate reference frequency is addressed and three approaches are proposed to deal with real VSP data. In addition, an approach to identify the localized low Q zone of reflection data is proposed and evaluated using synthetic 2D data and field 2D data. Among all the Q-estimation methods evaluated in this

thesis, the match-filter method is significantly superior to other methods in terms of accuracy and robustness to noise when applied to both VSP data and reflection data.

As a nonstationary processing approach to compensate for seismic attenuation, Gabor deconvolution is investigated, and a practical way to correct the white-reflectivity assumption is presented. A definition of nonstationary phase rotation is proposed for the removal of phase rotation. The temporal color and spectral color of reflectivity are defined, and their influence on reflectivity estimation is analyzed in detail for Gabor deconvolution. The color correction method is applied to a field 2D line to restore the high frequency components and obtain a better well-tie.

Acknowledgements

I am grateful to my supervisor Dr. Gary F. Margrave for his instruction and continuous support during my Ph.D. studies. I would like to thank members of my PhD committee, Dr. Laurence R. Lines, Dr. Robert J. Ferguson and Dr. Kristopher Innanen, for their help to my research. I also thank Dr. Mauricio D. Sacchi and Dr. Jörn Davidsen for their valuable suggestion on my dissertation manuscript.

I would like to express my appreciation to all CREWES members for their help, support and friendship. Special thanks are given to Hanxing Lu and Helen Isaac for their expertise in seismic data processing, David Henley for ProMAX programming, Faranak Mahmoudian for her help with Tiger software, Kevin Hall and Rolf Maier for IT support, Laura Baird and Catherine Hubbell for their assistance, Wenyong Pan for the help with thesis editing. I would like to thank the sponsors of CREWES for their financial support.

I thank Andrew James Carter and Rainer Tonn for their reminder of reference work of my research.

I am grateful to Xiaoqin Cui, Zimin Zhang and Zaiming Jiang for their help and support. I want to give deepest gratitude to my parents and brother for their continuous encouragement and support all these years.

Dedication

To my family.

Table of Contents

List of Tables

List of Figures

List of Symbols and Abbreviations

Symbol	Definition
t, τ, t_1, t_2	Time values
$s_{stat}(t)$	Stationary seismic trace
$w(t)$	Source wavelet
$r(t)$	Reflectivity
$\boldsymbol{s}_{stat}$	Colum vector representing sampled stationary seismic trace
$\boldsymbol{W}$	A Toeplitz matrix formed from source wavelet
$\boldsymbol{r}$	Colum vector representing sampled reflectivity
$a(t,\tau)$	Impulse response representing an attenuation process with travel time t
$A(t,f)$	Amplitude spectrum of $a(t,\tau)$
$\varphi(t,f)$	Phase spectrum of $a(t,\tau)$
$i(t)$	Impulse response of a absorptive media with reflectivity $r(t)$
$s(t)$	Attenuated seismic trace
$S(f)$	Fourier spectrum of attenuated seismic trace $s(t)$
$S_1(f), S_2(f)$	Fourier spectrum of attenuated seismic traces with different traveltimes
$W(f)$	Fourier spectrum of source wavelet
$\boldsymbol{S}$	Colum vector representing $s(t)$
$\boldsymbol{A}$	A non-Toeplitz matrix representing $a(\tau, t-\tau)$
Δt_k	Interval traveltime
Q_k	Interval Q corresponding to Δt_k
$Q_{ave}(t)$	Average Q corresponding to a total traveltime of t
$Q_{\text{est}}, Q_{est1}, Q_{est2}, Q_{est3}$	Estimated Q value
$Q(\omega)$	Frequency dependent Q
$\alpha_i, \beta_i, \rho_i, d_i, z_i$	P wave velocity, S wave velocity, density, thickness, and depth of the i-th layer of a layered media
z_s	Depth of source point in a layered media
$\boldsymbol{R}^+$	Total reflection coefficient matrix corresponds to the upper half space above source location
$\boldsymbol{R}^-$	Total reflection coefficient matrix corresponds to the lower half space below the source position
$\boldsymbol{T}^+$	total transmission coefficient matrix corresponds to the upper half space
ω	Angular frequency
k_h	Horizontal wavenumber
u	Horizontal slowness
θ_m	Incident angel of plane wave at layer m
$\boldsymbol{F}$	Single force for point source with frequency dependent component (F_1, F_2, F_3)
(r, φ, z)	Cylindrical coordinates
Φ_s, Ψ_s	Displacement potential for P, SV waves of single force respectively

$J_l(u\omega r)$	Bessel function of integer order l
${\Phi_s}^{\mathrm{d}}$, ${\Psi_s}^{\mathrm{d}}$	Displacement potential for downgoing P, SV waves respectively
${\Phi_s}^{\mathrm{u}}$, ${\Psi_s}^{\mathrm{u}}$	Displacement potential for upgoing P, SV waves respectively
$\mathbf{S}_{\mathrm{i}}^{\mathrm{d}}$, $\mathbf{S}_{\mathrm{i}}^{\mathrm{u}}$	Source amplitude vectors for downgong P, SVwaves, and upgoing P, SV waves respectively
$\boldsymbol{V}_{\mathrm{i}}$	Amplitude vectors for the complete upgoing wavefields
$\boldsymbol{V}_{\mathrm{i}}^{\mathbf{0}}$	Amplitude vectors for the wavefields at $z \leq 0$
Φ^0, Ψ^0	Displacement potentials for P, SV waves at $z \leq 0$
$\mathbf{I}$	An identity matrix
$\mathrm{u_r}$, $\mathrm{u_z}$	Radial and vertical components of displacements respectively
ω_r,	Reference frequency
$v(\omega)$	Frequency dependent complex phase velocity of seismic wave in absorptive media
$W_F(\omega)$	A two-sided Hanning window to taper signal in frequency domain
$W_S(u)$	A one-sided Hanning window is used to taper the signal in slowness domain
Δu, $\Delta\omega$	Step sizes of horizontal slowness u, angular frequency ω respectively
x_{max}	The largest offset of interest
Λ	Relaxation function of viscoelastic media
M_R	Relaxed modulus of viscoelastic media
$\tau_{\varepsilon l}$, $\tau_{\sigma l}$	The strain and stress relaxation times of the l-th relaxation mechanism
$H(t)$	The Heaviside function
$M_c(\omega)$	The complex bulk modulus of viscoelastic media
$\sigma(t)$, $\varepsilon(t)$	Stress, strain history of viscoelastic media
p	Pressure wavefield
ξ_l	Memory variables
v	Particle velocity
G, $g(t)$	Geometrical spreading term
$a_1(t)$, $a_2(t)$	Local wavelets around t_1, t_2
$r_1(t)$, $r_2(t)$	Local reflectivities around t_1, t_2
Q_1, Q_2	Average-Q values corresponding to traveltime t_1, t_2
Q_{int}	Interval- Q value corresponding to traveltime $t_2 - t_1$
$A_1(f)$, $A_2(f)$	Fourier spectra of $a_1(t)$, $a_2(t)$
$R_1(f)$, $R_2(f)$	Fourier spectra of $r_1(t)$, $r_2(t)$
$B(f)$	Impulse response of the absorptive media in frequency domain
$v(f)$	Frequency dependent phase velocity
f_0	Reference frequency
$\widetilde{\mathrm{B}}(f)$	Linear phase delayed version of $B(f)$
k	Slope of straight-line

$k(f)$	Frequency dependent local slope
x_1, x_2	Distances
Re, I_m	Real and imaginary parts of logarithmic spectral ratios
$\alpha(Q_{int})$	Q-value dependent scaling factor
$h_{12}(t)$	Filter predicting $a_2(t)$ from $a_1(t)$
$h_{21}(t)$	Filter predicting $a_1(t)$ from $a_2(t)$
$H_{12}(f), H_{21}(f)$	Fourier spectra of $h_{12}(t)$, $h_{21}(t)$ respectively
$P_1(f), P_2(f)$	Power spectra of $a_1(t)$ and $a_2(t)$ respectively
$w_1(\mathrm{t}), w_2(t)$	Estimated minimum-phase wavelets corresponding to local wavelets $a_1(t),\ a_2(t)$
$I(Q_{int}, t)$	Forward Q filter, impulse response of attenuation process with a quality factor Q_{int}
μ	Scaling factor for matching $w_1(\mathrm{t})$ to $w_2(t)$ with $I(Q_{int}, t)$
ψ_n	Discrete prolate spheroidal sequences
$\Psi(f)$	Fourier spectrum of ψ_n
$\boldsymbol{\psi}, \boldsymbol{\psi}^m$	Vector form of discrete prolate spheroidal sequences
$A_1^m(f)$	Spectrum of tapered data
$d^m(f)$	Frequency dependent weight function
$\widetilde{A_1}(f)$	Weighted sum of $A_1^m(f)$
$L_j(f)$	Spectral leakage at frequency f
$\hat{A}_1(f)$	True unknown version of $A_1(f)$
$\overline{\lvert A_1(f)\rvert}$	Estimated smooth amplitude spectrum
$d(t)$	Deconvolution operator
$D(f)$	Fourier spectrum of $d(t)$
$A_{d1}(f), A_{d2}(f)$	Fourier spectra of deconvolved $a_1(t)$, $a_2(t)$
$S_G(\tau, f)$	Gabor spectrum of attenuated seismic trace
$\gamma(t)$	Gabor synthesis window
$\vartheta(t)$	Gabor analysis window
$\vartheta_{m,n}(t)$	Gabor frame operator
$\gamma_{m,n}(t)$	The dual Gabor frame
V_G	The signal recovered from the Gabor frame operator
$s_k(t)$	Signal windowed by Gabor analysis window
$S_k(f)$	Fourier transform of $s_k(t)$
$\hat{S}(f)$	Summed $S_k(f)$
δ	Gaussian half-width
$\Delta\tau$	Time spacing of Gaussian
$h(k\Delta\tau)$	Summation curve of Gabor transform
$\hat{s}_k(f)$	Normalized Gabor transform
$\alpha_Q(\tau, f)$	Constant-Q transfer function
$R_G(\tau, f)$	Gabor transform of reflectivity
$\mathrm{D}(\tau, f)$	Gabor transform of deconvolution operator
$\varphi(\tau, f)$	Phase term of Gabor deconvolution operator
$R_G(\tau, f)_{est}$	Gabor transform of estimated reflectivity
$r_c(t)$	Nonwhite reflectivity
$R_G^{'}(\tau, f)$	Gabor spectrum of nonwhite reflectivity

$D_c(\tau, f)$	Gabor deconvolution operator with color correction
$\varphi_c(\tau, f)$	Phase term of Gabor deconvolution operator with color correction
A_{max}	Maximum magnitude of the Gabor spectrum of seismic trace
$R'_G(\tau, f)_{est}$	Gabor spectrum of estimated reflectivity with color correction
$\acute{R}_c(f)$	Fourier spectrum of nonwhite reflectivity
$a_i(\tau)$	Coefficient curves of the polynomial fitting for the Gabor spectrum of nonwhite reflectivity
AGC	Automatic gain correction
AVO	Amplitude versus offset
CDP	Common depth point
GT	Gabor transform
NMO	Normal move out
QVO	Q versus offset
RMS	Root mean square
SNR	Signal-to-noise ratio
VSP	Vertical seismic profile

Chapter One: Introduction

1.1 Attenuation and dispersion of seismic waves

When seismic waves propagate in the earth, they experience energy loss. The attenuation of propagating wave due to absorption has long been observed (e.g. McDonal et al., 1958; Knopoff and MacDonald, 1958). However, little emphasis is given to the associated dispersion in early literature, which leads to the change in the shape of the transient waveforms. The absence of dispersion implies that nonlinear friction is the dominant attenuation mechanism (McDonal et al., 1958; Knopoff, 1964; White, 1966). Futterman (1962) shows that the attenuation is consistent with linear theory of wave propagation, in which the dispersion is a necessary consequence of absorption. The resulting dispersion equations are of Kramers-Krönig type and can be obtained by applying an integral transform, which is a consequence of the requirement of causality (Futterman, 1962).

The seismic attenuation is commonly quantified by quality factor Q. There are different definitions of Q, which is most often defined as the maximum energy stored during a cycle divided by the energy loss during the cycle. This definition becomes impractical for the case of small Q. O' Connell and Budiansky (1978) give a definition of Q in terms of the mean stored energy and the energy loss during a cycle. Early laboratory experiments show that Q is essentially independent of frequency for the seismic bandwidth (Kjartansson, 1979).

Based on linear theory of wave propagation, there are various models to describe the attenuation and the attendant dispersion. For the nearly constant-Q model given by Futterman (1962), Q is independent of frequency for frequencies above a certain characteristic value, which can be chosen low enough to be outside our interested frequency range. Between various nearly

constant-Q models of Lomnitz (1957), Futterman (1962), Strick (1967), Liu et al. (1976), the physical implication of the cut-off frequency is different, which can be chosen quite arbitrarily. For the above nearly constant Q models, the description of attenuation is restricted to the case where Q is large ($Q > 30$).

Kjartansson (1979) presents a linear model for attenuation with Q exactly independent of frequency, which is completely specified by two parameters, e.g., Q and phase velocity at an arbitrary reference frequency. This constant-Q model can describe the attenuation for cases with any positive Q value. Kjartansson (1979) states that the assumption of linearity of wave propagation is well justified for seismic waves while it is likely that Q is weakly dependent on frequency, and also shows that the results obtained from the nearly constant-Q models and the constant-Q model approach the same limit when frequency range is limited and Q is large.

1.2 Modeling of seismic attenuation

The attenuation of the earth media affects the amplitude and phase of propagating seismic waves. Such an effect, if ignored, can be the source resulting in errors in forward modeling, imaging and inversion (e.g. Samec and Blangy, 1992). To obtain realistic and accurate modeling results for wave propagation, Q attenuation should be incorporated into modeling algorithm appropriately, and this can be done either in frequency domain or time domain.

Usually, it is more convenient to account for Q attenuation in frequency domain. For the modeling of 1D seismic trace, attenuation can be addressed by nonstationary convolution model (Clark, 1968; Margrave, 1998). The attenuated seismic trace is a superposition of scaled nonstationary impulse responses, which represent corresponding attenuation process and are calculated in frequency domain based on constant-Q model. For the 2D or 3D seismic modeling of absorptive media, the Q attenuation can be incorporated by replacing the real velocity with a

frequency dependent complex velocity in the algorithm such as the moment method (Pratt and Worthington, 1990; Liao and McMechan, 1996) and reflectivity method (Fuchs and Müller 1971; Kennett, 1983). The moment method uses an implicit finite-difference scheme to solve the monochromatic viscoacoustic wave equation, which is obtained by transforming the acoustic wave equation into space-frequency domain and replacing real velocity with the complex velocity. However, this scheme needs to solve a matrix equation for each frequency component and the size of the matrix is very large, especially for 3D. The reflectivity method is a frequency-wavenumber domain method for seismic modeling of layered media, which automatically includes contributions from all possible rays within the reflecting zone. The reflectivity method was originally developed by Fuchs and Müller (1971). Their pioneering work was followed by Kennett (1975, 1979, 1980), Kind (1976), Stephen (1977), Kennett and Kerry (1979), Kennett and Illingworth (1981), Fryer (1981), Kennett and Clark (1983). For the reflectivity method, the reflectivity function for integration is calculated by a matrix or propagator techniques, which mainly deals with the computation of the reflection and transmission coefficients for plane waves, incident on a plane surface or a stack of homogenous layers. The coefficients for an interface are given analytically according to the Zoeppritz equations, and those for a stack of layers are derived by a recursive algorithm proposed by Kennett (1975). In addition, the attenuation effect of anelastic media can be incorporated conveniently in the frequency domain using frequency-dependent complex velocity (Kennett, 1975; Sipkin et al, 1978; O'Neil and Hill, 1979, Cheng and Margrave, 2011a). The main advantage of the reflectivity method is its capacity to give both a total solution of the wavefield and partial results of interest for a layered media. The reflectivity method also has some practical disadvantages. The reflectivity function

needs to be adequately sampled in wavenumber or slowness and frequency spaces to avoid spatial and temporal aliasing (Mallick and Frazer, 1987).

The incorporation of attenuation in time-domain methods is complicated by the convolution-integral form of the stress-strain relation (Christensen, 1982), which is intractable in numerical computation. On the other hand, finite-difference methods (e.g. Alterman and Loewental, 1972, Kelly et al., 1976) are widely used for the seismic modeling of 2D or 3D inhomogenous media, since these methods can produce complete synthetic seismograms for arbitrarily heterogeneous media. The definite disadvantage of the time-domain finite-difference methods is that they are generally restricted to pure elastic case. They are also difficult to push to high frequencies. With the development of linear viscoelastic theory, the convolution integral can be eliminated by introducing memory variables (Liu et al., 1976; Day and Minster, 1984), of which each satisfies a first-order differential equation in time. Then, the resulting system of the governing differential equation can be solved by various ways, which allow computing synthetic seismograms for models with arbitrary distribution of velocities and quality factors (Emmerich and Korn, 1987; Carcione, 1988a, 1988b, 1988c; Carcione, 1993; Krebes and Quiroga-Goode, 1994; Robertsson et al., 1994; Dong and McMechan, 1995; Xu and McMechan, 1995). For the viscoelastic seismic modeling, there is physical dispersion due to absorption, and the intrinsic numerical dispersion of the finite-difference scheme as well (Dablain, 1986). To avoid the confusion of these two types of dispersion, computation of the differential equation with high accuracy is necessary. The spatial derivatives can be calculated by pseudo-spectral schemes (Carcione, 1988a, 1988b, 1988c, 1993; Tal-Ezer et al., 1990), or high-order finite-difference schemes (Levander, 1988; Robertsson et al., 1994).

1.3 Estimation of seismic attenuation

The attenuation of seismic waves is a property of the earth which is quantified by Q. In global seismology, Q factor can be measured from the time decay of the free oscillations excited by earthquakes (Nowroozi, 1968). In exploration seismology, Q is conventionally estimated from transmission data, such as VSP data (Hague, 1981; Tonn, 1991), crosswell (Quan and Harris, 1997; Neep et al., 1996) and sonic logging (Sun et al., 2000). There are various methods for Q estimation such as analytical signal method (Engelhard, 1996), spectral-ratio method (Bath, 1974), the centroid frequency-shift method (Quan and Harris, 1997), the match-technique method (Raikes and White, 1984; Tonn, 1991), and the spectrum-modeling method (Janssen et al., 1985; Tonn, 1991; Blias, 2011), and each method has its strengths and limitations. An extensive comparison between various methods for Q estimation was made by Tonn (1991) using VSP data, and a conclusion was made that the spectral-ratio method is optimal in the noise-free case. However, the estimation given by spectral-ratio method may deteriorate drastically with increasing noise (Patton, 1988; Tonn, 1991). The question of reliable Q estimation remains.

Usually, it is more practical to estimate Q from the surface reflection data. For Q estimation from reflection data, the tuning effect (Sheriff and Geldart, 1995) of local thin-beds should be addressed properly. Dasgupta and Clark (1998) proposed a Q versus offset (QVO) method for estimating Q from surface data, which essentially applied the classic spectral-ratio method on a trace by trace basis to the designatured and NMO corrected CMP gather. Hackert and Parra (2004) proposed an approach to remove this tuning effect from the QVO method using reference well log data.

Generally, estimating Q from noisy data or surface reflection data needs further investigation. As an extension to classic spectral-ratio method, Cheng and Margrave (2008) propose a complex spectral-ratio method that employs both the amplitude spectra and the phase spectra of signal, in which Q is estimated by solving an inverse problem to minimize the misfit between the modeled and measured complex spectral ratios. For the classic spectral ratio method, it can be troublesome or impossible to find a fixed frequency range to give good Q -estimation results when calculated spectral ratios are not linearly distributed well. To address this problem, Cheng and Margrave (2011b) proposed an interpretive spectral-ratio method, which automatically choose an appropriate narrow frequency range to give the Q estimation.

In addition, a time-domain match-filter method for Q estimation was proposed by Cheng and Margrave (2012), and it has been shown to be robust to noise and suitable for application to surface reflection data. For the match-filter method, apparent minimum-phase equivalent wavelets corresponding to two signals are estimated, and then optimal Q is obtained by finding the forward Q filter that best matches the wavelets. Theoretically, the match-filter method is a sophisticated wavelet-modeling method, which is a time-domain alternative to spectrum-modeling method (Janssen et al., 1985; Tonn, 1991; Blias, 2011). The spectrum-modeling method is a modified approach to the spectral-ratio method without taking division of spectra. In addition, the match-filter method and the match-technique method (Raikes and White, 1984; Tonn, 1991) employ the idea of matching at different stages of their Q-estimation procedures. Therefore, the above four methods all have theoretical connections but are distinctly different. Cheng and Margrave (2013) give a comparison of these methods using synthetic VSP and reflection data and real VSP data.

1.4 Compensation of seismic attenuation

Seismic attenuation of real earth causes additional energy loss, especially for high frequency components, and waveform distortion of propagating wave. The attenuation should be taken account for in seismic data processing, to restore the high frequencies to enhance the seismic resolution, and to correct the phases associated with arrival timings of reflections. The compensation of Q attenuation is addressed by many authors. Their work generally falls into three classes: nonstationary deconvolution, inverse Q filtering, and inversion.

For the first category, Clark (1968) propose a nonstationary deconvolution method in time-domain. Griffths et al. (1977), and Koehler and Taner (1985) develope time-varying predictive deconvoluiton. Margrave and Lamoureux (2001) present a Gabor deconvolution method in Gabor domain based on the nonstationary convolution model given by Margrave (1998). The subsequent work about Gabor deconvolution is presented in Margrave et al. (2002, 2004, 2011), and Montana and Margrave (2006).

Inverse-Q filtering is investigated by a great many authors. Hargreaves and Calvert (1991) formulate inverse-Q filtering as a migration method. Q attenuation is compensated during wavefield extrapolation by adopting complex velocity. This approach is followed by Mittet et al. (1995), Wang (2002, 2008), Zhang and Wapenaar (2002). Stability is a common and important problem for these inverse-Q migration methods, because inverse-Q filtering means the exponential growth of wavefield with respect to both frequency and time, which is not stable. Zhang and Wapenaar (2002) address this problem by limiting the propagating angle of wavefield, and Wang (2008) uses an inverse approach to achieve a gain limit for a stable result. More recent work is to address the Q compensation by inversion methods (Causse et al., 1999; Innanen and Lira, 2010; Bai et al., 2012).

The inverse-Q filter schemes need quite accurate Q models and face the stability problem. The Gabor devonvolution is conducted by direct division in Gabor domain. The combined Gabor spectrum of attenuation process and source wavelet is estimated from data, and the resulting Gabor spectrum is used to divide the Gabor spectrum of seismic trace to give the reflectivity estimation. Therefore, Gabor deconvolution does not require a Q model, instead itestimates and compensates the attenuation in an adaptive way and does not suffer from instability.

Deconvolution algorithms usually assume that the reflectivity has a white amplitude spectrum. In practice, the reflectivity is colored, i.e., there are obvious variations in the amplitude spectrum of real reflectivity. Walden and Hosken (1985) analyse the refection coefficients from various rock sequences around the world, and they find that in most cases the reflectivities are pseudo-white only above a corner frequency and their power spectrum falls away at low frequencies according to a power law. To make correction to the white-reflectivity assumption, deconvolution algorithms should be modified accordingly. Cheng and Margrave (2009a) propose a color correction method for Gabor deconvolution, which gives improved estimation with better relative amplitude and smaller phase rotation. The feature of the true reflectivity color and its influence on Gabor deconvolution are analyzed by Cheng and Margrave (2010). Cheng and Margrave (2011c) apply the color correction to field data and they show that it can help to restore the high frequencies and obtain a better well-tie.

1.5 Motivation of the research in this thesis

Real earth attenuates and disperses seismic waves. For seismic modeling, incorporation of anelastic attenuation can make the modeling result more realistic. For seismic data processing, migration, and inversion, the fundamental goal is to obtain correct reflection coefficients for the

subsurface. The anelastic behavior of real earth can decease the amplitude and distort the waveform of seismic wave and thus has significant effect on the obtained results. For example, amplitude analysis for AVO is complicated by Q attenuation because the attenuation effects are superimposed on AVO signature; Gas clouds can significantly attenuate seismic waves and such an attenuation effect can reduce the resolution of migration result. It is important to compensate for the anelastic attenuation to make the final result more accurate and reliable. In addition, the attenuation can be quantified by quality factor Q, which depends on lithology, porosity, and fluid or gas saturation. Measurement of Q can provide important information about the subsurface to facilitate seismic interpretation. Therefore, it is valuable to investigate the anelastic attenuation in seismic data. This thesis investigates various aspects of the Q attenuation, including modeling, measurement, and correction using Gabor deconvolution.

1.6 Contribution of this thesis

The objective of this thesis is to review the modeling methods for seismic attenuation, including the nonstationary convolution model for seismic trace, the reflectivity method, and finite-difference method for viscoelastic modeling, to develop new methods for Q estimation that are more robust to noise and more suitable to be applied to reflection data, and to investigate Gabor deconvolution and develop a practical method to correct the distortion caused by the white-reflectivity assumption.

The contributions of this thesis are summarized as follows:

- For the implementation of nonstationary convolution model, distortion to constant- Q model caused by direct truncation of the impulse response corresponding to the attenuation process is identified. A band-limited version and a circle-shifted version of the original impulse response are adopted to make the implementation accurate.

- The reflectivity method is implemented for stratified anelastic media, and the implementation is verified in terms of correct events, amplitudes, accurate incorporation of Q attenuation, and the flexibility to give total and partial response of the media.
- A complex spectral-ratio method for Q estimation is presented, which takes an inversion approach to estimate Q using both the amplitude spectra and the phase spectra information.
- An interpretive spectral-ratio method for Q estimation is presented, which automatically obtains an optimal localized slope of logarithmic spectra-ratios to give Q estimation.
- A match-filter method for Q estimation is presented.
- The multitaper method for spectrum estimation is implemented, and the effect of spectrum smoothing for various Q-estimation methods is investigated, including classic spectral-ratio method, spectrum-modeling method, math-technique method, and match-filter method.
- The effect of stationary deconvolution on Q estimation is analyzed theoretically and verified with numerical tests.
- For the complex spectral-ratio method, the influence of inaccurate reference frequency for the modeling of phase difference is investigated. Three approaches are proposed to address this problem for its application to real data.
- A comparison of performance for various Q-estimation methods is made using synthetic VSP data, real VSP data and synthetic 1D reflection data, including the

classic spectral-ratio method, complex spectral-ratio method, interpretive spectral-ratio method, spectrum-modeling method, match-technique method, and match-filter method.

- Using the match-filter method, an approach to identify the localized low Q zone of subsurface is proposed and verified with synthetic and field 2D reflection data, and this can be used in conjunction with other observations to identify gas reservoir.
- A color-correction method is presented for Gabor deconvolution, which corrects the distortion caused by the white-reflectivity assumption.
- A practical approach to approximate the time-varying color feature of true reflectivity is presented, which makes the color correction method insensitive to specific well-log information and regional well-log information useful.
- A practical way to define and remove the nonstationary phase rotation between two wavelets/signals is proposed and verified with numerical test.
- The temporal color and spectral color of reflectivity color are defined, and their connection with relative amplitude distortion and phase rotation is revealed with synthetic and real data.
- The color correction method for Gabor deconvolution is applied to 2D field data, which restores high frequency components of seismic data and obtains a better well-tie.

1.7 Outline of this thesis

In Chapter 2, some modeling methods for seismic attenuation are introduced, including a nonstationary convolution model, the reflectivity method and finite-difference method for viscoelastic seismic modeling. For the implementation of the nonstationary convolution model,

the practical issue of accurate incorporation of the impulse response of attenuation process is addressed. Two approaches to implement the nonstationary convolution model with accurate constant-Q attenuation are proposed and tested. The reflectivity method is implemented for stratified anelastic media, and the implementation is evaluated in term of producing correct events and amplitudes, accurate incorporation of Q attenuation, and the flexibility to give total and partial response of the media. For the finite-difference method of viscoelastic modeling, results obtained from Tiger software are evaluated.

In chapter 3, the theory of various Q-estimation methods is introduced, including classic spectral-ratio method, complex spectral-ratio method, interpretive spectral-ratio method, spectrum-modeling method, match-technique method, and match-filter method. The effects of spectrum smoothing, frequency band, stationary deconvolution on Q estimation are investigated using synthetic data. For the complex spectral ratio method, the issue of inaccurate reference frequency for modeling phase difference is addressed using synthetic and real VSP data. The performance of above methods is compared in terms of robustness to noise and the capacity of dealing with reflection data. In addition, an approach to identify the localized low Q zone of refection data is proposed and evaluated using synthetic 2D data and field 2D data.

In chapter 4, Gabor deconvolution is introduced, and a color correction method is presented. A practical way to approximate the time-variant color of well-log reflectivity is proposed. Synthetic data are used to evaluate the color correction method. Then, the influence of the reflectivity color is analyzed in detail. Following that, the color correction method is evaluated using a field 2D line with reference well-log information available.

In chapter 5, final conclusions and some comments are made, and some suggestions on future work are provided.

Chapter Two: Reviews of modeling of seismic attenuation

2.1 Introduction

Wave propagation in the earth has been known to be anelastic. Such an anelasticity of real earth media can cause significant change to both the amplitude and the phase of propagating waveform. Attenuation of propagating waveform, if ignored, can be the source resulting in errors in forward modeling, imaging and inversion (e.g. Samec and Blangy, 1992). Therefore, realistic simulation of seismic wave propagation in earth media should account for the effect of attenuation and dispersion.

Depending on the circumstance and the actual needs, different methods can be chosen to incorporate attenuation into seismic modeling. This chapter gives a brief introduction to a nonstationary convolution model for seismic trace, the reflectivity method, and finite-difference method for viscoelastic seismic modeling. The nonstationary convolution model is used to incorporate Q attenuation into 1D seismic trace (Clark, 1968; Margrave, 1998). For its implementation, we propose two approaches to incorporate constant Q attenuation accurately. The reflectivity method (Fuchs and Müller, 1971; Kennett, 1975, 1979) is widely used for the computation of synthetic seismograms for layered media due to its capacity of modeling all kinds of wave propagation and attenuation for a given model with sufficient accuracy and relatively low computation cost. We implement the reflectivity method for stratified anelastic media, and evaluate our implementation in term of generating correct events and accurate incorporation of Q attenuation (Cheng and Margrave, 2011a). The finite-difference technique for viscoelastic modeling has been widely investigated by geophysicists (Emmerich and Korn, 1987, Carcione et al., 1988a, 1988b, 1988c; Krebes and Quiroga-Goode, 1994; Robertsson et al., 1994). This

chapter introduces the scheme proposed by Robertsson et al. (1994), and evaluates the modeling result from the Tiger software developed by the SINTEF research group.

2.2 A non-stationary convolution model for 1D attenuated seismic trace

2.2.1 Theory of a non-stationary convolution model

In this section, we follow Margrave et al. (2011) to give an introduction to the stationary and nonstationary convolution models of seismic trace. A 1D reflection seismic trace is usually formed by the convolution of the response function corresponding to a layered earth with some source wavelet. For a stationary convolution model, the source wavelet is assumed to be constant, meaning that its amplitude and shape do not change with traveltime. The stationary convolution model can be approximated in its most simplified form as

$$s_{stat}(t) = w(t) * r(t) = \int_{-\infty}^{\infty} w(t-\tau) r(\tau) d\tau, \qquad (2.1)$$

where $s_{stat}(t)$ is the stationary seismic trace, $w(t)$ is the source wavelet, $r(t)$ is the corresponding reflectivity of layered earth in two-way traveltime, and "$*$" denotes the conventional convolution.

One way to numerically implement equation (2.1) employs the multiplication of matrices, which can be formulated as

$$\boldsymbol{s}_{stat} = \boldsymbol{W}\boldsymbol{r}, \qquad (2.2)$$

where $\boldsymbol{s}_{stat}$ is a column vector representing the sampled seismic trace, $\boldsymbol{W}$ is a Toeplitz matrix formed from $w(t)$, and column vector $\boldsymbol{r}$ contains the sampled reflectivity. Each column of the Toeplitz matrix corresponds to a progressively delayed version of sampled source wavelet. Therefore, the matrix-vector multiplication in equation (2.2) is the superposition of different versions of source wavelet incorporating the traveltime delay and scaling effect of reflectivity coefficient, which clearly demonstrates the linear nature of the stationary convolution model.

In practice, when propagating in the earth, a seismic wave is subject to the influence of geometrical spreading, anelastic attenuation, transmission loss, etc. As a result, the source wavelet evolves as it propagates. The resulting seismic trace would be more realistic if we allow the appropriate evolution of source wavelet in equation (2.1) or (2.2). Then, to address the attenuation of seismic trace, the source wavelet should evolve according to the attenuation law of earth.

The attenuation effect of earth is most widely described by the constant- Q attenuation model (Futterman, 1962; Kjartasson, 1979), in which Q is independent of frequency or, more practically, can be regarded as a constant within the frequency band of interest. Given a traveltime t and the corresponding attenuation quality factor Q, the impulse response of the attenuation process for the specific traveltime t can be obtained from its Fourier amplitude as

$$a(t,\tau) = \int_{-\infty}^{\infty} A(t,f) e^{j\varphi(t,f)} e^{2\pi j f \tau} df, \qquad (2.3)$$

where $A(t,f)$ and $\varphi(t,f)$ are the amplitude spectrum and phase spectrum of $a(t,\tau)$ respectively. For constant- Q attenuation theory (Futterman, 1962; Kjartasson, 1979; Aki and Richards, 1980), $a(t,\tau)$ is considered to be a minimum-delay pulse. $A(t,f)$ is given by

$$A(t,f) = e^{-\pi |f| t/Q}, \qquad (2.4)$$

and the phase spectrum $\varphi(t,f)$ can be obtained by the Hilbert transform over frequency of the natural logarithm of $A(t,f)$.

We can infer from the above attenuation function that the attenuation of seismic wave is nonstationary, meaning that it depends on both time and frequency. To address this problem, the stationary convolution model was generalized to include attenuation explicitly by Clarke (1968)

and Margrave (1998). Assuming a unit impulsive source wave, the 1D nonstationary seismogram corresponding to reflectivity $r(t)$ can be formulated as

$$i(t) = \int_{-\infty}^{\infty} a(\tau, t-\tau) r(\tau) \mathrm{d}\tau. \quad (2.5)$$

Equation (2.5) is the linear superposition of the impulse response of attenuation process scaled by corresponding reflectivity coefficients, which forms a nonstationary convolution by allowing the temporal evolution of signal. Then, for a source wavelet $w(t)$, the resulting seismogram is

$$s(t) = w(t) * i(t) = \int_{-\infty}^{\infty} w(t-\tau) i(\tau) d\tau. \quad (2.6)$$

Inserting equation (2.5) into equation (2.6) and transforming to the Fourier domain, equation (2.6) becomes (Margrave, 1998)

$$S(f) = W(f) \int_{-\infty}^{\infty} A(t, f) e^{j\varphi(t,f)} r(t) e^{-2\pi j f t} dt, \quad (2.7)$$

where $W(f)$ is the Fourier spectrum of source wavelet.

Then, the numerical implementation of equation (2.6) can be formulated as

$$\boldsymbol{S} = \boldsymbol{W}\boldsymbol{A}\boldsymbol{r}, \quad (2.8)$$

where $\boldsymbol{S}$ is a column vector that contains the 1D attenuated seismic trace, $\boldsymbol{A}$ is a non-Toeplitz matrix representing $a(\tau, t-\tau)$.

It should be pointed out that the Q value in equation (2.4) is the average Q value for the specific two-way traveltime t and it is allowed to vary with traveltime. For a layered media, each layer may have different Q value, so the average Q value should be derived from interval Q values. Suppose there are M layers for a given travel-time t with corresponding interval Q values Q_k and interval traveltime Δt_k $(k = 1,2, \dots, M)$. The average Q can be obtained from

$$\frac{t}{Q_{ave}(t)} = \sum_{k=1}^{M} \frac{\Delta t_k}{Q_k}. \quad (2.9)$$

In addition, the Q attenuation described above is the intrinsic attenuation of the earth. The stratigraphic filtering effect of layered media can also case apparent attenuation of seismic wave (O'Doherty and Anstey, 1971). The stratigraphic filter is low-frequency preferable and minimum phase (Banik et al., 1985). In this sense, the apparent attenuation is similar to the intrinsic attenuation. Therefore, the two attenuation process can be combined to form an effective attenuation operator or function which, in most cases, can be used in the nonstationary convolution model to account for both intrinsic absorption and stratigraphic filtering of layered media (Mateeva et al., 2002).

The stationary convolution model is theoretically the non-absorptive limit ($Q \to \infty$) of the nonstationary convolution model. When $Q \to \infty$, $a(t, \tau)$ in equation (2.3) becomes a Dirac's delta function $\delta(\tau)$, then $i(\mathrm{t})$ in equation (2.5) reduces to $r(t)$, which makes equation (2.6) equivalent to equation (2.1). For the numerical implementation of nonstationary convolution model, non-Toeplitz matrix $\boldsymbol{A}$ in equation (2.8) becomes an identity matrix in the non-absorptive limit and the result is the same as equation (2.2).

A practical issue for the numerical implementation of the nonstationary convolution model given by equation (2.6) is the calculation of the impulse response $a(\tau, t-\tau)$. The exponential decay of the amplitude spectrum of the impulse response demonstrates the attenuation of the absorptive media. According to equation (2.4), the amplitude spectrum does not vanish with increasing frequency. The minimum-phase delay of the impulse response represents the dispersion of absorptive media to seismic waves, which is a necessary consequence of the requirement of causality (Futterman, 1962). The phase spectrum of the

impulse response can be obtained from the Hilbert transform of the logarithmic amplitude spectrum, which is an integral over the entire frequency range. Theoretically, the calculated impulse response should be a causal signal. However, in practice, computation can only be conducted over a limited frequency range. Therefore, both the amplitude spectrum and phase spectrum are not incorporated perfectly in the inverse Fourier transform to give the response impulse. Such an imperfect computation leads to that the calculated impulse response is not causal. This non-causal signal has a tail of nontrivial values, since the discrete Fourier transform gives a periodic result and the non-causal part of the result locates at the end of each time cycle. Conventional truncation of the tail can cause the amplitude spectrum of truncated pulse not to match the exponential decay described by equation (2.4), which, in turn, makes the nonstationary model lose accuracy. We propose two approaches to address this problem. One is that, instead of direct truncation, the tail of the calculated pulse is circle-shifted to the beginning, and then truncation can be made if needed. By introducing a small time delay to the impulse response, the amplitude spectrum of exponential decay is preserved. Another approach is that the original amplitude spectrum of the impulse response is modified to a bandlimited version by applying a taper to the high frequency part while the part within frequency band of interest remains unchanged. Then, the alternative minimum-phase impulse response corresponding to the modified amplitude spectrum is calculated.

2.2.2 Numerical example

The conventional convolution is illustrated by Figure 2.1. The seismic trace is created from a minimum-phase source wavelet with a dominant frequency of $30Hz$ and random reflectivity. There is no noticeable attenuation for the resulting trace, since it is a superposition of the time-delayed source wavelet scaled by the reflectivity. Using the same source wavelet and

random reflectivity, an attenuated seismic trace is created with a constant Q value of 50, as shown in Figure 2.2. Like the stationary convolution, the seismic trace is obtained from a matrix-vector product. The matrix is obtained from convolving the minimum-phase source wavelet with a time-delayed minimum-phase pulse corresponding to the attenuation process, which does not possess Toeplitz symmetry. Compared to the seismic trace shown in Figure 2.1, the resulting seismic trace has obvious amplitude decay with traveltime.

The key of the nonstationary convolution model described by equation (2.8) is the calculation of the impulse response (or pulse) $a(\tau, t-\tau)$ corresponding to the attenuation process. Figure 2.3 shows the pulse corresponding to the attenuation process with a traveltime of 0.2s and constant Q of 100, which is calculated from its Fourier spectrum. Due to the imperfection calculation in practice, the result is a non-causal signal and the non-causal part will appear as a tail of the signal. We can see that calculated pulse has a large spike at the beginning and a relatively smaller tail that can not be ignored. To form the matrix $\boldsymbol{WA}$ in equation (2.8), truncation is necessary during the calculation. However, direct truncation of the pulse can lead to the distortion to the original amplitude spectrum that decays exponentially with frequency. As demonstrated in Figure 2.4, the amplitude spectrum of the direct truncated pulse deviates from the theoretical exponential decay with respect to frequency. Then, adoption of direct truncation of the pulse $a(\tau, t-\tau)$ may cause the nonstationary convolution model to lose accuracy to some degree. To address this problem, as mentioned previously, a circle-shifted version and a bandlimited version of the original pulse are proposed for adoption. Figure 2.5 shows three synthetic seismic traces corresponding to three different versions of pulses chosen to form matrix $\boldsymbol{WA}$, using the same source wavelet, constant Q of 100 and two isolated reflectors. A zoomed comparison of the first event in Figure 2.5 is demonstrated in Figure 2.6. We can see

that the circle-shift of original pulse introduces a small time delay to the resulting seismic trace, and the waveform generated from bandlimited pulse is slightly different from that created from directly truncated pulse. The amplitude spectra of the first events of the three seismic traces are shown in Figure 2.7. The event created from the bandlimited pulse has the same amplitude spectrum as that from circle-shifted pulse at low frequency part, and its amplitude spectrum decays to zero more quickly at the high frequency part since a taper is applied to band-limit the original pulse. The distortion to amplitude spectrum caused by direct truncation also can be observed in Figure 2.7. In addition, when the direct truncated pulse is employed, the resulting events have slightly smaller amplitude both in time domain and frequency domain, which is due to the loss of signal energy (the tail shown in Figure 2.3) caused by truncation. Q estimation by spectral-ratio method (this method will be described in chapter 3) is conducted using the events of the three seismic traces in Figure 2.5, and the results are shown in Figure 2.8, 2.9 and 2.10. The estimated Q for the seismic trace created from direct truncated pulse is 110.81, which deviates from true value 100. For the cases of circle-shifted pulse and bandlimited pulse, the estimation results are 100.04 and 99.96 respectively. The two proposed approaches improve the accuracy of the nonstationary convolution model.

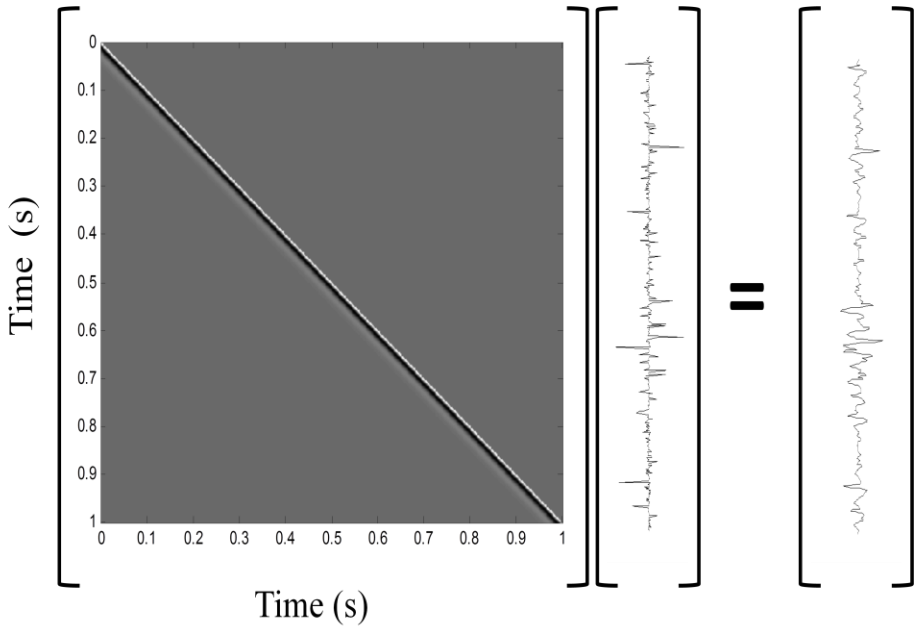

Figure 2.1. Illustration of the stationary convolution model described by equation (2.2). The matrix is a Toeplitz matrix formed from a minimum-phase source wavelet. The resulting seismic trace is a superposition of time-delayed source wavelet scaled by reflectivity.

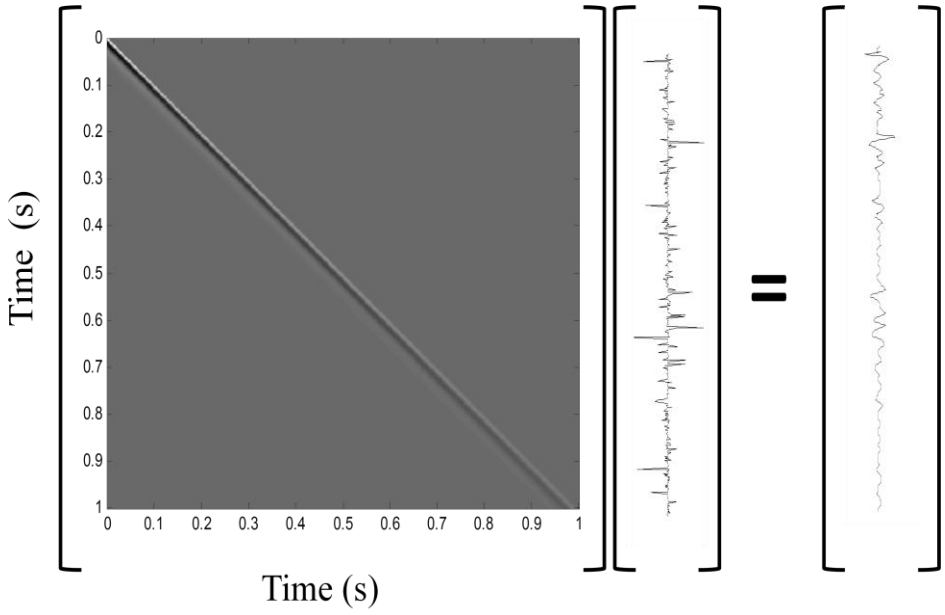

Figure 2.2. Illustration of the nonstationary convolution model described by equation (2.8). The matrix is a matrix formed from convolving a minimum-phase source wavelet with a time-delayed minimum-phase pulse $a(\tau, t-\tau)$ corresponding to the attenuation process.

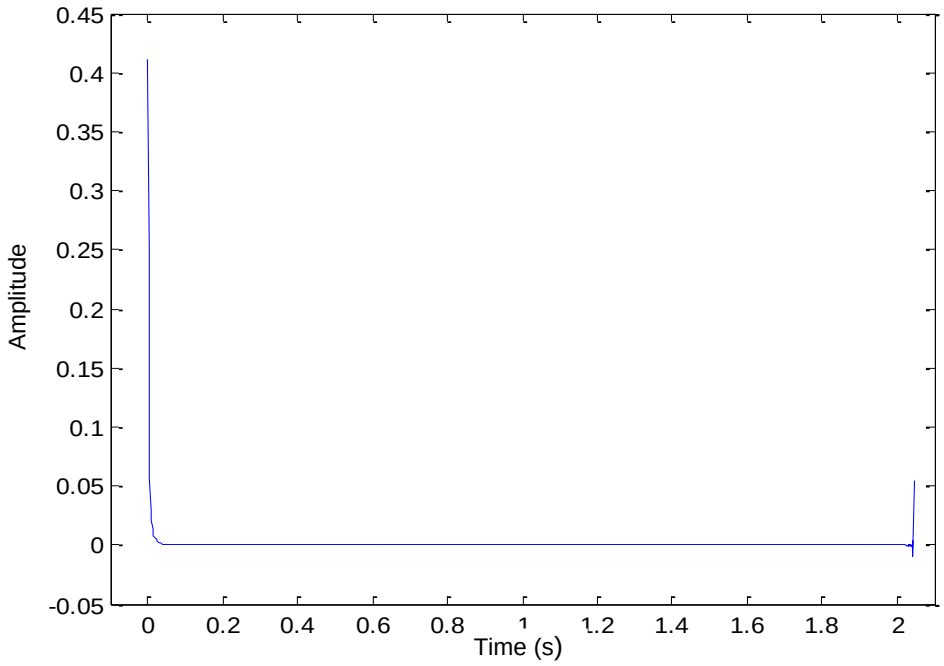

Figure 2.3. The impulse response (pulse) corresponding to the attenuation process with a traveltime of $0.2s$ and a constant Q of 100.

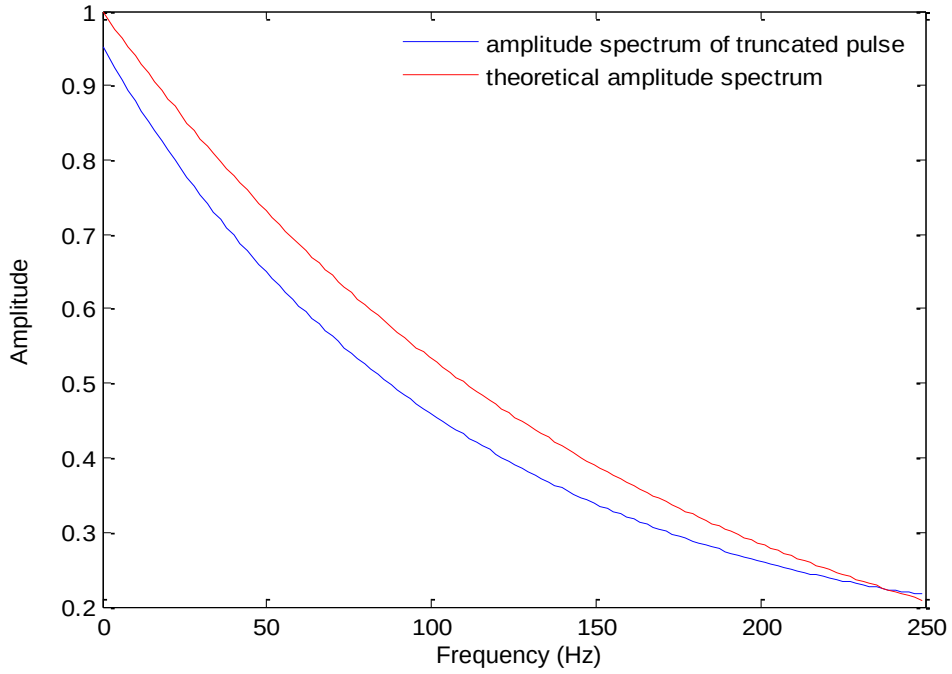

Figure 2.4. The amplitude of spectrum of a direct truncated pulse shown in Figure 2.3.

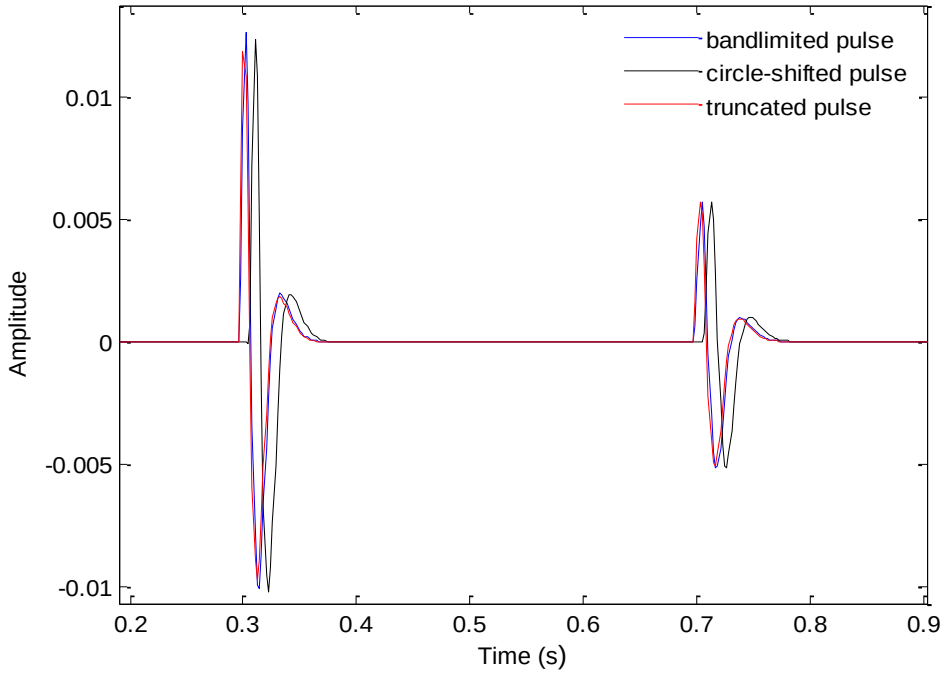

Figure 2.5. Three synthetic seismic traces corresponding to truncated, circle-shifted and bandlimited pulse $a(\tau, t-\tau)$ respectively, using the same source wavelet, two isolated reflector and a constant Q of 100.

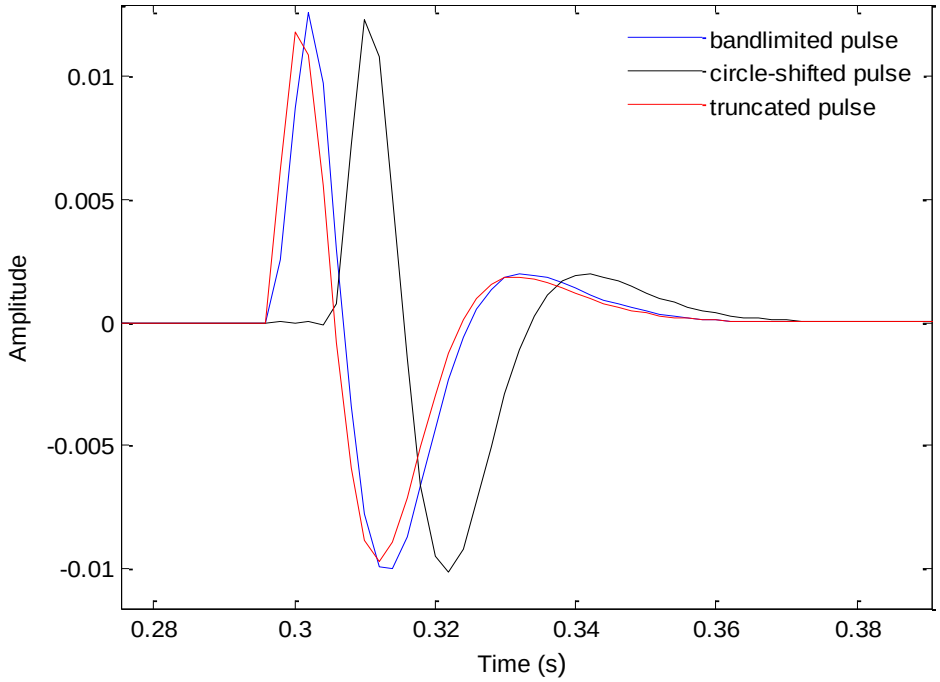

Figure 2.6. Comparison of the first event shown in Figure 2.5

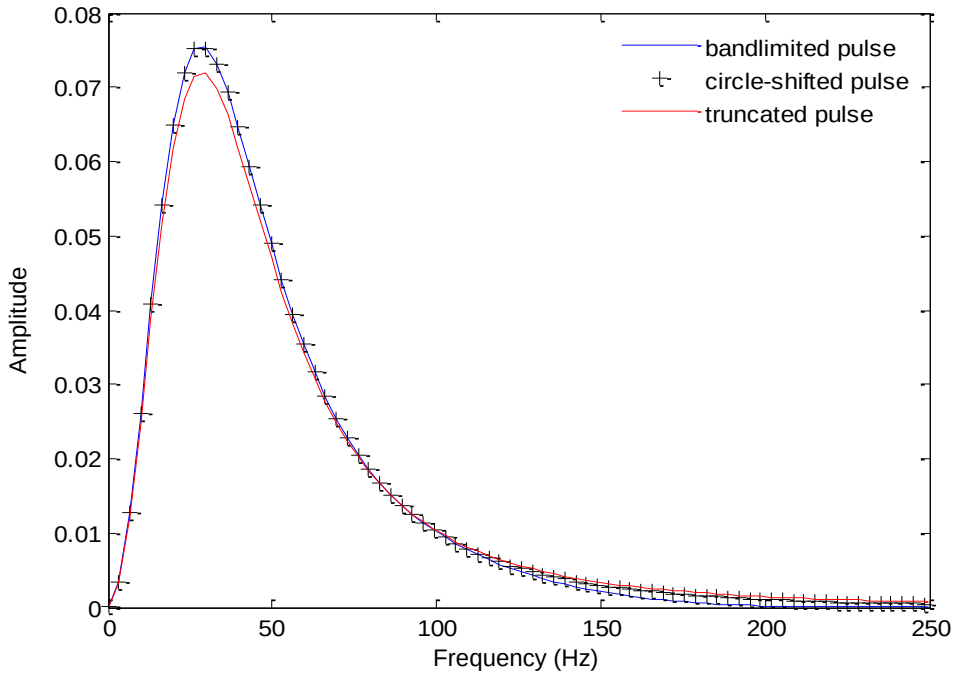

Figure 2.7 Amplitude spectra of the first events of the three seismic trace shown in Figure 2.5.

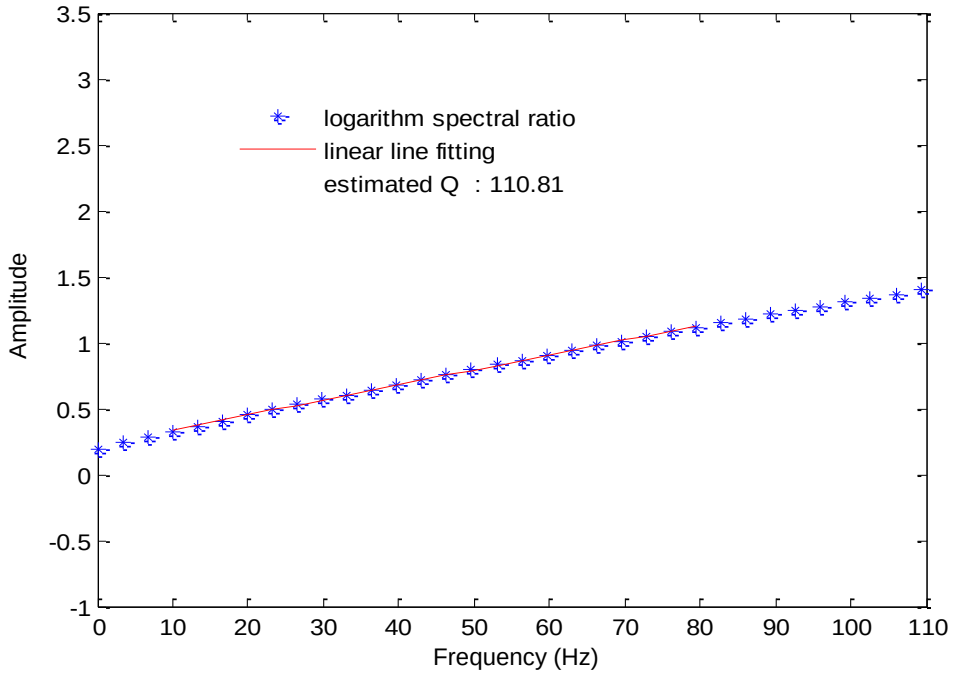

Figure 2.8. Q estimation using the seismic trace shown in Figure 2.5, which is created from the nonstationary convolution model with directly truncated pulse $a(\tau, t-\tau)$.

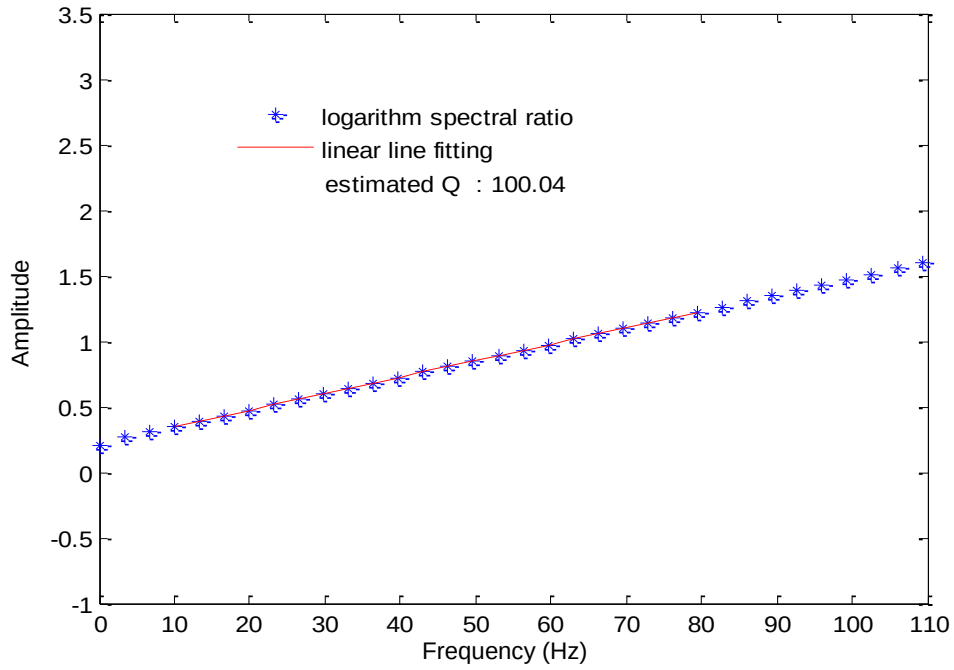

Figure 2.9. Q estimation using the seismic trace shown in Figure 2.5, which is created from the nonstationary convolution model with circle-shifted pulse $a(\tau, t-\tau)$.

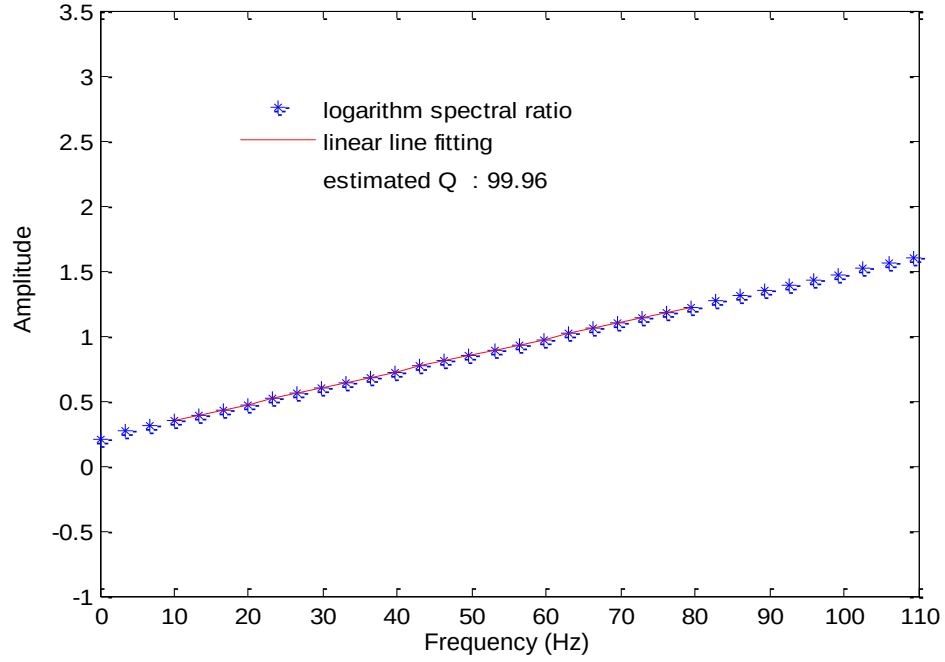

Figure 2.10. Q estimation using the seismic trace shown in Figure 2.5, which is created from the nonstationary convolution model with bandlimited pulse $a(\tau, t-\tau)$.

2.3 Reflectivity method for seismic modeling of stratified anelastic media

2.3.1 Theory of reflectivity method

The reflectivity method was originally developed by Fuchs and Müller (1971). Their work was followed by Kennett (1975, 1979, 1980), Kind (1976), Stephen (1977), Kennett and Kerry (1979), Kennett and Clark (1983). The reflectivity method is a wavenumber or slowness integration method, which computes the response of a model in the frequency-wavenumber domain and automatically includes contributions from all possible rays within the reflecting zone. In reflectivity modeling, the wavenumber or slowness integration is calculated by a matrix or propagator technique, which mainly deals with the computation of the reflection and transmission coefficients for plane waves, incident on a plane surface or a stack of homogenous layers. The coefficients for an interface are given analytically according to the Zoeppritz equations, and those for a stack of layers are derived by a recursive algorithm proposed by Kennett (1975). For a stratified earth model, the reflectivity method decomposes the propagating waves into downgoing waves and upgoing waves, and waves can be decoupled into P, SV and SH waves. The reflection, transmission and conversion of all wave modes can be fully described. In addition, the attenuation effect of anelastic media can be incorporated conveniently in the frequency domain using frequency-dependent complex velocity (Kennett, 1975; Cheng and Margrave, 2011a).

The implementation of the reflectivity method in this chapter is an update of the work of Ma et al (2004), which follows the algorithm described by Müller (1985). A brief introduction to the theory of reflectivity method is given below, and the modeling result is derived for P-SV waves. More details of the algorithm can be found in the tutorial given by Müller (1985).

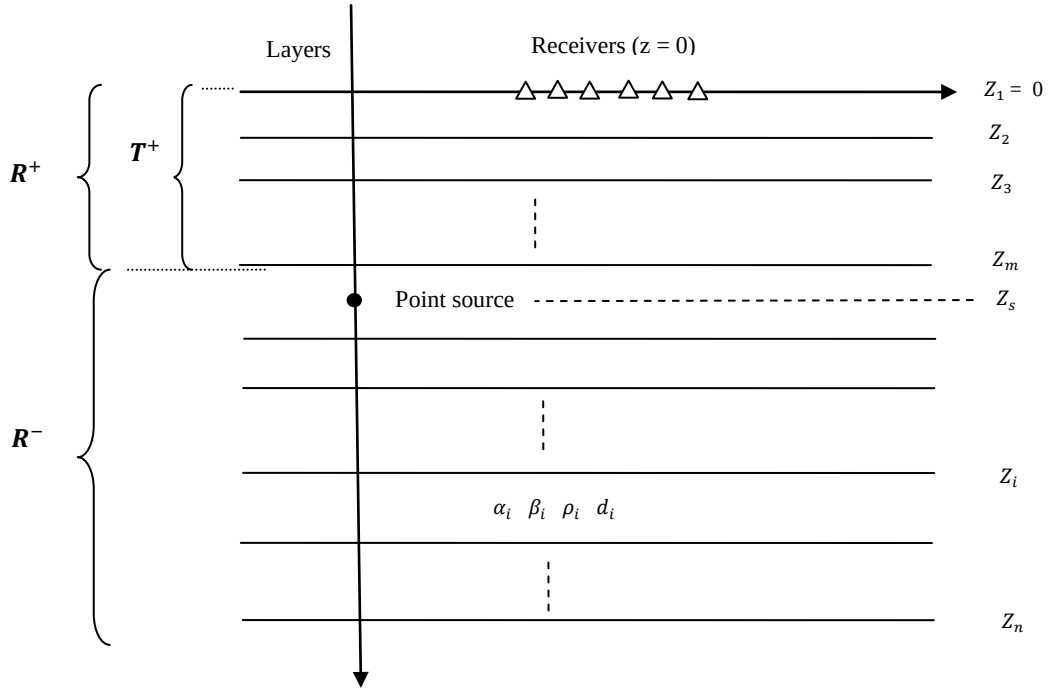

Figure 2.11. Layered media. α_i - p wave velocity; β_i - S wave velocity; ρ_i - density; d_i - thickness of the i-th layer; z_i - depth to the surface; z_s - depth of point source. $\boldsymbol{R}^+$ - total reflection coefficient matrix corresponds to the upper half space above source location; $\boldsymbol{R}^-$ - total reflection coefficient matrix corresponds to the lower half space below the source position; $\boldsymbol{T}^+$ - total transmission coefficient matrix corresponds to the upper half space.

Figure 2.11 shows a layered earth model with a single-force point source at depth z_s in layer m. For the i-th layer $(i = 0, 1, 2, \dots, n)$, α_i is the P wave velocity, β_i is the shear wave velocity, ρ_i is the density, d_i is the thickness of the layer, and z_i is the depth of the interface with respect to surface. For such a layered media, according to Snell's law, all waves travel horizontally with the same horizontal wavenumber k_h. Suppose the traveling plane wave has an incident angle θ_m at the interface of layer m, then we have

$$k_h = \frac{\omega}{\alpha_m} sin\theta_m, \qquad (2.10)$$

where ω is the angular frequency, θ_m is the angle between the wavefront normal and the interface normal in layer m . The horizontal slowness of traveling waves can be formulated as

$$u = \frac{k_h}{\omega} = \frac{sin\theta_m}{\alpha_m}, \tag{2.11}$$

and the vertical slowness a_i for P waves and b_i for SV waves respectively can be formulated as

$$a_i = \sqrt{\alpha_i{}^{-2} - u^2},\ b_i = \sqrt{\beta_i{}^{-2} - u^2}. \tag{2.12}$$

Assume that the single force $\boldsymbol{F}$ for the point source in Figure 2.11 has frequency dependent components (F_1, F_2, F_3) in Cartesian coordinate system. The displacement potentials of the single force can be given by slowness-integration with cylindrical coordinates (r, φ, z) as (Müller, 1985)

$$4\pi\rho_m\Phi_s = \varepsilon_1 \int_0^\infty sign(z - z_s) u J_0(u\omega r) e^{-j\omega a_m|z-z_s|}\, du + \varepsilon_2 \int_0^\infty \frac{u^2}{j a_m} J_1(u\omega r) e^{-j\omega a_m|z-z_s|}\, du, \tag{2.13}$$

and

$$4\pi\rho_m\Psi_s = \varepsilon_1 \int_0^\infty \frac{u}{j\omega b_m} J_0(u\omega r) e^{-j\omega b_m|z-z_s|}\, du + \varepsilon_2 \int_0^\infty \frac{sign(z-z_s)}{\omega} J_1(u\omega r) e^{-j\omega b_m|z-z_s|}\, du, \tag{2.14}$$

where ε_1 and ε_2 are given by

$$\varepsilon_1 = F_3,\ \varepsilon_2 = F_1 cos\varphi + F_2 sin\varphi. \tag{2.15}$$

In equation (2.13) and (2.14), $J_l(u\omega r)$ is the Bessel function of integer order $l = 0, 1$; Φ_s, Ψ_s are the displacement potentials for P waves and SV waves respectively. The traveling P-SV waves can be divided into downgoing and upgoing waves. For downgoing waves ($z > z_s$), the displacement potential $\Phi_s{}^{\mathrm{d}}$ for P waves and potential $\Psi_s{}^{\mathrm{d}}$ for SV waves can be obtained as (Müller, 1985)

$$4\pi\rho_m {\Phi_s}^{\mathrm{d}} = \int_0^{\infty} (\varepsilon_1 A_{\mathrm{s}1} J_0(u\omega r) + \varepsilon_2 A_{\mathrm{s}2} J_1(u\omega r)) e^{-j\omega a_m (z-z_m)}\, du, \quad (2.16)$$

and

$$4\pi\rho_m {\Psi_s}^{\mathrm{d}} = \int_0^{\infty} \frac{1}{ju\omega} (\varepsilon_1 C_{\mathrm{s}1} J_0(u\omega r) + \varepsilon_2 C_{\mathrm{s}2} J_1(u\omega r))\, e^{-j\omega b_m (z-z_m)} du, \quad (2.17)$$

where related scaling terms are given by

$$A_{\mathrm{s}1} = u e_{\alpha},\ A_{\mathrm{s}2} = \frac{u^2}{j a_m} e_{\alpha},\ C_{\mathrm{s}1} = \frac{u^2}{b_m} e_{\beta},\ C_{\mathrm{s}2} = j u e_{\beta}, \quad (2.18)$$

and

$$e_{\alpha} = \mathrm{e}^{\mathrm{j}\omega a_m (z_s - z_m)},\ e_{\beta} = \mathrm{e}^{\mathrm{j}\omega b_m (z_s - z_m)}. \quad (2.19)$$

For upgoing waves ($z < z_s$), similar expressions hold for the displacement potentials as

$$4\pi\rho_m {\Phi_s}^{\mathrm{u}} = \int_0^{\infty} (\varepsilon_1 B_{\mathrm{s}1} J_0(u\omega r) + \varepsilon_2 B_{\mathrm{s}2} J_1(u\omega r)) e^{j\omega a_m (z-z_m)}\, du, \quad (2.20)$$

and

$$4\pi\rho_m {\Psi_s}^{\mathrm{u}} = \int_0^{\infty} \frac{1}{ju\omega} (\varepsilon_1 D_{\mathrm{s}1} J_0(u\omega r) + \varepsilon_2 D_{\mathrm{s}2} J_1(u\omega r)) e^{j\omega b_m (z-z_m)}\, du, \quad (2.21)$$

where the related scaling terms are given by

$$B_{\mathrm{s}1} = -u {e_{\alpha}}^{-1},\ B_{\mathrm{s}2} = \frac{u^2}{j a_m} {e_{\alpha}}^{-1},\ D_{\mathrm{s}1} = \frac{u^2}{b_m} {e_{\beta}}^{-1},\ D_{\mathrm{s}2} = -j u {e_{\beta}}^{-1}. \quad (2.22)$$

The terms in equations (2.18), (2.22) can be regarded as source amplitudes for the downgoing and upgoing wavefields associated with point source, which can be reorganized as vectors

$$\mathbf{S}_{\mathrm{i}}^{\mathbf{d}} = \begin{pmatrix} A_{\mathrm{si}} \\ C_{\mathrm{si}} \end{pmatrix},\ \ \mathbf{S}_{\mathrm{i}}^{\mathbf{u}} = \begin{pmatrix} B_{\mathrm{si}} \\ D_{\mathrm{si}} \end{pmatrix},\ \mathrm{i} = 1, 2. \quad (2.23)$$

To obtain the wavefield at receiver level ($z = 0$), the complete upgoing wavefield in layer m that contains the point source should be determined first, which is the sum of direct upgoing waves and all possible reflections and multiples at the layer stacks above and below the level $z = z_m$. Suppose that $\mathbf{R}^{-}$ and $\mathbf{R}^{+}$ represent the P-SV reflectivity matrices for the part

$z > \mathrm{z}_m$ and the part $z \leq \mathrm{z}_m$ respectively. $\mathbf{R}^-$ and $\mathbf{R}^+$ are formed from the reflection coefficients for the interaction between P waves and SV waves and can be specified as

$$\mathbf{R}^- = \begin{pmatrix} \mathrm{R}_{\mathrm{pp}}^{\mathrm{d}} & \mathrm{R}_{\mathrm{sp}}^{\mathrm{d}} \\ \mathrm{R}_{\mathrm{ps}}^{\mathrm{d}} & \mathrm{R}_{\mathrm{ss}}^{\mathrm{d}} \end{pmatrix}, \mathbf{R}^+ = \begin{pmatrix} \mathrm{R}_{\mathrm{pp}}^{\mathrm{u}} & \mathrm{R}_{\mathrm{sp}}^{\mathrm{u}} \\ \mathrm{R}_{\mathrm{ps}}^{\mathrm{u}} & \mathrm{R}_{\mathrm{ss}}^{\mathrm{u}} \end{pmatrix}. \tag{2.24}$$

Then, the amplitude vectors for the complete upgoing wavefield in layer m, similar to $\mathbf{S}_{1,2}^{\mathbf{d}}$ and $\mathbf{S}_{1,2}^{\mathbf{u}}$, can be given as (Müller, 1985)

$$\begin{aligned} \boldsymbol{V}_{\mathrm{i}} &= (\mathbf{I} + \mathbf{R}^-\mathbf{R}^+ + \mathbf{R}^-\mathbf{R}^+\mathbf{R}^-\mathbf{R}^+ + \cdots)\left(\mathbf{S}_{\mathrm{i}}^{\mathbf{u}} + \mathbf{R}^-\mathbf{S}_{\mathrm{i}}^{\mathbf{d}}\right) \\ &= [\mathbf{I} + \mathbf{R}^-\mathbf{R}^+]^{-\mathbf{1}}\left(\mathbf{S}_{\mathrm{i}}^{\mathbf{u}} + \mathbf{R}^-\mathbf{S}_{\mathrm{i}}^{\mathbf{d}}\right), (\mathrm{i} = 1, 2), \end{aligned} \tag{2.25}$$

where $\mathbf{I}$ is an identity matrix. Assume that $\mathbf{T}^+$ is the transmissivity matrix between the layer $z = {z_m}^+$ and layer $z = {z_1}^- = 0^-$. The amplitude vectors for the wavefields at $z \leq 0$ can be obtained as

$$\boldsymbol{V}_{\mathrm{i}}^{\mathbf{0}} = \begin{pmatrix} B_{\mathrm{i}}^{\mathbf{0}} \\ D_{\mathrm{i}}^{\mathbf{0}} \end{pmatrix} = \mathbf{T}^+\boldsymbol{V}_{\mathrm{i}}\ , (\mathrm{i} = 1, 2). \tag{2.26}$$

So, the displacement potentials for P-SV waves at $z \leq 0$ are

$$4\pi\rho_m\Phi^0 = \int_0^\infty (\varepsilon_1 B_1^{\mathbf{0}} J_0(u\omega r) + \varepsilon_2 B_2^{\mathbf{0}} J_1(u\omega r)) e^{j\omega a_0 z}\, du, \tag{2.27}$$

and

$$4\pi\rho_m\Psi^0 = \int_0^\infty \frac{1}{ju\omega} (\varepsilon_1 D_1^{\mathbf{0}} J_0(u\omega r) + \varepsilon_2 D_2^{\mathbf{0}} J_1(u\omega r)) e^{j\omega b_0 z}\, du. \tag{2.28}$$

Finally, the displacement components can be calculated from the potentials, and the far-field results at level $z = 0$ are

$$4\pi\rho_m \begin{pmatrix} \mathrm{u_r} \\ \mathrm{u_z} \end{pmatrix} = \omega \sum_{\mathrm{i}=1}^{2} \varepsilon_{\mathrm{i}} \int_0^\infty \mathbf{J}_{\mathrm{i}}\mathbf{U}\mathbf{T}^+\boldsymbol{V}_{\mathrm{i}}\, du, \tag{2.29}$$

where $\mathrm{u_r}$, $\mathrm{u_z}$ are radial and vertical components of displacements respectively. The matrices $\mathbf{J}_{\mathrm{i}}$, $\mathbf{U}$ in equation (2.29) are given by

$$\mathbf{J}_1 = \begin{pmatrix} -J_1(u\omega r) & 0 \\ 0 & jJ_0(u\omega r) \end{pmatrix}, \ \mathbf{J}_2 = \begin{pmatrix} J_0(u\omega r) & 0 \\ 0 & jJ_1(u\omega r) \end{pmatrix}, \qquad (2.30)$$

and

$$\mathbf{U} = \begin{pmatrix} u & b_o \\ a_o & -u \end{pmatrix}. \qquad (2.31)$$

The displacements given by equation (2.29) are valid for the case that the velocities α_0, β_0 and density ρ_0 of the upper half-space are of nonzero values. For the calculation of a realistic seismogram, the free-surface condition at $z = 0$ can be approximated by choosing α_0, ρ_0 as the values of air, and $\beta_0 \ll \alpha_0$. More accurate free-surface condition can be obtained by the limiting process $\alpha_0 \to 0$, $\beta_0 \to 0$, $\rho_0 \to 0$ (Müller, 1985). The parameters α_0, β_0, ρ_0 are contained in the matrix multiplication $\mathbf{UT}^+$ in equation (2.29). By taking the limit, $\mathbf{UT}^+$ becomes

$$\mathbf{UT}^+ = \mathbf{H}\widetilde{\mathbf{T}}, \qquad (2.32)$$

where $\widetilde{\mathbf{T}}$ is the transmissivity matrix between the layer $z = z_m{}^+$ and layer $z = z_1{}^+ = 0^+$ for upgoing waves, and $\mathbf{H}$ is given by

$$\mathbf{H} = \frac{2}{(1-2\beta_1{}^2u^2)^2+4\beta_1{}^4u^2a_1b_1} \cdot \begin{pmatrix} 2\beta_1{}^2ua_1b_1 & (1-2\beta_1{}^2u^2)b_1 \\ (1-2\beta_1{}^2u^2)a_1 & -2\beta_1{}^2ua_1b_1 \end{pmatrix}. \qquad (2.33)$$

Then, equation (2.29) combined with equation (2.32) gives the exact free-surface response of a layered media for a single force point source.

The reflectivity matrices $\mathbf{R}^+$, $\mathbf{R}^-$ and transmissivity matrices $\mathbf{T}^+$, $\widetilde{\mathbf{T}}$ mentioned above for the layer stack can be calculated from the reflection coefficients and transmission coefficients of layer interfaces, using a recursive scheme (Kennett, 1974; Müller, 1985). The tutorial by Müller (1985) gives a detailed description about the recursive algorithm.

The result in equation (2.29) is due to single force $\boldsymbol{F} = (F_1, F_2, F_3)$ with frequency dependent components. The extension to the case with source wavelets in time domain is

straightforward. Let F_i be the Fourier transform of the corresponding time-domain component, then the seismogram with time-domain displacements can be obtained from the inverse Fourier transform of the results given by equation (2.29).

The reflectivity method has the capacity to compute a complete wavefield for a given layered model, including all possible wave types and associated interactions. Such a capacity is the main advantage of reflectivity method. In addition, computing a partial media response is very convenient for the reflectivity method, which may be of great practical importance. For instance, the primary only reflection seismogram can be obtained by setting $\boldsymbol{V}_{\mathrm{i}} = \mathbf{R}^{-}\mathbf{S}_{\mathrm{i}}^{\mathbf{d}}$. By choosing the components of $\boldsymbol{V}_{\mathrm{i}}$, various partial results can be obtained. It is worthwhile to include some of the partial results as options in the computer program. Such a flexibility of reflectivity method is a main advantage compared to wave equation methods that usually gives the complete response of the media only.

2.3.2 Practical issues for the implementation of reflectivity method

2.3.2.1 Incorporation of Q attenuation

For realistic media, the absorption of seismic waves should be taken into account. Since the seismogram calculation is conducted in frequency-slowness domain, the most convenient way to incorporate attenuation is to make the seismic velocities complex and frequency dependent. The adoption of complex velocities can incorporate realistic attenuation into seismic modeling (Mallick and Frazer, 1987). The frequency dependency of velocity reflects the dispersion of seismic waves, which is connected with absorption and is a requirement for causality (Futterman, 1962, Müller, 1985; Mallick and Frazer, 1987). Depending on the dependency of Q on frequency, i.e. different Q laws, there are various ways to construct the complex and frequency (Müller, 1985; Mallick and Frazer, 1987). For the reflectivity method for

stratified anelastic media described in this chapter, we assume that Q is independent of frequency, and the complex velocity adopted in our implementation can be approximated as when $Q \gg 1$ (Müller, 1985)

$$v(\omega) \approx v(1 + \frac{1}{\pi Q} ln \frac{\omega}{\omega_r} + \frac{j}{2Q}), \tag{2.34}$$

where ω_r is a reference frequency, v is the real part of complex velocity $v(\omega_r)$.

2.3.2.2 Windowing of integral signal

The synthetic seismogram is obtained by integration over slowness and inverse Fourier transform, as shown in equation (2.29). Practical computation is bandlimited because the integration is conducted within some finite frequency-band and limited slowness-range. Such a truncation of the integral is equivalent to convolving the desired function with a certain kernel, which can distort the desired impulse response. To improve the results, it is necessary to use some window to taper the signal at its limits .

In the frequency domain, we use a two-sided Hanning window to taper the signal, which is given as

$$W_F(\omega) = \begin{cases} 1 & |\omega| \le \omega_1 \\ \frac{1}{2}\left(1 + \cos\pi \frac{|\omega| - \omega_1}{\omega_2 - \omega_1}\right) & \omega_1 < |\omega| < \omega_2 \\ 0 & |\omega| \ge \omega_2 \end{cases}, \tag{2.35}$$

For the slowness integration in equation (2.29), vertically traveling waves have zero horizontal slowness and should be included in the resulting synthetic seismograms. Then, a one-sided Hanning window is used to taper the signal, which is given as

$$W_S(u) = \begin{cases} 1 & u \le u_1 \\ \frac{1}{2}\left(1 + cos\pi \frac{u-u_1}{u_2-u_1}\right) & u_1 < u < \omega_2 \\ 0 & u \ge u_2 \end{cases}. \qquad (2.36)$$

2.3.2.3 Treatment of aliasing

The reflectivity method computes the reflectivity function in the frequency-wavenumber domain and then transforms it back to time-distance domain. Like any other frequency-domain techniques for seismic modeling, the reflectivity method needs to address the aliasing problem appropriately. In order to avoid aliasing, the calculation of the reflectivity function should be adequately sampled in both wavenumber domain and frequency domain.

The integral in equation (2.29) is oscillatory in that the argument of the Bessel function is the product of frequency, slowness and travel distance. A large number of steps are necessary to compute the integral accurately when ωr is large. To avoid spatial aliasing, the step size for slowness should be inversely proportional to ωr. Mallick and Frazer (1987) use a step size of

$$\Delta u \le \pi/(5\omega x_{max}), \qquad (2.37)$$

where x_{max} is the largest offset of interest. To reduce the computation cost, Frazer (1978) and Frazer and Gettrust (1984) propose a generalized Filon method to compute the integral, which reduces the step size to be proportional to $(\omega r)^{-1/2}$. We will choose Δu based on equation (2.37).

To avoid temporal aliasing, the step size $\Delta\omega$ of frequency ω should be small. Small $\Delta\omega$ means a greater computation cost. As an alternative to small $\Delta\omega$, a complex frequency technique is proposed to conduct the integration over frequency (Phinney, 1965; Bouchon and Aki, 1977; Spudich and Ascher, 1983). A complex frequency $\omega + ja$ instead of ω is adopted, which means

that, instead of desired result $f(t)$, a dampened version $f(t)e^{-at}$ is calculated, and the desired result is recovered from the dampened version by applying a gain correction.

2.3.3 Numerical test

A two layer earth model is used to evaluate the reflectivity method, and the physical parameters of the layered media are shown in table 2.1. The point source at depth $z = 5m$ radiates both P and S waves, and has a minimum-phase wavelet with a dominant frequency of $40Hz$. The receivers are located at the surface. The reflectivity modeling results for P-SV waves are shown in Figure 2.12 and 2.13. We can see that all the events are modeled including direct P and S waves, reflected PP, PS/SP, SS waves and multiples. For the reflectivity method, we can choose to model the primary reflection events only, and the results are shown in Figure 2.14 and 2.15. Since a two layer model is used and the source location is close to surface, the PS and SP waves have nearly the same traveltime. In Figure 2.14 and 2.15, each trace has three events corresponding to PP, PS/SP, SS waves respectively. We can see that reflectivity method can model all kinds of waves with flexibility.

Table 2.1 A two layer earth model

Layer index	P wave velocity (m/sec)	S wave velocity (m/sec)	Density (kg/m^3)	Thickness (km)	Q_P	Q_S
1	2500	1600	1800	1	10000	10000
2	3200	1800	2100	2	10000	10000

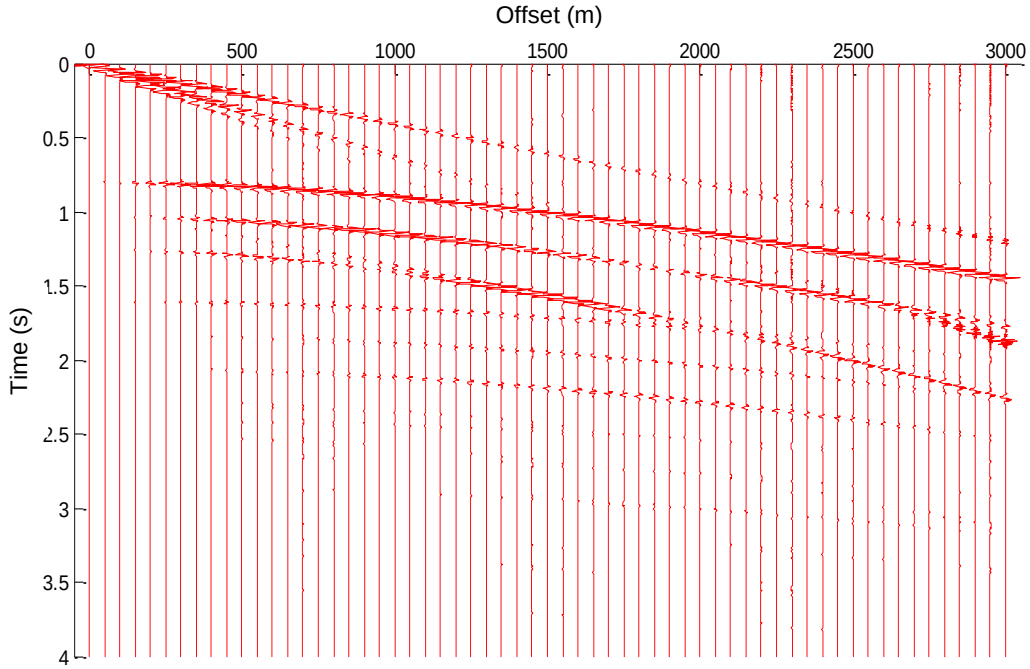

Figure 2.12. Vertical components of P-SV waves for the two-layer model shown in table 2.1.

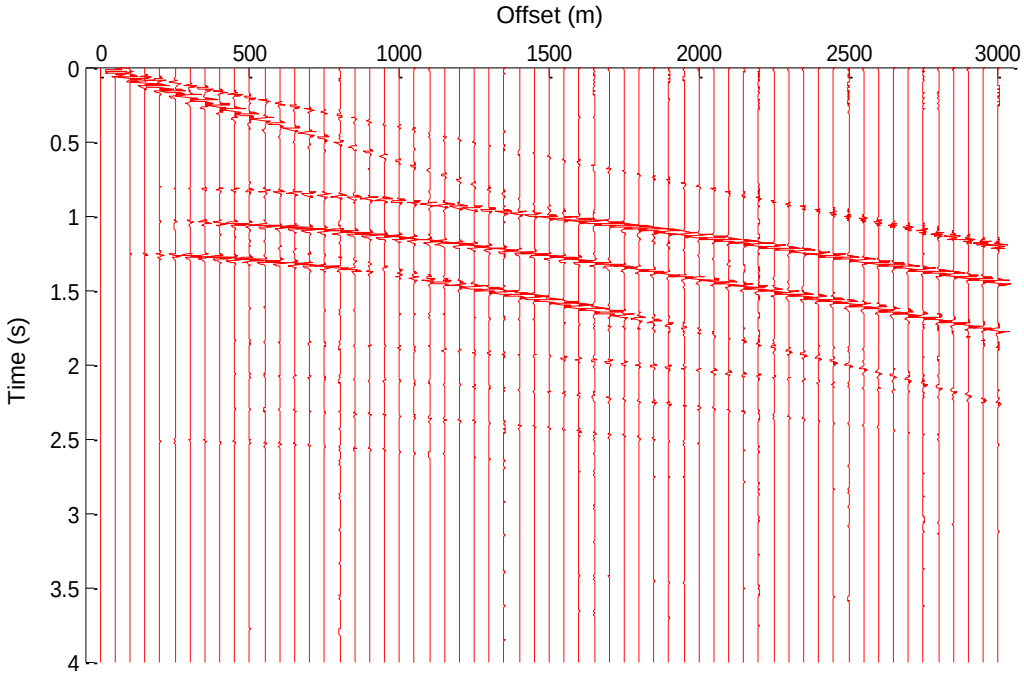

Figure 2.13. Radial components of P- SV waves for the two-layer model shown in table 2.1.

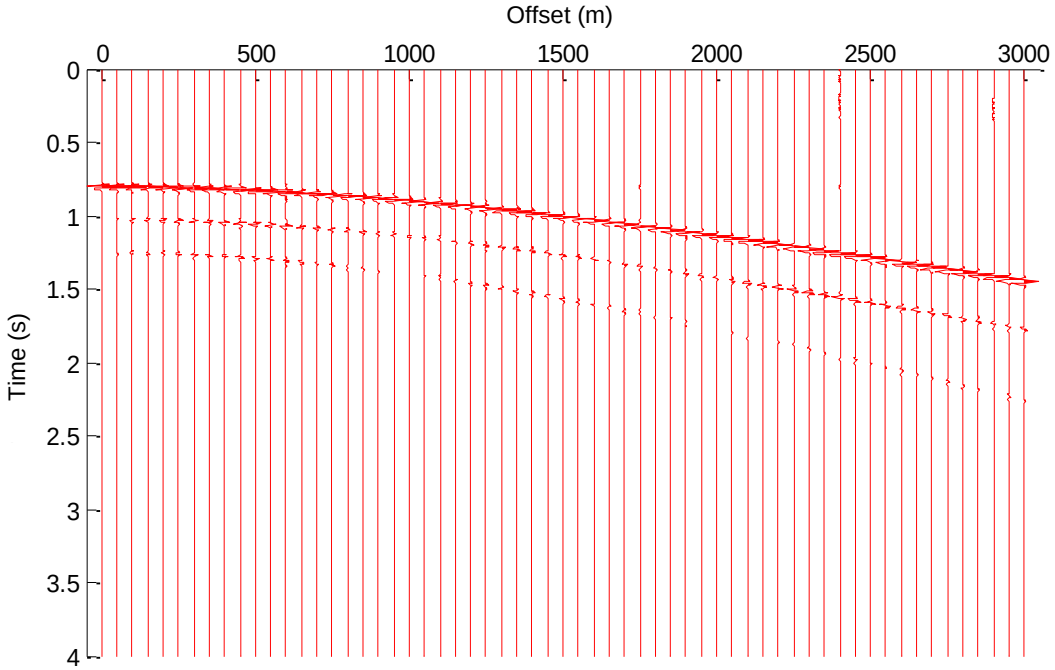

Figure 2.14. Vertical components of primary reflection events for the earth model shown in table 2.1.

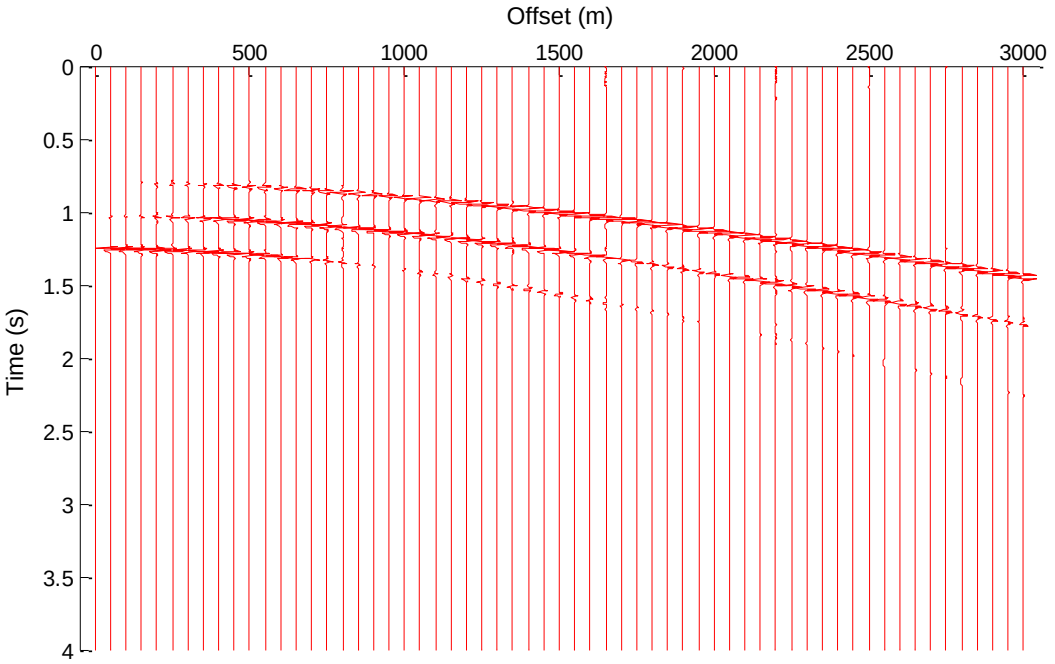

Figure 2.15. Radial components of primary reflection events for the earth model shown in table 2.1.

To evaluate the amplitudes of the events for the reflectivity method, we use the vertical components of the primary reflection events shown in Figure 2.14 as an example to derive the reflection coefficients for PP and SS waves. First, a one-layer model is used to estimate the amplitudes for incident waves that experience the same geometrical spreading effect as the reflected waves. This one layer model has the same physical parameters as the first layer of the earth model shown in table 2.1, while the point source is shifted to the image point $z = 1995m$ with respect to the interface in the two layer model and the receivers are remained at the same positions. The vertical components of the direct arrival waves for this one layer model are shown in Figure 2.16. Figure 2.17 shows the amplitudes of the direct P waves in Figure 2.16 and the amplitudes of the reflected PP waves in Figure 2.14, from which the reflection coefficients for the PP waves can be derived. From Figure 2.18, we can see that the derived PP reflection coefficients match the Zoeppritz ones perfectly before the critical incident angle is reached at an offset around $1600m$. Similarly, the reflection coefficients for SS waves are derived and shown in Figure 2.19, which match theoretical results as well. We do not expect a match near or beyond the critical angle because the reflectivity method calculates spherical reflection coefficients through an integration over plane waves while the Zoeppritz equations are for a single plane wave.

In order to evaluate the incorporation of Q attenuation for the modeling method, we use a two-layer model shown in table 2.2 to test the reflectivity method, which has the same physical parameters, source locations, source wavelet and receiver stations as the two-layer model shown in table 2.1 except the Q values for P wave and S wave. The vertical components of the primary reflection events are shown in Figure 2.20, which corresponds to the case without Q attenuation shown in Figure 2.14. Using the trace with an offset of $1000m$ as an example, a comparison

between modeling with Q attenuation and without Q attenuation is demonstrated by Figure 2.21. The amplitude decays due to Q attenuation is obvious. Figure 2.22 shows the amplitude spectra of the PP events in Figure 2.21. Then, the spectral-ratio method is used to estimate Q_P, as shown in Figure 2.23. The estimated $Q_P = 83.8$ is consistent with the Q model. Similarly, using the SS events shown in Figure 2.21, Q_S is estimated to be 61.6, as shown in Figure 2.24, which is close to theoretical value as well. We can see that the reflectivity method can incorporate the Q attenuation with sufficient accuracy.

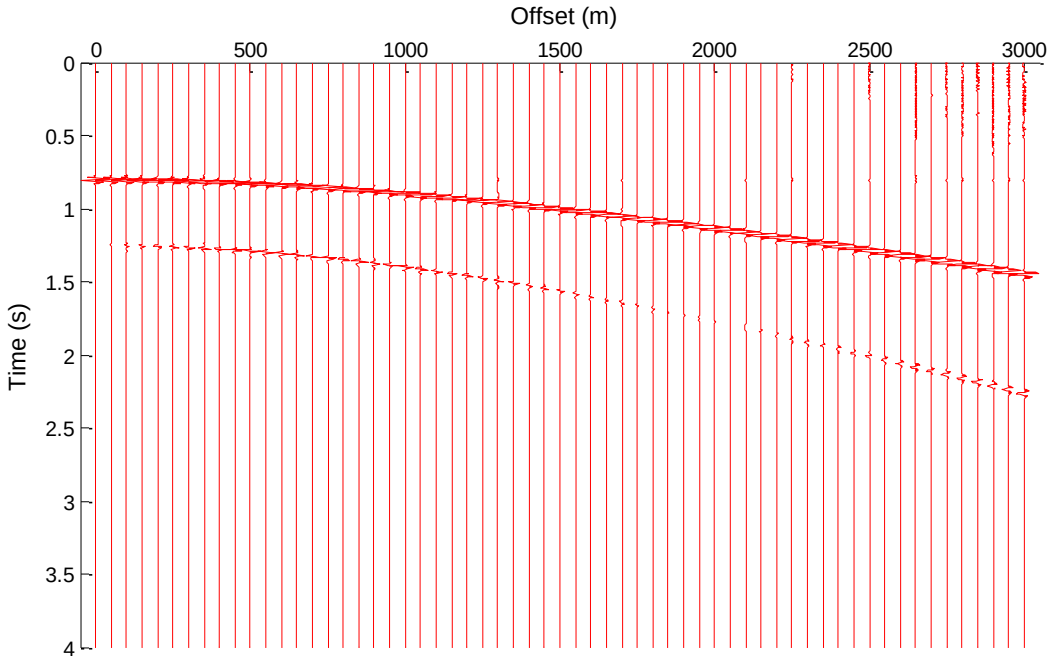

Figure 2.16. Vertical components of the direct arrivals of a homogenous media with the physical parameters of the layer 1 shown in table 1 and a point source at depth $z = 1995m$.

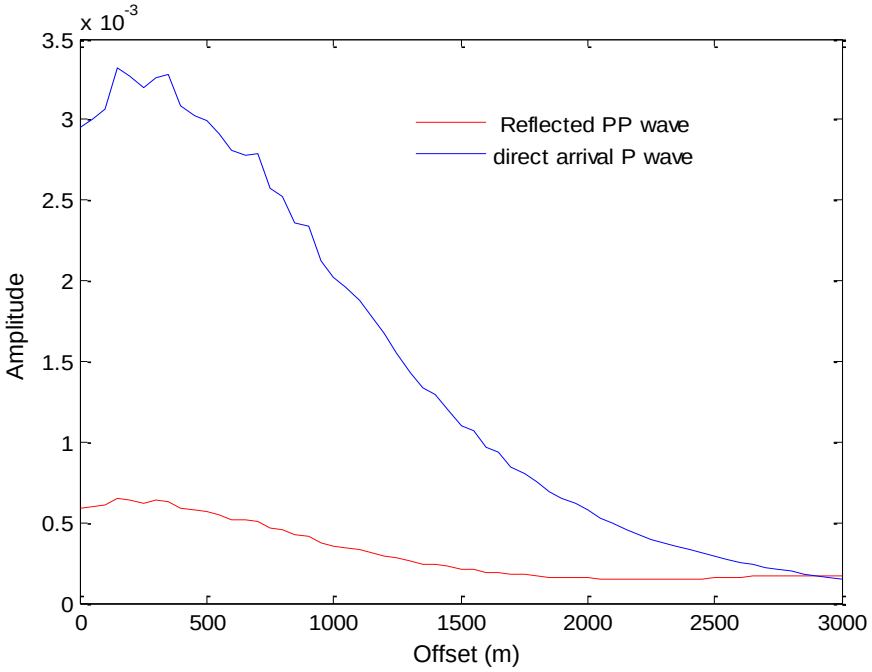

Figure 2.17. Amplitudes of the direct P waves in Figure 2.16 and reflected PP waves in Figure 2.16.

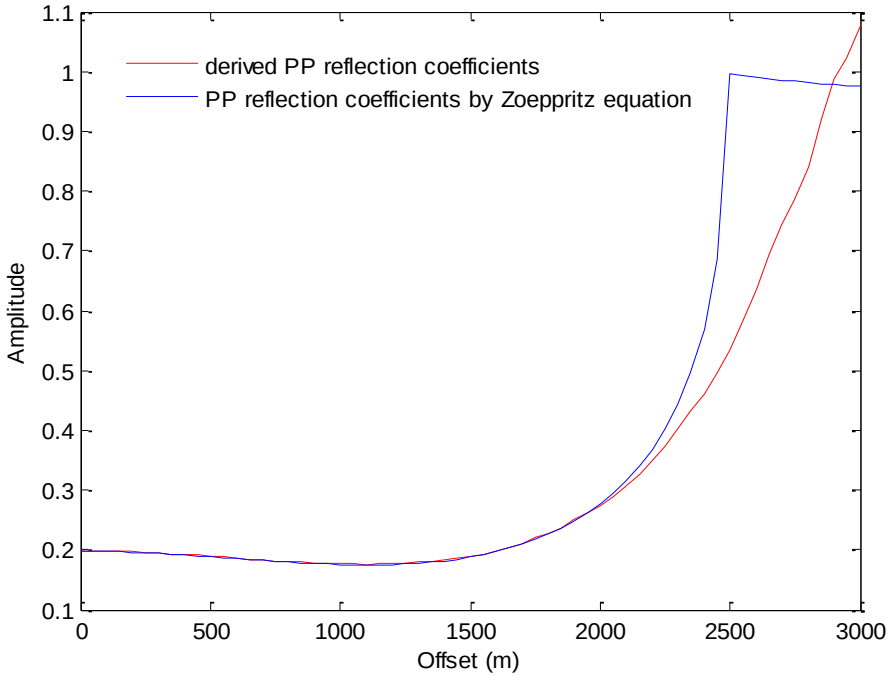

Figure 2.18. Comparison of PP reflection coefficients.

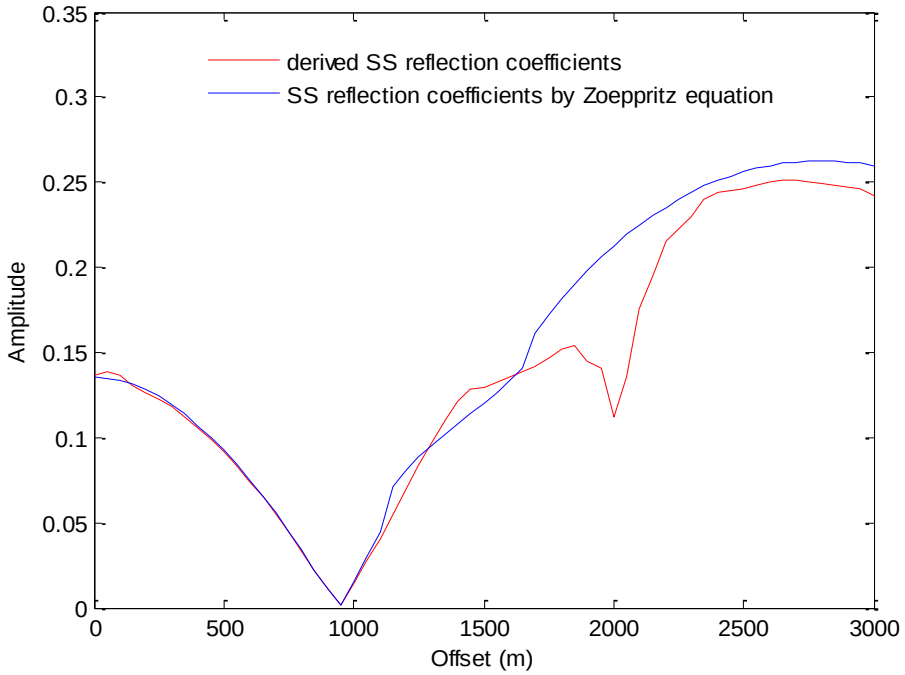

Figure 2.19. Comparison of SS reflection coefficients.

Table 2.2 A two layer earth model

Layer index	P wave velocity (m/sec)	S wave velocity (m/sec)	Density (kg/m^3)	Thickness (km)	Q_P	Q_S
1	2500	1600	1800	1	80	60
2	3200	1800	2100	2	80	60

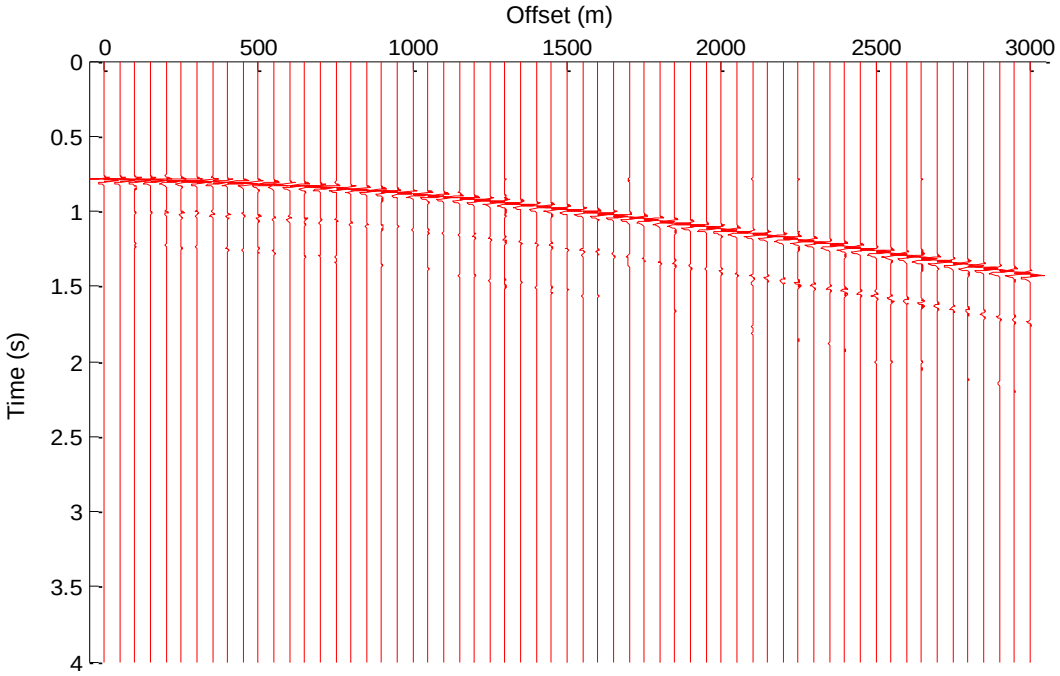

Figure 2.20. Vertical components of primary reflection events for the earth model shown in table 2.2.

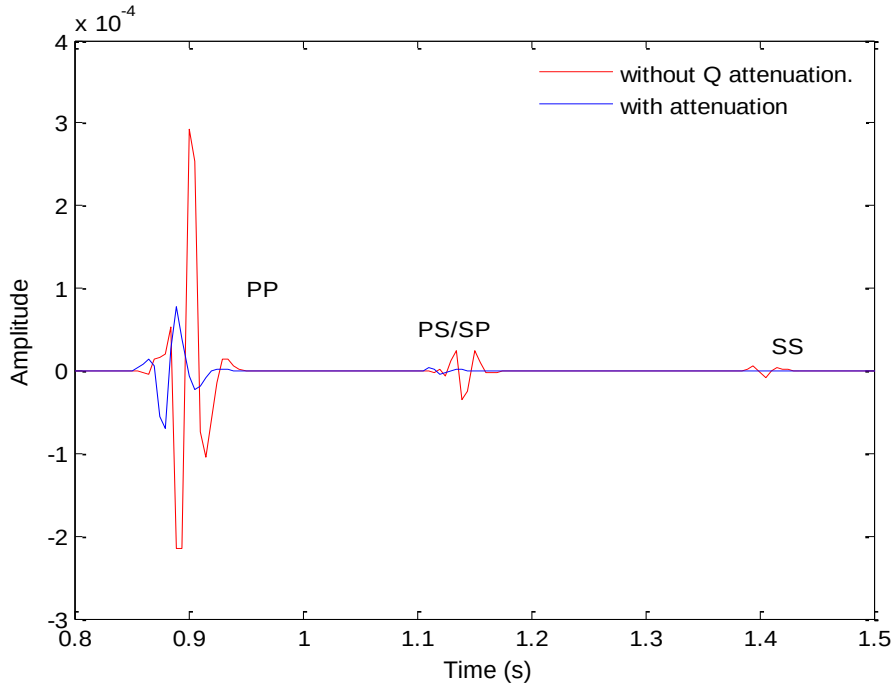

Figure 2.21. Comparison of the traces with an offset of $1000m$ shown in Figure 2.14 and Figure 2.20 respectively.

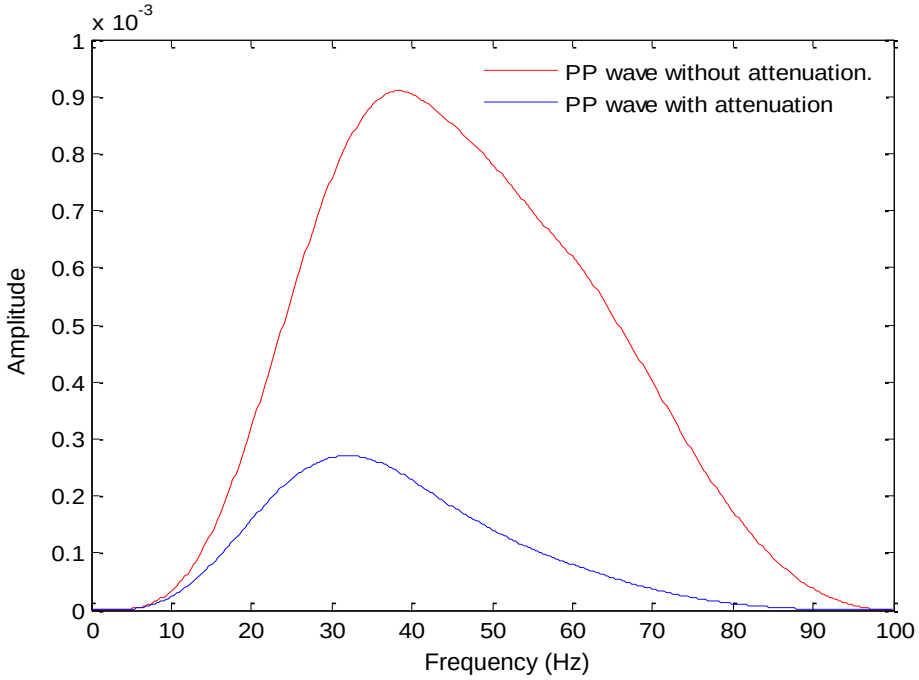

Figure 2.22. Amplitude spectra of the PP events shown in Figure 2.21.

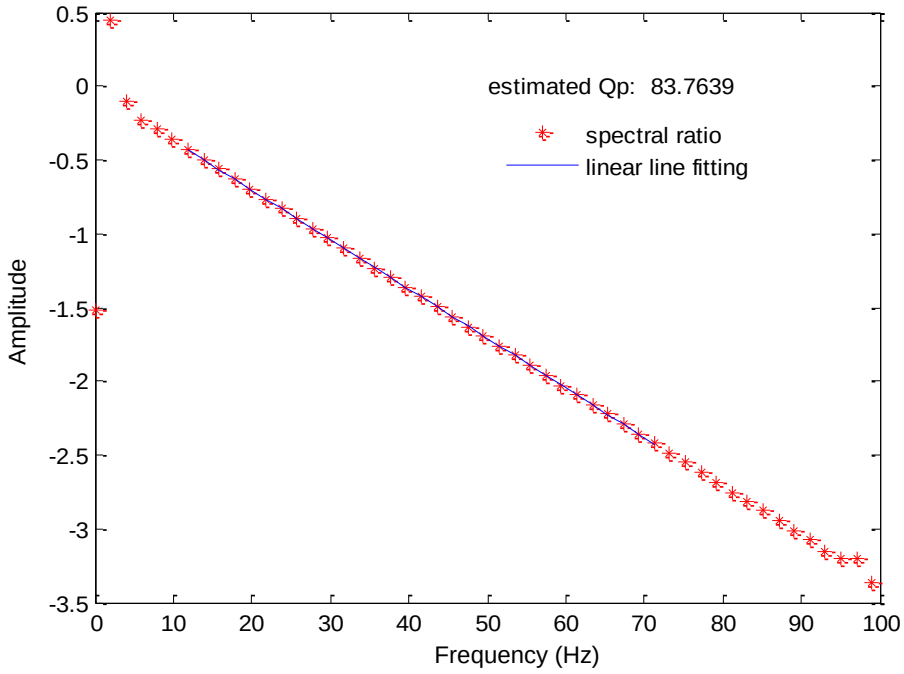

Figure 2.23 . Q_P estimation using spectral-ratio method for the PP events shown in Figure 2.21.

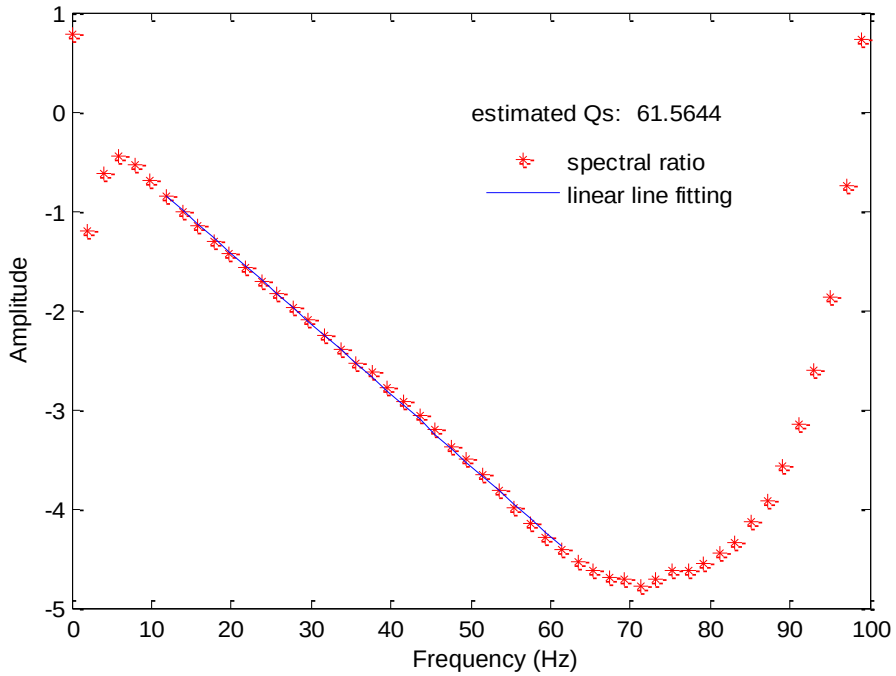

Figure 2.24. Q_S estimation using spectral-ratio method for the SS events shown in Figure 2.21.

2.4 Finite-difference simulation of wave propagation in viscoelastic media

2.4.1 Basic theory

For simplicity, we confine our discussion to 1D case. According to Hooke's law, stress is directly proportional to the instantaneous strain in a perfectly elastic media. For realistic media such as earth, the stress depends on both the instantaneous strain and the history of strain. Christensen (1982) gives a theoretical description of the viscoelastic behavior of material. For the 1D special case of pure shear wave in an isotropic homogenous material, the relation between stress σ and strain ε can be formulated as

$$\sigma = \Lambda * \dot{\varepsilon} = \int_{-\infty}^{t} \Lambda(t-\tau)\dot{\varepsilon}\,(\tau)d\tau, \qquad (2.38)$$

where $*$ denotes time convolution and an overhead dot indicates partial differentiation with respect to time. Λ is the relaxation function that determines the behaviour of material, which can be given as (Liu et al., 1976; Carcione et al., 1988c; Blanch et al., 1993)

$$\Lambda(t) = M_R \left[1 - \sum_{l=1}^{L} \left(1 - \frac{\tau_{\varepsilon l}}{\tau_{\sigma l}}\right) e^{-\frac{t}{\tau_{\sigma l}}}\right] H(t), \qquad (2.39)$$

where $M_R = \Lambda(\infty)$ is the relaxed modulus of the media (Pipkin, 1986) and $H(t)$ is the Heaviside function, $\tau_{\varepsilon l}$ and $\tau_{\sigma l}$ are the strain and stress relaxation times of the l-th relaxation mechanism. In equation (2.39), the relaxation function is described by L parallel connected standard linear solids (Blanch et al., 1993), which is also the best Padé approximation of a constant Q (Day and Minster, 1984).

The Fourier transform of the time derivative of the relaxation function is identified as the complex bulk modulus of the media, which can be given as (Carcione et al., 1987)

$$M_c(\omega) = M_R \left[1 - \mathrm{L} + \sum_{l=1}^{L} \frac{1+\omega\tau_{\varepsilon l}}{1+\omega\tau_{\sigma l}}\right]. \qquad (2.40)$$

The quality factor is then defined as

$$Q(\omega) = \frac{Re(M_c(\omega))}{Im(M_c(\omega))}. \qquad (2.41)$$

In seismic application, Q is usually assumed to be constant or slowly frequency varying within frequency range of interest. This assumption is supported by experimental results (Spencer, 1981; Murchy, 1982). To approximate a constant Q over a targeted frequency range based on equation (2.39) and (2.40), $1/\tau_{\sigma l}$ should be distributed logarithmically over the interested frequency band (Emmerich and Korn, 1987), and the magnitude of Q is determined by the difference $\tau_{\varepsilon l} - \tau_{\sigma l}$ between strain relaxation time and stress relaxation time (Liu et al., 1976; Blanch et al., 1993). An approximation to constant Q can be obtained through this approach with sufficient accuracy.

Now, following Robertsson et al. (1994), we will derive the equations for viscoelastic media from the stress relaxation function. From the definition of stress and strain, we have

$$\sigma = -p, \tag{2.42}$$

and

$$\dot{\varepsilon} = \frac{\partial v}{\partial x}, \tag{2.43}$$

where p is pressure and v is particle velocity. From equation (2.38), (2.42) and (2.43), we have

$$-\dot{p} = \dot{G} * \dot{\varepsilon}, \tag{2.44}$$

where the overhead dot denotes partial differentiation with respect to time. Substitution of equation (2.39) into equation (2.44) yields

$$-\dot{p} = M_R \left[1 - \sum_{l=1}^{L} \left(1 - \frac{\tau_{\varepsilon l}}{\tau_{\sigma l}}\right)\right] \frac{\partial v}{\partial x} + \sum_{l=1}^{L} \xi_l, \tag{2.45}$$

where the variables ξ_l are so-called memory variables (Carcione et al., 1988c), which are given by

$$\xi_l = M_R \left[\frac{1}{\tau_{\sigma l}} \left(1 - \frac{\tau_{\varepsilon l}}{\tau_{\sigma l}}\right) e^{-\frac{t}{\tau_{\sigma l}}}\right] H(t) * \frac{\partial v}{\partial x}, \quad 1 \le l \le L. \tag{2.46}$$

Taking the time derivative of equation (2.46) leads to

$$\dot{\xi}_l = -\frac{1}{\tau_{\sigma l}} \xi_l + M_R \frac{1}{\tau_{\sigma l}} \left(1 - \frac{\tau_{\varepsilon l}}{\tau_{\sigma l}}\right) \frac{\partial v}{\partial x}, \quad 1 \le l \le L. \tag{2.47}$$

From Newton's second law, we get the equation of motion for 1D case as

$$\rho \dot{v} = -\frac{\partial p}{\partial x}, \tag{2.48}$$

where ρ is the density.

Wave propagation in the 1D viscoelastic media with *L* sets of linear solids is entirely governed by equation (2.45), (2.47) and (2.48).

2.4.2 Finite difference scheme for implementation

There are various finite-difference schemes to solve the equations (2.45), (2.47) and (2.48). Finite-difference schemes are intrinsically dispersive (Dablain, 1986). In order not to

confuse this numerical dispersion with the physical dispersion of absorptive media, it is important to adopt highly accurate schemes to simulate viscoelastic wave propagation while keeping the computation cost at moderate level. We will introduce the $O(2,4)$ scheme proposed by Robertsson et al. (1994), which is second-order accurate in time and fourth-order accurate in space. Their $O(2,4)$ scheme is implemented by a staggered grid scheme, which can be defined for one relaxation mechanism as

$$\begin{cases} \frac{p_i^{j+\frac{1}{2}}-p_i^{j-\frac{1}{2}}}{\Delta t} = -M_R \frac{\tau_{\varepsilon l}}{\tau_{\sigma l}} \frac{-v^j_{i+\frac{3}{2}}+27v^j_{i+\frac{1}{2}}-27v^j_{i-\frac{1}{2}}+v^j_{i-\frac{3}{2}}}{24\Delta x} \\ \qquad\qquad -\frac{1}{2}(\xi_i^{j+1/2}+\xi_i^{j-1/2}) \\ \frac{\xi_i^{j+\frac{1}{2}}-\xi_i^{j-\frac{1}{2}}}{\Delta t} = -M_R \frac{1}{\tau_{\sigma l}}\left(\frac{\tau_{\varepsilon l}}{\tau_{\sigma l}}-1\right) \frac{-v^j_{i+\frac{3}{2}}+27v^j_{i+\frac{1}{2}}-27v^j_{i-\frac{1}{2}}+v^j_{i-\frac{3}{2}}}{24\Delta x}, \\ \qquad\qquad -\frac{1}{2\tau_{\sigma l}}\left(\xi_i^{j+\frac{1}{2}}+\xi_i^{j-\frac{1}{2}}\right) \\ \rho \frac{v_i^{j+1/2}-v_i^{j-1/2}}{\Delta t} = -\frac{-p^j_{i+3/2}+27p^j_{i+1/2}-27p^j_{i-1/2}+p^j_{i-3/2}}{24\Delta x} \end{cases} \tag{2.46}$$

where Δt and Δx are time step and space step respectively, the indices i and j correspond to time and space coordinates respectively. The 1D scheme described above can be extended to 2D or 3D cases easily. The details about the higher dimension scheme can be found in Robertsson et al. (1994).

2.4.3 Numerical examples

The synthetic VSP and reflection data in this section are generated from the Tiger software developed by the SINTEF research group. To incorporate the Q attenuation into the seismic modeling, we use a viscoacoustic media to which The Tiger software gives time-domain finite-difference solution in 3D. The source wavelet used for seismic modeling is a Ricker wavelet with the peak at $0.1s$ and a maximum frequency of $70Hz$.

Figure 2.25 shows a simple two-layer velocity model and the zero-offset VSP data with a constant Q of 50. It is clear that the downgoing wavelets decay with traveltime or depth. To make a comparison between the two cases with constant-Q attenuation and without Q attenuation, we obtain the VSP data for the corresponding acoustic case. Figure 2.26 shows the VSP records at depths of $150m$ and $450m$ for these two cases. We can see that the downgoing wavelet experiences geometrical spreading, transmission loss and Q attenuation, and the former two factors are the main sources of energy loss. To conduct Q estimation, some tapering window should be employed to retrieve the downgoing wave from the VSP records. For the traces shown in Figure 2.26, a box-car window is sufficient. Figure 2.27 shows the logarithmic spectral ratios calculated using the wavelets shown in Figure 2.26. The estimated Q values for the viscoacoustic and acoustic cases are 51.6 and 874.8 respectively, which are consistent with the theoretical Q values. The results show that the finite-difference scheme incorporates the attenuation of absorptive media with sufficient accuracy.

Using the velocity model in Figure 2.25 and a layered Q model of $Q_1 = 50$ and Q_2=100, another VSP data are obtained. The two VSP traces at depth $150m$ and $450m$ are shown in Figure 2.28. Using these two traces to conduct Q estimation by spectral ratio method, the corresponding logarithmic spectral ratios are shown in Figure 2.29. Choosing a frequency-band of $10 - 60Hz$, the estimated Q value is 62.3. Based on the relation between average Q and interval Q given in equation (2.9), the theoretical average Q value from depth $150m$ to depth $450m$ is 60. Therefore, Q estimation theoretically gives average Q estimation and can work under layered Q subsurface, then interval Q can be derived from the average Q.

Figure 2.30 shows a velocity and Q model with three layers. A synthetic shot record is generated from this three-layer model, as shown in Figure 2.31. The zero-offset trace after first break removal is shown in Figure 2.32. For this case, we can retrieve the two reflection events by windowing the seismic trace, and then conduct the Q estimation using spectral ratio method. The calculated logarithmic spectral ratios between the two reflection events are shown in Figure 2.33. The estimated Q value is 70.2, which is close to the true Q value 80.

Figure 2.34 shows a velocity model calculated from well log. Using this true velocity model with a constant Q of 50, Zero-offset VSP data are obtained. The two records at depth $200m$, $700m$ are shown in Figure 2.35. Applying the box-car window to retrieve the first breaks of downgoing wavelets, and then calculating the amplitude spectra leads to the logarithmic spectral ratios shown in Figure 2.36. With a frequency band of $10-70Hz$, the estimated Q is 56.1. Using the same velocity and Q model, a shot record gather is obtained. The zero-offset shot record is shown in Figure 2.37, for which the amplitude decays with traveltime drastically. The Q estimation from reflection data will not be discussed here, which will be addressed in chapter 3.

From the above tests, we can see that the VSP and reflection data are consistent with the velocity and Q models, which demonstrate that the finite-difference scheme gives realistic modeling result for absorptive media and incorporates the Q attenuation with sufficient accuracy.

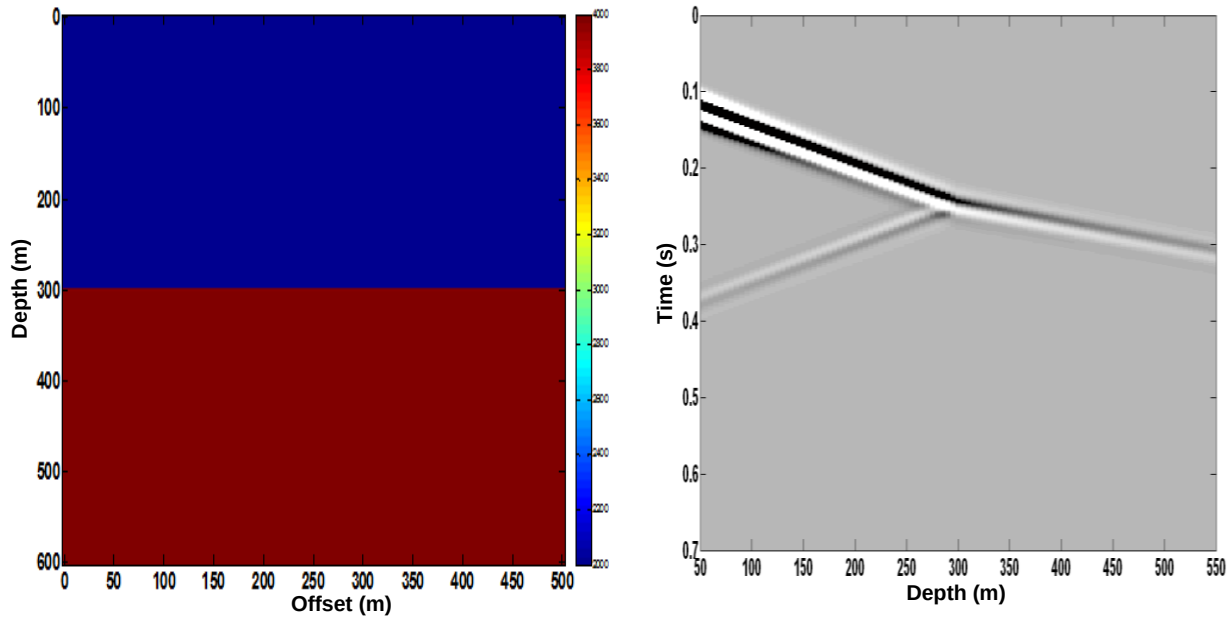

Figure 2.25. (left) a two layer velocity model; (right) the VSP data recorded from $50m - 550m$ using the left velocity model and $Q = 50$.

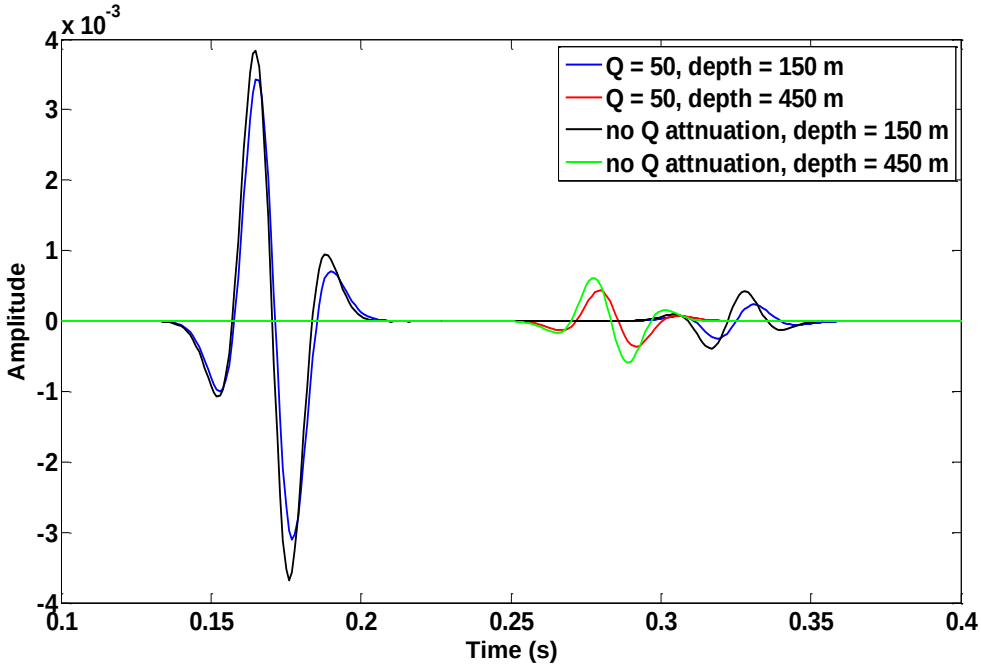

Figure 2.26. Comparison of VSP traces with/without constant Q attenuation.

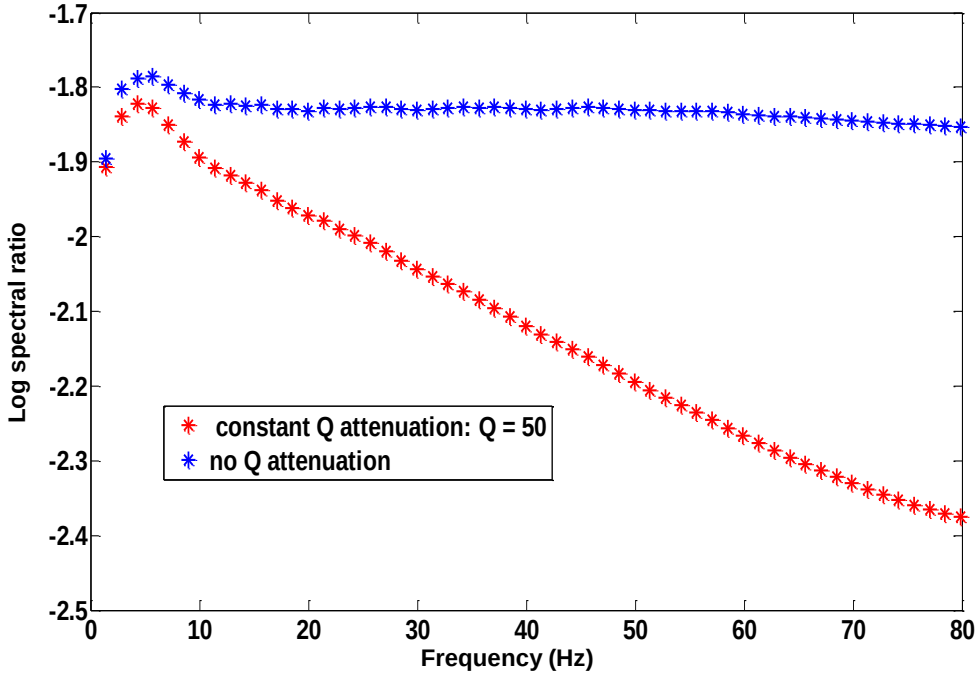

Figure 2.27. The logarithmic spectral ratios calculated from the VSP traces shown in Figure 2.26. The estimated Q is 51.6 for the viscoacoustic case with constant $Q = 50$, and 874.8 for the acoustic case (box-car window applied before spectrum calculation).

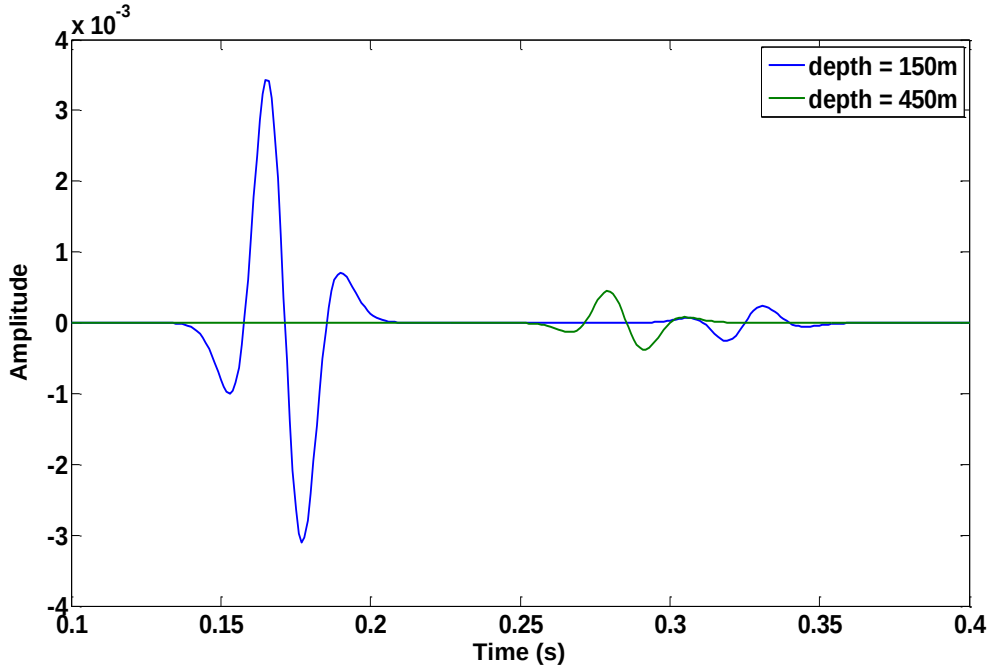

Figure 2.28. Two VSP traces recorded at depth of $150m$ and $50m$ for a two-layer model with $(v_1 = 2000m/s, Q_1 = 50)$ and $(v_2 = 3000m/s, Q_2 = 100)$.

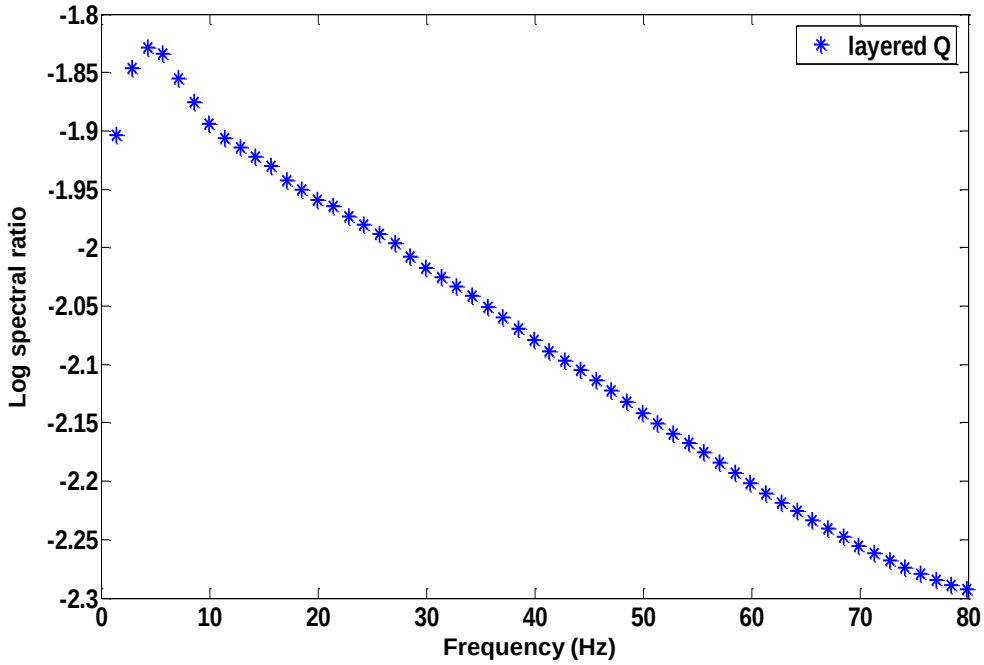

Figure 2.29. The logarithmic spectral ratios calculated from the VSP Traces shown in Figure 2.28 (box-car window applied before spectrum calculation).

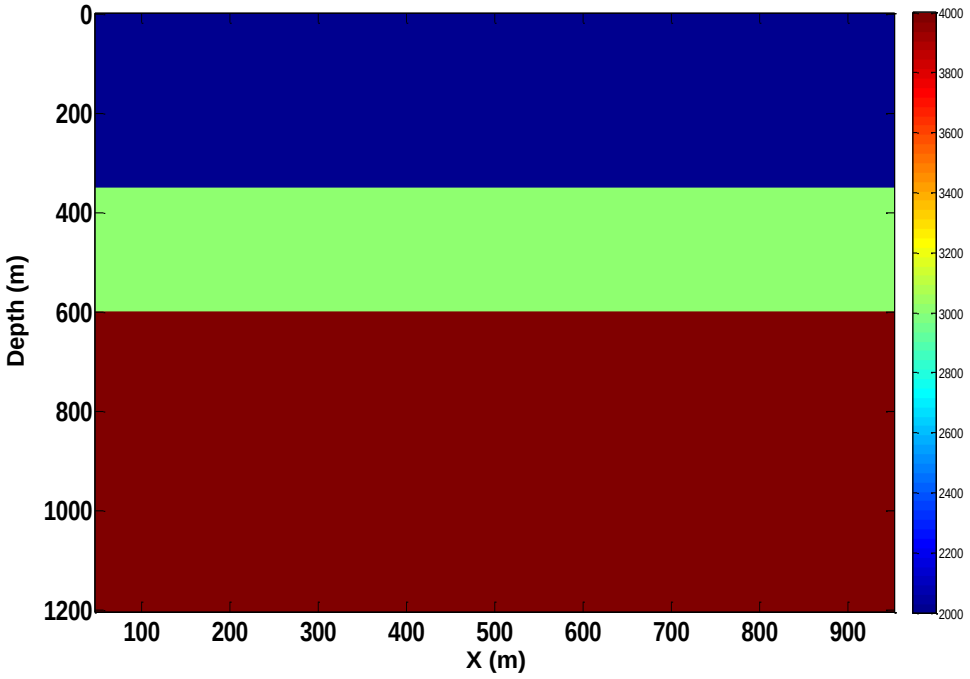

Figure 2.30. A three-layer velocity and Q model with ($v_1 = 2000m/s, v_2 = 3000m/s, v_3 = 4000m/s$) and ($Q_1 = 50, Q_2 = 80, Q_3 = 100$).

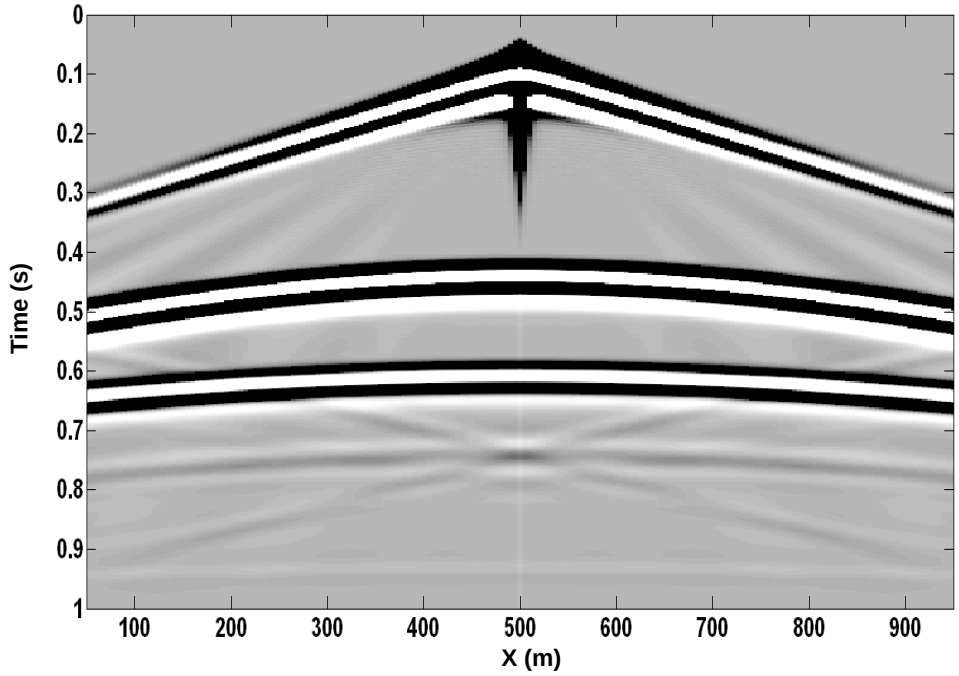

Figure 2.31. A synthetic shot record generated from the velocity and Q model shown in Figure 2.30.

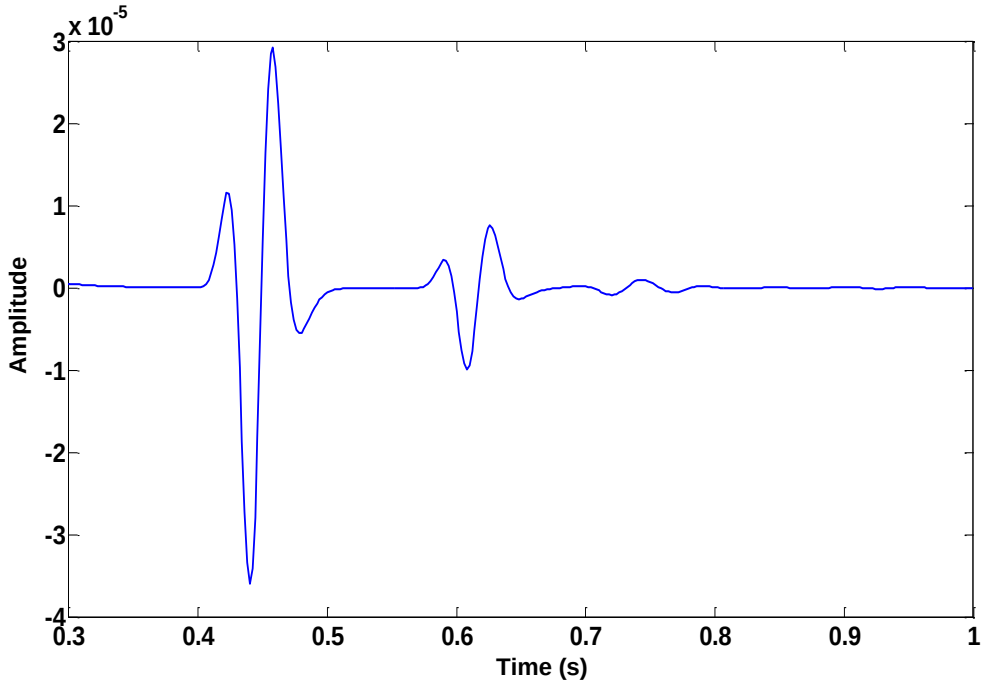

Figure 2.32. The zero offset seismic trace in Figure 2.31 (first break removed).

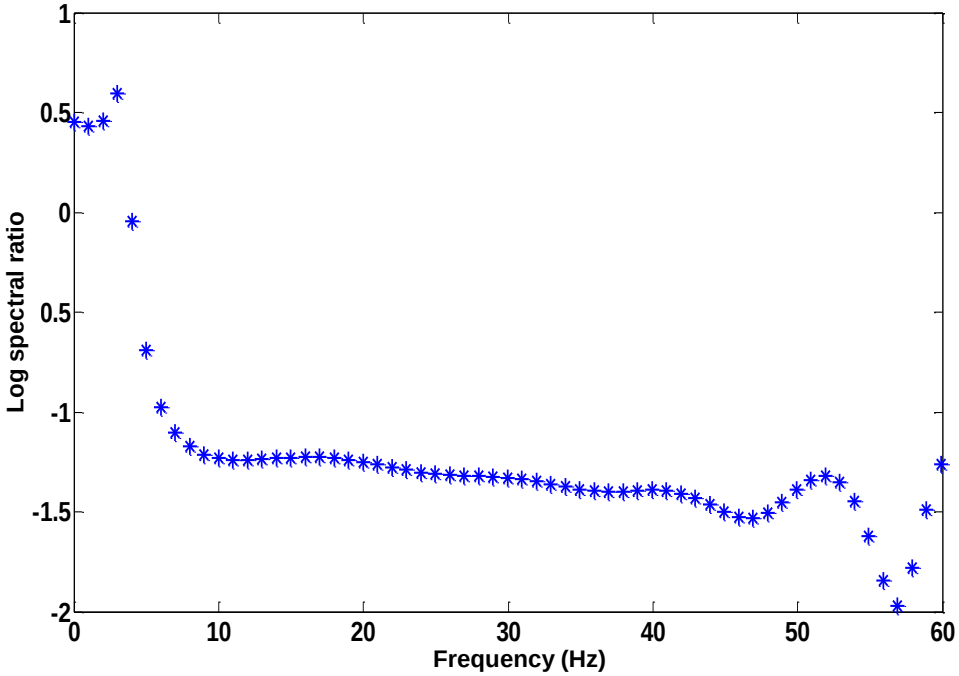

Figure 2.33. The logarithmic spectral ratio for the two reflection events in Figure 2.32 (box-car window used to retrieve separate events before spectrum calculation). Estimated Q is 70.2 compared to true Q value of 80 for the 2nd layer shown in Figure 2.30.

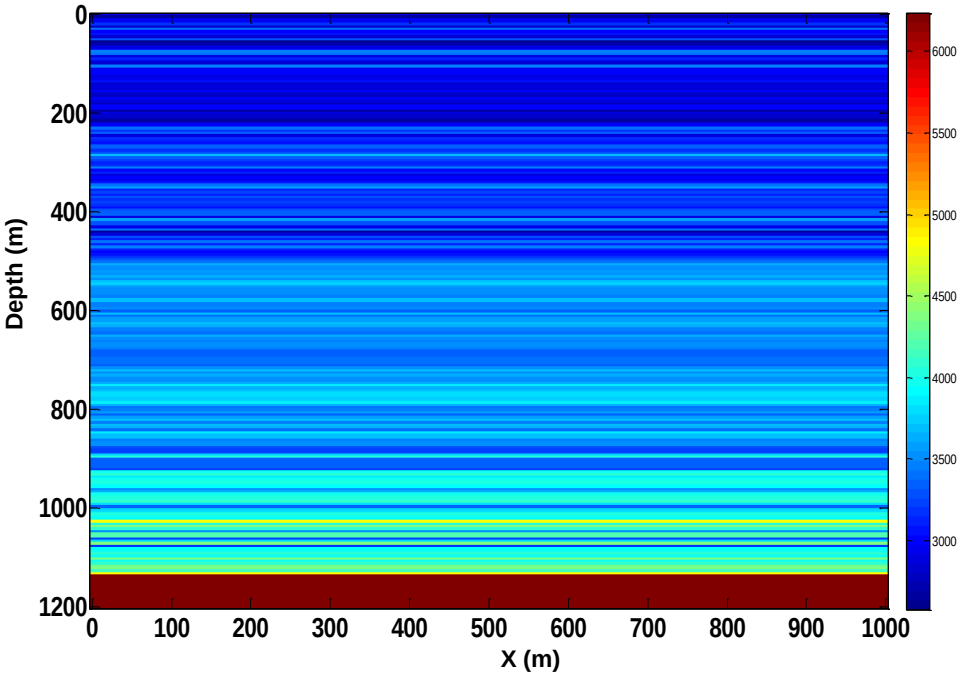

Figure 2.34. Velocity model calculated from a well log 0/14-09-023-23W4 in Alberta.

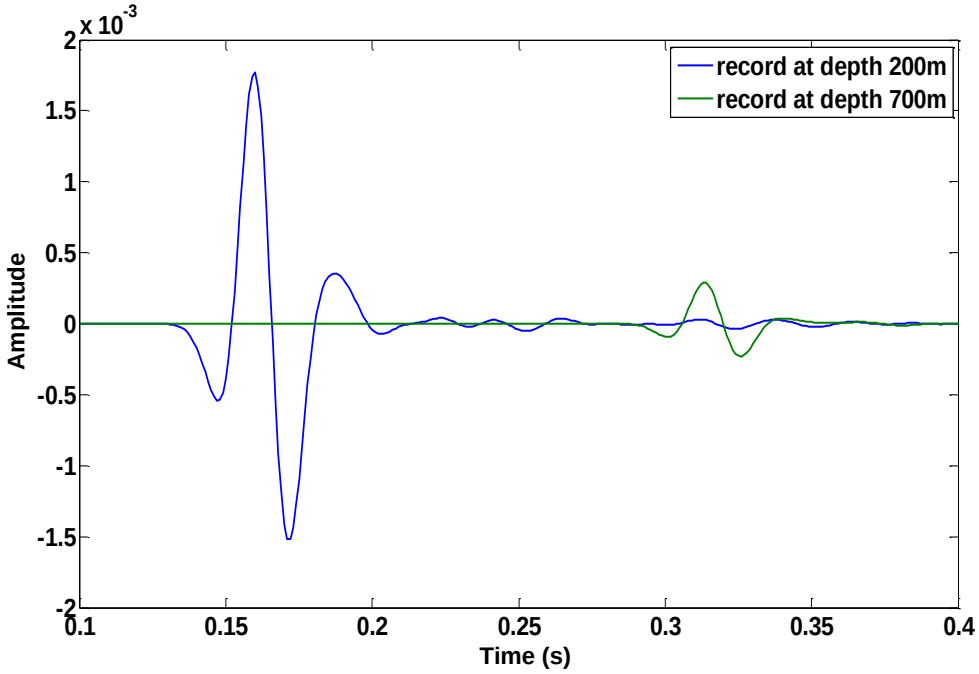

Figure 2.35. Two VSP records at depth $200m$ and $700m$ using the velocity model in Figure 2.34 and a constant $Q = 50$.

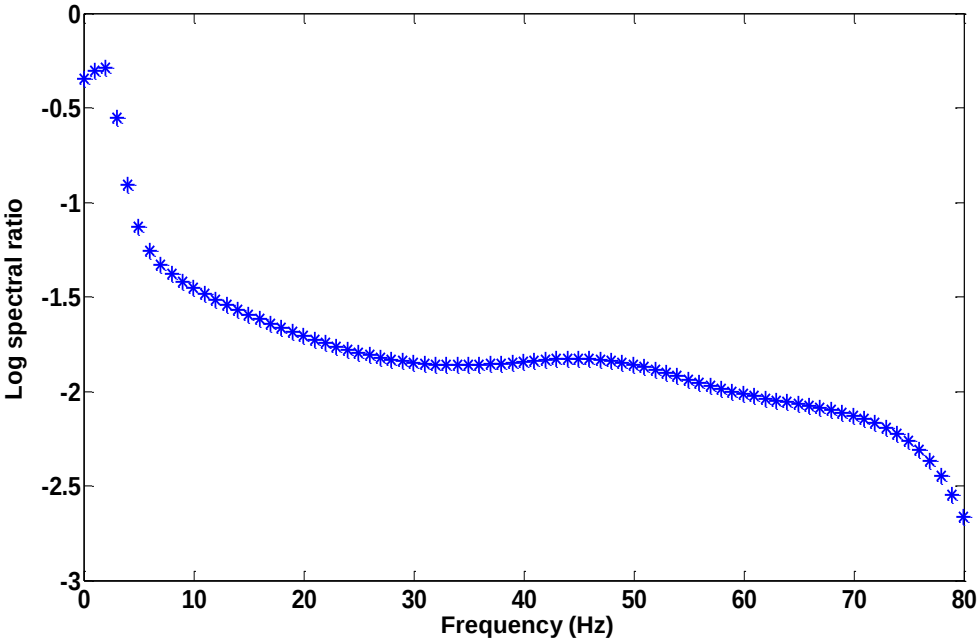

Figure 2.36. The logarithmic spectral ratio calculated from the two traces shown in Figure 2.35 (box-car window applied to retrieve first breaks before spectrum calculation). Estimated Q is 56.1 and true Q value is 50.

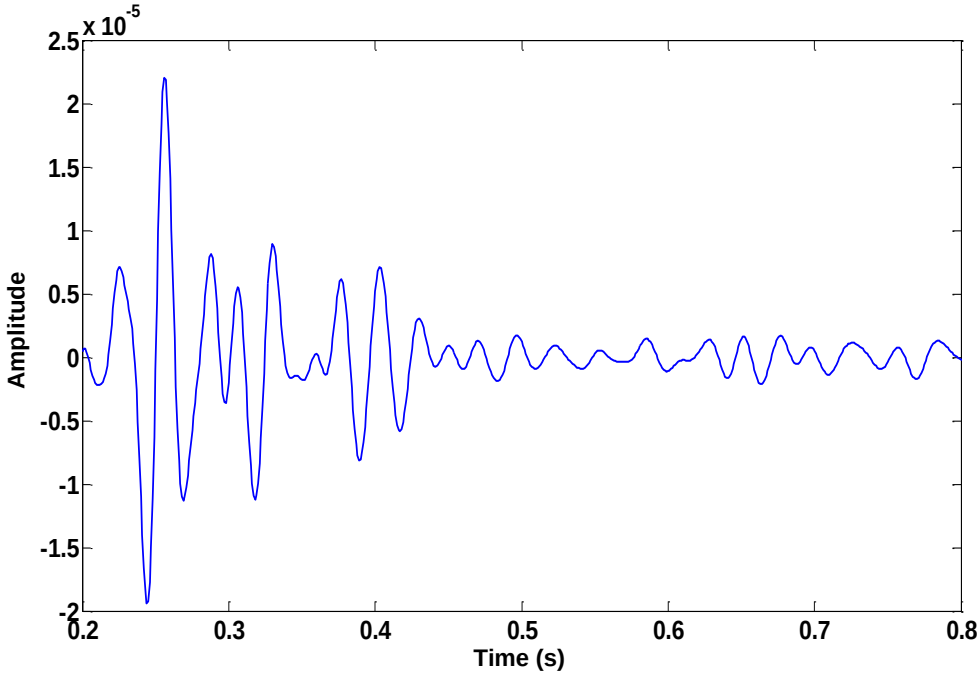

Figure 2.37. A zero offset shot record using the velocity model shown in Figure 2.34 and a constant Q of 50 (first break removed).

2.5 Summary

A nonstationary convolution model, the reflectivity method, and a finite-difference technique for viscoelastic modeling are described in this chapter. All of them can incorporate the attenuation into their modeling results with sufficient accuracy.

The nonstationary convolution model is useful to create 1D attenuated seismic trace. We propose two approaches to incorporate the impulse response representing attenuation accurately. A bandlimited version or a circle-shifted version of the original impulse response can be adopted to preserve its amplitude spectrum, which makes the nonstationary convolution model accurate.

The reflectivity method is very useful for the seismic modeling of stratified media. We implement this method for stratified anelastic media. It can model all kinds of waves and address the geometrical spreading and Q attenuation, which makes the modeling result realistic and gives

sufficient information for layered earth model. Another advantage is that the reflectivity method can give total and partial results of the layered model with flexibility.

The finite-difference technique is a powerful tool for viscoelastic seismic modeling, which can deal with structured subsurface. Testing results shows that the Tiger software gives very realistic results.

Chapter Three: Measurement of seismic attenuation: Q estimation

3.1 Introduction

There are various methods for Q estimation, and each method has its strengths and limitations. An extensive comparison between various methods for Q estimation was made by Tonn (1991) using VSP data, and a conclusion was made that the spectral-ratio method is optimal in the noise-free case. However, the estimation given by spectral-ratio method may deteriorate drastically with increasing noise (Patton, 1988; Tonn, 1991). The question of reliable Q estimation remains. In addition, it is more practical to estimate Q from the surface reflection data. The development of a Q estimation method that is suitable for application to reflection data is still under investigation.

The classic spectral ratio method is probably the most wildly used method. As an extension to it, Cheng and Margrave (2008) propose a complex spectral-ratio method that employs both the amplitude spectra and the phase spectra of signals. For the classic spectral ratio method, it can be troublesome to automatically choose an appropriate frequency band to conduct the Q estimation when calculated spectral ratios are not well linearly distributed. To address this problem, Cheng and Margrave (2011b) propose an interpretive spectral-ratio method, which automatically chooses a narrow frequency band to give the Q estimation.

A time-domain match-filter method for Q estimation is proposed by Cheng and Margrave (2012) and has been shown to be robust to noise and suitable for application to surface reflection data. Theoretically, the match-filter method is a sophisticated wavelet-modeling method with wavelet estimation employed, which is a time-domain counterpart to spectrum-modeling method (Janssen et al., 1985; Tonn, 1991; Blias, 2011). The spectrum-modeling method is a modified approach to the spectral-ratio method without taking division of spectra. In addition, the match-

filter method and the match-technique method (Raikes and White, 1984; Tonn, 1991) employ the idea of matching at different stages of their Q-estimation procedures. Therefore, the above four methods all have theoretical connections but are distinctly different. A comparison between these methods in terms of their underlying theory, accuracy and reliability of estimation results is given by Cheng and Margrave (2013).

This chapter introduces the theory of various Q estimation methods including the classic spectral ratio method, complex spectral ratio method, interpretive spectral ratio method, spectrum modeling method, match-technique method and match-filter method. The performance of above method is evaluated using synthetic and real VSP data, reflection data.

3.2 Theory of Q-estimation methods

The theory of the constant-Q model for seismic attenuation is well established (Futterman, 1962; Kjartansson, 1979; Aki and Richards, 1980). Suppose that a seismic wavelet with amplitude spectrum $|S_1(f)|$ has a amplitude spectrum $|S_2(f)|$ after traveling in the attenuating media for an interval time t. Then, this theory predicts that

$$|S_2(f)| = G|S_1(f)| \exp\left(\frac{-\pi f t}{Q}\right), \tag{3.1}$$

where f is the frequency, G is a geometrical spreading factor. More generally, G can represent all frequency-independent energy loss in total, including spherical divergence, reflection and transmission loss.

For Q estimation, the case of VSP data is similar to the case of reflection data with isolated reflectors. So, we use the reflection data to form the Q-estimation problem. Assume that a source wavelet $w(t)$ with a spectrum $w(f)$ travels through a layered earth with a corresponding reflectivity $r(t)$ in two-way time, and $g(t)$ denotes the geometrical spreading loss

of amplitudes. Consider a localized reflected wavelet $a_1(t)$. It has the contribution from a corresponding subset of reflectivity $r_1(t)$, which is around two-way time t_1. We have

$$a_1(t) \approx g(t) \int_{-\infty}^{\infty} w(\tau)\, r_1(t-\tau) d\tau. \tag{3.2}$$

Then the spectrum of the localized signal $a_1(t)$ near time t_1 can be approximated by

$$A_1(f) \approx g(t_1) W(f) R_1(f), \tag{3.3}$$

where $R_1(f)$ is the Fourier transform of $r_1(t)$ and we assume that $g(t)$ changes slowly with respect to $w(t)$. If the attenuation of the layered media is taken into account and the attenuation mechanism can be described by the constant Q model, equation (3.3) can be modified as

$$|A_1(f)| \approx g(t_1)|W(f)||R_1(f)|\, exp\left(\frac{-\pi f t_1}{Q_1}\right), \tag{3.4}$$

where Q_1 is the average-Q value corresponding to the attenuation process with traveltime of t_1. Similarly, consider a localized reflected wavelet $a_2(t)$ near time t_2 with a corresponding local reflectivity series $r_2(t)$, it amplitude spectrum can be approximated as

$$|A_2(f)| \approx g(t_2)|W(f)||R_2(f)|\, exp\left(\frac{-\pi f t_2}{Q_2}\right), \tag{3.5}$$

where $R_2(f)$ is the Fourier transform of $r_2(t)$, Q_2 is the average-Q value corresponding to the attenuation process with traveltime of t_2.

There are various methods for Q estimation, in which Q is usually derived from the local wavelets $a_1(t)$, $a_2(t)$ or their Fourier spectra.

3.2.1 Spectral-ratio methods

3.2.1.1 Classic spectral-ratio method

From equation (3.4) and (3.5), the spectral ratio becomes

$$ln\left(\left|\frac{A_2(f)}{A_1(f)}\right|\right) = ln\left(\frac{g(t_2)}{g(t_1)}\right) + ln\left(\left|\frac{R_2(f)}{R_1(f)}\right|\right) - \frac{\pi f(t_2-t_1)}{Q_{int}}, \quad (3.6)$$

where Q_{int} is the interval Q corresponding to the attenuation process between the two local wavelets with traveltime of $t_2 - t_1$. Q_{int} can be derived from Q_1 and Q_2 as

$$Q_{int} = (t_2 - t_1)/(\frac{t_2}{Q_2} - \frac{t_1}{Q_1}). \quad (3.7)$$

Based on equation (3.6), the Q factor can be estimated from fitting a straight line to the logarithmic spectral ratio over a finite frequency range. Assuming the reflectivities are essentially white and there are no significant notches in either spectrum, then the term $\ln\left(\left|\frac{R_2(f)}{R_1(f)}\right|\right)$ can be regarded as nearly constant and the estimated Q has a direct relation with the slope k of the best-fit straight line as

$$Q_{\text{est}} = -\frac{\pi f(t_2-t_1)}{k}. \quad (3.8)$$

The above is the basic theory of the classic spectral-ratio method (Spencer et al., 1982), which is originally derived for application to VSP data. When $r_1(t)$ and $r_2(t)$ represent single isolated reflectors, Q estimation from reflection data is similar to the case using VSP data. At this occasion, the $\ln\left(\left|\frac{R_2(f)}{R_1(f)}\right|\right)$ term in equation (3.6) can be approximately constant or, more generally, frequency independent. The computed spectra are smooth when SNR is sufficiently high. In this circumstance, reliable Q estimation can be obtained.

For reflection data, the spectrum of local wavelets can be significantly affected by the corresponding local reflectors, which makes Q estimation from surface data difficult. In this case, $\left|\frac{R_2(f)}{R_1(f)}\right|$ varies with frequency, and Q is not strictly proportional to the slope of the logarithmic spectral ratio given by equation (3.6). Even when the data is noise free, the estimated Q can significantly deviate from the true value. The accuracy of the estimated result

depends on both the SNR level and the degree to which $\left|\frac{R_2(f)}{R_1(f)}\right|$ can be taken as frequency independent, i.e. the extent to which $R_2(f)$ resembles $R_1(f)$. A correction method to the tuning effect of local reflectors was discussed by several publications (Raikes and White, 1984; White, 1992; Hackert and Parra, 2004). If well-log data is available, r(t) can be calculated from the impedance, then correction can be made to equation (3.6) (Hackert and Parra, 2004)

$$ln\left(\left|\frac{A_2(f)/R_2(f)}{A_1(f)/R_1(f)}\right|\right) = ln\left(\frac{g(t_2)}{g(t_1)}\right) - \frac{\pi f(t_2-t_1)}{Q_{int}}. \qquad (3.9)$$

Therefore, for reflection data, Q can also be estimated using the spectral-ratio method. However, the strong dependence of this method on well control makes it most suitable near a well.

3.2.1.2 Complex spectral-ratio method

The classic spectral-ratio method described above is commonly used to estimate Q from VSP data. However, this method only uses the amplitude spectra of the downgoing wavelets. Cheng and Margrave (2008) investigate a complex spectral-ratio method, in which both amplitude spectrum and phase spectrum are employed to obtain improved estimation of Q.

In the constant-Q theory, the earth can be model as a linear filter, which can be fully characterized by the corresponding impulse response. Kjartansson (1979) gives the impulse response of the absorptive media in frequency domain as

$$B(f) = exp\left[\frac{-\pi fx}{Qv(f)}\right]exp\left[j\frac{2\pi fx}{v(f)}\right], \qquad (3.10)$$

where $v(f)$ is the phase velocity. The frequent dependency of phase velocity is the dispersion of seismic wave, which is an essential part of the constant-Q attenuation theory. The dispersion relation can be approximated as (Kjartansson, 1979, Aki and Richards, 1980)

$$v(f) \approx v(f_0)\left[1 + \frac{1}{\pi Q} ln\left|\frac{f}{f_0}\right|\right], \tag{3.11}$$

which gives the phase velocity $v(f)$ at any frequency in terms of the phase velocity $v(f_0)$ at an arbitrary reference frequency f_0. When all the frequencies of interest satisfy the condition

$$\frac{1}{\pi Q} ln\left|\frac{f}{f_0}\right| \ll 1, \tag{3.12}$$

equation (3.10) can be approximated by the following formulation with sufficient precision

$$B(f) \approx exp\left[-\frac{\pi f x}{Q v(f_0)}\right] exp\left[-j\frac{2\pi f x}{v(f_0)}\left(1 - \frac{1}{\pi Q} ln\left|\frac{f}{f_0}\right|\right)\right]. \tag{3.13}$$

If time shift is applied to the attenuated impulse response to remove the linear phase delay, equation (3.13) becomes

$$\widetilde{\mathrm{B}}(f) \approx exp\left[-\frac{\pi f x}{Q v(f_0)}\right] exp\left[j\frac{2 f x}{Q v(f_0)} ln\left|\frac{f}{f_0}\right|\right]. \tag{3.14}$$

Consider two attenuated wavelets with travel-distance x_1 and x_2 respectively. Their Fourier spectra can be expressed as

$$\mathrm{A}_1(f) = W(f)\widetilde{\mathrm{B}}_1(f) = W(f) exp\left[-\frac{\pi f x_1}{Q_1 v(f_0)}\right] exp\left[j\frac{2 f x_1}{Q_1 v(f_0)} ln\left|\frac{f}{f_0}\right|\right., \tag{3.15}$$

and

$$\mathrm{A}_2(f) = W(f)\widetilde{\mathrm{B}}_2(f) = W(f) exp\left[-\frac{\pi f x_2}{Q_2 v(f_0)}\right] exp\left[j\frac{2 f x_2}{Q_2 v(f_0)} ln\left|\frac{f}{f_0}\right|\right]. \tag{3.16}$$

In equation (3.15) and (3.16), Q_1 and Q_2 are the average-Q values corresponding to traveltime $x_1/v(f_0)$ and $x_2/v(f_0)$ respectively. Then, the amplitude decay and phase variation between these two wavelets can be expressed in frequency domain as

$$ln\left[\frac{\mathrm{A}_2(f)}{\mathrm{A}_1(f)}\right] = -\frac{\pi f(x_2 - x_1)}{Q_{int}v(f_0)} + j\,[\frac{2f(x_2 - x_1)}{Q_{int}v(f_0)}\,ln\left|\frac{f}{f_0}\right|], \tag{3.17}$$

where Q_{int} is the interval-Q value corresponding to the traveltime of $(x_2 - x_1)/v(f_0)$. Similarly, Q_{int} in equation (3.17) is directly connected to the average-Q values Q_1 and Q_2 in equation (3.15) and (3.16) according to equation (3.7).

For the classic spectral-ratio method (Spencer et al., 1982), only the real part of spectral ratio in equation (3.17) is considered, and Q can be estimated by fitting a straight line to the calculated spectral ratios. Either the least-squares (L_2 norm) solution or the L_1 norm solution can be chosen for straight-line fitting. For all types of spectral ratio methods described in this chapter, the least-squares solution is adopted. Then, similar to the classic spectral-ratio method, Q can be estimated as

$$Q_{\mathrm{est}} = -\frac{\pi\tau}{k}, \tag{3.18}$$

where k is the slope of the straight line fitted to the real part of calculated spectral ratios, and τ is the travel time given by

$$\tau = (x_2 - x_1)/v(f_0). \tag{3.19}$$

Now, we will use the complex spectral ratios to conduct Q estimation. Suppose that N complex spectral ratios are obtained for frequency components $f_1, f_2, \ldots, f_N$. Let R_e, I_m, M_1 and M_2 be the column vectors with N elements expressed as

$$\begin{cases} Re = \left[Re\left(ln\left[\frac{A_2(f_1)}{A_1(f_1)}\right]\right), Re\left(ln\left[\frac{A_2(f_2)}{W_{d1}(f_2)}\right]\right), \cdots, Re(ln\left[\frac{A_2(f_N)}{A_1(f_N)}\right])\right]^{\mathrm{T}} \\ I_m = \left[Im\left(ln\left[\frac{A_2(f_1)}{A_1(f_1)}\right]\right), Im\left(ln\left[\frac{A_2(f_2)}{A_1(f_2)}\right]\right), \cdots, Im(ln\left[\frac{A_2(f_N)}{A_1(f_N)}\right])\right]^{T} \\ M_1 = [-\pi f_1\tau, -\pi f_2\tau, \cdots, -\pi f_N\tau]^T \\ M_2 = \left[-2f_1\tau \cdot ln\left|\frac{f_1}{f_0}\right|, -2f_2\tau \cdot ln\left|\frac{f_2}{f_0}\right|, \cdots, -2f_{\mathrm{N}}\tau \cdot ln\left|\frac{f_N}{f_0}\right|\right]^T \end{cases}. \tag{3.20}$$

Then, equation (3.17) can be rewritten as

$$R_e + jI_m = M_1 m + \mathrm{j} M_2 m, \tag{3.21}$$

where m is the reciprocal of Q_{int}, i.e

$$Q_{int} = 1/m. \tag{3.22}$$

If only the real part of equation (3.21) is considered, the least-squares solution for Q estimation is

$$Q_{est1} = 1/\left[(M_1{}^{\mathrm{T}} M_1)^{-1} M_1{}^{\mathrm{T}} R_{\mathrm{e}}\right]. \tag{3.23}$$

Similarly, considering the imaginary part of spectral ratios only, the estimated Q value can be formulated as

$$Q_{est2} = 1/\left[(M_2{}^{\mathrm{T}} M_2)^{-1} M_2{}^{\mathrm{T}} I_m\right]. \tag{3.24}$$

The estimation results in equation (3.23) and (3.24) only use either amplitude spectrum or phase spectrum information of the attenuated wavelets. By making full use of the spectral information, a complex spectral-ratio method can be developed. Based on equation (3.21), the Q value can be estimated by solving the following matrix equation

$$\begin{bmatrix} M_1 \\ M_2 \end{bmatrix} m = \begin{bmatrix} R_e \\ I_m \end{bmatrix}. \tag{3.25}$$

Then, the estimated Q value for the complex spectral ratio method can be formulated as

$$Q_{est3} = 1/[(M^T M)^{-1} M^T D], \tag{3.26}$$

where the M and D are two vectors with $2N$ elements formulated as

$$M = \begin{bmatrix} M_1 \\ M_2 \end{bmatrix}, D = \begin{bmatrix} R_e \\ I_m \end{bmatrix}. \tag{3.27}$$

For Q estimation in practice, the frequency independent energy loss should be taken into account. Accordingly, equation (3.21) should be modified as

$$R_e + iI_m = M_1 m + E_N b + \mathrm{i} M_2 m, \tag{3.28}$$

where E_N is a column vector with N unit elements, and b is a constant term representing the frequency independent energy loss. Therefore, Q can be obtained by solving the forward model

$$L\mathbf{m} = D, \tag{3.29}$$

where L is a matrix given as

$$L = \begin{bmatrix} M_1 & E_N \\ M_2 & 0 \end{bmatrix}, \tag{3.30}$$

and **m** is a vector of that only contains parameter m and b. Then, the least-squares solution for equation (3.29) can be formulated as

$$\widehat{\mathbf{m}} = (L^T L)^{-1} L^T D. \tag{3.31}$$

Equation (3.31) shows one way to combine amplitude spectrum and phase spectrum to give Q estimation. The contributions from amplitude spectrum and phase spectrum might be unbalanced. To address this issue, matrix $L$and vector D in equation (3.29) can be modified as

$$\hat{L} = \begin{bmatrix} \varepsilon M_1/e_1 & E_{\mathrm{N}}/e_1 \\ (1-\varepsilon)M_2/e_2 & 0 \end{bmatrix}, \tag{3.32}$$

and

$$\widehat{D} = \begin{bmatrix} \varepsilon R_e/e_1 \\ (1-\varepsilon)I_m/e_2 \end{bmatrix}, \tag{3.33}$$

where ε is a scaling factor between 0 and 1, and can be given manually, e_1 and e_2 are the least-squares errors when only amplitude spectrum or phase spectrum is employed for the Q estimation. For instance, e_1 and e_2 can be formulated as

$$e_1 = \|R_e - M_1 Q_{\mathrm{est1}}\|, \tag{3.34}$$

and

$$e_2 = \|I_m - M_2 Q_{\text{est2}}\|. \tag{3.35}$$

So, the least-squares solution to the alternative of equation (3.29) can be formulated as

$$\widehat{\mathbf{m}} = (\hat{L}^T \hat{L})^{-1} \hat{L}^T \hat{\mathrm{D}}. \tag{3.36}$$

The result in equation (3.36) is a generalized complex spectral-ratio method. The contribution to estimation result from amplitude spectrum information and phase spectrum information is normalized, and can be adjusted by changing the scaling factor ε as well. It reduces to the classic spectral-ratio method when $\varepsilon = 1$. Only phase information is used for Q estimation when $\varepsilon = 0$.

The complex spectral-method described here is developed only for VSP data. For the complex spectral-ratio method, the reference frequency f_0 and frequency component f_i should be chosen to satisfy equation (3.12). Theoretically, the estimation result varies with reference frequency f_0. In addition, the two wavelets used to conduct Q estimation should be aligned properly to minimize the linear phase shift.

When applied to real data, a practical but important issue for the complex spectral-ratio method is that an appropriate reference frequency f_0 should be determined first to model the phase difference between the local wavelets, since there is no relevant prior knowledge available. For real VSP data with good quality, the Q estimation based on phase information only should obtain a result that is similar to the result given by classic spectral-ratio method. This criterion can be used to roughly choose the reference frequency. An alternative approach can be that f_0 is determined by minimizing the mismatch between modeled phase difference and measured phase difference. Another approach can be that minimum-phase equivalent wavelets are computed for the two original wavelets to conduct subsequent Q-estimation, then f_0 can be chosen with the

calibration from other Q-estimation methods. These three approaches will be investigated using real VSP data.

3.2.1.3 An interpretive spectral-ratio method

For the classic spectral-ratio method, the calculated spectral ratios, at some circumstance, are not suitable for straight-line fitting over a wide frequency band because of effects such as unfavorable SNR, tuning effect. The straight-line fitting might be better conducted over a narrow frequency band instead, which can be chosen interpretively case by case.

Cheng and Margrave (2011b) propose an approach to address this problem. First, the calculated spectral ratios are approximated by a polynomial curve as

$$ln\left(\left|\frac{A_2(f)}{A_1(f)}\right|\right) \approx \mathrm{a}_0 + \mathrm{a}_1 f + \mathrm{a}_2 f^2 + \cdots + \mathrm{a}_n f^n, \tag{3.37}$$

where n is the order of the polynomial and can be manually chosen according to SNR level, a_i ($i = 0, 1, 2, \ldots, n$) is the coefficient of the polynomial, which can be estimated from the least-squares solution of the polynomial fitting in equation (3.37). Then, the local slopes can be derived from the first order derivative of the polynomial as

$$k(f) \approx \mathrm{a}_1 + 2\mathrm{a}_2 f + \cdots + n\mathrm{a}_n f^{n-1}. \tag{3.38}$$

The local slopes in equation (3.38) could be of either positive or negative values. Theoretically, the slopes should be of negative values. Then, we can specify a range for the slopes to limit the range of estimated Q values. Finally, Q can be estimated from a median or mean value of the local slopes within the specified range based on equation (3.8). Compared to the classic spectral-ratio method, the basic idea of this approach is to obtain a piecewise straight-line fitting scheme instead of a single straight-line fitting scheme.

3.2.2 Spectrum-modeling method

The spectrum-modeling method directly compares the amplitude spectra of the local wavelets, where $|A_1(f)|$ is modified by varying Q until an optimum approximation to $|A_2(f)|$ is obtained. If the L_2-norm criterion is used for optimization, Q can be estimated as (Blias, 2011)

$$Q_{est} = min_{Q_{int}} \left\| |A_2(f)| - \alpha(Q_{int})|A_1(f)| \; exp\left(\frac{-\pi f(t_2-t_1}{Q_{int}}\right)\right\|^2, \qquad (3.39)$$

where the scaling factor $\alpha(Q_{int})$ addresses the frequency-independent energy loss and can be formulated as

$$\alpha(Q_{int}) = \frac{\int_{-\infty}^{\infty}|A_2(f)||A_1(f)| \; exp\left(\frac{-\pi f(t_2-t_1}{Q_{int}}\right)\mathrm{d}f}{\int_{-\infty}^{\infty}|A_1(f)|^2 \; exp\left(\frac{-2\pi f(t_2-t_1}{Q_{int}}\right)\mathrm{d}f}. \qquad (3.40)$$

The spectrum-modeling method differs from the classic spectral-ratio method in the following aspects. Firstly, the criterion used to minimize the objective function for the classic spectral-ratio method is least-squares error, which is not necessary for spectrum-modeling. The objective function for minimization in equation (3.39) can be of other criteria, for instance, L_1 norm. Secondly, the classic spectral-ratio method assumes that reflection coefficients and phase velocities of propagating waves are frequency independent (Jannsen et al., 1985). Spectrum modeling does not necessarily need this assumption.

Spectrum-modeling method avoids taking spectral division, which can stabilize the estimation in presence of noise. In addition, if the L_2-norm criterion is used for minimization of misfit, the result can be significantly affected by the matching for the frequency components with large amplitudes.

3.2.3 Match-technique method

A match technique for Q estimation is proposed by Raikes and White (1984). By matching the two local wavelets as

$$a_2(t) \approx a_1(t) * h_{12}(t), \tag{3.41}$$

where $*$ denotes convolution, $h_{12}(t)$ is the forward filter predicting $a_2(t)$ from $a_1(t)$. Similarly, a backward filter $h_{21}(t)$ can be obtained by predicting $a_1(t)$ from $a_2(t)$. Then, the transfer functions $H_{12}(f)$ and $H_{21}(f)$ can be computed from $h_{12}(t)$ and $h_{21}(t)$ by taking Fourier transform. Therefore, the spectral power ratio of the two local wavelets is given by

$$\frac{P_2(f)}{P_1(f)} = \frac{|H_{12}(f)|}{|H_{21}(f)|}, \tag{3.42}$$

where $P_1(f)$ and $P_2(f)$ are the power spectra of $a_1(t)$ and $a_2(t)$ respectively. Then, Q can be estimated from the spectral power ratio by the classic spectral-ratio method.

Actually, $h_{12}(t)$ gives an approximate estimation of the attenuation operator combined with a constant scaling factor. The amplitude spectrum of the operator can be distorted in presence of noise. The spectral coherence of $H_{12}(f)$ and $H_{21}(f)$ is used to calculate confidence limit on which the spectral ratios are computed (Raikes and White, 1984). The discrepancy between $|H_{12}(f)|^2$ and $|H_{21}(f)|^{-2}$ indicates the SNR level and interference due to local reflectors. The convergence of the two curves and their confidence limits can be used to define the frequency range within which the spectral ratios are considered reliable. To sum up, the match-technique method for Q estimation is conducted in four stages. First, power transfer functions $|H_{12}(f)|^2$ and $|H_{21}(f)|^{-2}$ are estimated by matching the two local wavelets. Then, a frequency range is defined by examining the behavior of power transfer functions. Following that, the power spectral ratios over a specific frequency range are estimated from the geometric

mean value of $|H_{12}(f)|^2$ and $|H_{21}(f)|^{-2}$. Finally, Q is estimated from the logarithmic spectral ratios. Generally, the match-technique method described here can be regarded as a spectral-ratio method with spectrum estimation using some matching technique.

3.2.4 A match-filter method

Cheng and Margrave (2012) proposed a match-filter method for Q estimation. The procedure of this method consists of three stages. First the smoothed amplitude spectra of the local wavelets are computed. From equation (3.4) and (3.5), the smoothed amplitude spectra can be expressed as

$$\overline{|A_1(f)|} \approx g(t_1)\overline{|W(f)||R_1(f)|}\, exp\left(\frac{-\pi f t_1}{Q_1}\right), \tag{3.43}$$

where the overbar indicates smoothing, and

$$\overline{|A_2(f)|} \approx g(t_2)\overline{|W(f)||R_2(f)|}\, exp\left(\frac{-\pi f t_2}{Q_2}\right). \tag{3.44}$$

Suppose $\overline{|A_1(f)|}$, $\overline{|A_2(f)|}$ are smoothed amplitude spectra. Then, the minimum-phase wavelets with amplitude spectra $\overline{|A_1(f)|}$ and $\overline{|A_2(f)|}$ can be formulated as

$$w_1(\mathrm{t}) = F^{-1}(\overline{|A_1(f)|}e^{iH(ln\,(\overline{|A_1(f)|}))}) \tag{3.45}$$

and

$$w_2(t) = F^{-1}(\overline{|A_2(f)|}e^{iH(ln\,(\overline{|A_2(f)|}))}), \tag{3.46}$$

where F^{-1} denotes inverse Fourier transform; H denotes Hilbert transform. Finally, Q can be estimated by

$$Q_{\mathrm{est}} = min_{Q_{int}}\|w_1(t) * I(Q_{int}, t) - \mu w_2(t)\|^2, \tag{3.47}$$

where $*$ denotes convolution, and $I(Q,t)$ is the impulse response of attenuation process with a quality factor Q and traveltime $(t_2 - t_1)$, which can be formulated as

$$I(Q_{int},t) = F^{-1}(exp\left(\frac{-\pi f(t_2-t_1)}{Q_{int}} - \mathrm{i}H(\frac{\pi f(t_2-t_1)}{Q_{int}})\right)), \qquad (3.48)$$

and μ is a constant scaling factor which accounts for frequency independent loss and can be estimated as

$$\mu = \frac{\int_{-\infty}^{\infty}(w_1(t)*I(Q_{int},t))\, w_2(t)dt}{\int_{-\infty}^{\infty} {w_2}^2(t)dt}. \qquad (3.49)$$

In words, equation (3.47) says that the optimal Q is the one whose corresponding impulse response best converts $\mathrm{w}_1(\mathrm{t})$ into $\mathrm{w}_2(\mathrm{t})$. The scalar μ is the unique least-squares scalar required to minimize the difference of two signals (often this is called least-squares subtraction).

For the match-filter method described by equation (3.47), the optimal Q is found by a direct search over an assumed range of Q values with a particular increment since it is a nonlinear minimization. $w_1(t)$ and $w_2(t)$ in equation (3.45) and (3.46) can be regarded as the embedded wavelets at time t_1 and t_2 respectively. For absorptive media, the embedded wavelet evolves with time. Then, Q can be estimated by fitting the evolution of embedded wavelet to constant-Q model. Although we assume the embedded wavelet to be minimum phase, in practice, this assumption is a convenience and not a prerequisite for our match-filter method, since equation (3.47) can be generally regarded as a way to fit the change of spectra in time domain using constant-Q model.

In addition, the match-filter method can be regarded as a sophisticated wavelet-modeling method. For the wavelet-modeling method (Jannsen et al., 1985), $a_1(t)$ is modified synthetically by attenuation operators corresponding to varying Q values until an optimal approximation to $a_2(t)$ is obtained. The wavelet-modeling method requires that the difference of the phase spectra of the two local waves can be approximated by the phase spectrum of a minimum-phase signal, which may be troublesome in practice. Theoretically, the wavelet-modeling method does

not work well for reflection data. By estimating the embedded wavelets of minimum-phase first, the match-filter method ensures that matching of them can be conducted successfully.

The three types of spectral-ratio methods, spectrum modeling method and match-technique method are frequency-domain methods. All of them need to define a frequency range where the signal dominates for better estimation. For the implementation of these frequency-domain methods in this chapter, the frequency range is given manually as an input parameter. Compared to the spectral-ratio methods and match-technique method, the match-filter method avoids taking spectral division. Compared to the spectrum-modeling method, the match-filter method matches the spectra in time domain.

3.3 Multitaper method for amplitude-spectrum estimation

For Q estimation, many methods involve calculating the amplitude spectra from local short-time wavelets. It is not a trivial problem since the local wavelets are subject to tuning effects and noise. For real data, there are usually spikes or notches in the original amplitude spectra caused by interaction with reflectivity, which may cause problem for Q estimation. Appropriate smoothing of amplitude spectra can improve the estimation result. Therefore, it is necessary to obtain an appropriately smoothed spectrum for each individual wavelet at some occasion. The smoothing of amplitude spectra is an important part of match-filter method, and can be easily incorporated into the classic spectral-ratio method, interpretive spectral-ratio method, spectrum-modeling method and match-technique method discussed in section 3.2.

Thomson (1982) proposed a multitaper method used to produce a smooth, high resolution spectral estimation, which has been shown to provide low variance estimation with less spectral leakage when applied to seismic data (Park et al., 1987; Neep et al., 1996, Cheng and Margrave, 2009b). When applying the Fourier transform to a finite-length signal or a finite-length segment

of infinite signal, it appears that some energy has leaked out of the original spectrum into neighbouring frequencies. Such an effect is called spectral leakage. The basic idea of mutitaper technique is to weight the data by several spectral leakage resistant tapers, and then to form a single spectral estimation through combining the spectra of tapered data. The details can be found in the original work by Thomson (1982). We follow the outline given by Park et at (1987) to introduce the multitaper method.

Suppose that our goal is to estimate the smoothed amplitude spectrum $\overline{|A_1(f)|}$ from the finite time series $a_{1n}\ (n = 0, 1, 2, \dots, N-1)$ corresponding to the local wavelet $a_1\ (t)$, and the taper series is $\psi_n\ (n = 0, 1, 2, \dots, N-1)$. Then, the discrete Fourier transform (DFT) of the taper is

$$\Psi(f) = \sum_{n=0}^{N-1} \psi_l\ e^{j2\pi fn}. \tag{3.50}$$

Here, we assume the interval time between two successive samples is unit one. The frequency can be defined on the principal domain (-1/2, 1/2]. The spectral leakage property of the taper can be deduced from its DFT. Suppose the taper is designed to minimize the bias at a given frequency f_0 caused by the spectral leakage from outside the frequency band $|f - f_0| \le F$. This is equivalent to maximizing the fraction of energy within the $2F$ frequency band, which can be formulated as

$$\lambda(N, F) = \frac{\int_{-F}^{F} |\Psi(f)|^2 \mathrm{d}f}{\int_{-1/2}^{1/2} |\Psi(f)|^2 \mathrm{d}f}. \tag{3.51}$$

Substitute equation (3.50) into equation (3.51). The $\lambda(N, F)$ can be expressed in a matrix form

$$\lambda(N, F) = \frac{\boldsymbol{\psi} \cdot \boldsymbol{C} \cdot \boldsymbol{\psi}}{\boldsymbol{\psi} \cdot \boldsymbol{\psi}}, \tag{3.52}$$

where $\boldsymbol{\psi}$ is the taper vector , and matrix $\boldsymbol{C}$ has following components

$$C_{kl} = \frac{sin\,[2\pi F(k-l)]}{\pi(k-l)},\ k,l = 0,1,2,\dots,N-1. \tag{3.53}$$

Then, equation (3.53) becomes an eigenvalue problem as

$$\mathbf{C}\boldsymbol{\psi} = \lambda\boldsymbol{\psi}, \tag{3.54}$$

which has a solution with N eigenvalues $1 > \lambda_0 > \lambda_1 > \cdots > \lambda_{N-1} > 0$ and the associated normalized eigenvectors $\boldsymbol{\psi}^m$, $m = 0, 1,\ 2, \dots,\ N-1$. The $\boldsymbol{\psi}^m$ are so-called discrete prolate spheroidal sequences (Slepian, 1978), and are also referred as prolate eigentapers (Park et al, 1987). A prolate eigentaper with a time-bandwidth product of $q = NF$ is called a pπ prolate taper, which concentrates the spectral energy within a bandwidth of $2F$. Note that the matrix $\boldsymbol{C}$ is a Hermitian matrix. So, the N eigentapers are orthogonal to each other, and each of them provides an orthogonal sample of the original wavelet. In general, the tapers are constructed in such a way that different parts of wavelet are recovered by different tapers without interference while optimizing the resistance to spectral leakage.

To obtain the spectral estimation by multitaper method, the spectra of tapered data are calculated first as

$$A_1^m(f) = \sum_{n=0}^{N-1} \psi_n^m a_{1n}\, e^{j2\pi fn},\ m,n = 0,1,2,\dots,N-1. \tag{3.55}$$

It is conventional to employ only several lowest order eigentapers in equation (3.55), because the resistant to spectral leakage becomes poor with the increase of the order of eigentaper. Then, an estimation can be made from weighted sum of the spectra $A_1^m(f)$ as

$$\widetilde{A_1}(f) = \frac{1}{\Upsilon}\sum_{n=0}^{\Upsilon-1} \frac{|A_1^m(f)|^2}{\lambda_n}, \tag{3.56}$$

where Υ is the highest order of the selected eigentapers. A better estimation can be obtained by an adaptive multitaper method formulated as

$$\overline{|A_1(f)|} = \frac{\sum_{m=0}^{Y-1} d^m(f)\,|A_1^m(f)|^2}{\sum_{m=0}^{Y-1} |A_1^m(f)|^2}, \tag{3.57}$$

where the frequency dependent weight function $d^m(f)$ is given by

$$d^m(f) = \frac{\sqrt{\lambda_m}\hat{A}_1(f)}{\lambda_m \hat{A}_1(f) + \mathrm{E}\{L_j(f)\}}. \tag{3.58}$$

$\hat{A}_1(f)$ is the unknown true amplitude spectrum and $L_j(f)$ is the spectral leakage at frequency f, which can be approximated as

$$E\{L_j(f)\} \approx (1-\lambda_n)\sum_{n=1}^{N-1} a_{1n}. \tag{3.59}$$

The true amplitude spectrum $\hat{A}_1(f)$ in equation (3.58) can be replaced by its estimation. Then, the adaptive estimation result $\overline{|A_1(f)|}$ can be obtained through iterative calculation.

For the multitaper method, it assumes that the input data is noise free. So, in practice, an appropriate band-pass filter should be applied to the input signal to suppress the noise before the spectrum smoothing.

3.4 Effect of deconvolution on Q estimation

For the processing of reflection data, denconvlution is an important step in the processing flow. Whether the application of deconvolution to reflection data will affect Q estimation is worthwhile to investigate.

Suppose that the deconvolution is a stationary deconvolution such as the Wiener spiking deconvolution or predictive deconvolution, and the deconvolution operator is $d(t)$ with a Fourier spectrum of $D(f)$. Then, the amplitude spectra of the two dencovolved wavelets can be approximated as

$$|A_{d1}(f)| \approx g(t_1)|\mathrm{S}(f)||\mathrm{R}_1(f)||D(f)|\,exp\left(\frac{-\pi f t_1}{Q_1}\right). \tag{3.60}$$

and

$$|A_{d2}(f)| \approx g(t_2)|S(f)||R_2(f)||D(f)|\, exp\left(\frac{-\pi f t_2}{Q_2}\right). \qquad (3.61)$$

We can see that the relation between above amplitude spectra can still be described by formula similar to equation (3.6) and (3.17). Therefore, stationary deconvolution will not significantly affect the estimation result for all spectral-ratio methods and spectrum-modeling method. For the match-technique method, it can be regarded as a sophisticated spectral-ratio method, and the spectral ratio of the deconvolved wavelets still fits the attenuation model. Stationary deconvolution does not affect the estimation result for match-technique method as well.

For the match-filter method, the estimated embedded wavelets can be approximated by $d(t) * w_1(t)$ and $d(t) * w_2(t)$ respectively, and these two embedded wavelets can still be connected by the forward Q filter. Then, Q can be estimated by

$$Q_{est} = min_Q \|d(t) * w_1(t) * I(Q_{int}, t) - \mu d(t) * w_2(t)\|^2, \qquad (3.62)$$

Generally speaking, the same deconvolution operator is applied to local wavelets at the case of stationary deconvolution. The relation between the deconvolved wavelets can still be described by the Q attenuation model. Therefore, stationary deconvolution will not affect Q-estimation result significantly. However, if the applied deconvolution is nonstationary, the local wavelets are actually altered by different deconvolution operators, which might affect the inherent attenuation relation between the local wavelets. At this occasion, nonstationary deconvolution may significantly change the Q estimation results.

3.5 Numerical tests

3.5.1 Comparison of Q estimation methods

3.5.1.1 Synthetic 1D VSP data or reflection data with isolated reflectors

The ideal case for Q estimation is computing Q from noise free VSP data, which can be simulated as reflection data with isolated reflectors. A synthetic attenuated seismic trace was created by the nonstationary convolution model proposed by Margrave (1998), using two isolated reflectors, a minimum-phase wavelet with dominant frequency of $40Hz$ and a constant Q value of 80, as shown in Figure 3.1. Using the two local events shown in Figure 3.1, Q estimations from the methods discussed in section 3.2 are shown in Figure 3.2 – 3.8.

The classic spectral-ratio method gives the exact estimation as shown in Figure 3.2. For the complex spectral ratio method, the exact reference frequency is use to construct vector M_2 formulated in equation (3.20) at this time. The estimation result is the same as the classic spectral-ratio method when only amplitude spectra are employed. Figure 3.3 shows the estimation result of 79.55 when only phase spectra are employed. The complex spectral-ratio method gives the accurate estimation as well. As shown in Figure 3.4 and 3.5, spectrum-modeling method obtains minimum error when $Q = 80.11$. The match-technique gives an estimation of 81.76 as shown in Figure 3.6. It is close to the exact Q value, but the difference is not negligible for the ideal case, which is caused by the approximation made to obtain the optimal forward and backward filters for the matching of the two local wavelets. The match-filter method gives an estimation of 80.06 when fitting error is minimized, as shown in Figure 3.7 and 3.8. All the above methods give accurate estimation for the ideal case.

Then, random noise is added to the synthetic data to evaluate the performance of the Q-estimation methods in more practical circumstances. Figure 3.9 shows a synthetic seismic trace

with a signal-to-noise ratio of $SNR = 4$ (we define this in the time domain as the ration of the RMS values of signal and noise). The amplitude spectra of the two events are show in Figure 3.10 and Figure 3.11, of which the noise levels are about $-25DB$ and $-20DB$ respectively. The two local events in Figure 3.9 are used to test the Q-estimation methods discussed in this chapter. For the frequency-domain methods, a frequency range of $15Hz - 75Hz$ is used for Q estimation. For the match-filter method, band-pass filters are applied to suppress the noise before estimating the embedded wavelets, and the passing bands for the two local wavelets are $10Hz - 140Hz$ and $10Hz - 90Hz$ respectively. The smoothing of amplitude spectra using multitaper method is not conducted at this time. The results of Q estimation are shown in Figure 3.12 – 3.16. We can see that the estimation results are deviated from the exact Q value due to the presence of noise. To make a more general comparison of performance for the estimation methods in presence of noise, 200 seismic traces are created by adding 200 different random noise series of the same level ($SNR = 4$) to the trace shown in Figure 3.1. Then Q estimation is conducted using these noise contaminated data. The histograms of the estimated Q values are shown in Figure 3.17 – 3.23. For the classic spectral-ratio method, the estimation results have a mean value of 87.08 and standard deviation of 26.74, as shown in Figure 3.17. For the complex spectral-ratio method, when only the phase spectra are used for Q estimation, the results have a mean value of 80.32 and standard deviation of 7.13. When both amplitude spectra and phase spectra are used for Q estimation, Figure 3.19 shows the results based on equation (3.31), and Figure 3.20 shows the results based on equation (3.36) with $\varepsilon = 0.5$. The results for both cases are comparable to those shown in Figure 3.18. We can see that the employment of phase information significantly improve the estimation results for the complex spectral-ratio method. For the spectrum-

modeling method, match-technique method and match-filter method, the standard deviations of their results are comparable, while the results of match-filter method have the closest mean value to true Q value. Overall, when the spectrum smoothing is not employed, the complex spectral ratio gives the best estimation results, and the result of match-filter is better than the results of classic spectral-ratio method, spectrum-modeling method and match-technique method.

Now, the multi-taper method is employed to smooth the amplitude spectrum for the classic spectral ratio method, spectrum-modeling method, match-technique method and match-filter method. For the local events in Figure 3.9 with a time-length of $200ms$ and a sample rate of $2ms$, the corresponding tapers should have 101 sample points. Figure 3.24 shows the five lowest order 4π prolate tapers. These tapers are orthogonal to each other and provide varying weight for different parts of the local events. An example of the spectrum estimation is illustrated in Figure 3.25. With the employment of spectrum smoothing, 200 seismic traces with a noise level of $SNR = 4$ are generated to evaluate classic spectral ratio method, spectrum-modeling method, match-technique method and match-filter method. The Q estimation results are shown in Figure 3.26 – 3.29. For the results of the three frequency domain methods, the mean values are obviously distorted while their standard deviation values remain the same level as the case when the spectrum estimation is not employed. For match-filter method, the estimation results, as shown in Figure 3.29, are significantly improved, and have accurate mean value of 80.79 and a small standard deviation of 7.07, which are comparable to the results of the complex spectral-ratio method. The above results indicate that the three frequency-domain methods can be sensitive to spectrum smoothing. The match-filter method, as a time-domain method, needs the embedded wavelets for matching to be smooth, which, in turn, make proper spectrum estimation

favorable. Therefore, incorporation of spectrum smoothing can help stabilize the estimation result for match-filter method.

To further investigate the effect of spectrum smoothing on Q estimation for the classic spectral-ratio method, spectrum-modeling method, match-technique method and match-filter method, we use the noise free VSP data to conduct the Q estimation with spectrum estimation employed (even though the spectrum smoothing is not necessary). For the classic spectral-ratio method, the spectrum-modeling method and the match-filter method, the bandlimited amplitude spectra of the two local events in Figure 3.1 are shown in Figure 3.30, which are estimated by multitaper method with frequency bands of $10Hz - 140Hz$ and $10Hz - 90Hz$ respectively. We can see that the original amplitude spectra are modified by the spectrum estimation. These smoothed amplitude spectra are used conduct following Q estimations. For the match-technique method, the two local wavelets are band-limited to $10Hz - 140Hz$ and $10Hz - 90Hz$ respectively, and the spectrum estimation by multitaper method is applied to smooth the amplitude spectra of the prediction filters for the two band-limited local wavelets. The results for these four methods are shown in Figure 3.31 – 3.34. We can see that estimated Q values for the three frequency-domain methods are significantly deviated from the true value. It indicates that the three methods are sensitive to the spectrum modification caused by spectrum estimation. For match-filter method, it still gives a quite accurate estimation of 76.55, compared to the exact value 80. It indicates that match-filter method is much less sensitive to the modification of amplitude spectra caused by spectrum estimation.

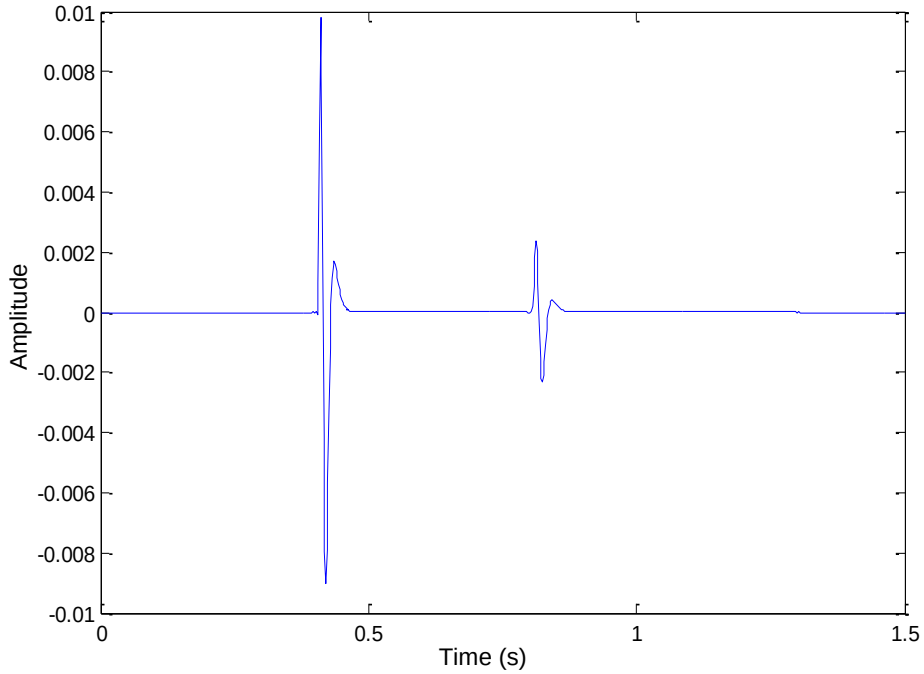

Figure 3.1. A synthetic seismic trace created with two events, created using two isolated reflectors, a minimum phase source wavelet with dominant frequency of $40Hz$, and a constant Q value of 80. Local event 1 at $0.34s - 0.54s$ and event 2 at $0.74s - 0.94s$ are picked for Q estimation tests.

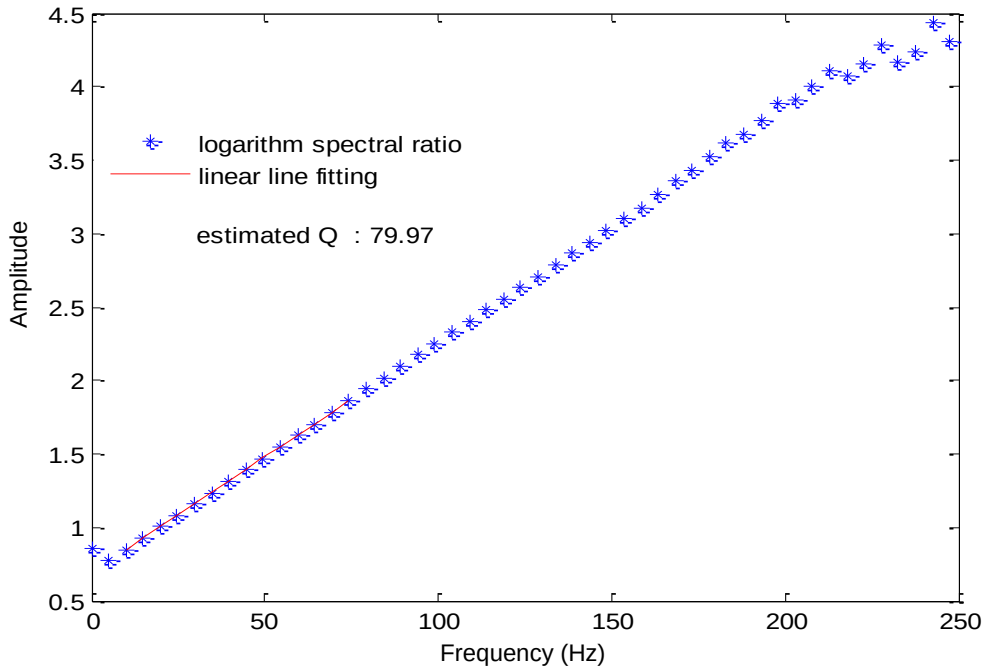

Figure 3.2. Q estimation by the classic spectral-ratio method using the two local events shown in Figure 3.1.

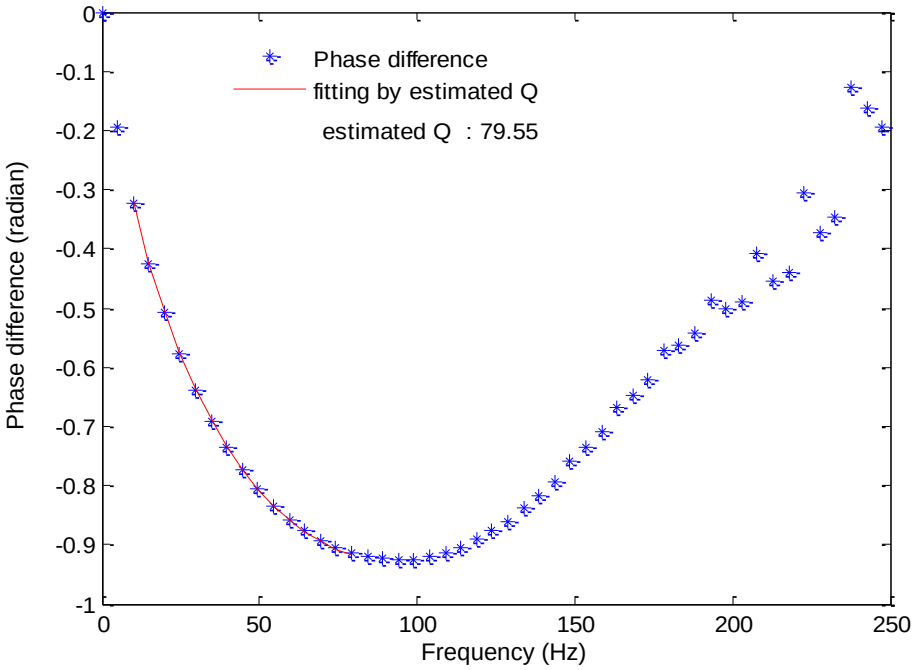

Figure 3.3. Q estimation by the complex spectral-ratio method using the two local events shown in Figure 3.1 when only phase spectra are employed.

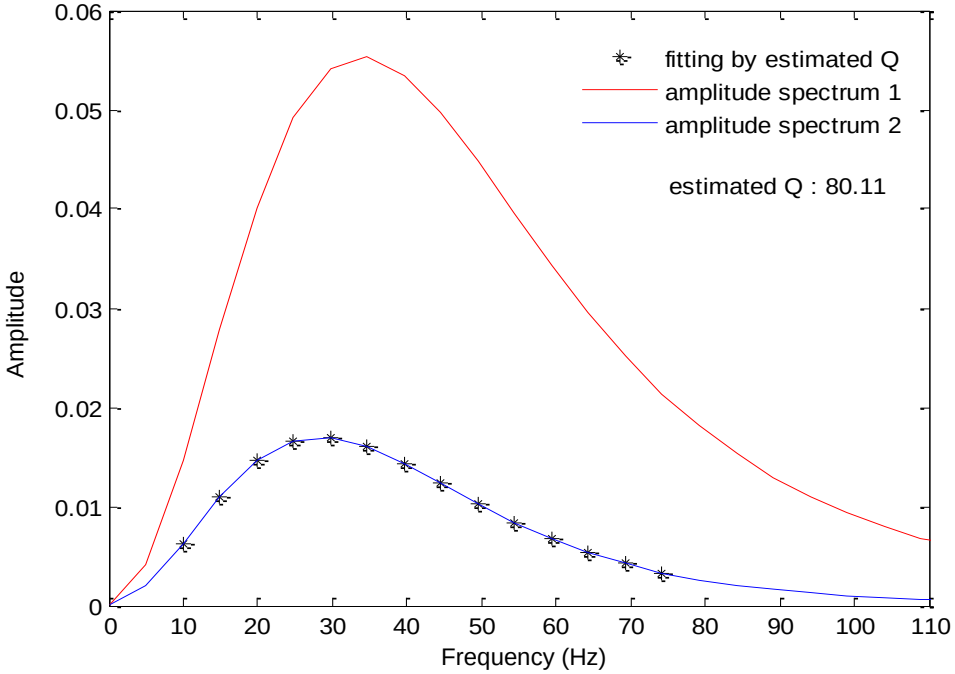

Figure 3.4. Q estimation by spectrum-modeling method using the two local events shown in Figure 3.1.

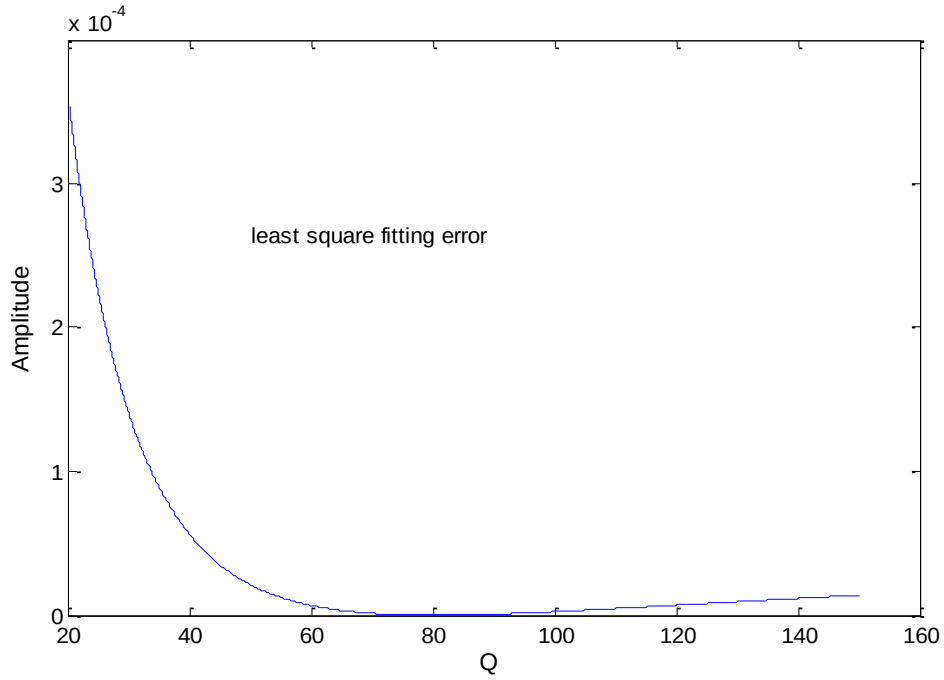

Figure 3.5.The fitting error curve for Q estimation by spectrum-modeling method corresponding to Figure 3.4.

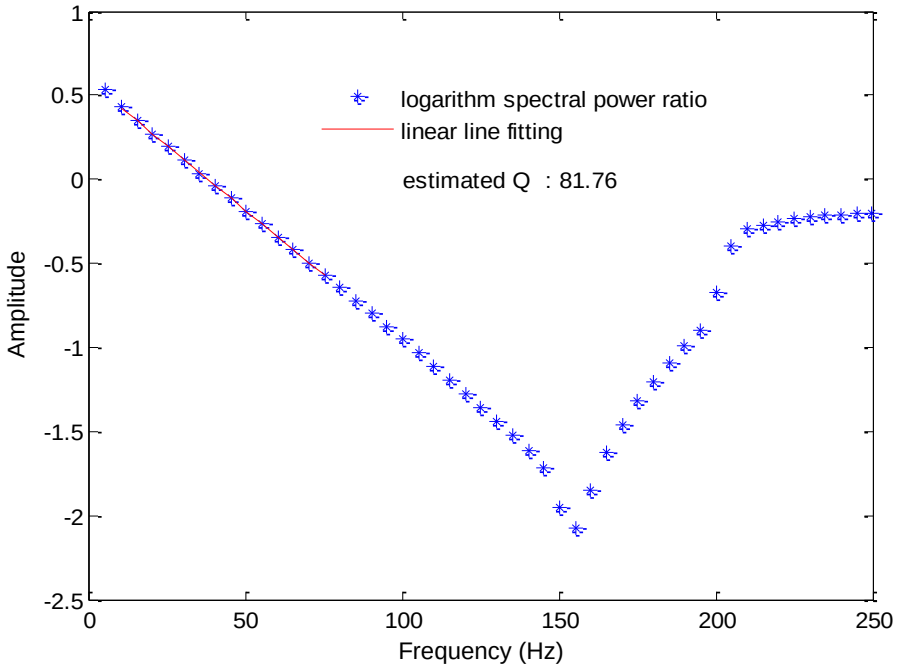

Figure 3.6. Q estimation by match-technique method using the two local events shown in Figure 3.1.

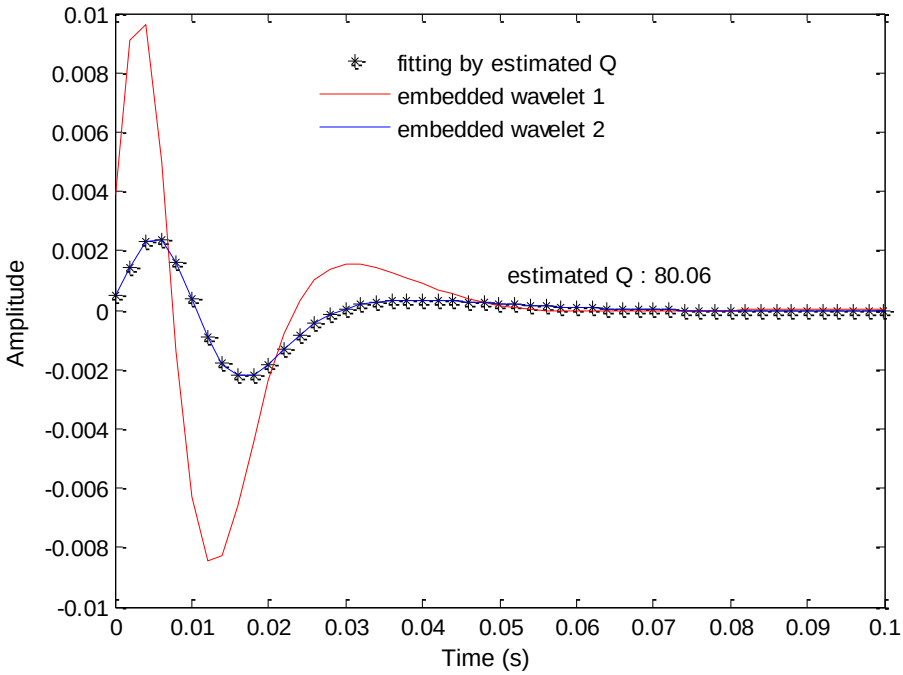

Figure 3.7. Q estimation by the match-filter method using the two local events shown in Figure 3.1.

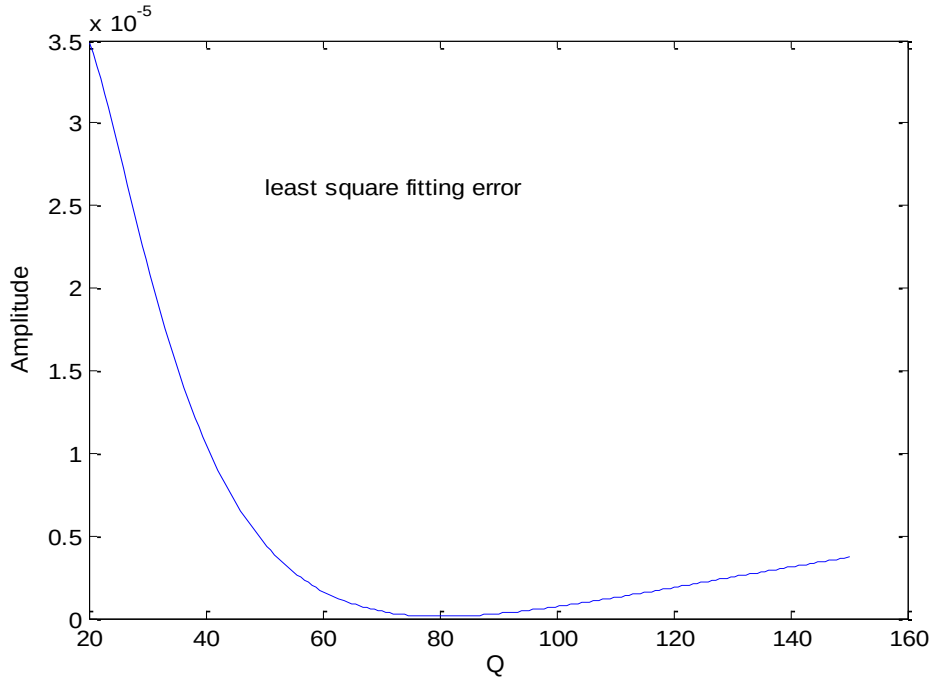

Figure 3.8. The fitting error curve for Q estimation by match-filter method corresponding to Figure 3.7.

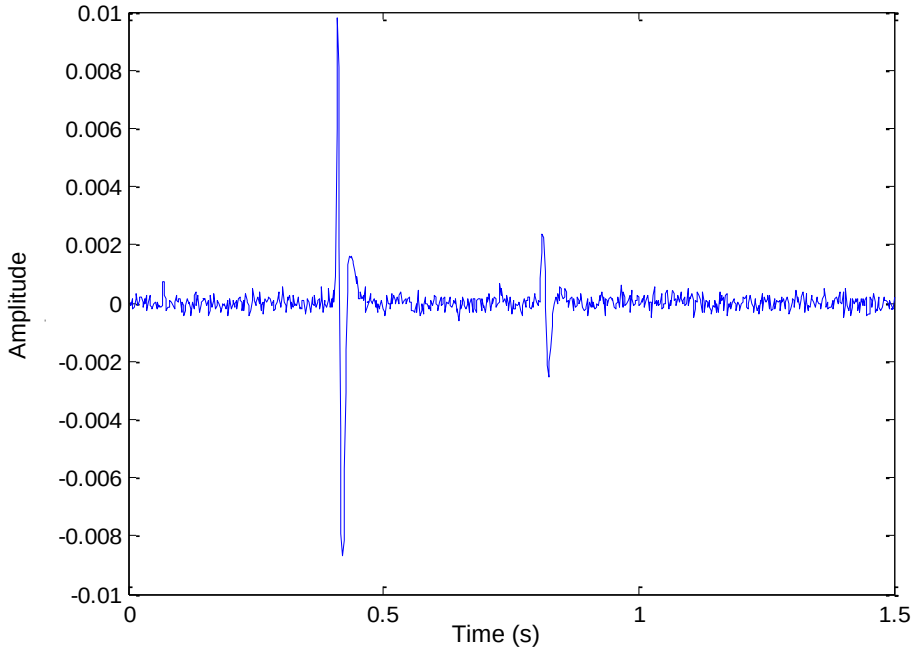

Figure 3.9. Synthetic seismic trace with noise, created by adding random noise to the seismic trace in Figure 3.1 with $SNR = 4$. Local event 1 at $0.34s - 0.54s$ and event 2 at $0.74s - 0.94s$ are picked for Q estimation tests.

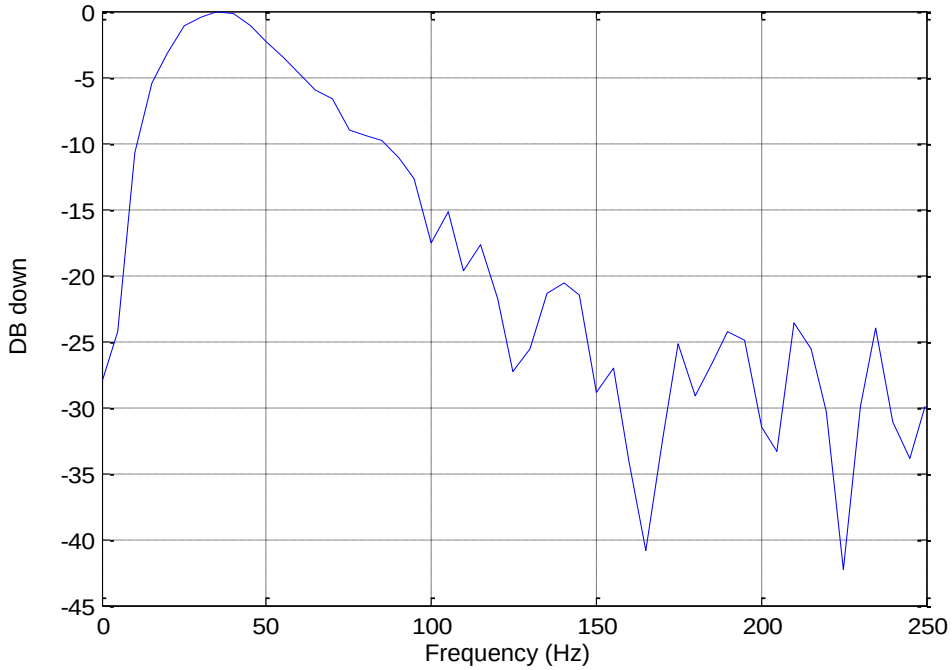

Figure 3.10. Amplitude spectrum of the local event 1 ($0.34s - 0.54s$) in Figure 3.9.

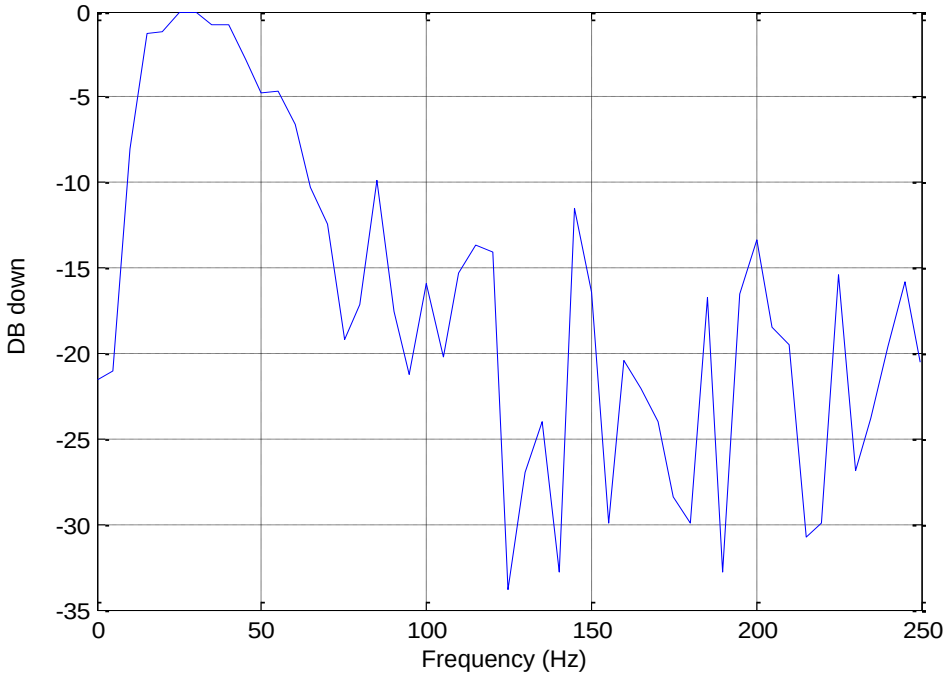

Figure 3.11. Amplitude spectrum of the event 2 ($0.74s - 0.94s$) second in Figure 3.9.

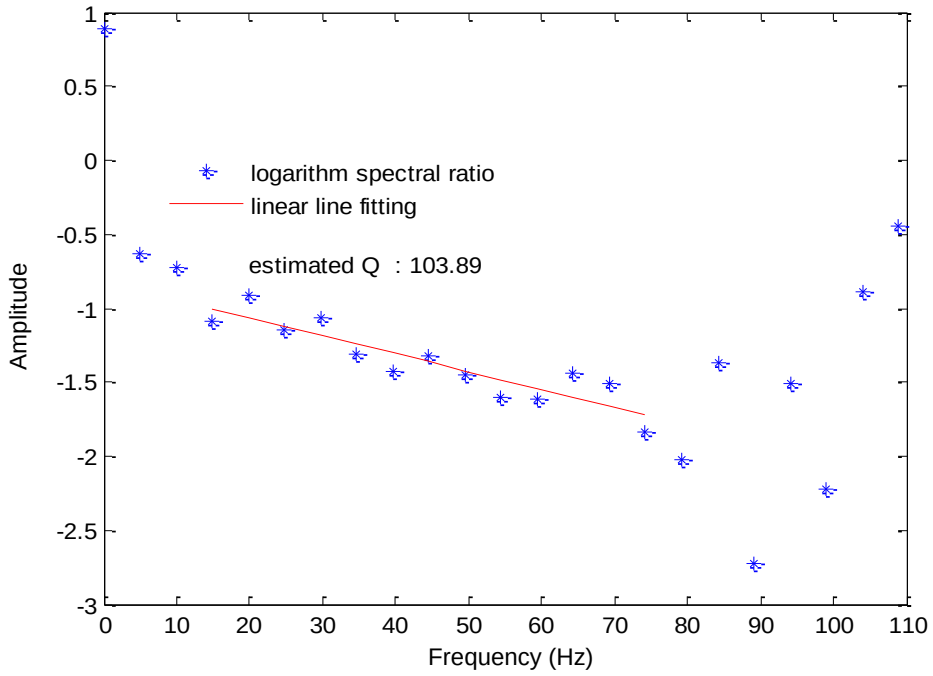

Figure 3.12. Q estimation by classic spectral-ratio method using the two local events shown in Figure 3.9.

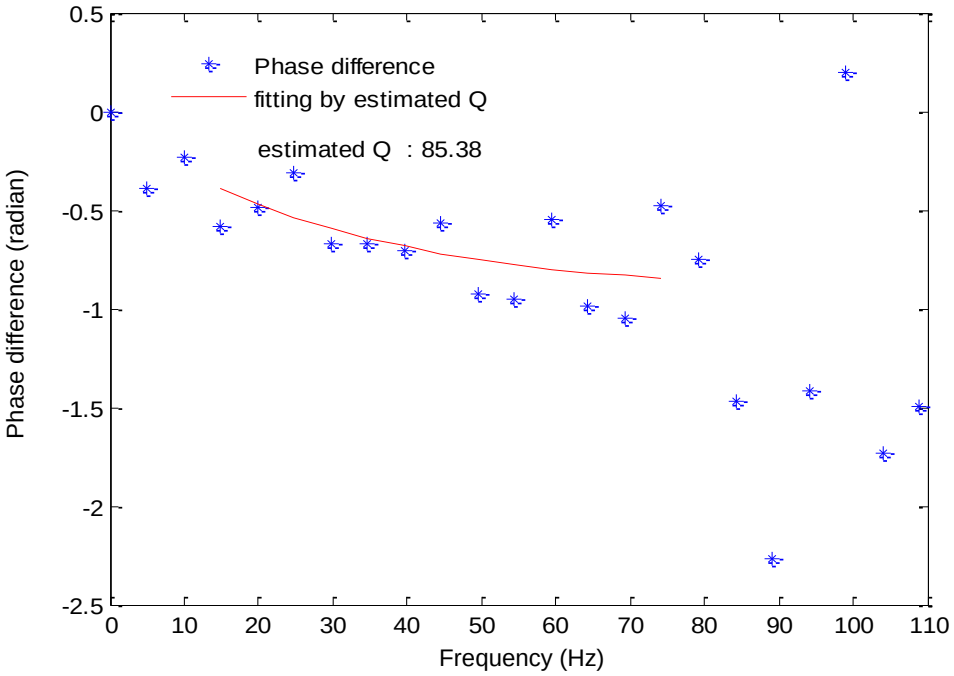

Figure 3.13. Q estimation by complex spectral-ratio method using the two local events shown in Figure 3.9.

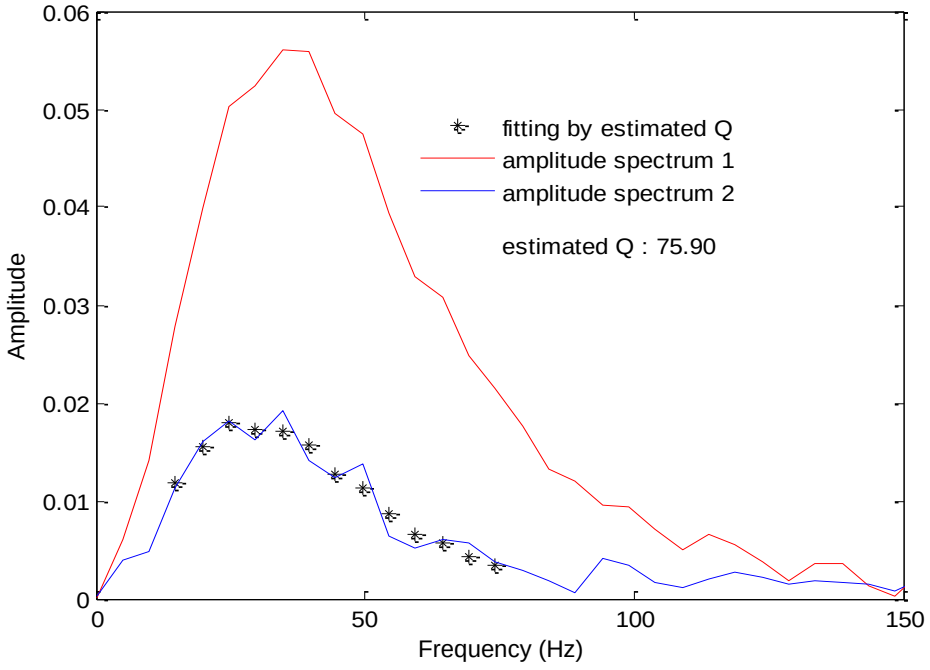

Figure 3.14. Q estimation by spectrum-modeling method using the two local events shown in Figure 3.9.

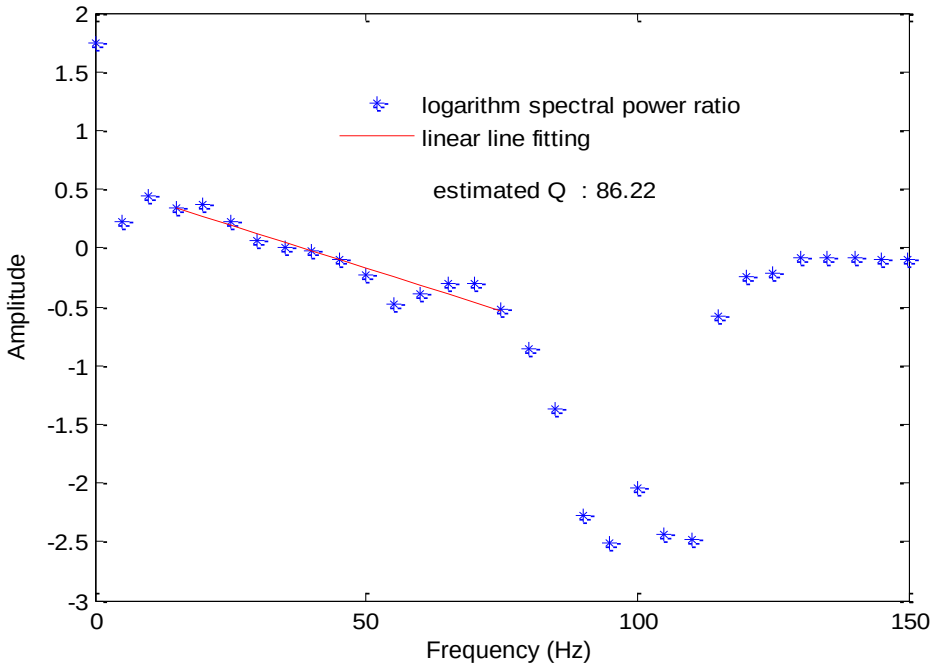

Figure 3.15. Q estimation by match-technique method using the two local events shown in Figure 3.9.

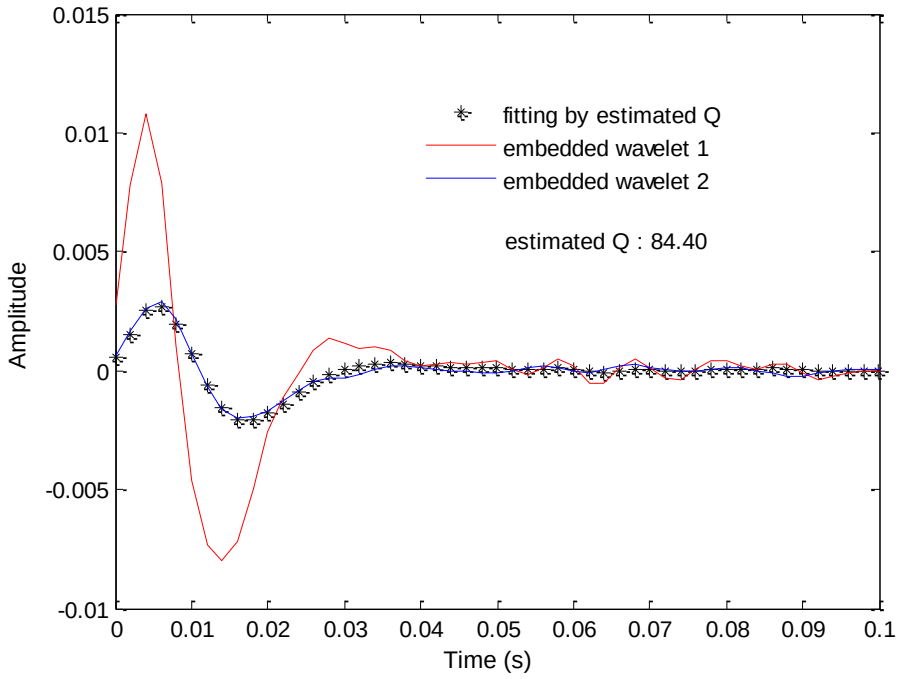

Figure 3.16. Q estimation by match-filter method using the two local events shown in Figure 3.9.

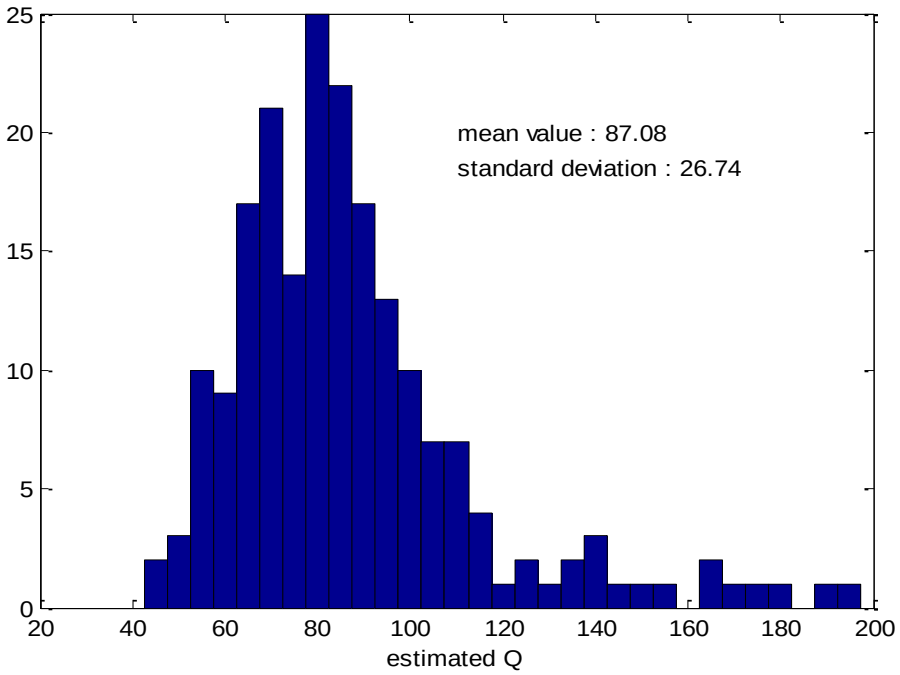

Figure 3.17. Histogram of the Q values estimated by classic spectral-ratio method using 200 seismic traces (similar to the one shown in Figure 3.9) with noise level of $SNR = 4$.

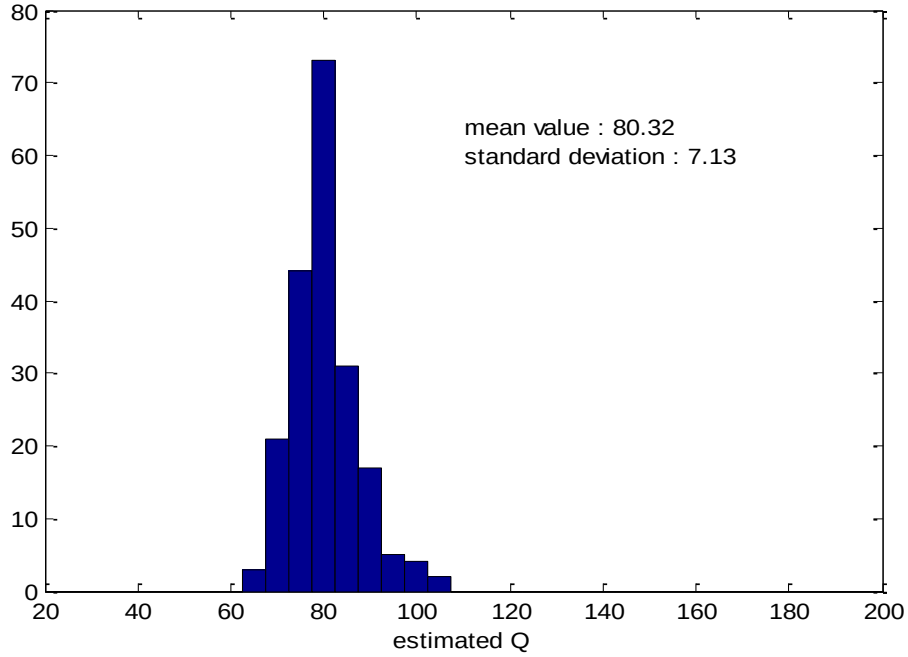

Figure 3.18. Histogram of the Q values estimated by complex spectral-ratio method (only phase spectra are employed) using 200 seismic traces (similar to the one shown in Figure 3.9) with noise level of $SNR = 4$.

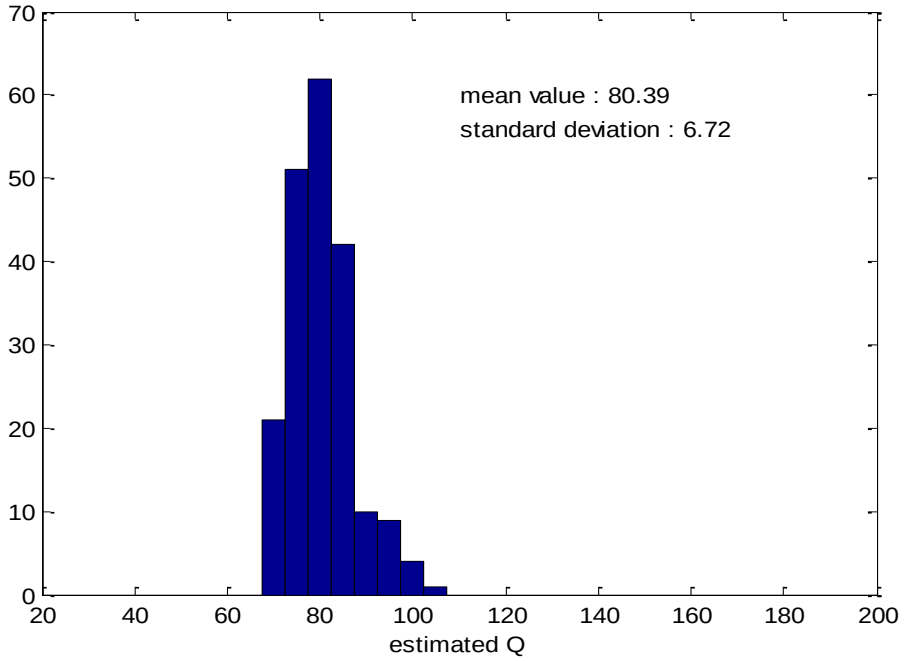

Figure 3.19. Histogram of the Q values estimated by complex spectral-ratio method based on equation (3.31), using 200 seismic traces (similar to the one shown in Figure 3.9) with noise level of $SNR = 4$.

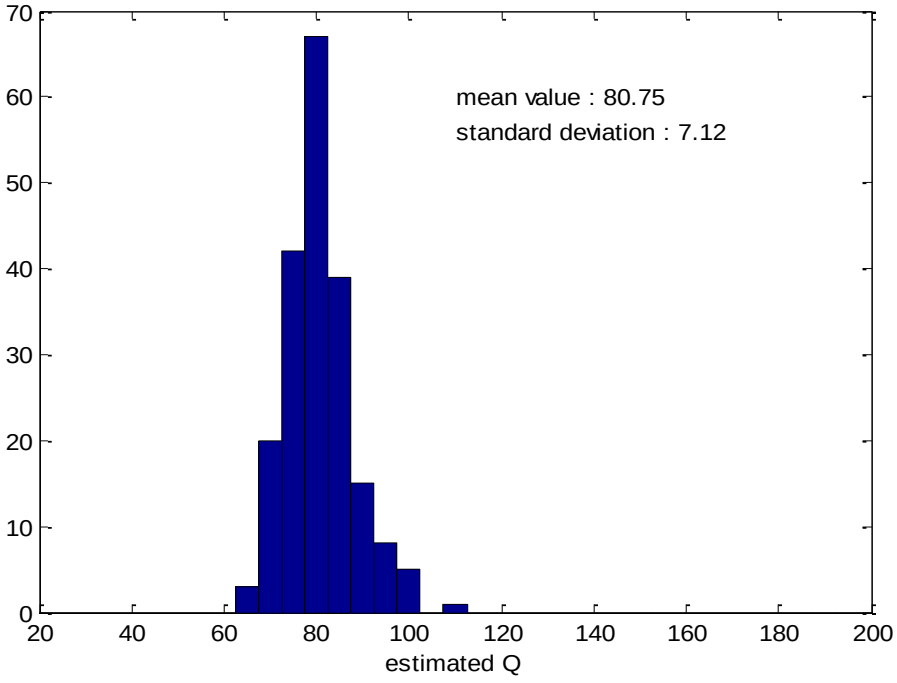

Figure 3.20. Histogram of the Q values estimated by generalized complex spectral-ratio method based on equation (3.36) with $\varepsilon = 0.5$, using 200 seismic traces (similar to the one shown in Figure 3.9) with noise level of $SNR = 4$.

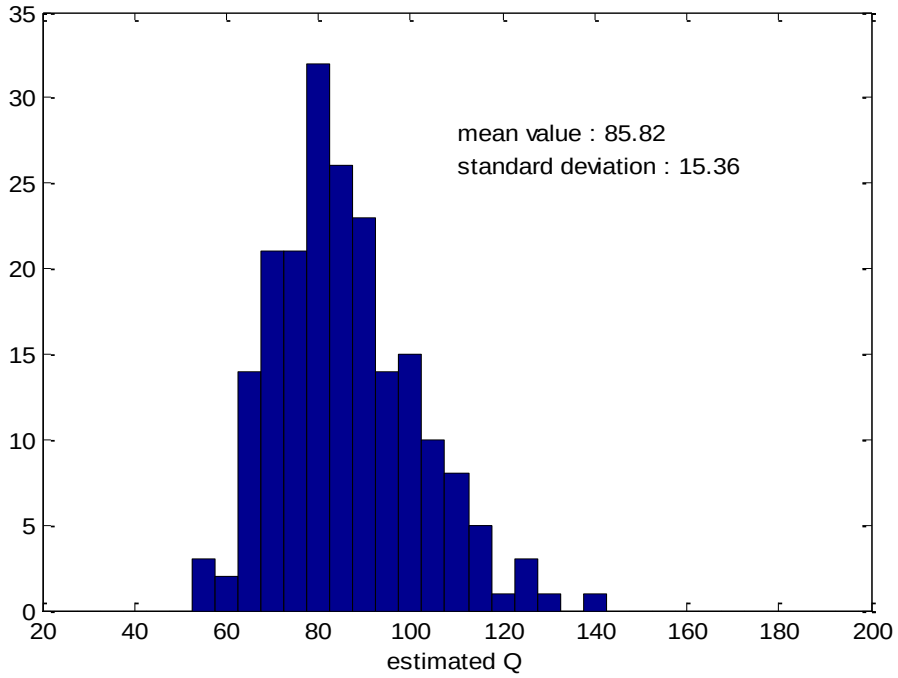

Figure 3.21. Histogram of the Q values estimated by spectrum-modeling method using 200 seismic trace (similar to the one shown in Figure 3.9) with noise level of $SNR = 4$.

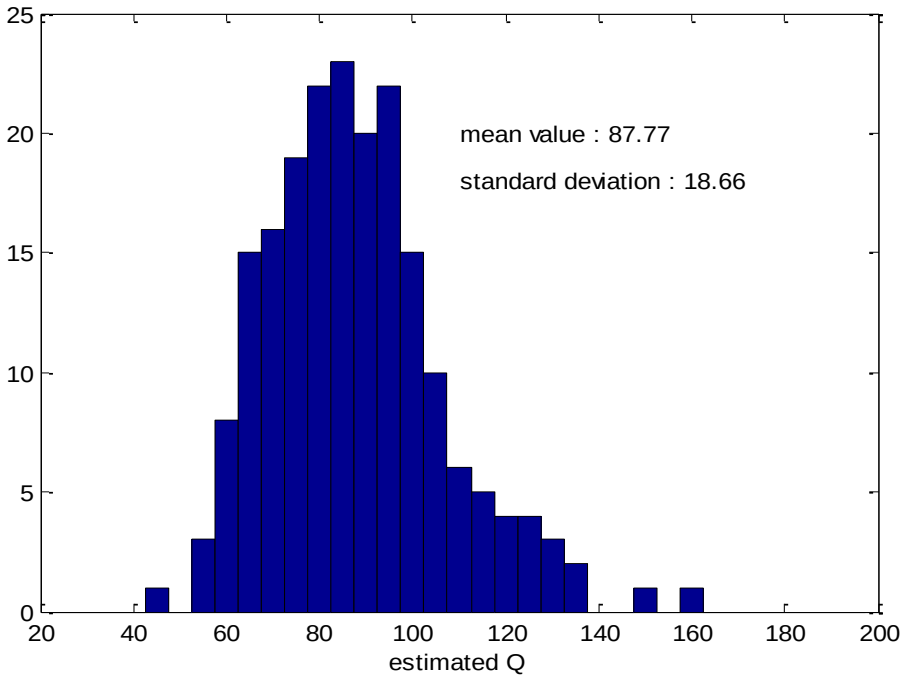

Figure 3.22. Histogram of the Q values estimated by match-technique method using 200 seismic trace (similar to the one shown in Figure 3.9) with noise level of $SNR = 4$.

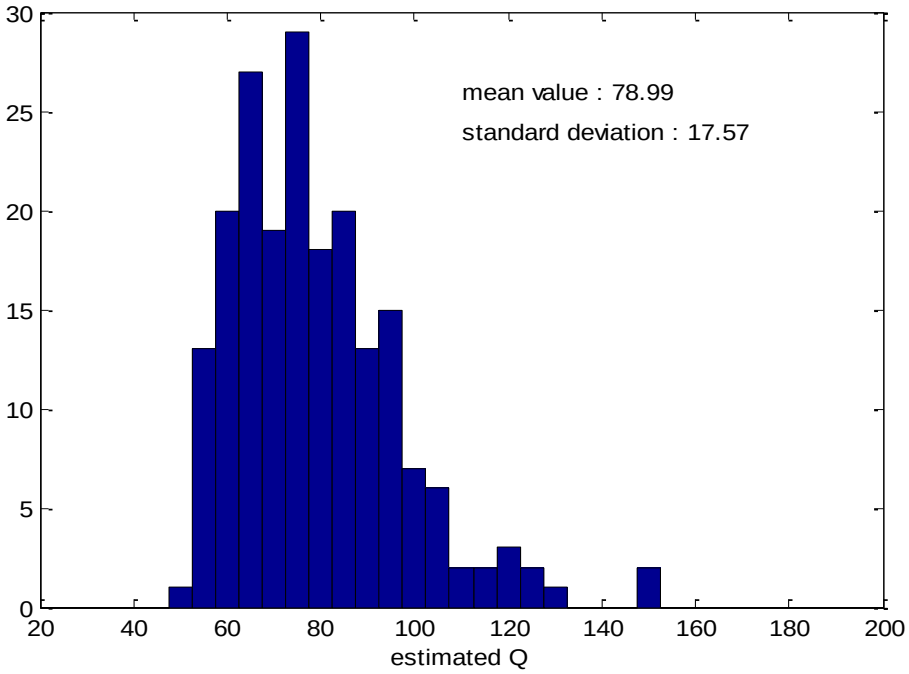

Figure 3.23. Histogram of the Q values estimated by the match-filter method using 200 seismic trace (similar to the one shown in Figure 3.9) with noise level of $SNR = 4$.

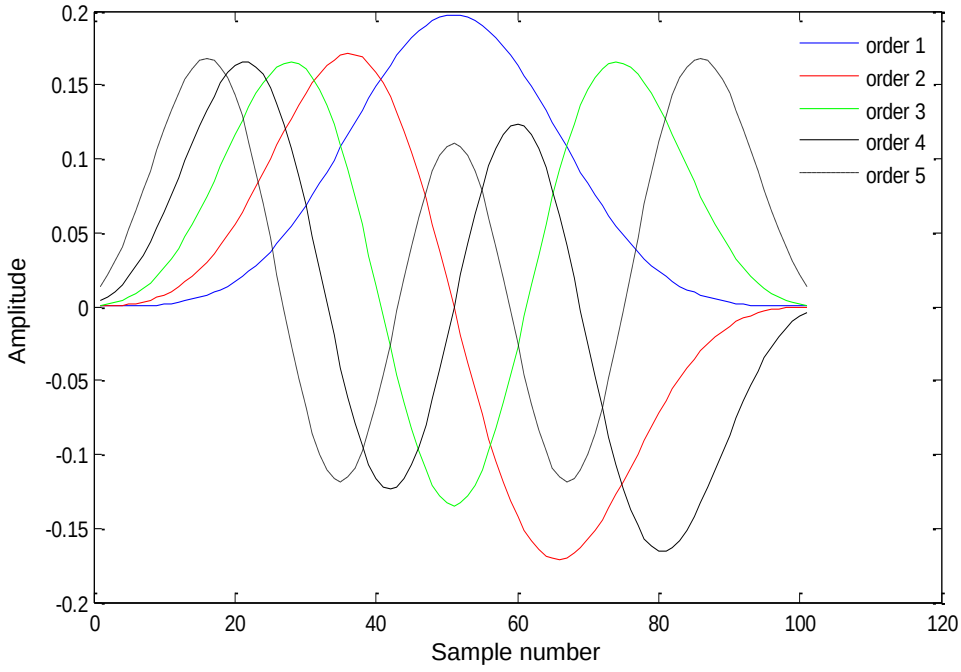

Figure 3.24. The five lowest order 4π prolate tapers with 101 sample points for the amplitude spectrum smoothing of the two local events shown in Figure 3.9.

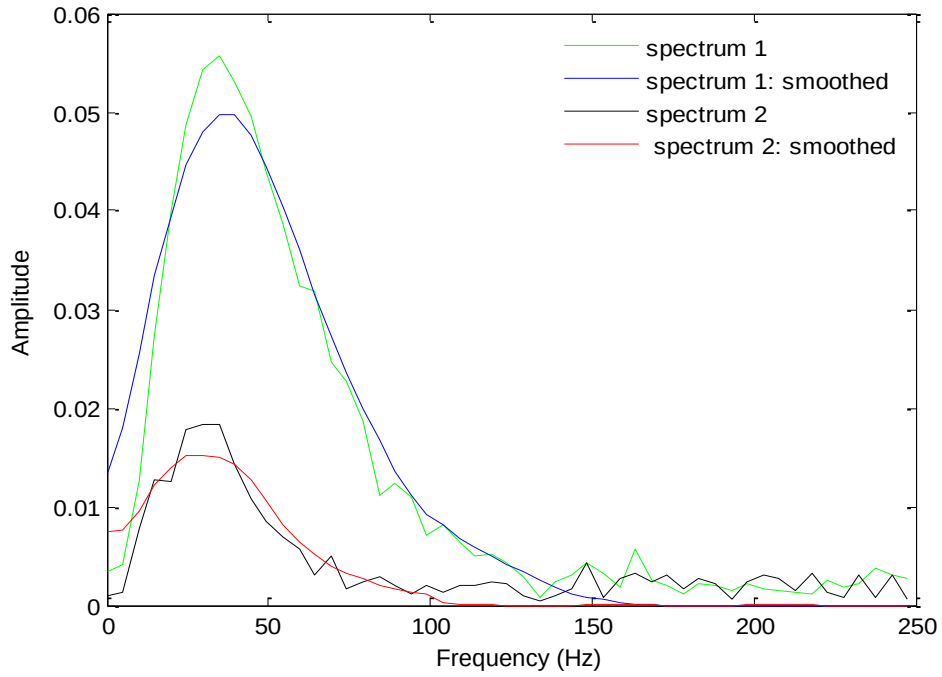

Figure 3.25. Amplitude spectra of the two local events shown in Figure 3.9. Amplitude spectrum of event 1(green); Smoothed amplitude spectrum of event 1 (blue); Amplitude spectrum of event 2 (black); Smoothed amplitude spectrum of event 2 (red).

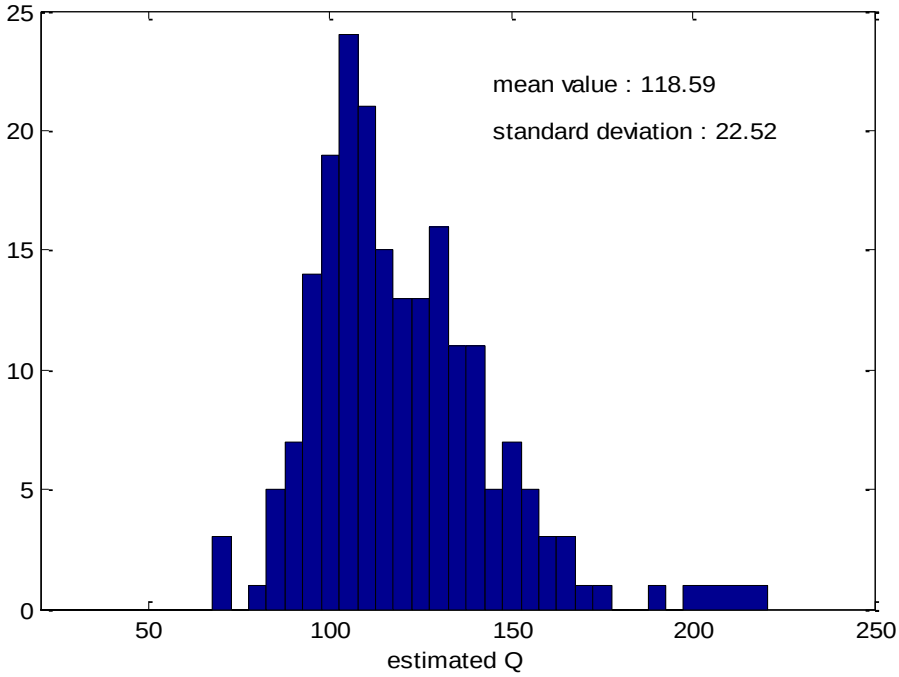

Figure 3.26. Histogram of the Q values estimated by classic spectral-ratio method using 200 seismic traces with noise level of $SNR = 4$ (multitaper method is employed for spectrum estimation).

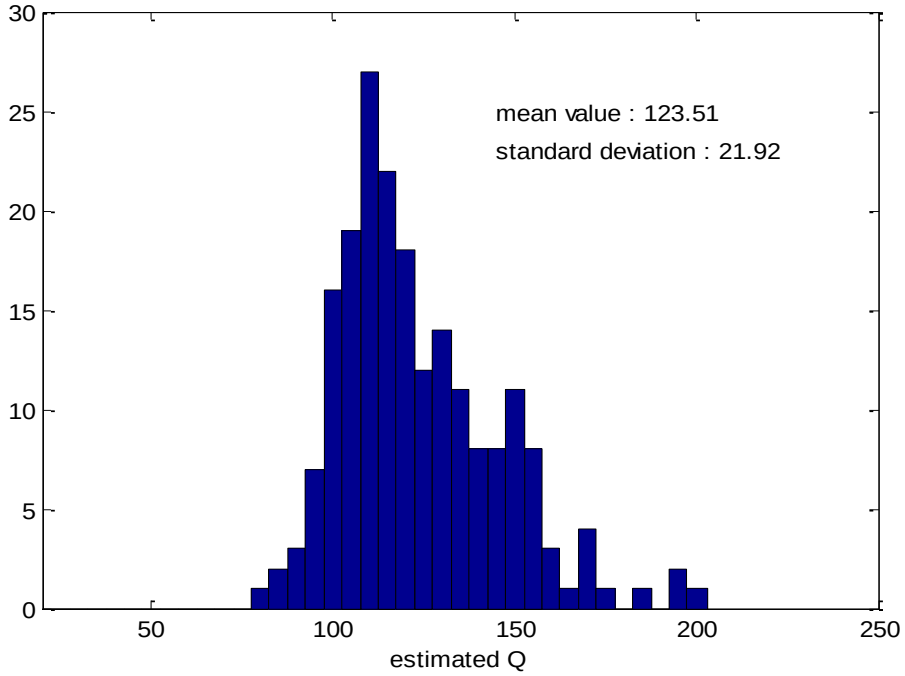

Figure 3.27. Histogram of the Q values estimated by spectrum-modeling method using 200 seismic traces with noise level of $SNR = 4$ (multitaper method is employed for spectrum estimation).

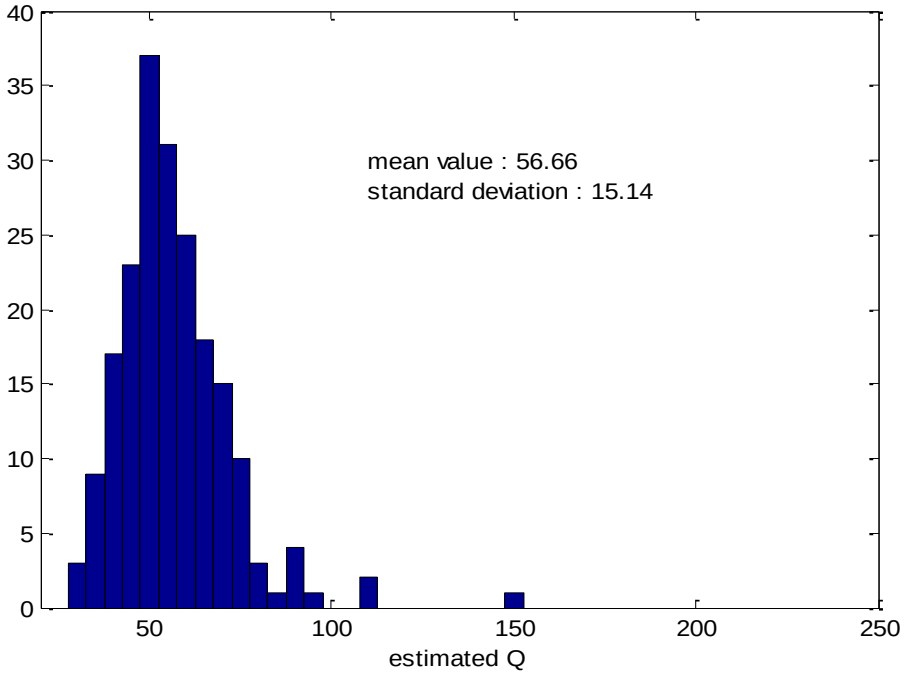

Figure 3.28. Histogram of the Q values estimated by match-technique method using 200 seismic trace with noise level of $SNR = 4$ (multitaper method is employed for spectrum estimation).

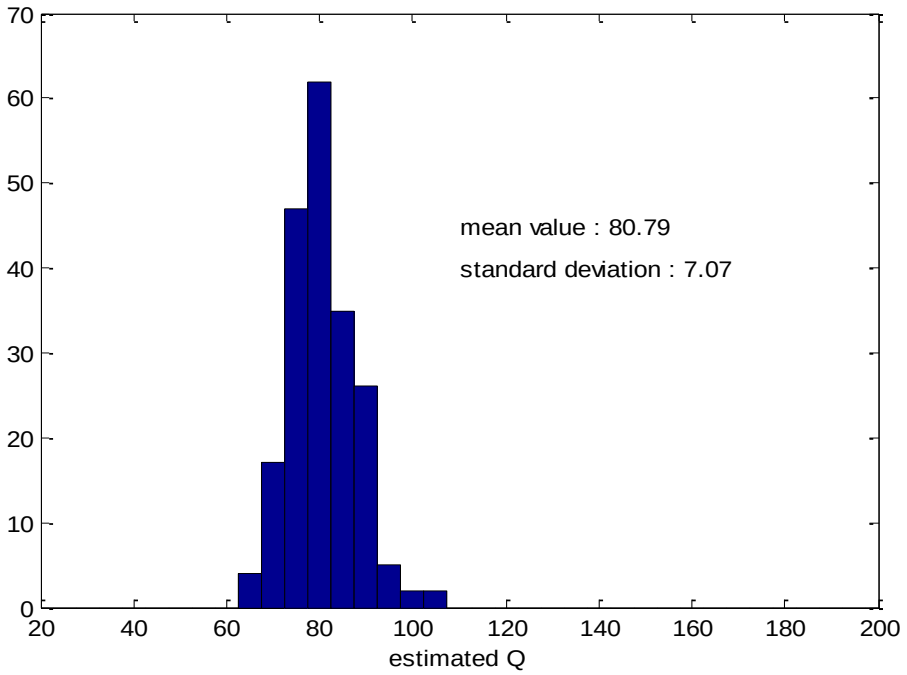

Figure 3.29. Histogram of the Q values estimated by the match-filter method using 200 seismic traces with noise level of $SNR = 4$ (multitaper method is employed for spectrum estimation).

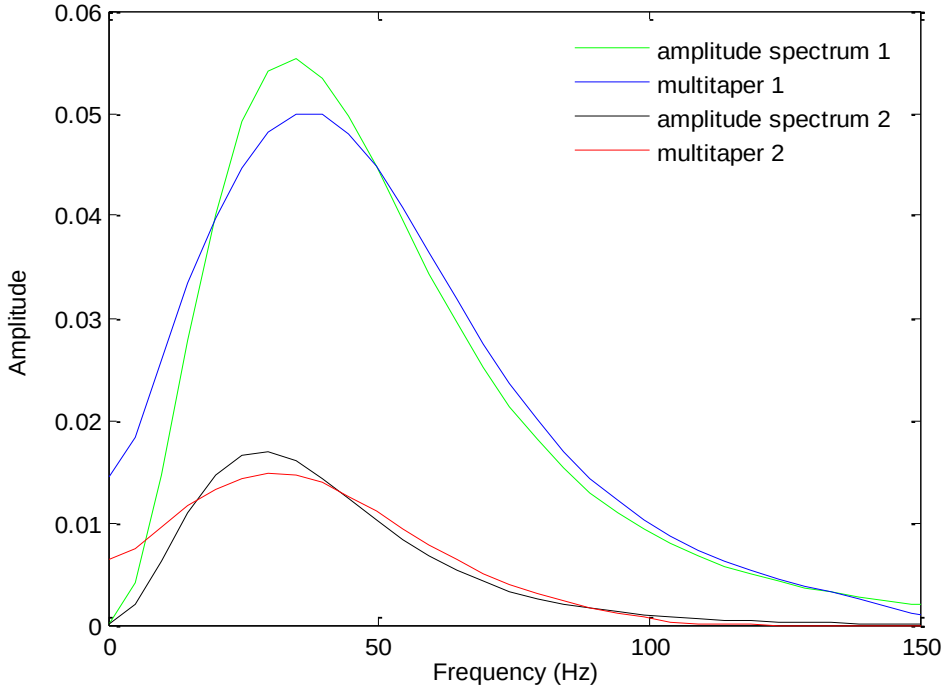

Figure 3.30. Spectrum estimation of for the two events in Figure 3.1 using multitaper method with frequency-band limit of $10Hz - 140Hz$ and $10Hz - 90Hz$ respectively.

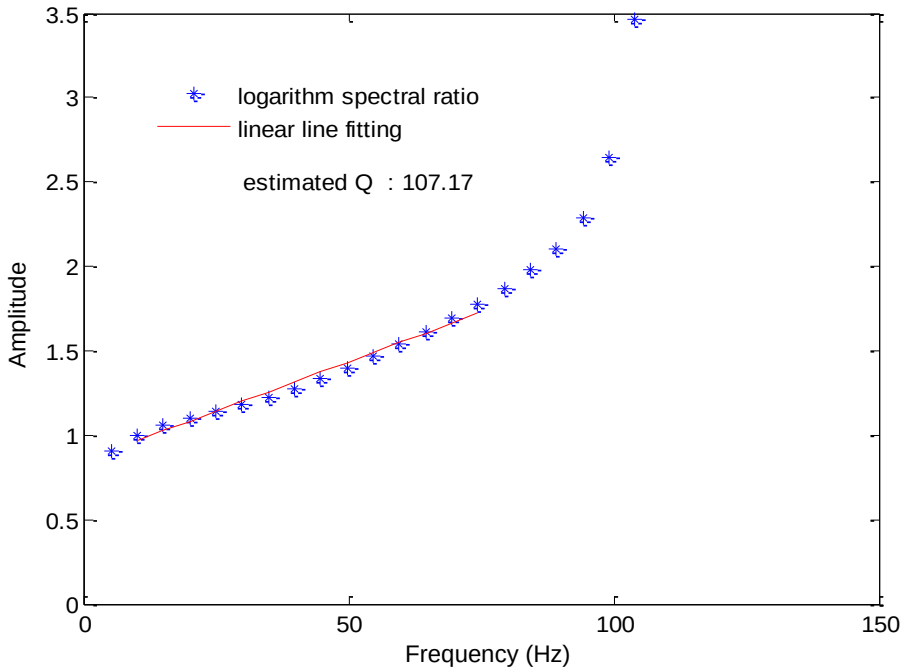

Figure 3.31. Q estimation by classic spectral-ratio method using the amplitude spectra estimated by multitaper method shown in Figure 3.30.

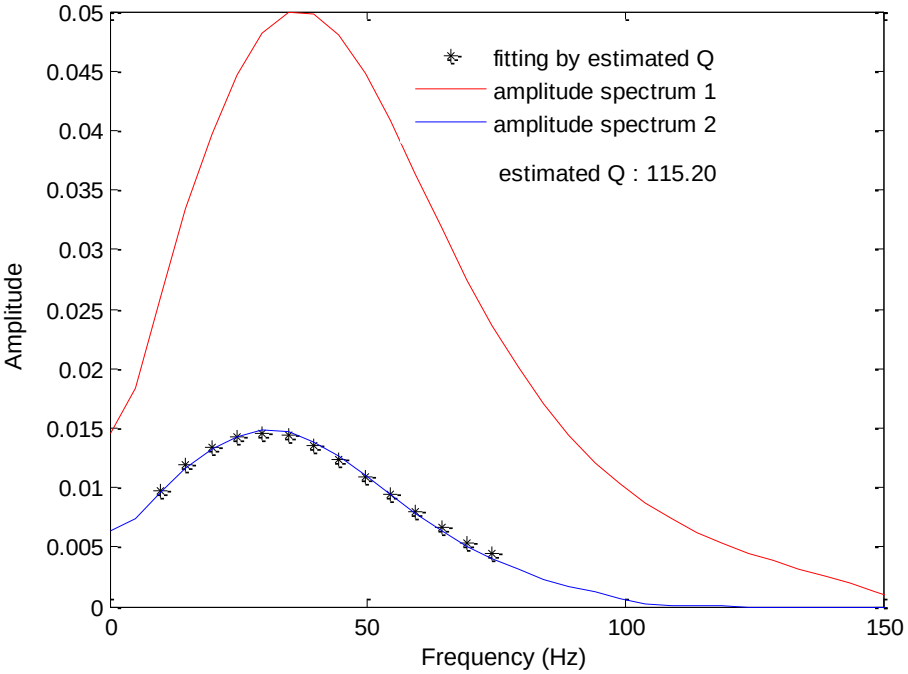

Figure 3.32. Q estimation by spectrum-modeling method using the amplitude spectra estimated by multitaper method shown in Figure 3.30.

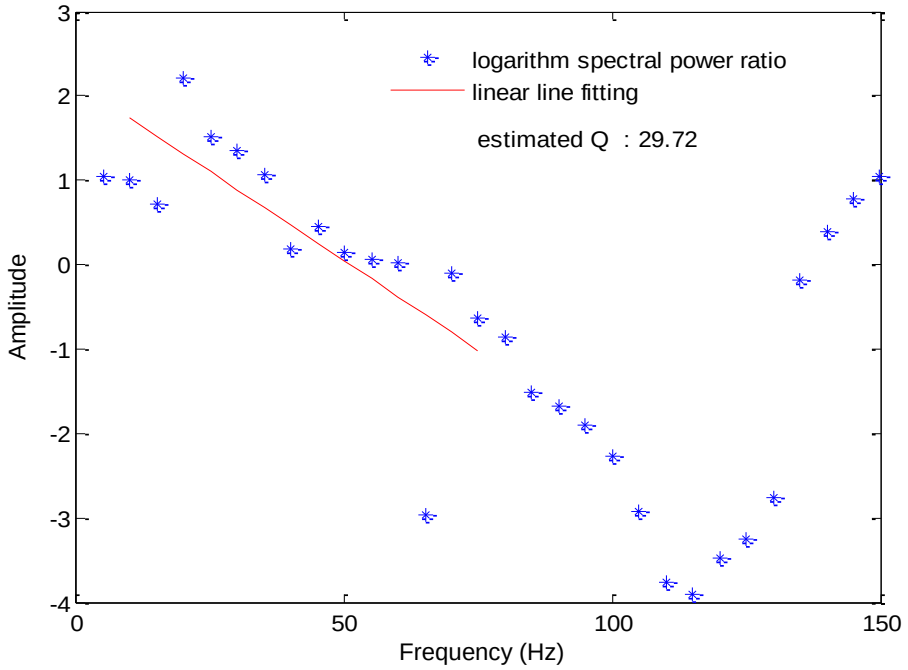

Figure 3.33. Q estimation by match-technique method using the band-pass filtered local events shown in Figure 3.1 with frequency band $10Hz - 140Hz$ and $10Hz - 90Hz$ respectively (multitaper method is employed for spectrum estimation of prediction filter).

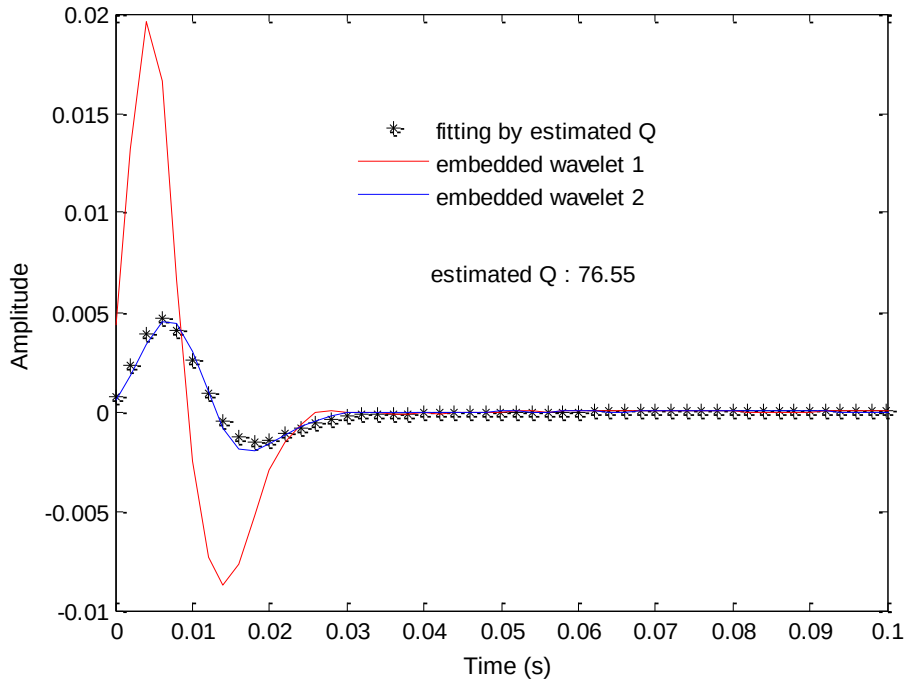

Figure 3.34. Q estimation by match-filter method using the amplitude spectra estimated by multitaper method shown in Figure 3.30

Theoretically, the frequency band used to filter the local wavelets for noise suppression can affect the result of match-filter method. If a band-pass filter with relatively lower high-cut frequency is applied to the local wavelet in the deep zone, the loss of high-frequency energy will be attributed to Q attenuation, which will lead to smaller estimated value than the true value. Therefore, in order to obtain accurate estimation, match-filter method requires the match of frequency bands for the local wavelets. From Figure 3.10 and 3.11, we can see that $90Hz$ and $140Hz$ correspond to the frequency components of the amplitude spectra that have relative magnitudes of -20dB with respective to the maximum amplitudes. Therefore, the frequency band $10Hz - 140Hz$ for local wave in shallow zone roughly matches the frequency band $10Hz - 90Hz$ for the wavelet in deep zone. Then, the estimated Q value is close to the true value. When the frequency band is poorly chosen for match-filter method, the result can be distorted. For instance, if we use a frequency band of $10Hz - 70Hz$ for the wavelet in deep zone, the bandlimited amplitude spectra estimated by the multitaper method are shown in Figure 3.35, which lead to a distorted Q estimation shown in Figure 3.36. For this case, the high-frequency energy loss of the local wave in deep zone caused by band-pass filtering is attributed to Q attenuation, which, in turn, leads to a significantly smaller Q value than the true one.

In addition, synthetic VSP data with extensive noise are used to evaluate Q estimation methods. The Q estimation is conducted using 200 seismic traces with noise level of $SNR = 2$. Since, as shown previously, frequency-domain methods are sensitive to spectrum modification, spectrum estimation is employed only for match-filter method at this time. The Q estimation results are shown in Figure 3.37 – 3.43. The classic spectral-ratio method, spectrum modeling method and match-technique method are affected by the increased noise level and give results

with significantly deviated mean values and large standard deviation values. Again, for the complex spectral ratio method, Q estimation is conducted for three cases. The first case is that only the phase spectra are used for Q estimation; the second one is Q estimation based on equation (3.31); the third one is the generalized complex spectral-ratio method based on equation (3.36) with $\varepsilon = 0.5$. As shown in Figure 3.38 – 3.40, the results of these three cases are comparable and are much better than the results for the other three frequency-domain method. It might indicate that the phase difference between the local wavelets is not significantly affected by the increased noise level. The match-filter method, as shown in Figure 3.43, still gives quite good estimation with a mean value of 80.02 and standard deviation of 11.82, which is slightly better than the results of complex spectral ratio method. Based on the above results, we can see that both match-filter method and complex spectral-ratio method are robust to noise.

For the complex spectral-ratio method, its result is subject to the choosing of reference frequency. The accurate reference frequency f_0 (the Nyquist frequency) is used for the above tests. To evaluate the influence of inaccurate reference frequency for the complex spectral-ratio method, only the phase spectra are used to give estimation result and f_0 is chosen as the Nyquist frequency scaled by 0.8. First, Q estimation is conducted using the two local events shown in Figure 3.1. As shown in Figure 3.44, the estimated Q of 68.32 is deviated from true value 80 for this ideal case. Then, Q estimation is conducted using 200 seismic traces, similar to the one shown in Figure 3.9, with noise level of $SNR = 4$ and $SNR = 2$ respectively. The distributions of corresponding estimated Q values are shown in Figure 3.45 and 3.46. We can see that the mean value of the estimation results is consistent with the ideal case shown in Figure 3.44, which is deviated from true value, and the standard deviation values of the estimated results remain at the same level as the cases with accurate reference frequency shown in Figure 3.18 and 3.38.

Therefore, the complex spectral-ratio method is robust to noise, however its accuracy will depend on how well the reference frequency is chosen to match the data.

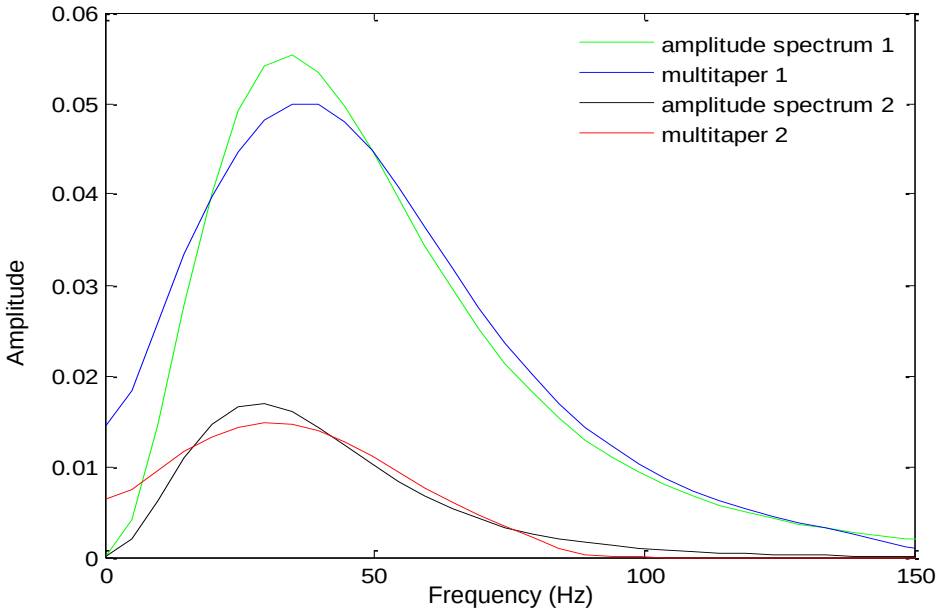

Figure 3.35. Spectrum estimation of for the two events $(0.34-0.54s, 0.74s-0.94s)$ in Figure 3.1 by multitaper method with frequency-band limit of $10Hz-140Hz$ and $10Hz-70Hz$ respectively.

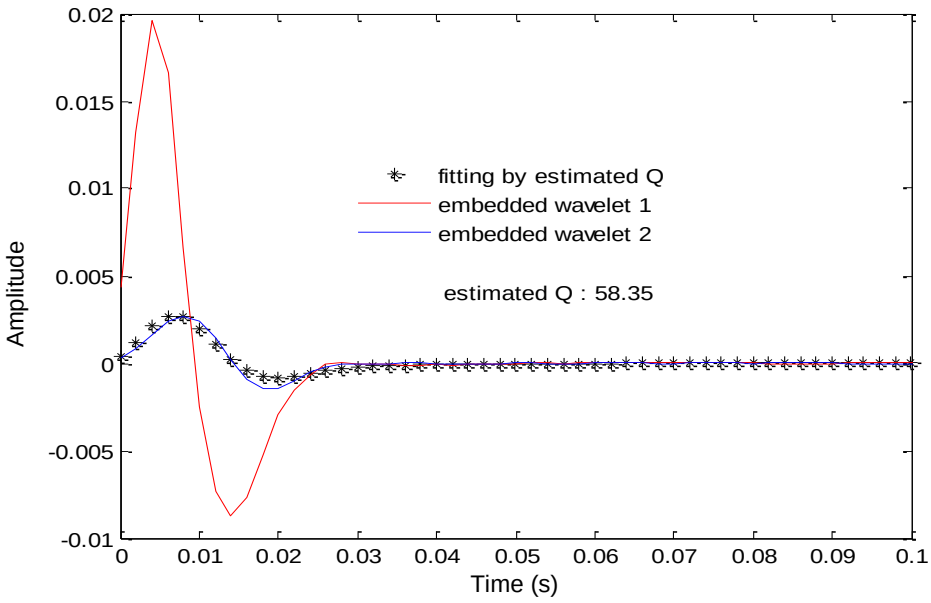

Figure 3.36. Q estimation by match-filter method using the local events in Figure1; Spectrum estimation for the two events by multitaper method is employed with frequency band $10Hz-140Hz$ and $10Hz-70Hz$ respectively.

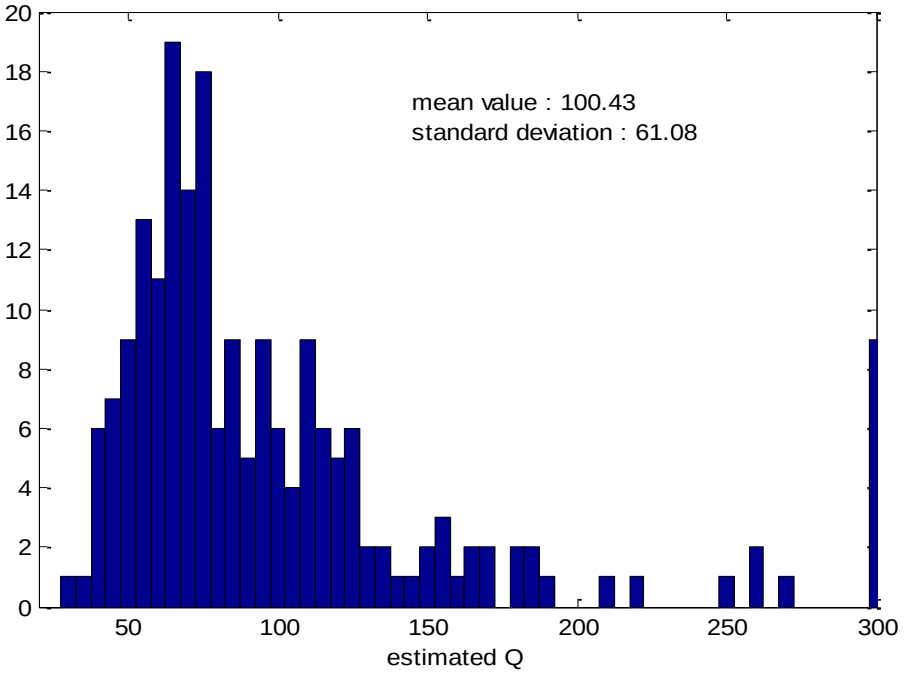

Figure 3.37. Histogram of the Q values estimated by classic spectral-ratio method using 200 seismic traces (similar to the one shown in Figure 3.9) with noise level of $SNR = 2$.

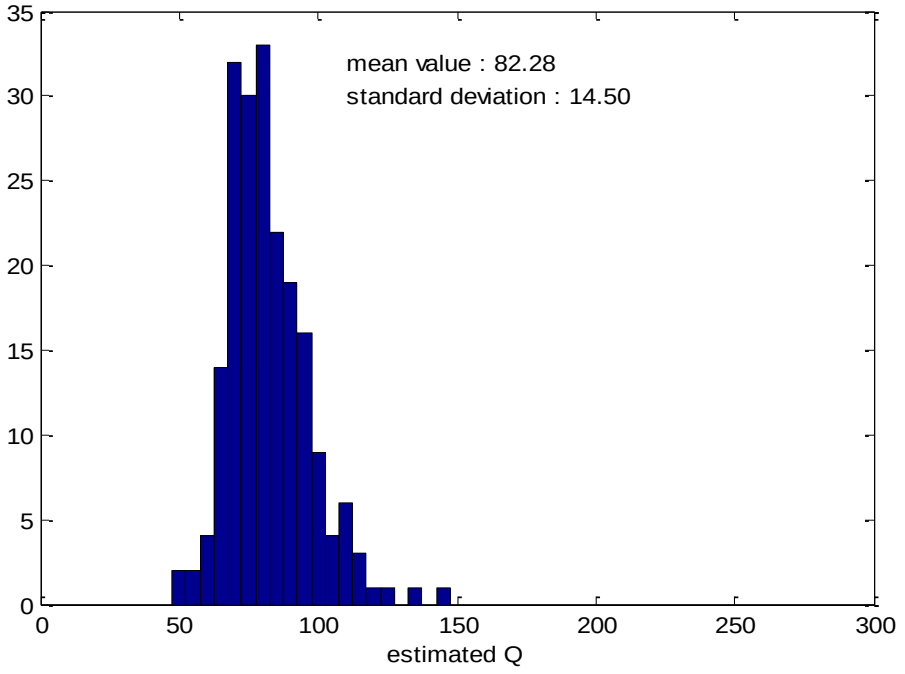

Figure 3.38. Histogram of the Q values estimated by complex spectral-ratio method (only phase spectra are employed) using 200 seismic traces (similar to the one shown in Figure 3.9) with noise level of $SNR = 2$.

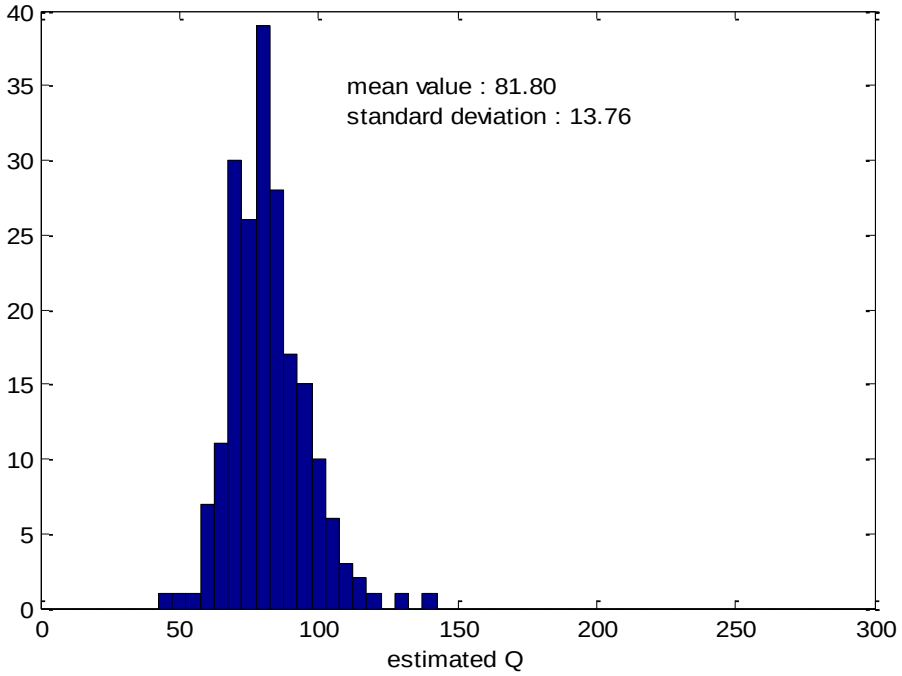

Figure 3.39. Histogram of the Q values estimated by complex spectral-ratio method based on equation (3.31), using 200 seismic traces (similar to the one shown in Figure 3.9) with noise level of $SNR = 2$.

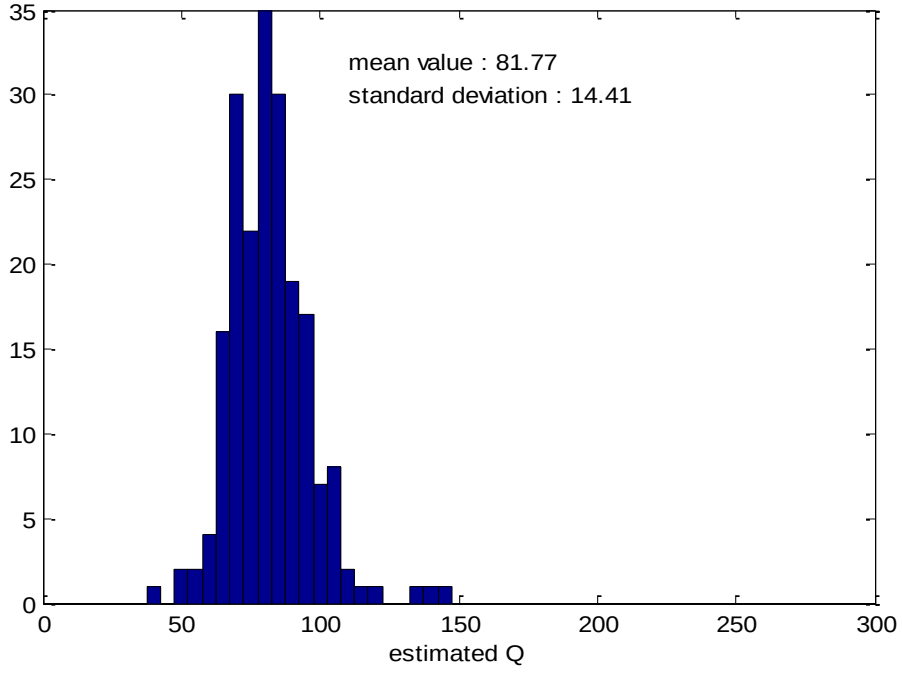

Figure 3.40. Histogram of the Q values estimated by generalized complex spectral-ratio method based on equation (3.36) with $\varepsilon = 0.5$, using 200 seismic traces (similar to the one shown in Figure 3.9) with noise level of $SNR = 2$.

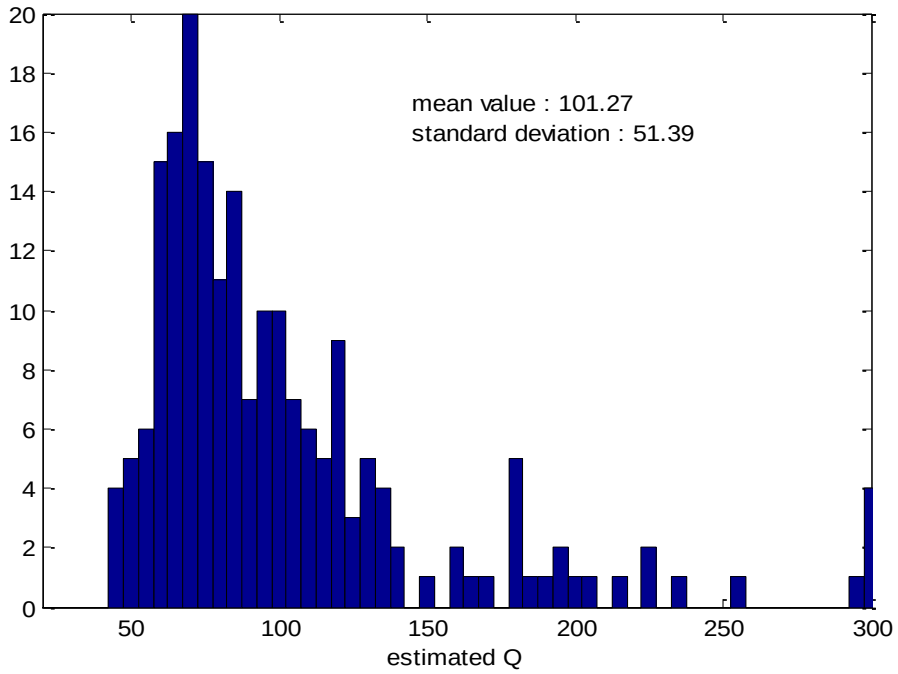

Figure 3.41. Histogram of the Q values estimated by spectrum-modeling method using 200 seismic trace (similar to the one shown in Figure 3.9) with noise level of $SNR = 2$.

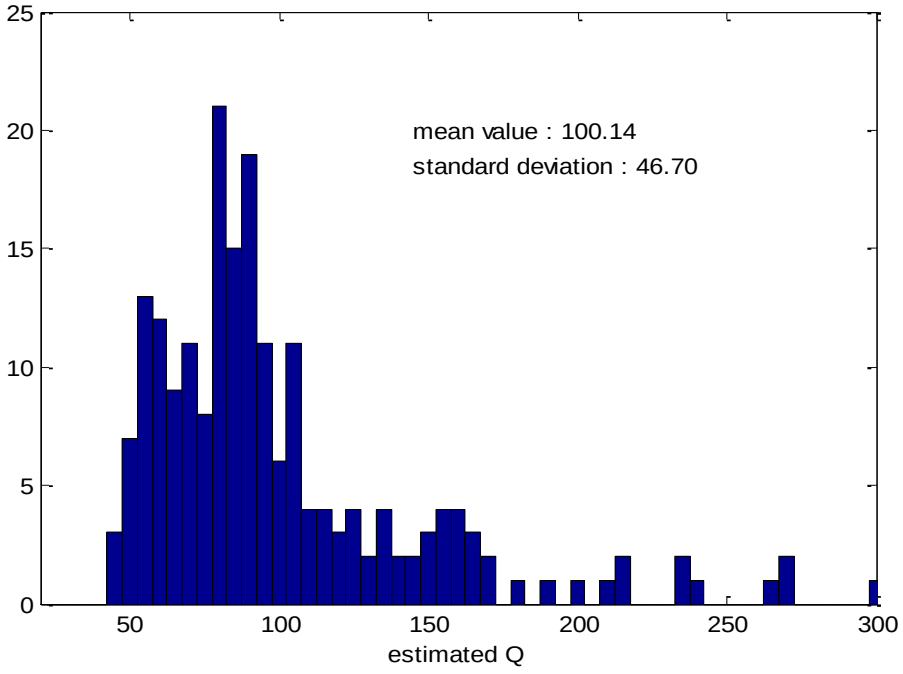

Figure 3.42. Histogram of the Q values estimated by match-technique method using 200 seismic trace (similar to the one shown in Figure 3.9) with noise level of $SNR = 2$.

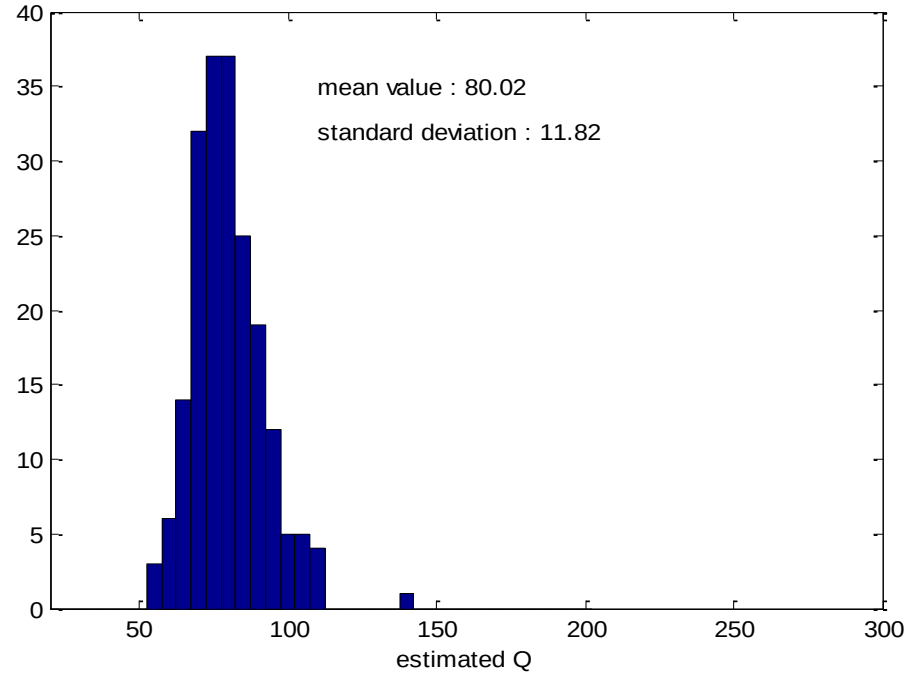

Figure 3.43. Histogram of the Q values estimated by the match-filter method using 200 seismic trace (similar to the one shown in Figure 8) with noise level of $SNR = 2$ (Multitaper method is employed for spectrum estimation).

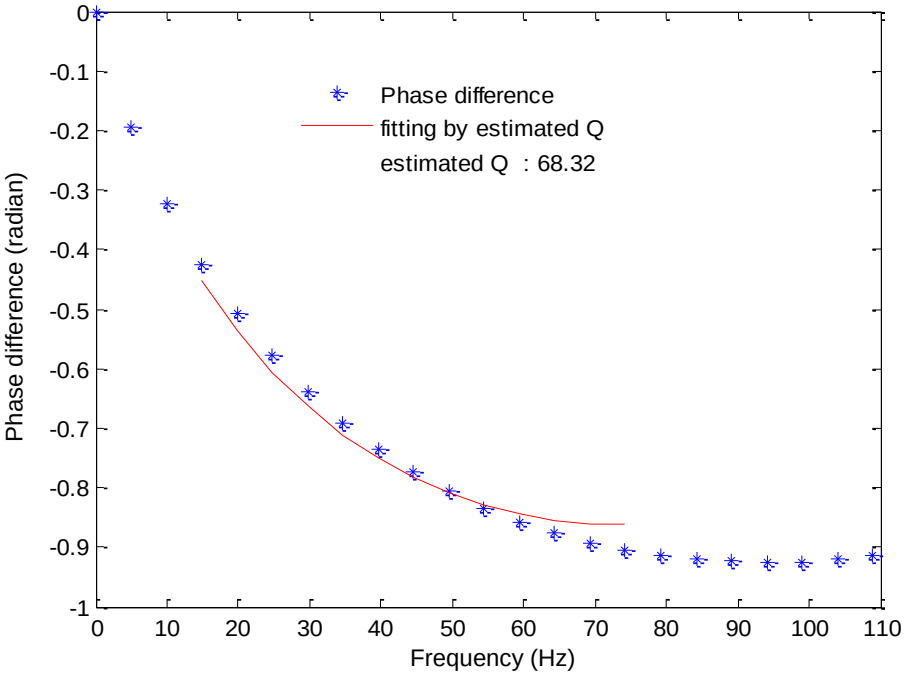

Figure 3.44. Q estimation by complex spectral-ratio method (only phase spectra are employed) using the two events shown in Figure 3.1(inaccurate reference frequency is used).

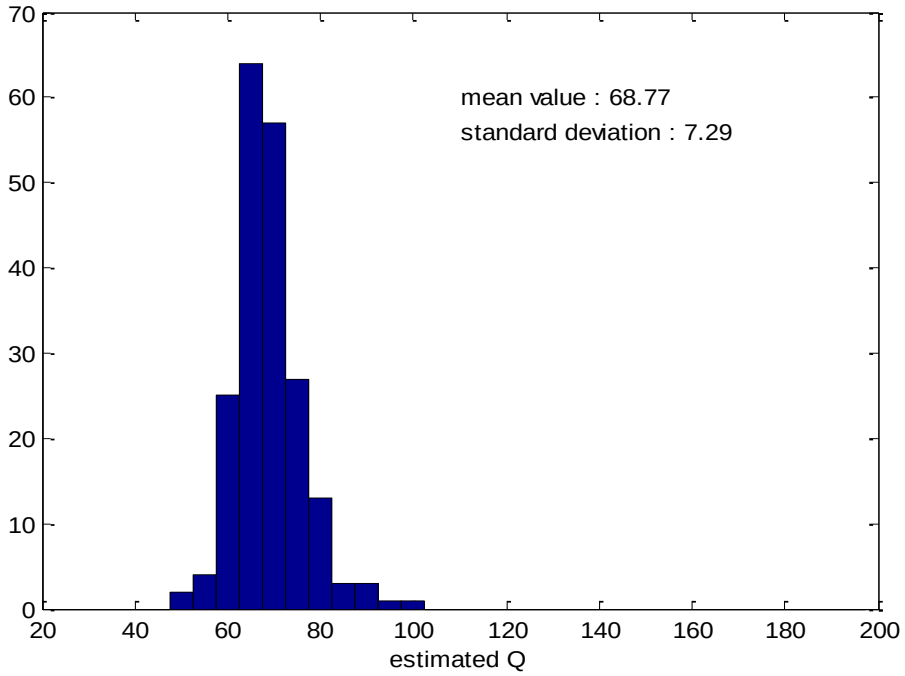

Figure 3.45. Histogram of the Q values estimated by complex spectral-ratio method (only phase spectra are employed) using 200 seismic traces (similar to the one shown in Figure 3.9) with noise level of $SNR = 4$ (inaccurate reference frequency is used).

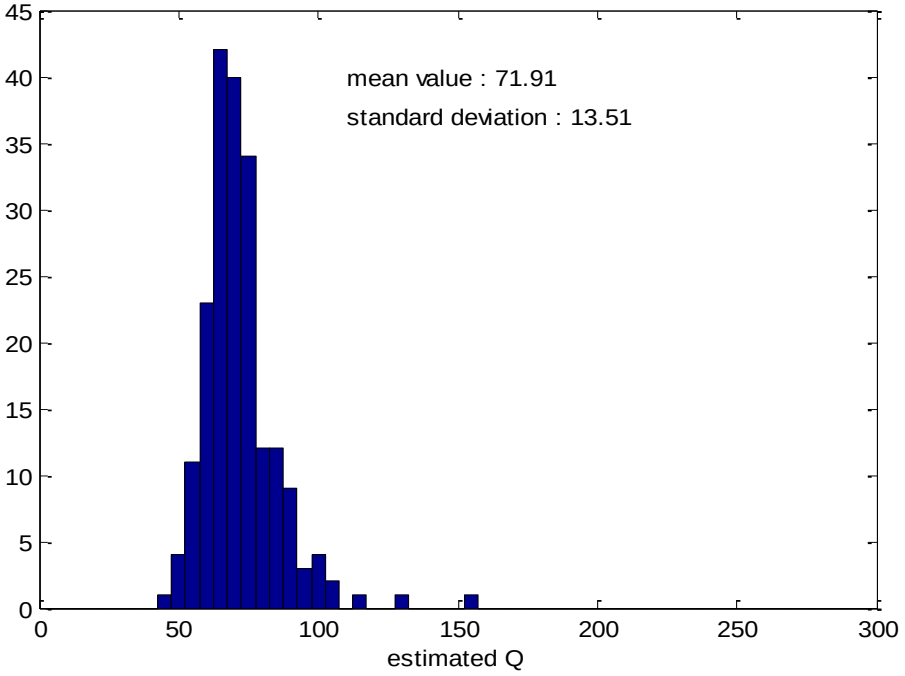

Figure 3.46. Histogram of the Q values estimated by complex spectral-ratio method (only phase spectra are employed) using 200 seismic traces (similar to the one shown in Figure 3.9) with noise level of $SNR = 2$ (inaccurate reference frequency is used).

3.5.1.2 Real VSP data example

Now, we will use the real VSP data to evaluate the Q estimation methods. Figure 3.47 shows field zero-offset P-wave VSP data. Since the VSP data consists of downgoing waves and upgoing waves, it is necessary to separate the downgoing waves for Q estimation. First, the first breaks of VSP data are picked and their corresponding time is shown in Figure 3.48. Linear move out is applied to align the events of VSP data. Then, median filtering is applied to the aligned VSP data for upgoing wave suppression. The downgoing wave VSP data are shown in Figure 3.49.

First, we evaluate the classic spectral ratio method, spectrum-modeling method, match-technique method and match-filter method. With a fixed trace interval of 100, 230 pairs of windowed VSP traces shown in Figure 3.49 are used to conduct Q estimation, of which the first pair are the VSP trace 101 and 201 and the last pair are VSP trace 330 and 430. At first, the multitaper method is not employed for the frequency-domain methods, and the results are shown in Figure 3.50. The estimation results are similar and have the same trend of variations at most cases, while match-filter method and spectrum-modeling method give more stable results. Then multitaper method is used to smooth the amplitude spectra for the three frequency-domain method, and the Q -estimation results are shown in Figure 3.51. We can see that the spectrum smoothing stabilizes the Q estimation for the spectral-ratio method, while match-technique method is sensitive to spectrum smoothing. Then, 80 pairs of windowed VSP traces with fixed trace interval of 250 are used to investigated the four method, of which the first pair are the VSP trace 101 and 351 and the last pair are VSP trace 180 and 430. When spectrum estimation is not conducted for the three frequency-domain method, the Q-estimation results are shown in Figure 3.52. With a larger trace interval (traveltime difference), the attenuation between the two trace

becomes more measurable. We can see that the results of spectral-ratio method and match-technique method are more stable, and all the four methods give more consistent estimation. Then, multitaper method for spectrum smoothing is employed for the three frequency-domain methods. The corresponding Q-estimation results are shown in Figure 3.53. With spectrum smoothing, the results of spectral-ratio method are stabilized. We also can observe that spectral-ratio method, spectrum-modeling method and match-filter method give quite close estimation results.

Now, we investigate on applying complex spectral-ratio method to real data. A practical issue for the complex spectral-ratio method is to choose an appropriate reference frequency f_0 to model the phase difference. One approach is to use the results given by other methods such as classic spectral-ratio method to calibrate the result of complex spectral-ratio method (only phase information is used for Q estimation). The reference frequency f_0 can be determined by this way. Figure 3.54 shows the Q estimation result by classic spectral-ratio method using VSP trace 101 and 351. When $f_0 = 22Hz$, similar result is obtained by complex spectral-ratio method, as shown in Figure 3.55. Then, with a fixed reference $f_0 = 22Hz$ and trace interval of 250, Q estimation is conducted for 80 pairs of windowed VSP traces, of which the first pair are the VSP trace 101 and 351 and the last pair are VSP trace 180 and 430. The Q-estimation results are shown in Figure 3.56. We can see that the complex ratio-method (only phase information employed) gives unreasonable results at some cases. Another approach is to choose f_0 by a least-squares error solution to the modeled phase difference and the computed phase difference. The Q-estimation results for the 80 pairs of VSP traces are shown in Figure 3.57, and the corresponding reference frequencies are shown in Figure 3.58. We can see that the estimated Q values are more stable than results shown in Figure 3.56, while they have significant variations

and are obviously deviated from the results given by other methods shown in Figure 3.52 and 3.53. We also can see that the reference frequencies vary significantly, which may not be physically true. Generally, both approaches do not work for the real data, which may indicates that the phase difference between wavelets is distorted during the propagation and is not suitable to be approximated by the phase of a minimum phase wavelet. To make the complex spectral-ratio method applicable, minimum-phase equivalent wavelets are computed before Q estimation for the VSP traces. Then, with the calibration from classic spectral-ratio method, a reference frequency $f_0 = 600Hz$ is chosen to model the phase difference. The Q-estimation results are shown in Figure 3.59, which are stable and similar to the results given by other methods.

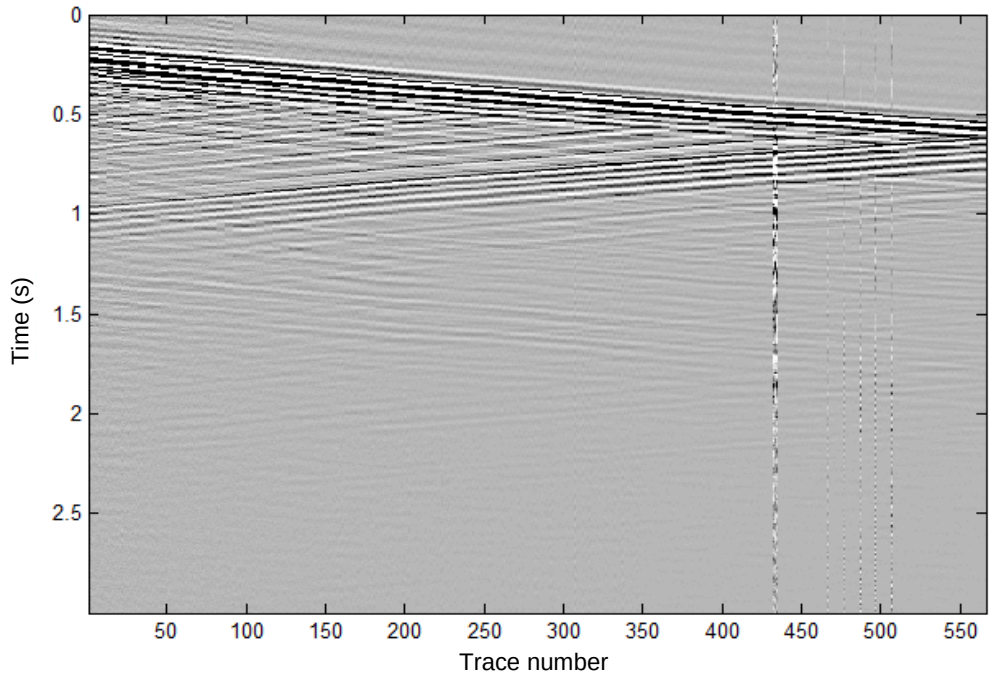

Figure 3.47. Ross Lake VSP data (vertical component P-wave).

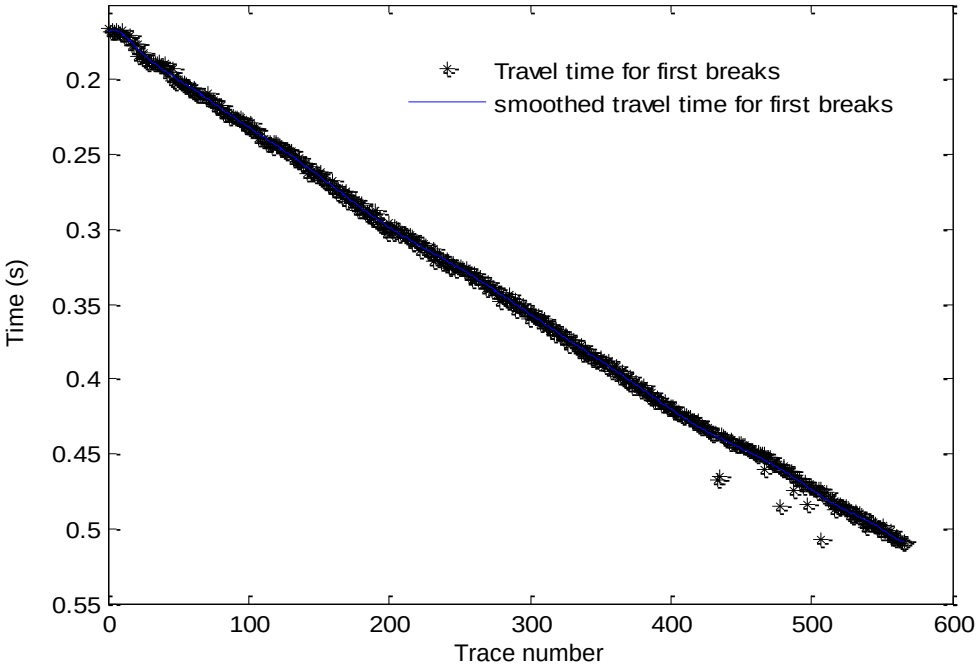

Figure 3.48. First breaks of VSP data shown in Figure 3.47.

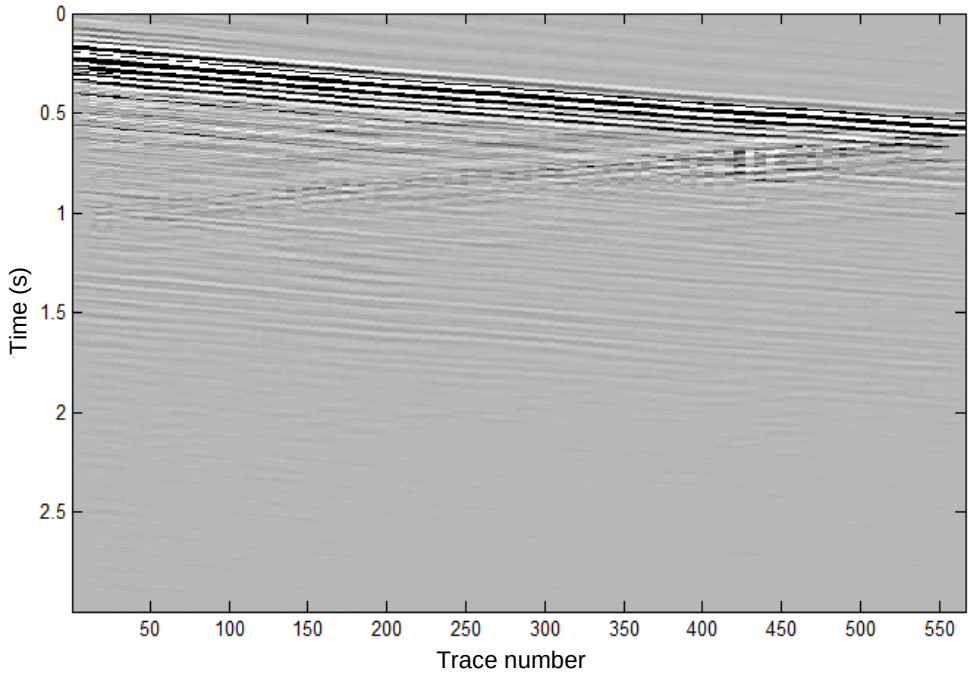

Figure 3.49. VSP data with upgoing wave suppression.

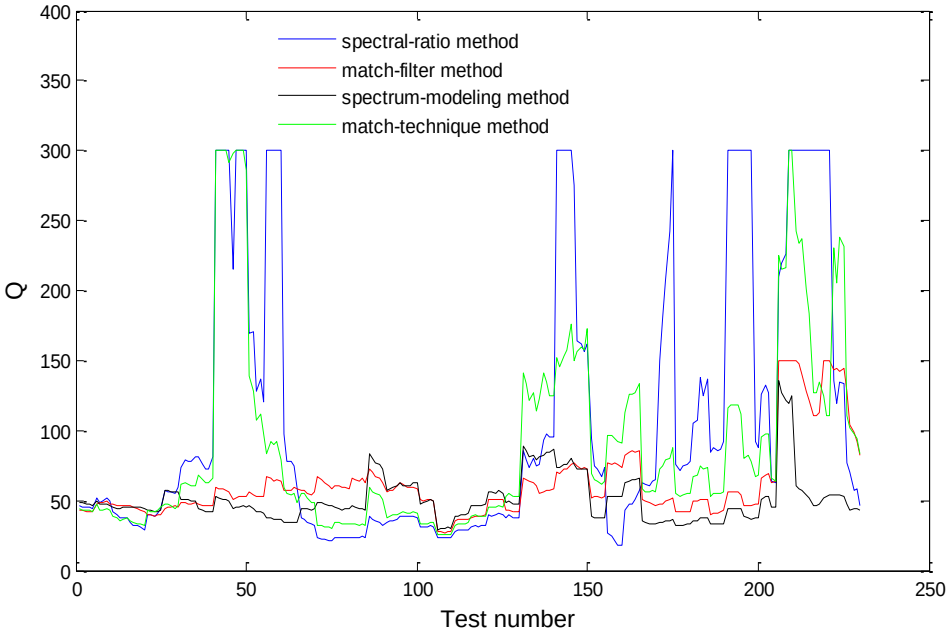

Figure 3.50. Q estimation using 230 pairs of VSP traces shown in Figure 3.49 (Each pair has a fixed trace interval of 100; the first pair are the VSP trace 101 and trace 201 and the last pair are VSP trace 330 and trace 430); Multitaper method for spectrum estimation is not employed for the three frequency-domain methods.

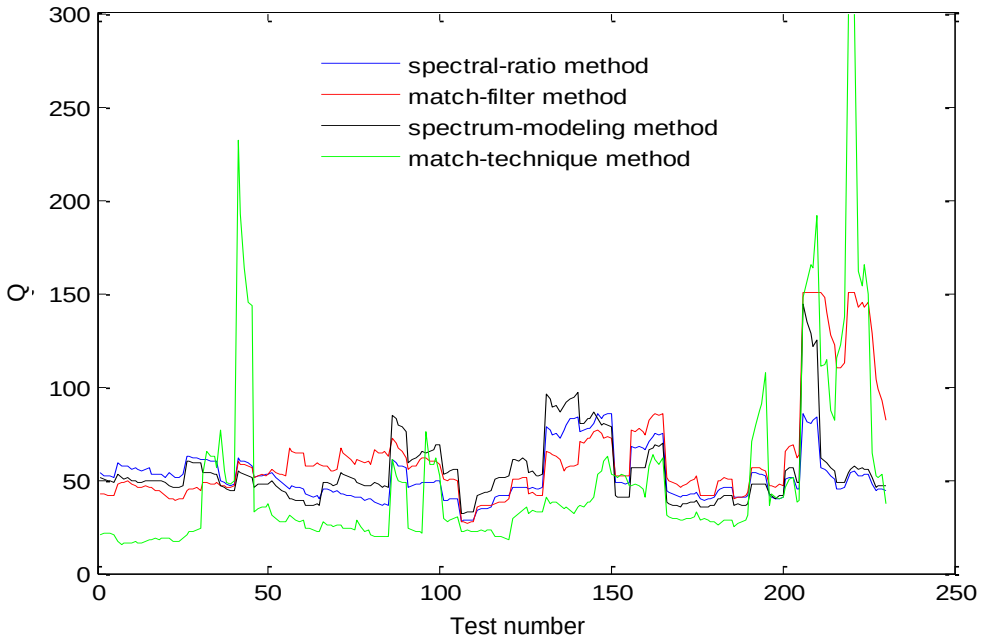

Figure 3.51. Q estimation using 230 pairs of VSP traces shown in Figure 3.49 (Each pair has a fixed trace interval of 100; the first pair are the VSP trace 101 and trace 201 and the last pair are VSP trace 330 and 430); Multitaper method for spectrum estimation is employed for the three frequency-domain methods.

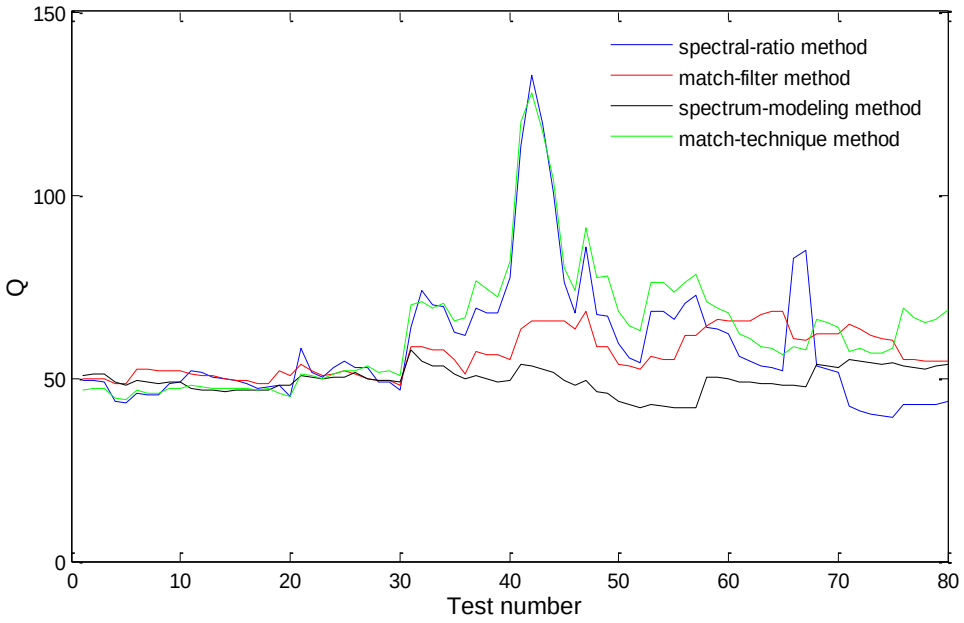

Figure 3.52. Q estimation using 80 pairs of VSP traces shown in Figure 3.49 (Each pair has a fixed trace interval of 250; the first pair are the VSP trace 101 and 351 and the last pair are VSP trace 180 and trace 430); Multitaper method for spectrum estimation is not employed for the three frequency-domain methods.

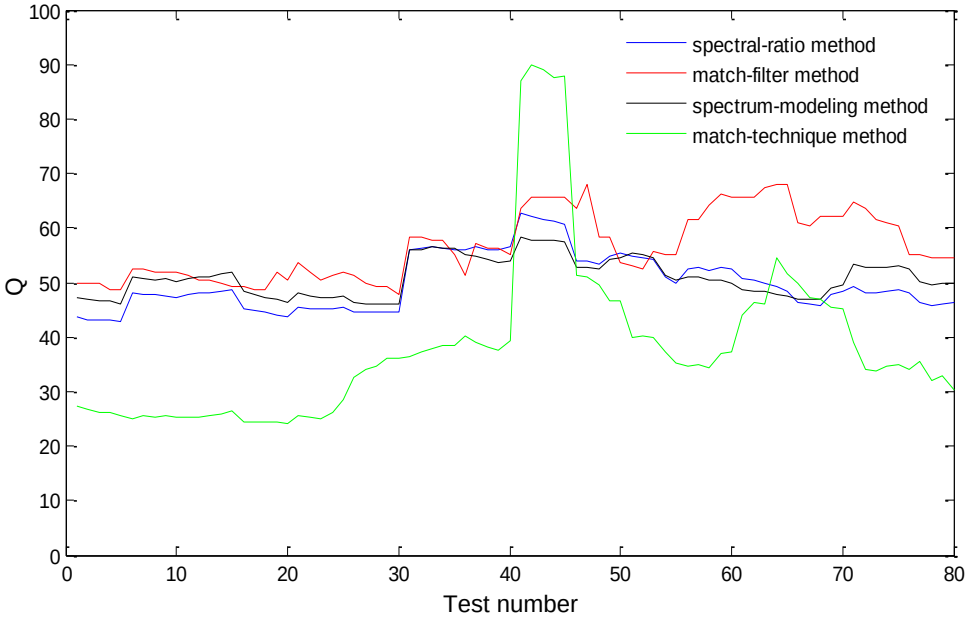

Figure 3.53. Q estimation using 80 pairs of VSP traces shown in Figure 3.49 (Each pair has a fixed trace interval of 250; the first pair are the VSP trace 101 and 351 and the last pair are VSP trace 180 and 430); Multitaper method for spectrum estimation is employed for the three frequency-domain methods.

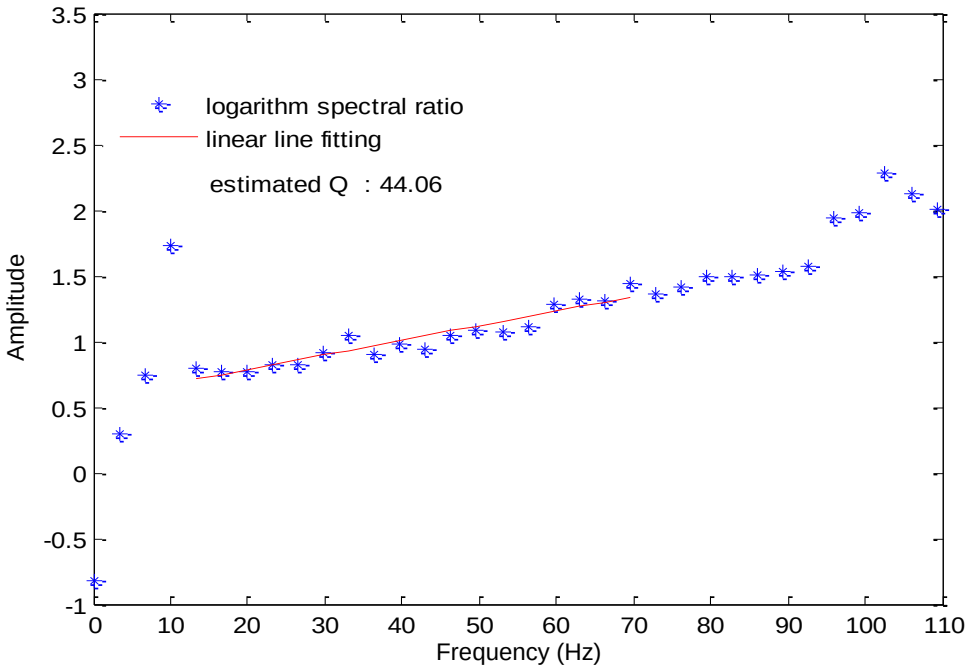

Figure 3.54. Q estimation by classic spectral-ratio method using of VSP traces 102 and 352 shown in Figure 3.49.

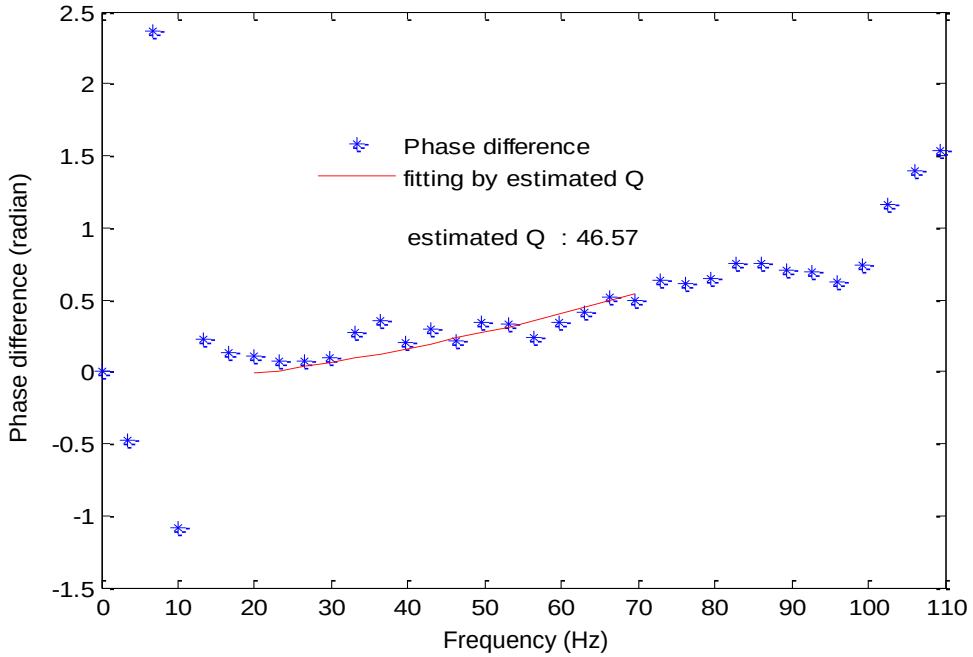

Figure 3.55. Q estimation by complex spectral-ratio method with only phase information employed (reference frequency $f_0 = 22Hz$), using of VSP traces 102 and 352 shown in Figure 3.49.

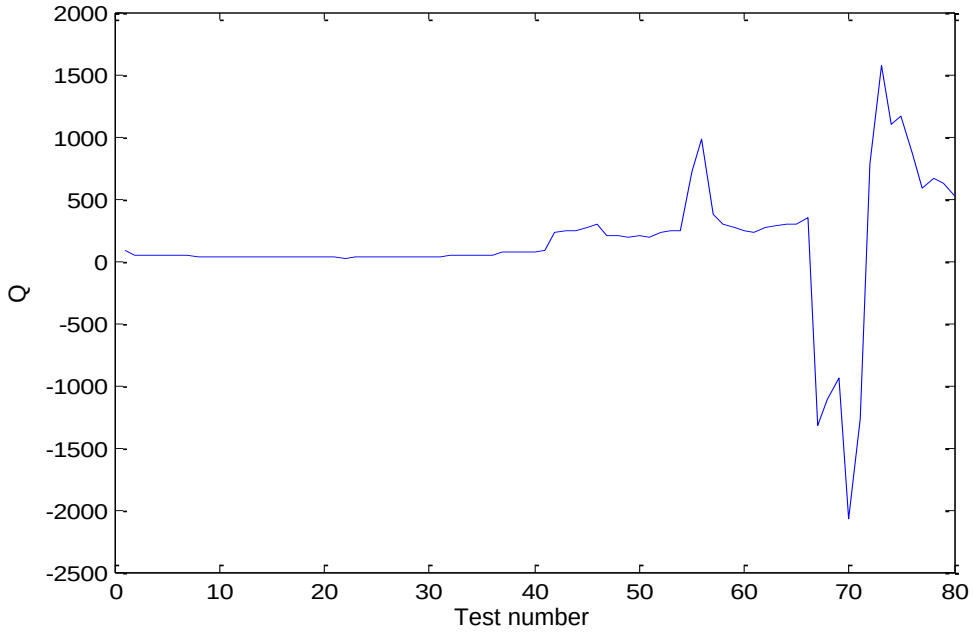

Figure 3.56. Q estimation by complex spectral-ratio method with only phase information employed (reference frequency $f_0 = 22Hz$), using 80 pairs of VSP traces shown in Figure 3.49 (Each pair has a fixed trace interval of 250; the first pair are the VSP trace 101 and 351 and the last pair are VSP trace 180 and 430).

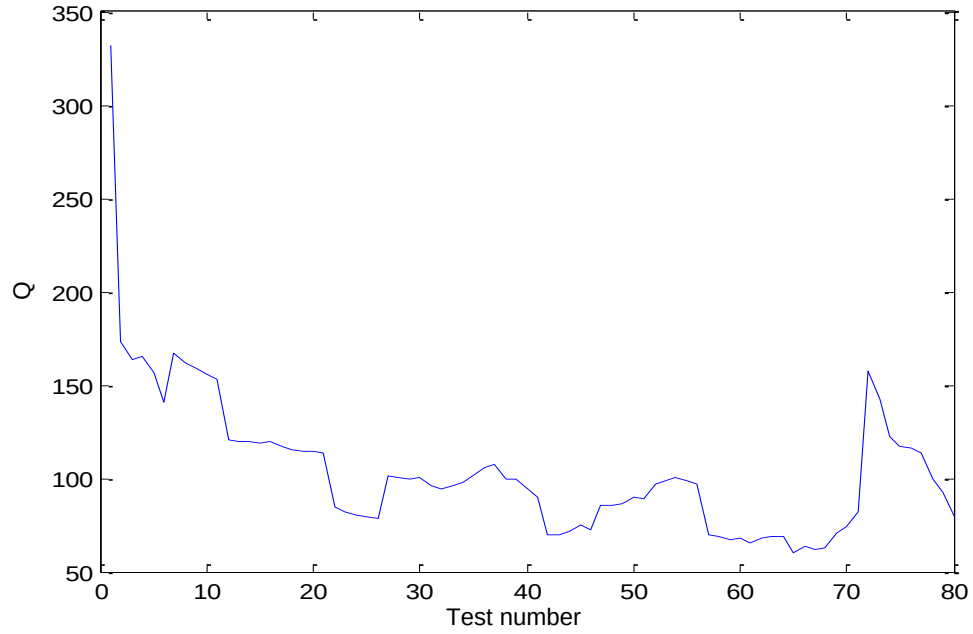

Figure 3.57. Q estimation by complex spectral-ratio method with only phase information employed (reference frequency is choose by a least-square minimization approach), using 80 pairs of VSP traces shown in Figure 3.49 (Each pair has a fixed trace interval of 250; the first pair are the VSP trace 101 and 351 and the last pair are VSP trace 180 and 430).

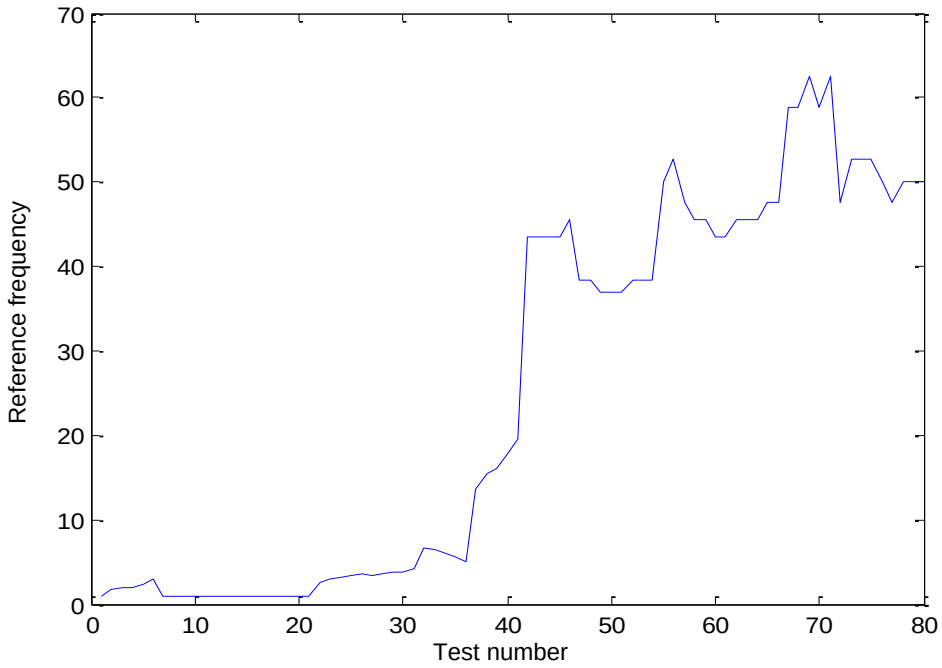

Figure 3.58. The chosen reference frequencies corresponding to the test shown in Figure 3.57.

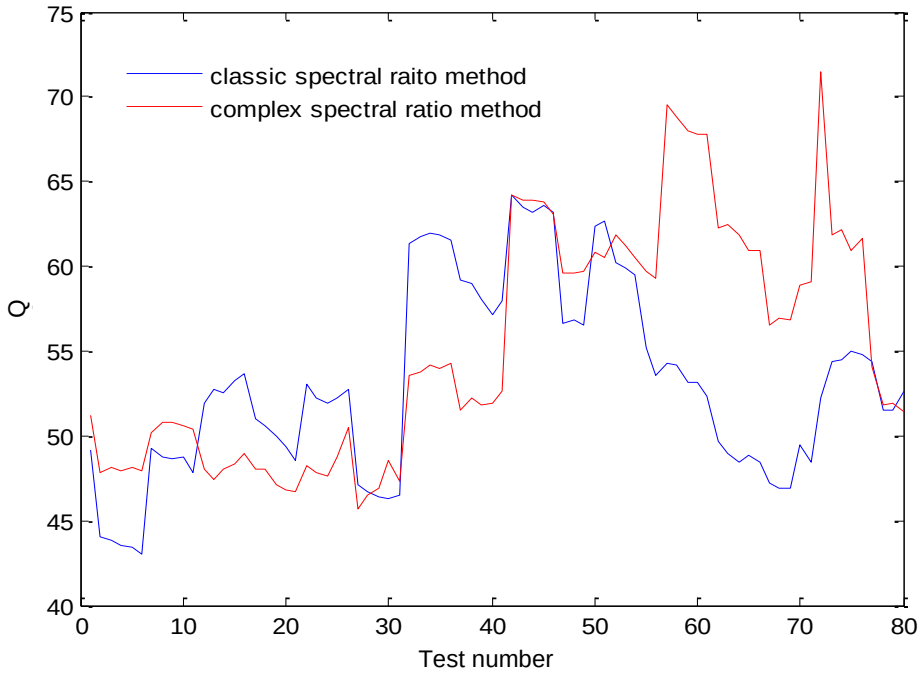

Figure 3.59. Q estimation by complex spectral-ratio method with only phase information employed (reference frequency $f_0 = 600Hz$), using 80 pairs of VSP traces shown in Figure 3.49 (Each pair has a fixed trace interval of 250; the first pair are the VSP trace 101 and 351 and the last pair are VSP trace 180 and 430). Minimum-phase equivalent wavelets are computed before Q estimation for the VSP traces.

3.5.1.3 Synthetic 1D reflection data example

In this section, synthetic 1D reflection data will be used to evaluate four methods: classic spectral-ratio method, spectrum-modeling method, match-technique method and match-filter method. A synthetic seismic trace is created using a random reflectivity series, a minimum-phase source wavelet with dominant frequency of $40Hz$ and a constant Q of 80, as shown in Figure 3.60. Two local reflected wavelets are obtained by applying time gates of $100ms - 500ms$ and $900ms - 1300ms$ to the attenuated seismic trace, and these two time gates will be used to obtain local wavelets for all tests in this section. Figure 3.61 shows the amplitude spectra given by multitaper method for these two local wavelets. The spikes and notches in the original spectra of local wavelets are smoothed by the multitaper method, which gives good spectrum estimations.

For Q estimation using reflection data, spectrum estimation is necessary and employed for all the four methods. Q estimation is conducted using the local wavelets. The results are shown in Figure 3.62 – 3.65. We can see that, even without noise, the estimation results are deviated from the true value due to the tuning effect. Then, attenuated seismic traces are created using 200 different random reflectivity series, from which 200 pairs of local reflected waves are obtained to conduct the Q estimation using the four Q estimations. The Q-estimation results are shown in Figure 3.66 – 3.69. The match-filter method gives best result with the closest mean value of 82.49 and the smallest standard deviation of 16.86. Next, the four Q-estimation methods are further evaluated using reflection date with noise level of $SNR = 4$ and $SNR = 2$. The corresponding Q-estimation results are shown in Figure 3.70 – 3.77. We can see that three frequency-domain methods give unreliable results with significantly distorted mean values and large standard deviation values, while match-filter method is robust to noise and obtains results

with accurate mean value and small standard deviation value, which are similar to the noise-free case.

For the classic spectral-ratio method, the results might be corrupted for two reasons. Firstly, even using the smoothed spectra, computed spectral ratios are sensitive to the spectrum modification caused by noise and the tuning effect of local reflectors. Secondly, the calculated spectral ratios are not suitable for straight-line fitting over a wide frequency range anymore. At this occasion, the interpretive spectral-ratio method presented in this chapter might be more suitable than the classic spectral-ratio method. Figure 3.78 and 3.79 demonstrate the Q estimation by these two spectral-ratio methods respectively, using one pair of local wavelets with noise level of $SNR = 2$ as an example. For this single example, the calculated spectral ratios are not suitable for straight-line fitting. The classic spectral-ratio method gives a distorted result of 148.46. The interpretive spectral-ratio method approximates a piecewise straight-line fitting scheme and gives an improved estimation of 71.47. Then, 200 pairs of local wavelets at different noise level are used to evaluate the interpretive spectral-ratio method, and the estimation results are shown in Figure 3.80 and 3.81. Compared to the results of classic spectral-ratio method shown in Figure 3.70 and 3.74, the Q-estimation results are significantly improved, but still have much larger standard deviation values than the results of match-filter method.

To evaluate the effect of deconvolution on Q estimation, 200 pairs of local wavelets are obtained from 200 deconvolved seismic traces using Wiener spiking deconvolution. Then, Q estimation is conducted using these local wavelets using match-filter method. As shown in Figure 3.82, the Q-estimation results are similar to the case without deconvolution shown in Figure 3.66, and have a smaller standard deviation value. This indicates that the Q estimation is not subject to the effect of stationary deconvolution.

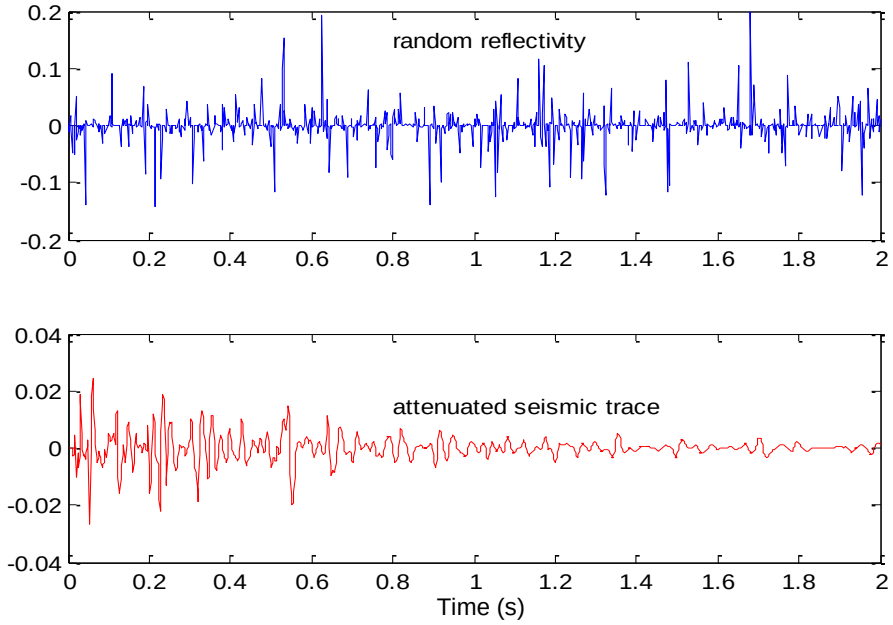

Figure 3.60. A random reflectivity series (upper). An attenuated seismic trace created using the reflectivity series, a minimum-phase wavelet with dominant frequency of $40Hz$ and a constant Q of 80.

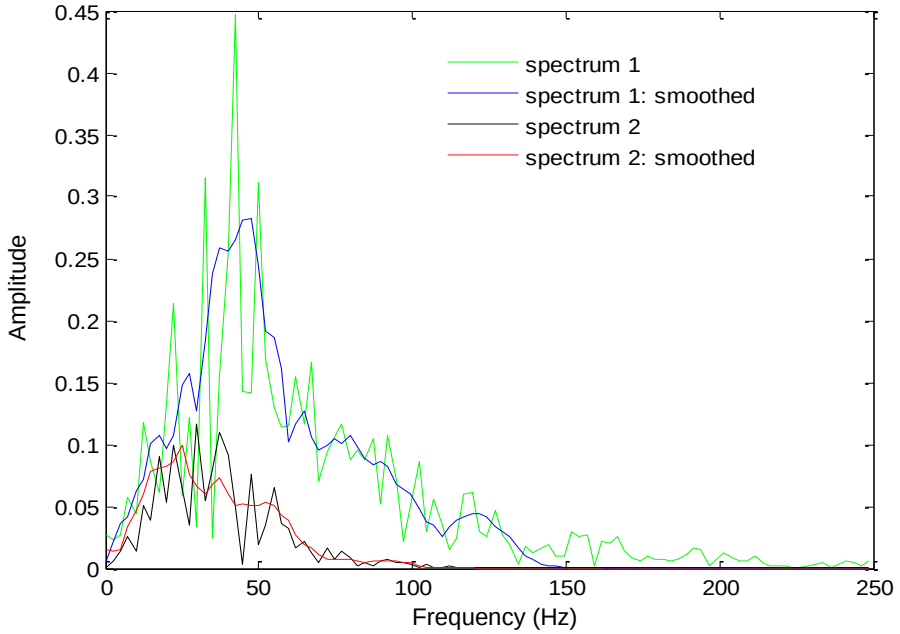

Figure 3.61. Amplitude spectrum of the $100ms - 500ms$ part of the seismic trace in Figure 3.60 (Green). Amplitude spectrum estimated by multitaper method for the $100ms - 500ms$ part of the seismic trace in Figure 3.60 (Blue). Amplitude spectrum of the $900ms - 1300ms$ part of the seismic trace in Figure 3.60 (Black). Amplitude spectrum estimated by multitaper method for the $900ms - 1300ms$ part of the seismic trace in Figure 3.60 (Red).

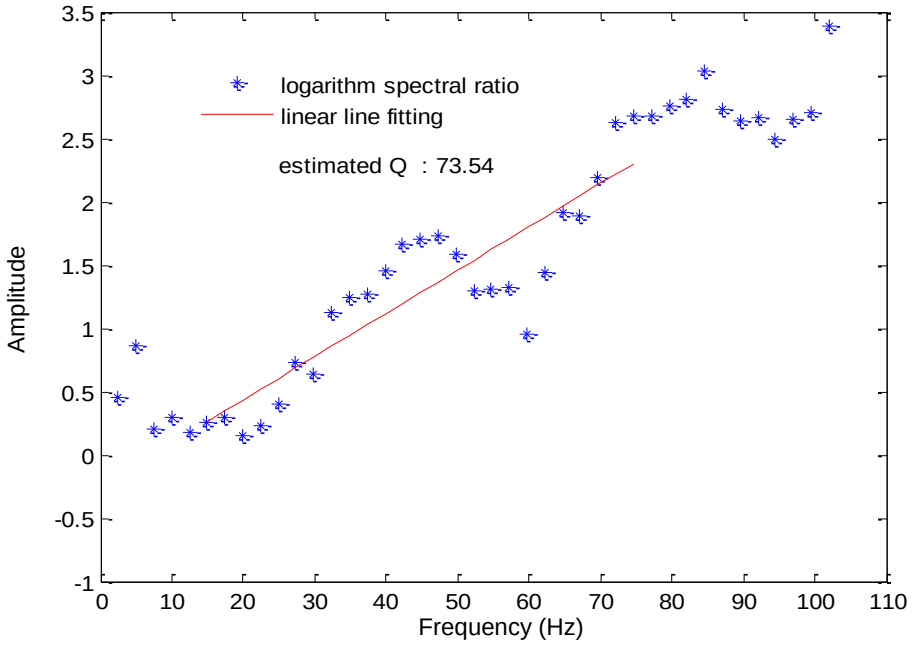

Figure 3.62. Q estimation by spectral-ratio method using the $100ms - 500ms$ and $900ms - 1300ms$ parts of the seismic trace shown in Figure 3.60.

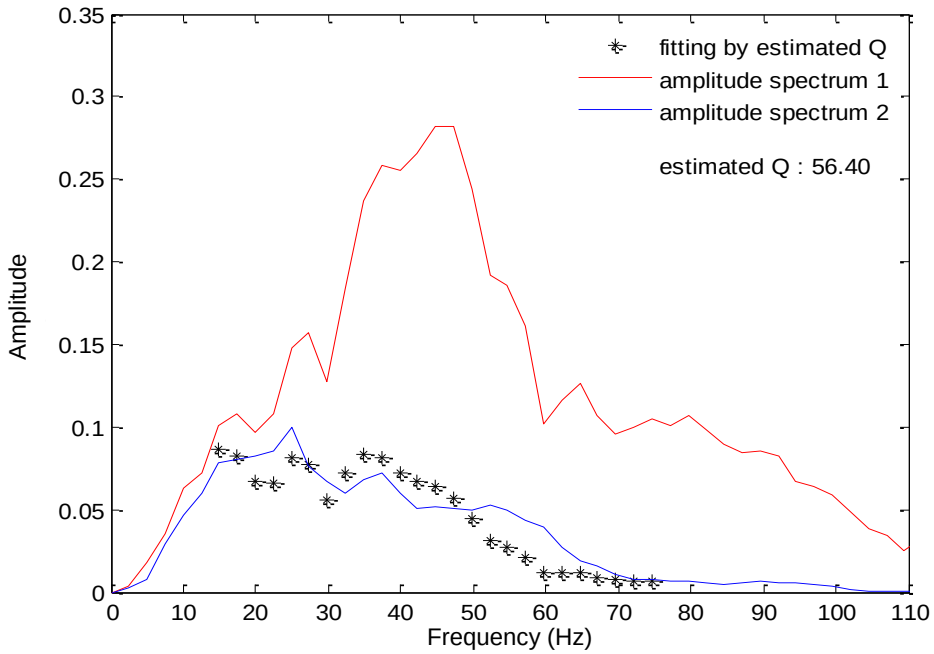

Figure 3.63. Q estimation by spectrum-modeling method using the $100ms - 500ms$ and $900ms - 1300ms$ parts of the seismic trace shown in Figure 3.60.

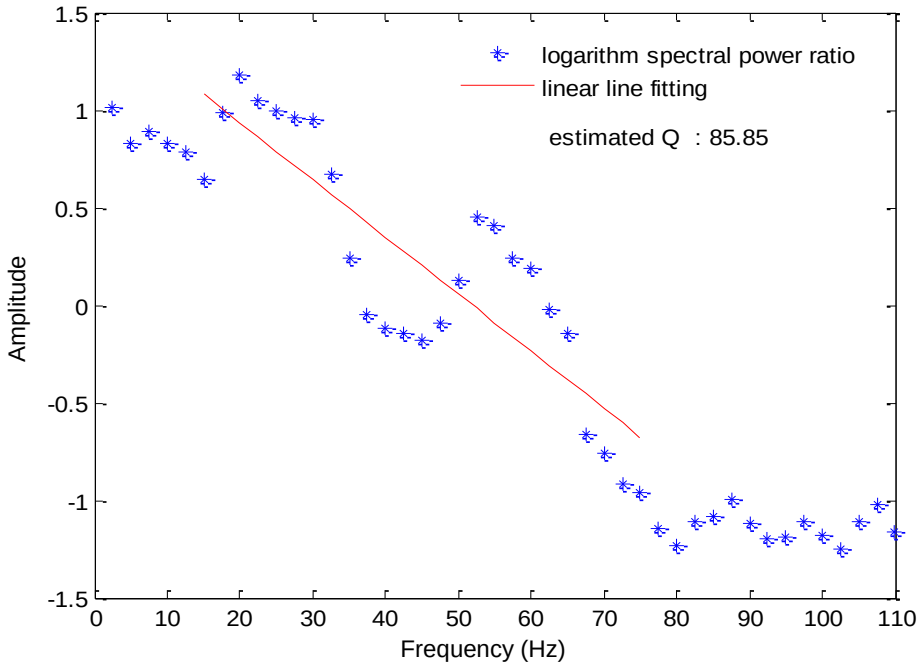

Figure 3.64. Q estimation by match-technique method using the $100ms - 500ms$ and $900ms - 1300ms$ parts of the seismic trace shown in Figure 3.60.

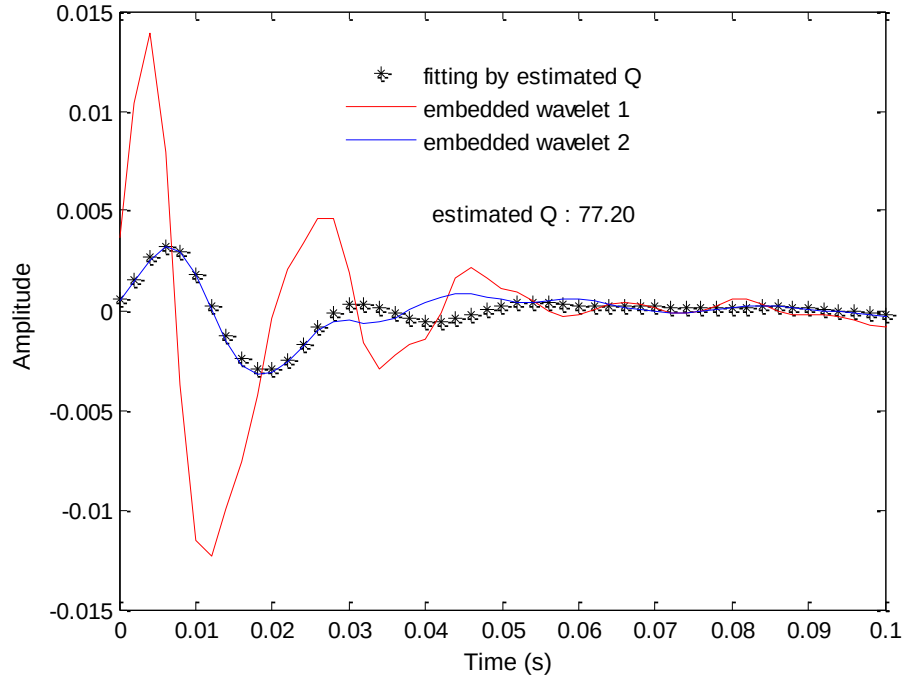

Figure 3.65. Q estimation by match-filter method using the $100ms - 500ms$ and $900ms - 1300ms$ parts of the seismic trace shown in Figure 3.60.

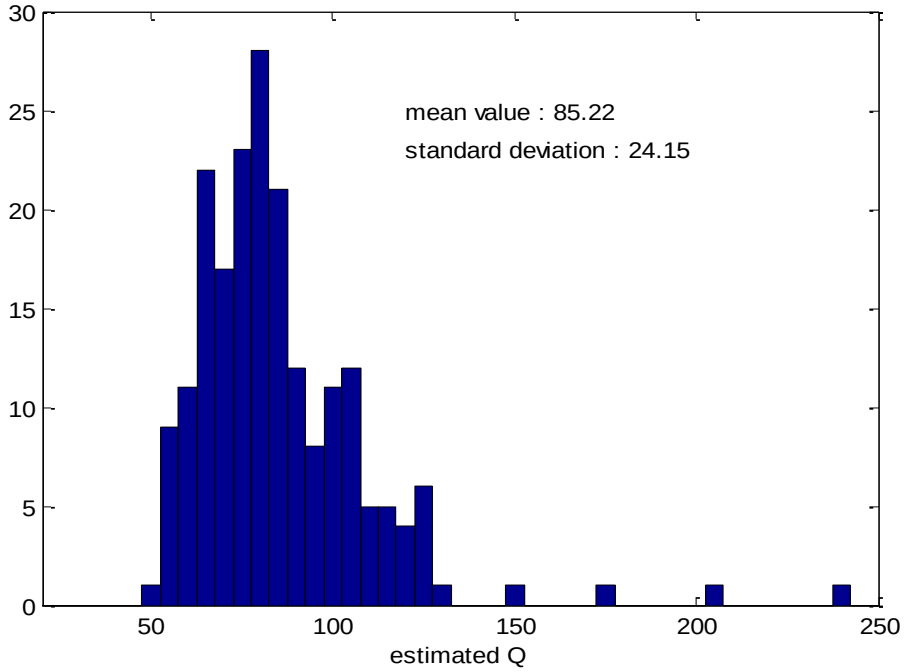

Figure 3.66. Histogram of the Q values estimated by classic spectral-ratio method using the $100ms - 500ms$ and $900ms - 1300ms$ parts of 200 seismic traces without noise, which are similar to the one shown in Figure 3.60.

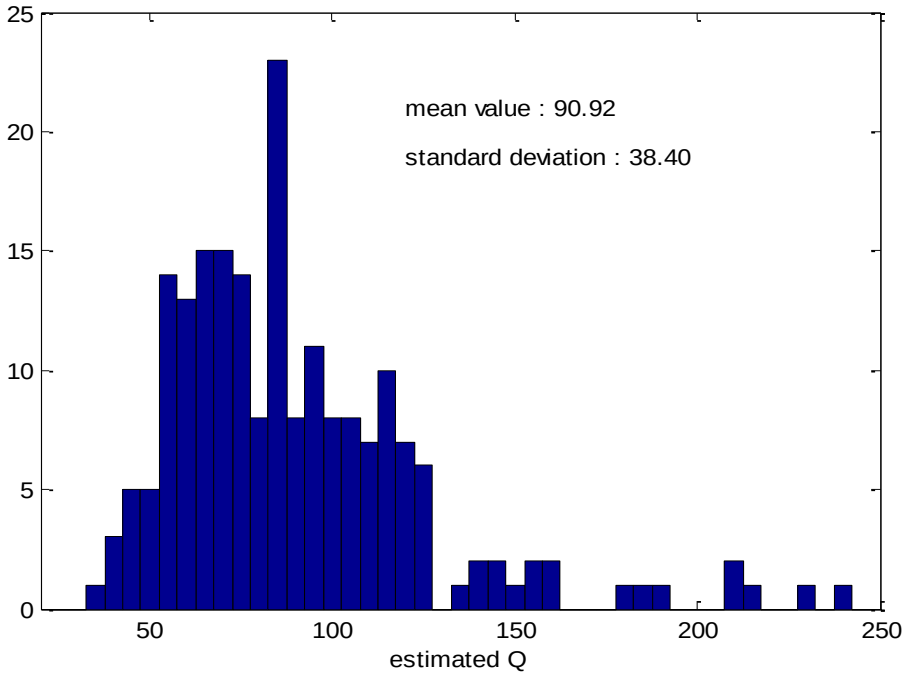

Figure 3.67. Histogram of the Q values estimated by spectrum-modeling method using the $100ms - 500ms$ and $900ms - 1300ms$ parts of 200 seismic traces without noise, which are similar to the one shown in Figure 3.60.

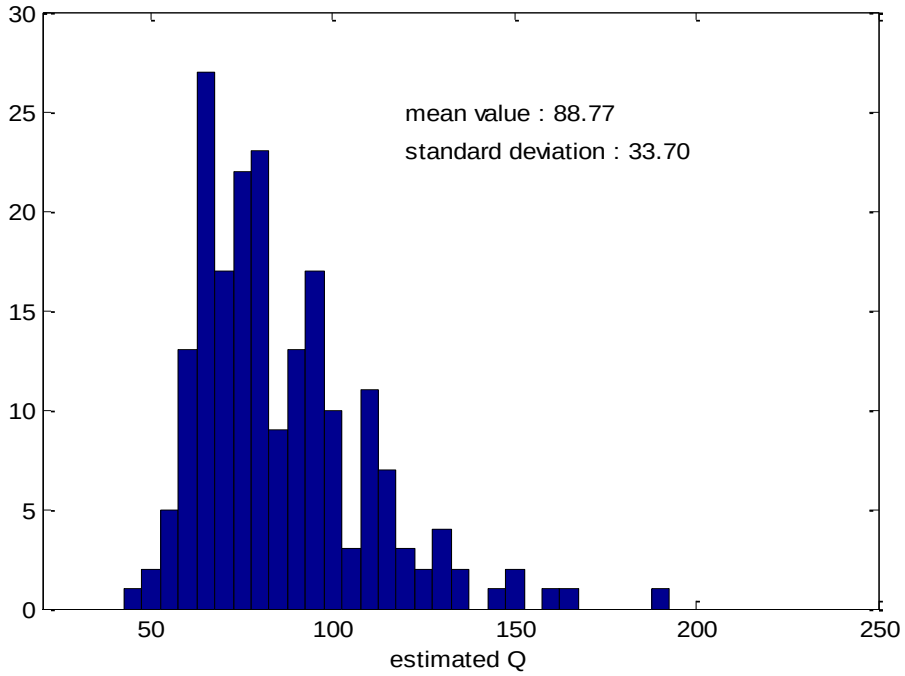

Figure 3.68. Histogram of the Q values estimated by match-technique method using the $100ms - 500ms$ and $900ms - 1300ms$ parts of 200 seismic traces without noise, which are similar to the one shown in Figure 3.60.

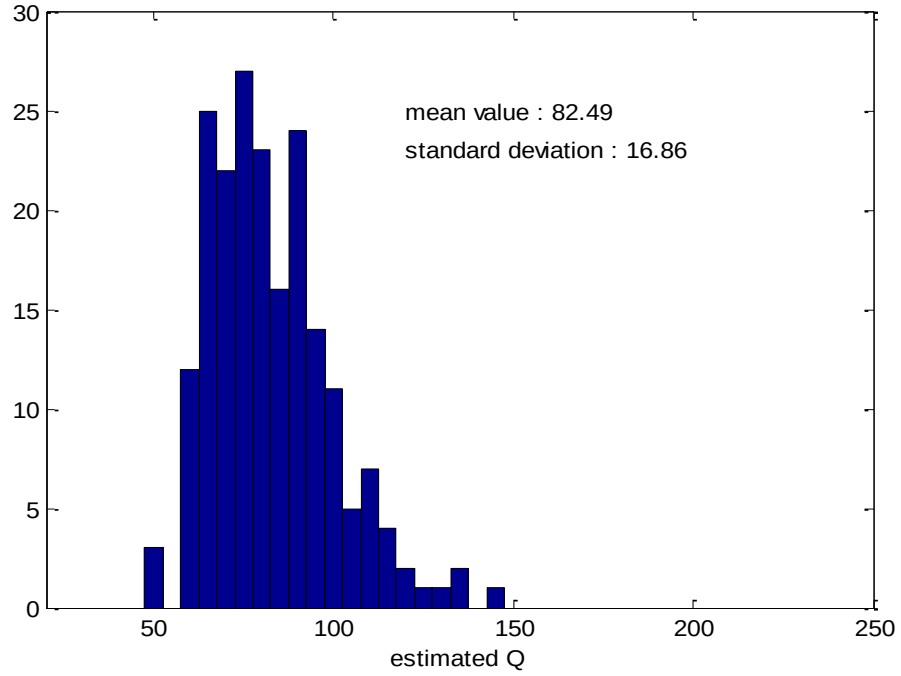

Figure 3.69. Histogram of the Q values estimated by match-filter method using the $100ms - 500ms$ and $900ms - 1300ms$ parts of 200 seismic traces without noise, which are similar to the one shown in Figure 3.60.

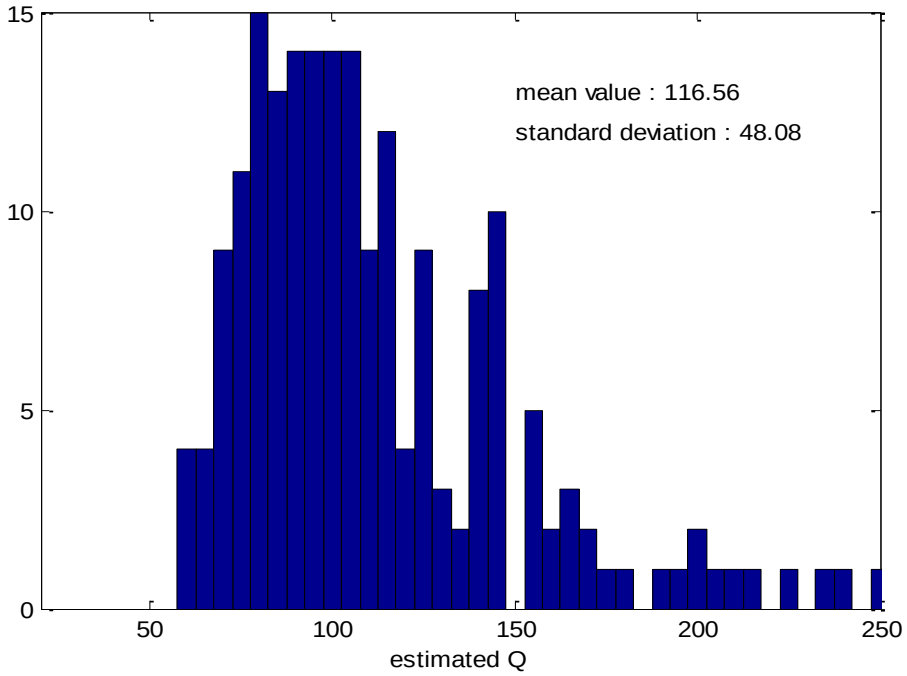

Figure 3.70. Histogram of the Q values estimated by classic spectral-ratio method using the $100ms - 500ms$ and $900ms - 1300ms$ parts of 200 seismic traces with noise level of $SNR = 4$, which are similar to the one shown in Figure 3.60.

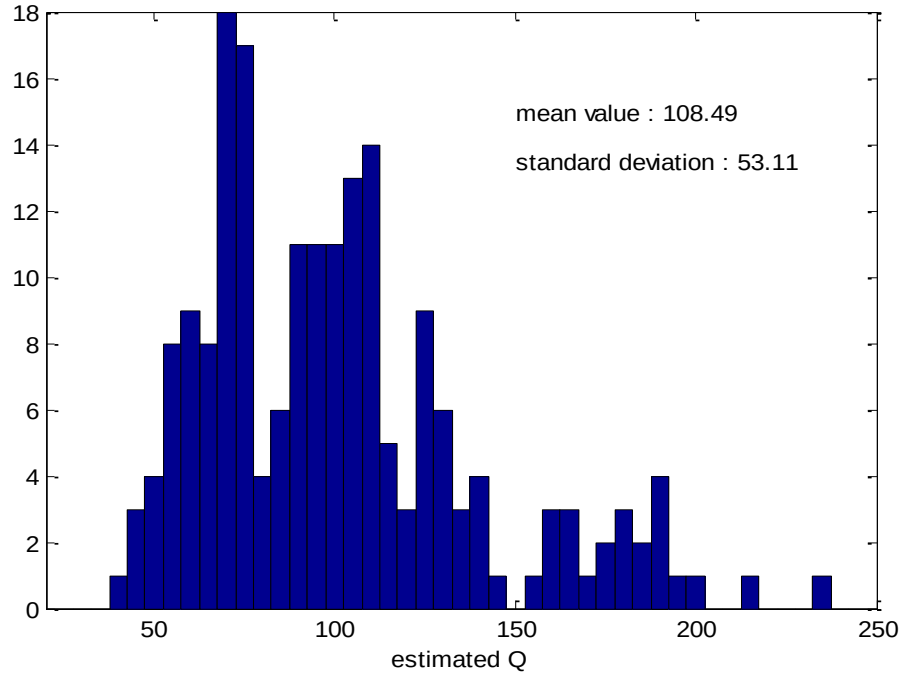

Figure 3.71. Histogram of the Q values estimated by spectrum-modeling method using the $100ms - 500ms$ and $900ms - 1300ms$ parts of 200 seismic traces with noise level of $SNR = 4$, which are similar to the one shown in Figure 3.60.

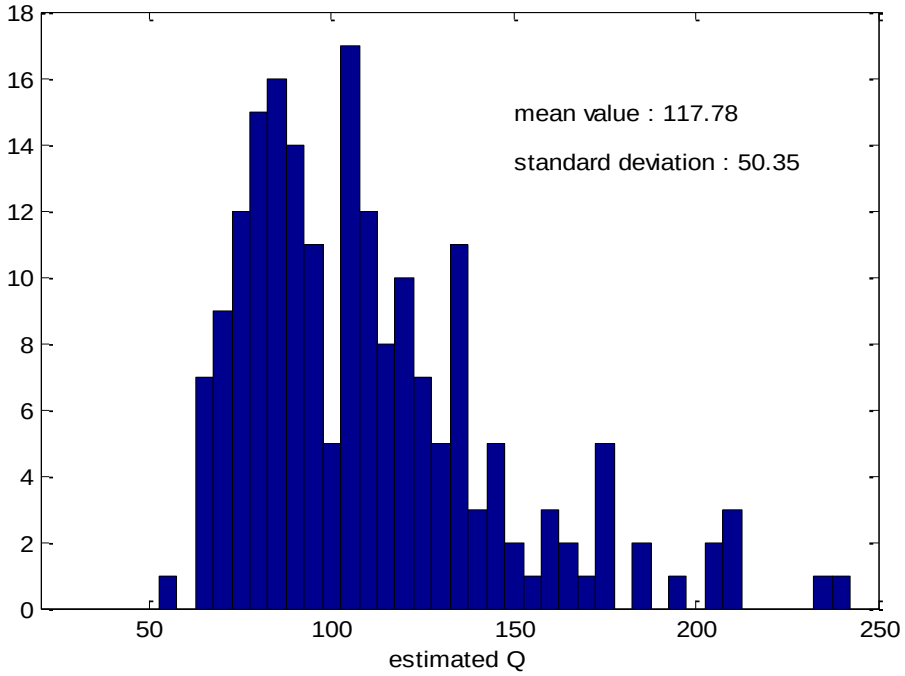

Figure 3.72. Histogram of the Q values estimated by match-technique method using the $100ms - 500ms$ and $900ms - 1300ms$ s parts of 200 seismic traces with noise level of $SNR = 4$, which are similar to the one shown in Figure 3.60.

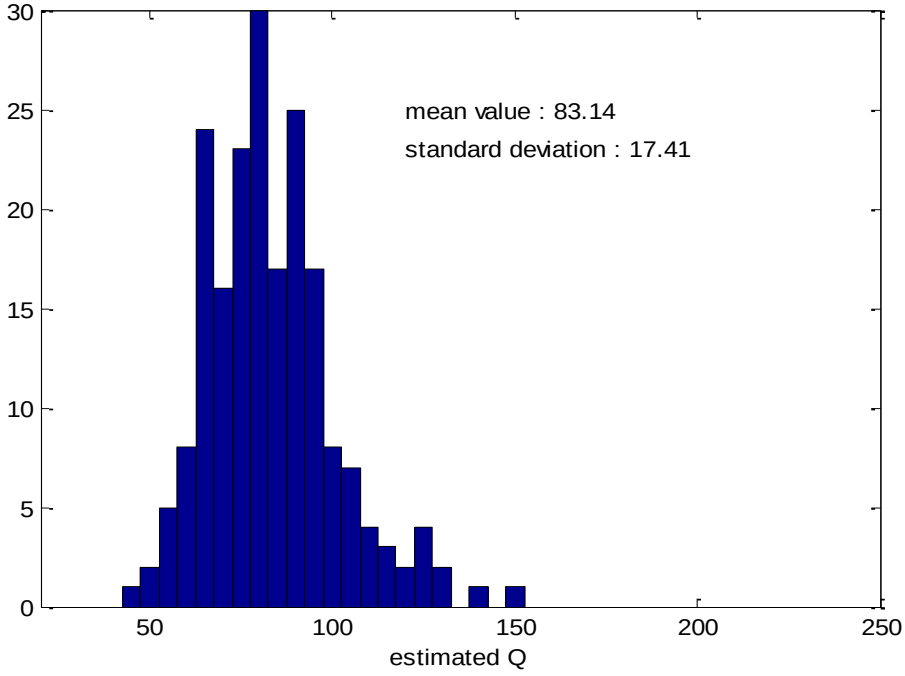

Figure 3.73. Histogram of the Q values estimated by match-filter method using the $100ms - 500ms$ and $900ms - 1300ms$ parts of 200 seismic traces with noise level of $SNR = 4$, which are similar to the one shown in Figure 3.60.

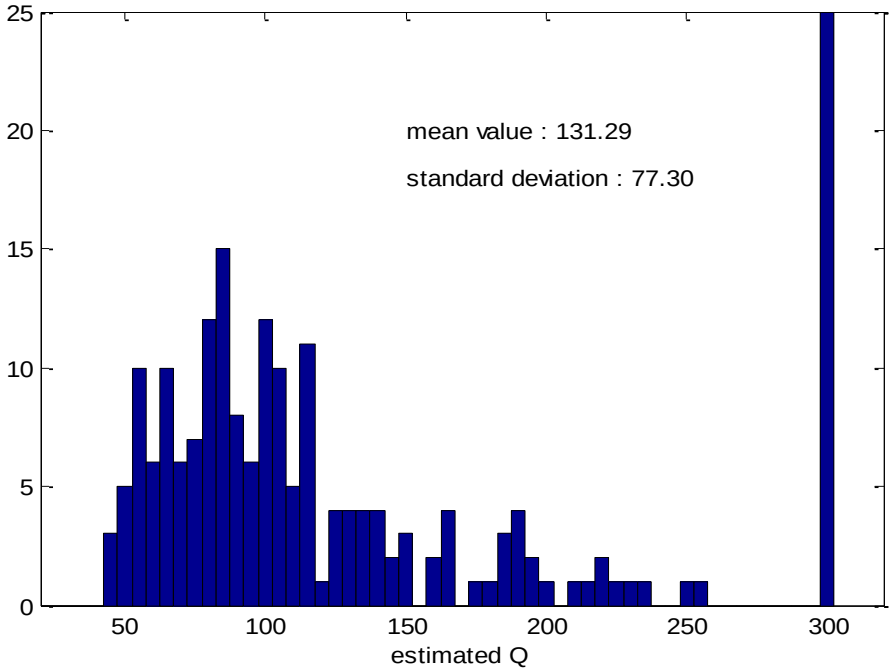

Figure 3.74. Histogram of the Q values estimated by classic spectral-ratio method using the $100ms - 500ms$ and $900ms - 1300ms$ parts of 200 seismic traces with noise level of $SNR = 2$, which are similar to the one shown in Figure 3.60.

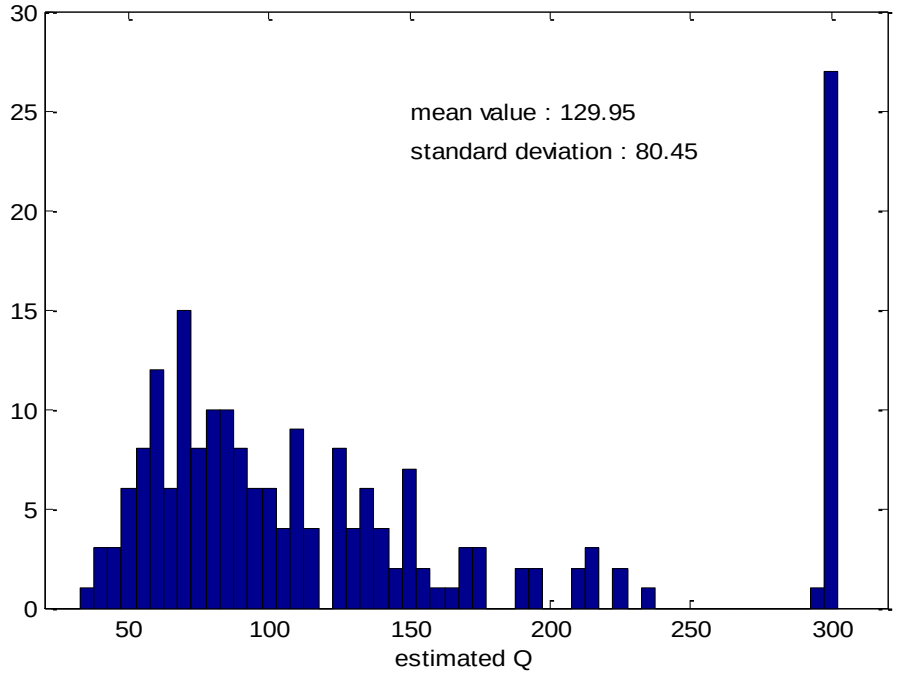

Figure 3.75. Histogram of the Q values estimated by spectrum-modeling method using the $100ms - 500ms$ and $900ms - 1300ms$ parts of 200 seismic traces with noise level of $SNR = 2$, which are similar to the one shown in Figure 3.60.

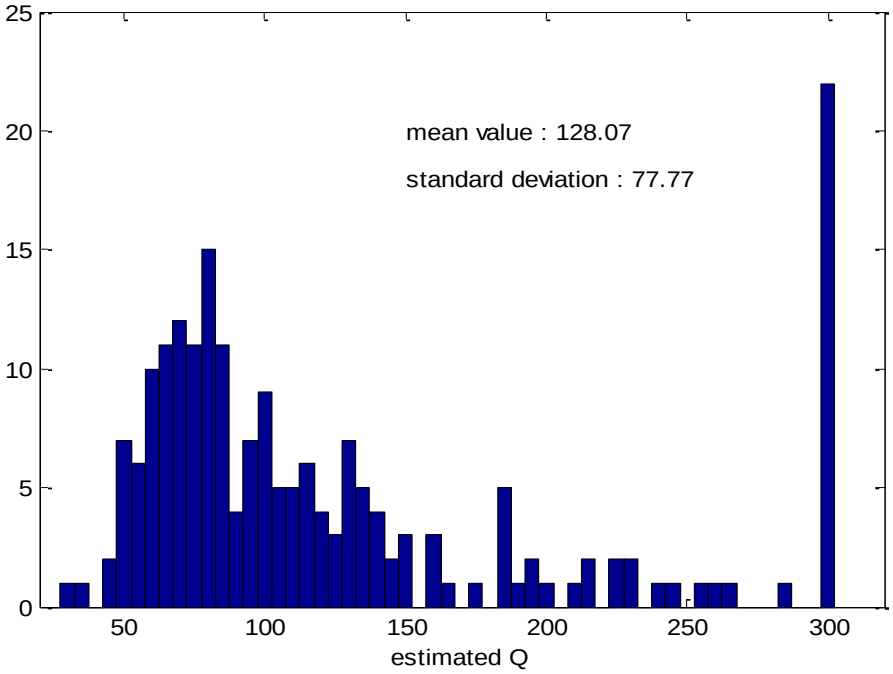

Figure 3.76. Histogram of the Q values estimated by match-technique method using the $100ms - 500ms$ and $900ms - 1300ms$ parts of 200 seismic traces with noise level of $SNR = 2$, which are similar to the one shown in Figure 3.60.

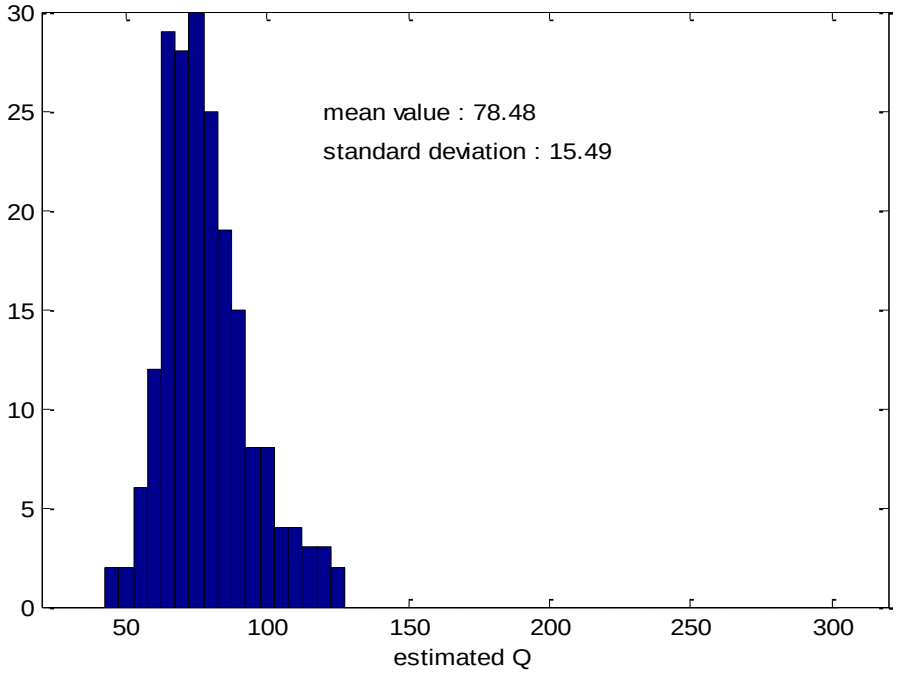

Figure 3.77. Histogram of the Q values estimated by match-filter method using the $100ms - 500ms$ and $900ms - 1300ms$ parts of 200 seismic traces with noise level of $SNR = 2$, which are similar to the one shown in Figure 3.60.

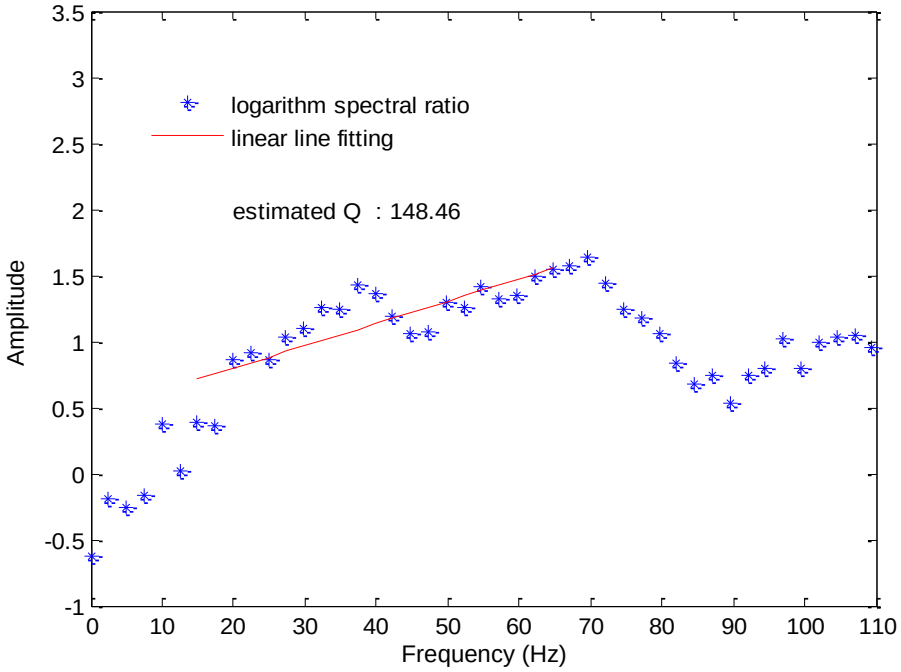

Figure 3.78. Q estimation by classic spectral-ratio method using the $100ms - 500ms$ and $900ms - 1300ms$ parts of a seismic traces with noise level of $SNR = 4$ which is similar to the one shown in Figure 3.60.

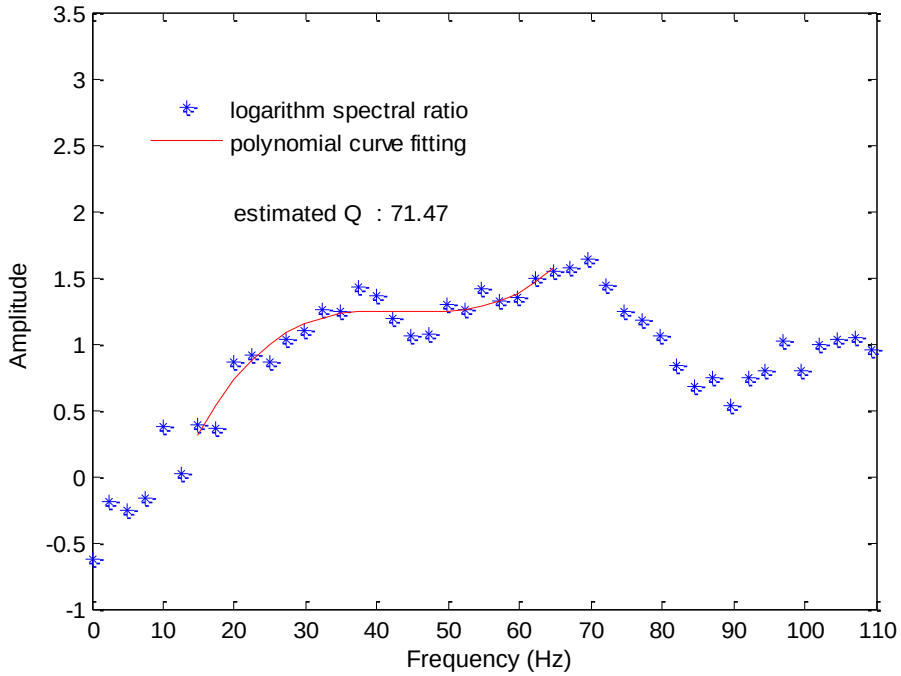

Figure 3.79. Q estimation by the interpretive spectral-ratio method using the $100ms - 500ms$ and $900ms - 1300ms$ parts of a seismic traces with noise level of $SNR = 4$ which is similar to the one shown in Figure 3.60.

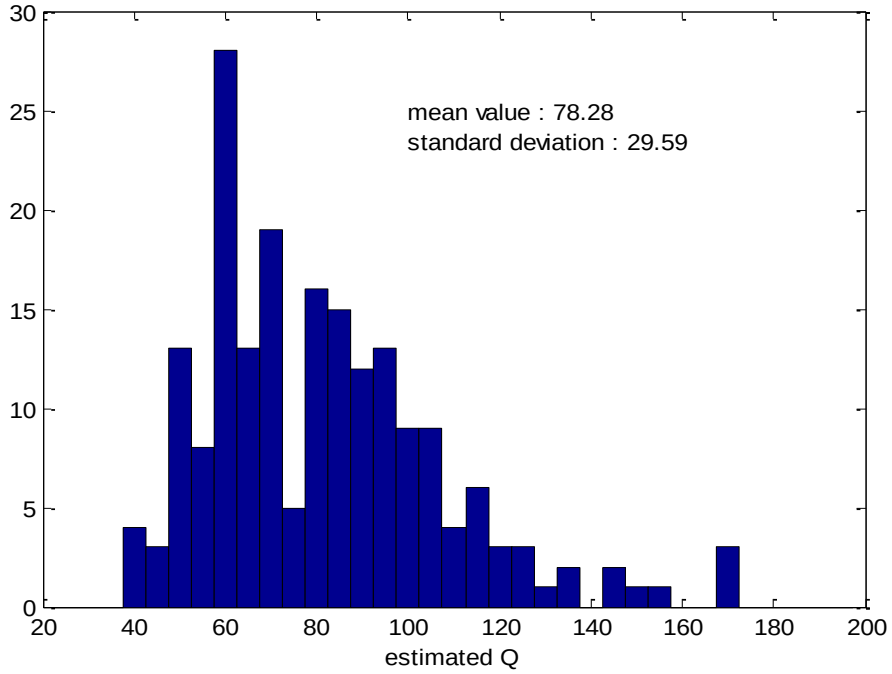

Figure 3.80. Histogram of the Q values estimated by the interpretive spectral-ratio method using the $100ms - 500ms$ and $900ms - 1300ms$ parts of 200 seismic traces with noise level of $SNR = 4$ which are similar to the one shown in Figure 3.60.

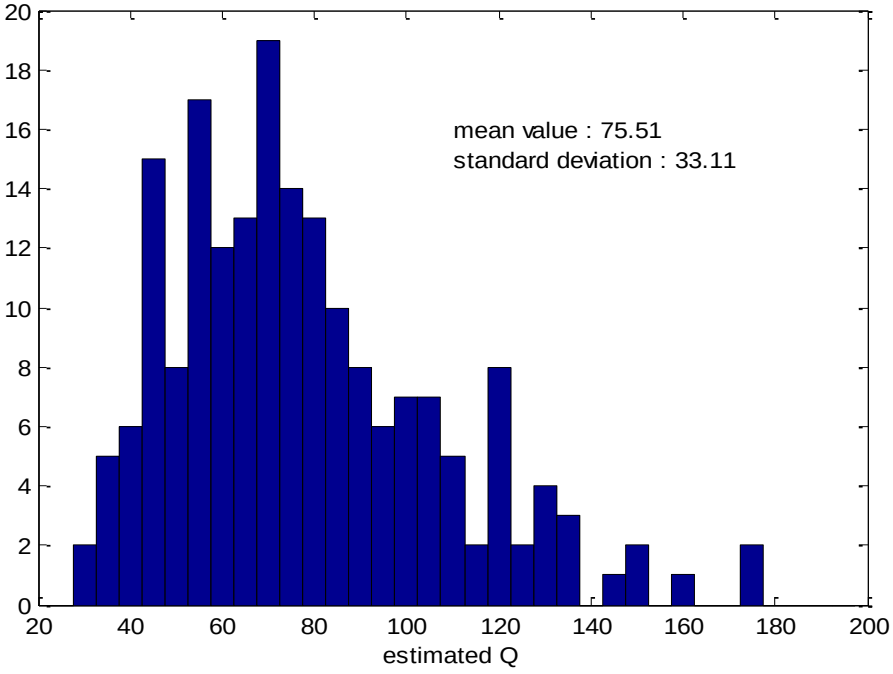

Figure 3.81. Histogram of the Q values estimated by the interpretive spectral-ratio method using the $100ms - 500ms$ and $900ms - 1300ms$ parts of 200 seismic traces with noise level of $SNR = 2$ which are similar to the one shown in Figure 3.60.

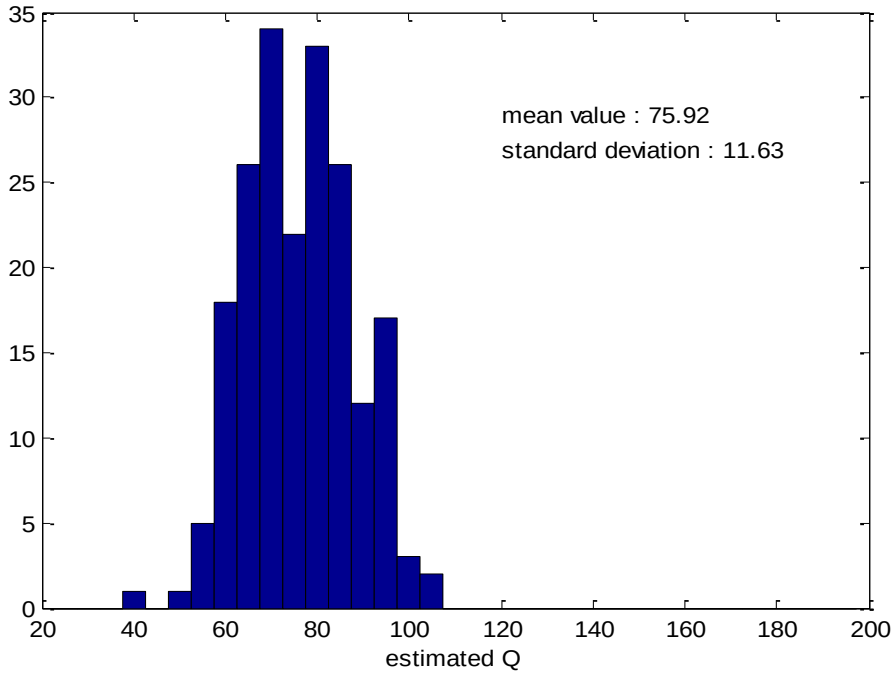

Figure 3.82. Histogram of the Q values estimated by match-filter method using the $100ms - 500ms$ and $900ms - 1300ms$ parts of 200 deconvolved seismic traces which are similar to the one shown in Figure 3.60.

3.5.2 2D synthetic reflection data example for match-filter method

An important application of Q estimation is that the estimation result can be used as a gas indicator in conjunction with other observations such as flat spots, bright spots, and AVO anomalies. The value of Q drops drastically in presence of gas so that the gas reservoir behaves like a localized low Q zone in the subsurface. Synthetic data for a layered earth model with a low Q zone is generated by 3D finite-difference viscoacoustic seismic modeling using Tiger software of SINTEF, and is used to test the match-filter method in term of its capacity to indentify the localized low Q zone. Figure 3.83 shows the reflectivity coefficients corresponding to the layered earth model in two-way time. To simplify the computation of traveltime, we use an earth model with a constant velocity and layered density structure which is calculated from the random reflectivity coefficients, as shown in Figure 3.84. The associated Q model is shown

in Figure 3.85. The low Q zone has an extension of $1.2s - 1.26s$ in two-way traveltime and $500m - 750m$ in horizontal coordinates. Three shot records corresponding to different source locations of the layered earth model are shown in Figure 3.86 – 3.88.

To indentify the low Q zone, two time windows with a fixed small interval slide along a seismic trace to obtain pairs of local wavelets. For each pair of them, a Q value can be estimated and attributed to the time centered between the two time windows. The Q estimation is conducted to the entire 2D seismic gather trace by trace. Through this approach, a Q profile can be obtained for the 2D seismic gather. Since the interval time involved with Q estimation is small, the attenuation between the two local reflected waves is usually not obvious except that the deeper one travels through the low Q zone and the shallow one does not. Therefore, the low Q zone in the Q model will cause a relatively low amplitude area in the estimated Q profile. A pair of time windows with a length of $200ms$ and an interval of $100ms$ are used to sample the seismic traces. The estimated Q profiles for the three shot records are shown in Figure 3.89, 3.90 and 3.91 respectively. We can see that there is hyperbolic distribution of estimated Q values, and the low amplitude area shifts with the varying source locations. Then three NMO corrected CDP gathers are obtained from the shot records with a NMO stretch limit of 30%. The Q profiles of the three CDP gathers are shown in Figure 3.92, 3.93 and 3.94. We can see that the hyperbolic distribution of estimated Q values are flattened, and the locations of low amplitude areas in the three Q profiles are corrected and consistent with each other, which match with the low Q zone of the Q model outlined by a rectangle area very well. To refine the low amplitude areas of the Q profiles, the variations of the mean value of Q with travel time or depth and horizontal position are derived from the zoomed low Q areas shown in Figure 3.92 – 3.94. AS illustrated by Figure

3.95 and 3.96, the estimated low Q zone should be the areas with a two-way traveltime centered at $1.23s$ and horizontal extension from about $500m\ to\ 750m$, which is a very good match to the Q model. Therefore, the match-filter method has the potential to indentify the low Q zone of 2D reflection data for a layered media.

To simulate the Q profile estimation for real data, random noise of level $SNR = 3$ is added to the NMO applied CDP gather corresponding to the shot record shown in Figure 3.86. Then, a Q profile is estimated from the noisy CDP gather. As shown in Figure 3.97, the Q profile is disturbed by noise. To address this problem, the amplitude spectrum of local wavelet can be estimated from a small ensemble of neighboring traces. First, the smoothed amplitude spectrum is estimated for each trace. Then, the smoothed amplitude spectra of an ensemble is scaled and summed using some weighting scheme to give the final spectrum estimation for the trace centered in this ensemble. Adopting this approach for spectrum estimation, Q profile for the noisy CDP gather is obtained and shown in Figure 3.98. We can see that the affect of noise is suppressed and the result is similar to the noise free case shown in Figure 3.92.

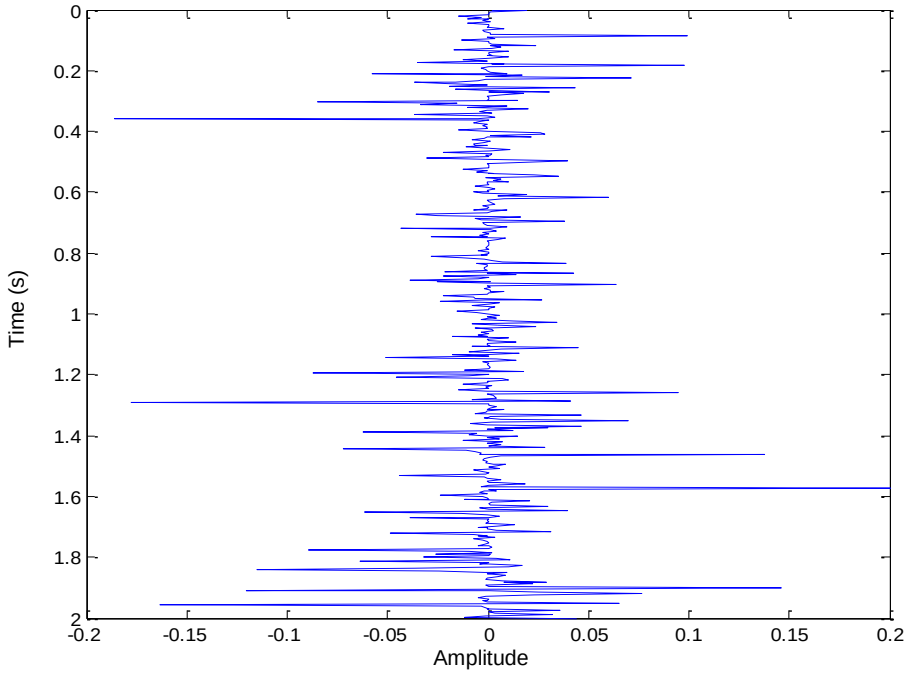

Figure 3.83. Reflectivity coefficients in two-way travel time for a layered earth model.

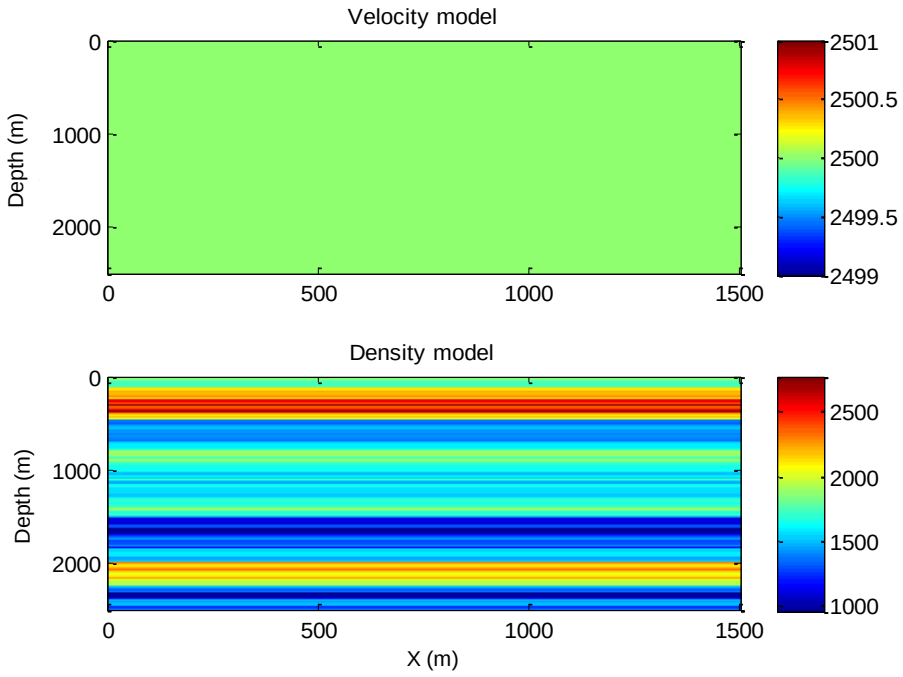

Figure 3.84. Velocity and density structure for a layered earth model which has the reflectivity coefficients shown in Figure 3.83.

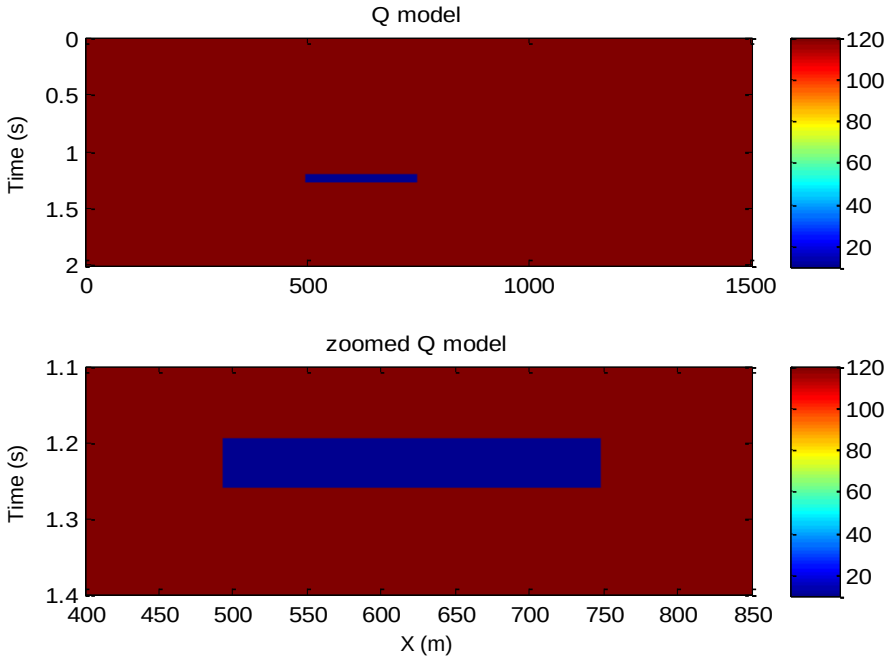

Figure 3.85. Q model for the layered earth model shown in Figure 3.84.

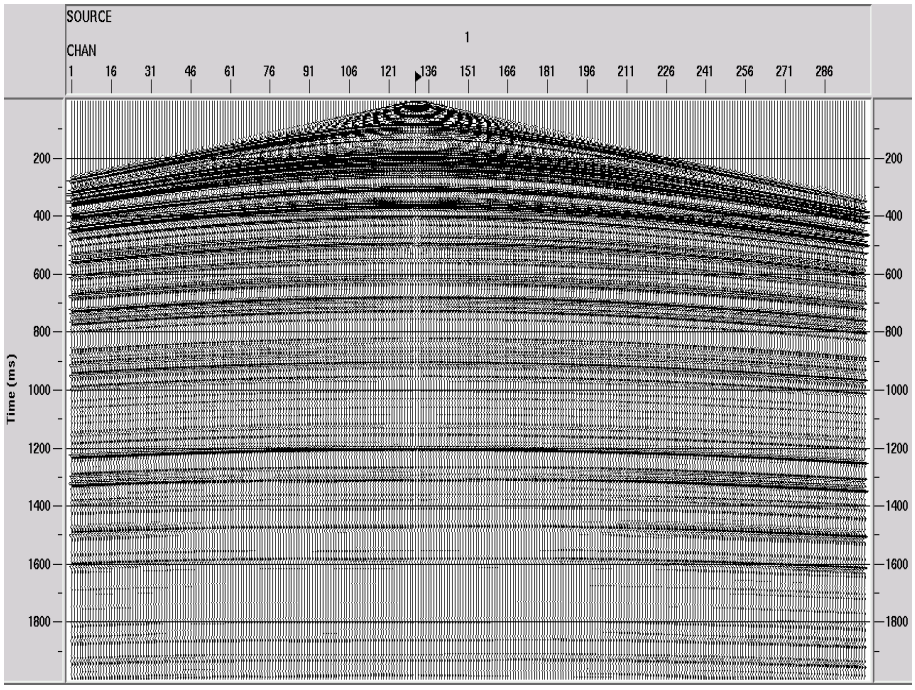

Figure 3.86. Shot record (geometric spreading compensated) for a layered earth model with velocity and density structure shown in Figure 3.84, Q attenuation structure shown in Figure 3.85; source location $(x, z) = (650m, 0m)$, receiver interval: $5m$.

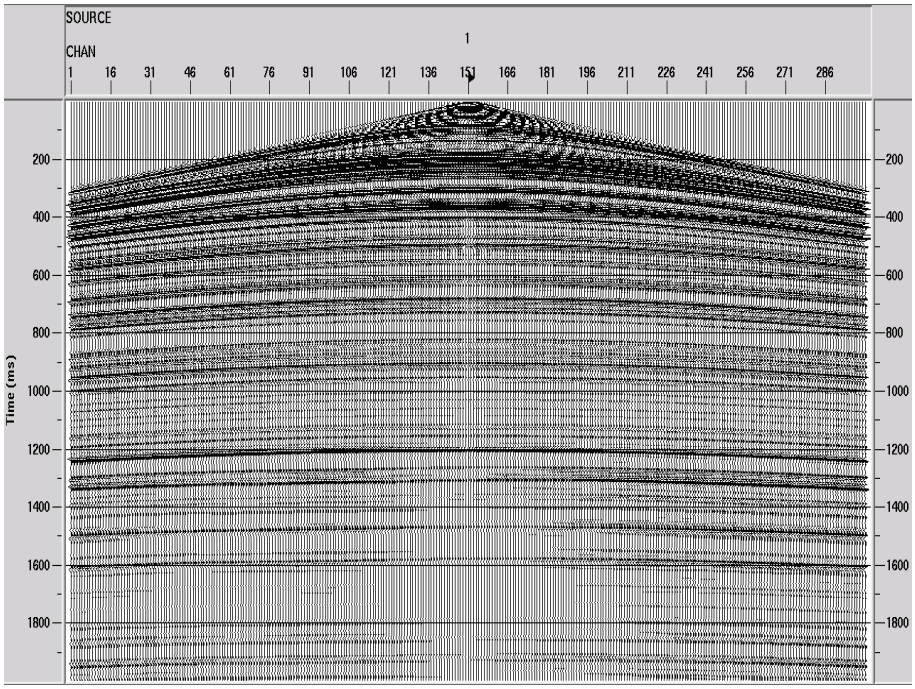

Figure 3.87. Shot record (geometric spreading compensated) for a layered earth model with velocity and density structure shown in Figure 3.84, Q attenuation structure shown in Figure 3.85; source location $(x, z) = (750m, 0m)$, receiver interval: $5m$.

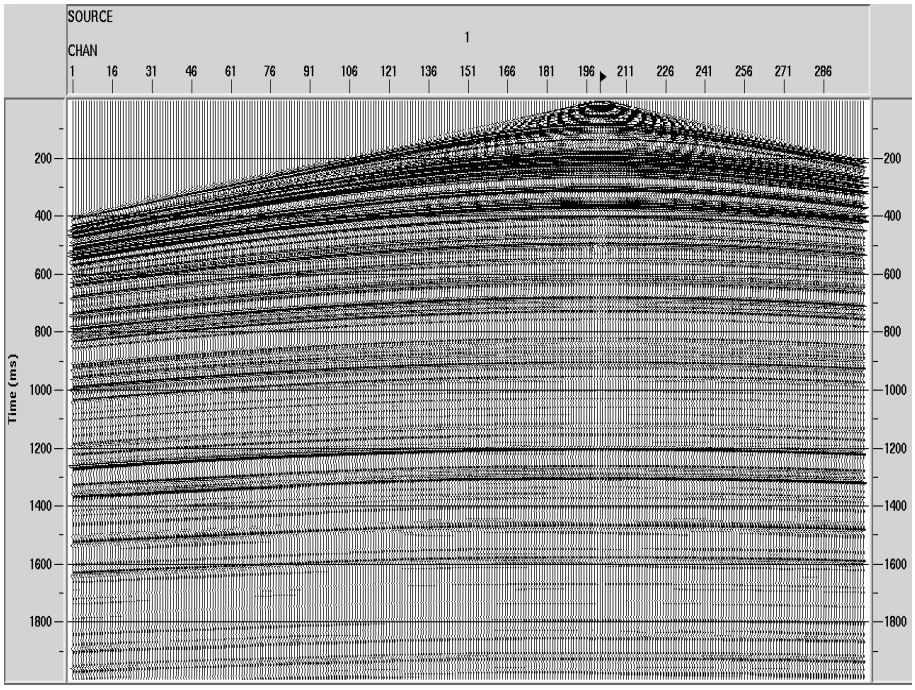

Figure 3.88. Shot record (geometric spreading compensated) for a layered earth model with velocity and density structure shown in Figure 3.84, Q attenuation structure shown in Figure 3.85; source location $(x, z) = (1000m, 0m)$, receiver interval: $5m$.

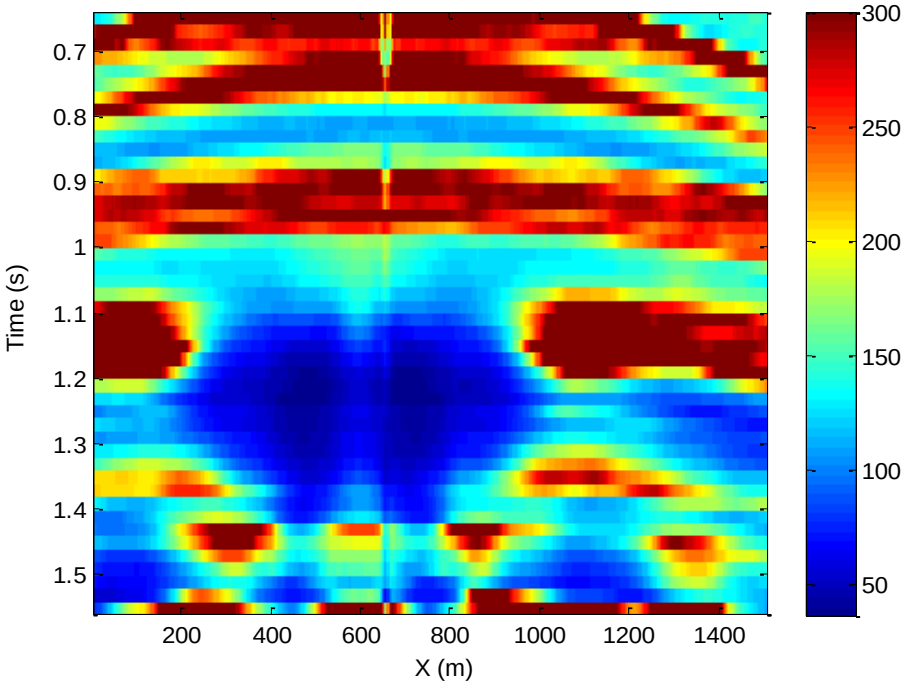

Figure 3.89. Q profile estimated by the match-filter method using the shot record shown in Figure 3.86.

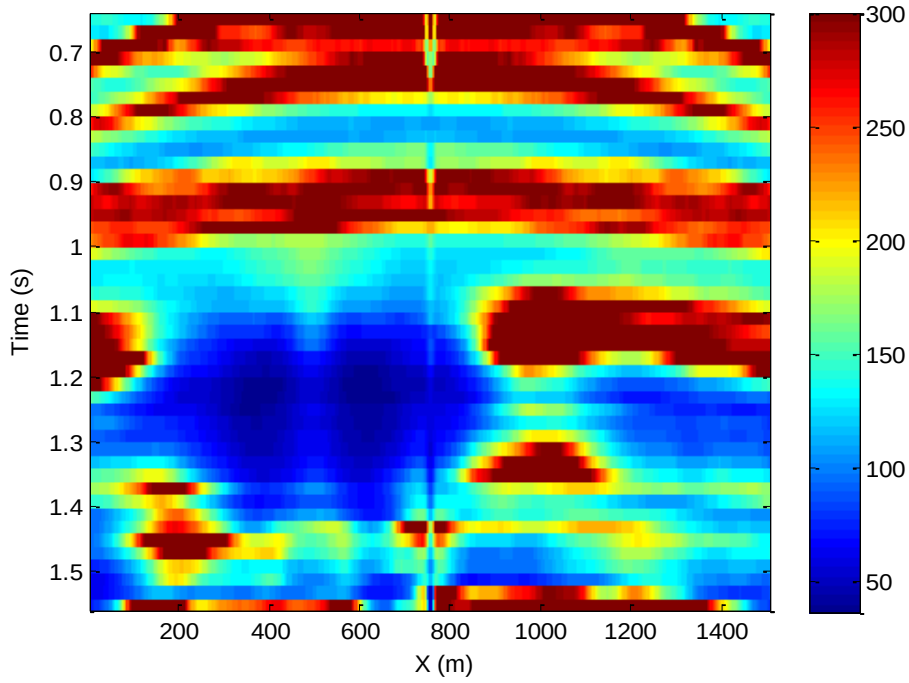

Figure 3.90. Q profile estimated by the match-filter method using the shot record shown in Figure 3.87.

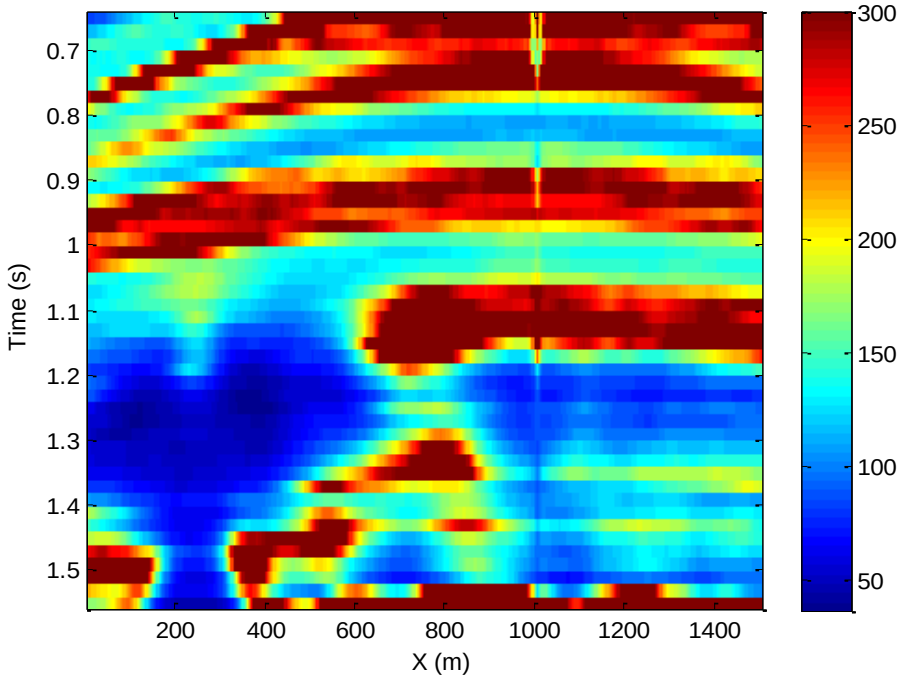

Figure 3.91. Q profile estimated by the match-filter method using the shot record shown in Figure 3.88.

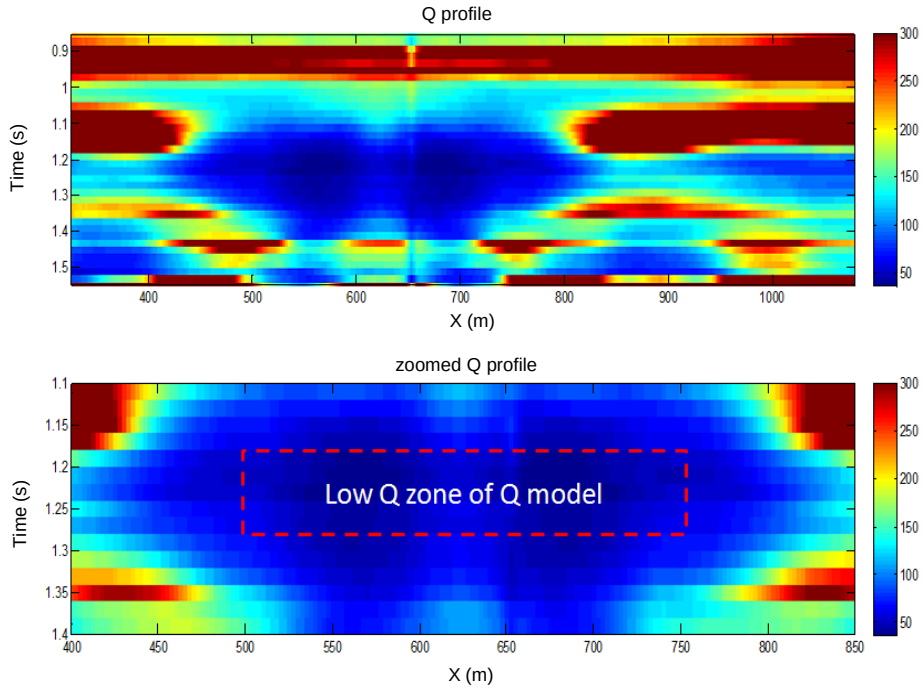

Figure 3.92. Q profile estimated by the match-filter method using the NMO corrected CDP gather corresponding to the shot record shown in Figure 3.86.

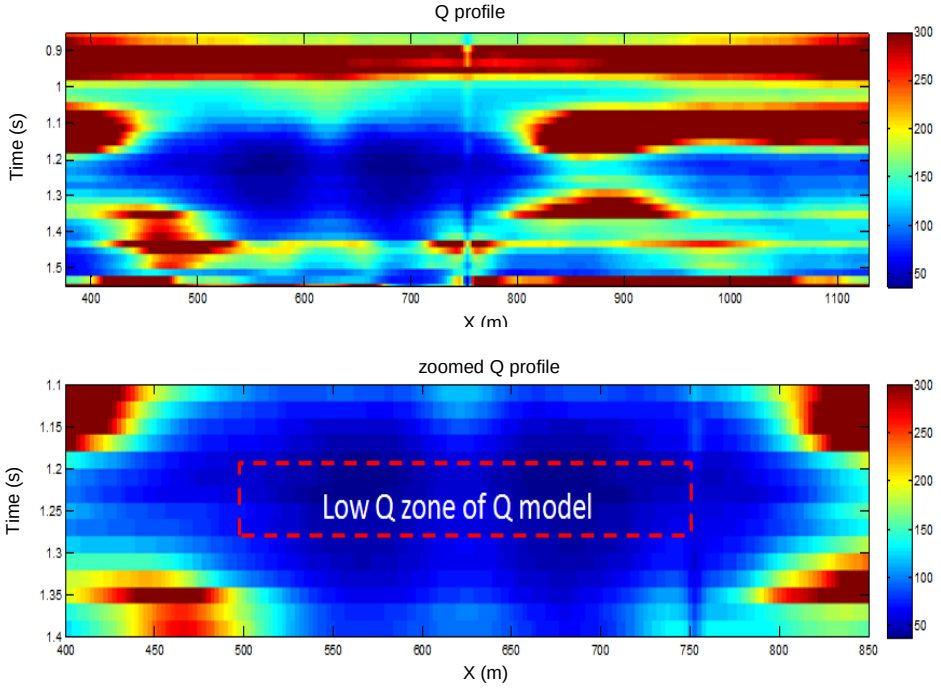

Figure 3.93. Q profile estimated by the match-filter method using the NMO corrected CDP gather corresponding to the shot record shown in Figure 3.87.

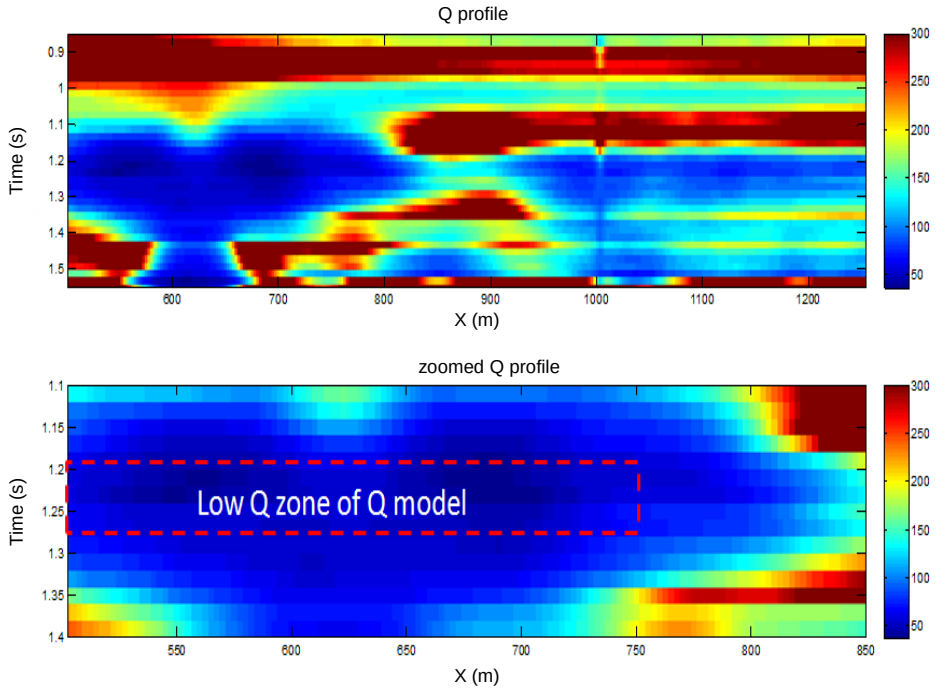

Figure 3.94. Q profile estimated by the match-filter method using the NMO corrected CDP gather corresponding to the shot record shown in Figure 3.88.

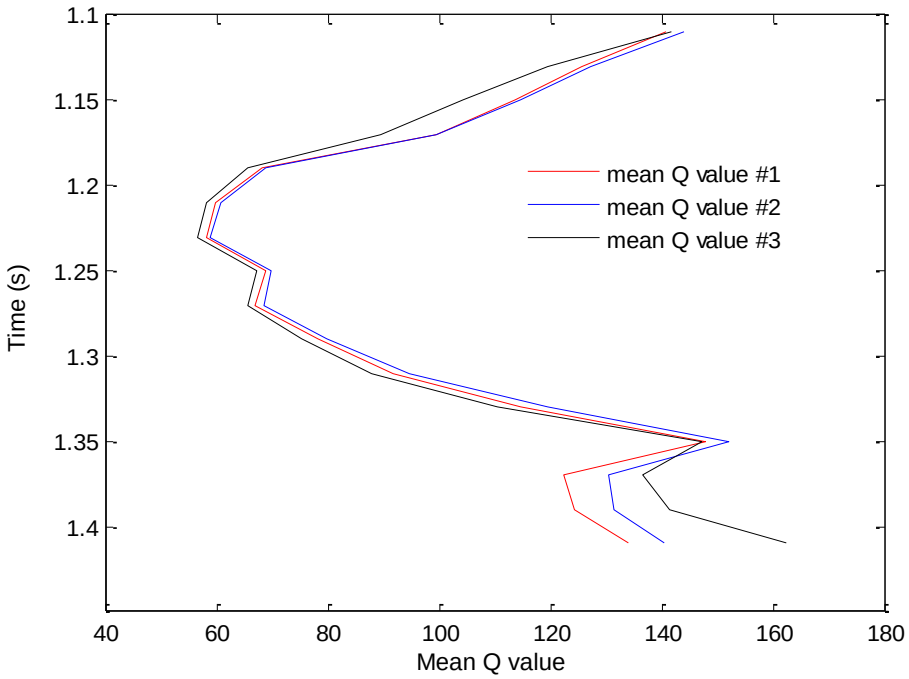

Figure 3.95. The variation of mean Q value with two-way time for the zoomed Q profiles (#1, #2, #3 – the zoomed Q profiles shown in Figure 3.92, 3.93, and 3.94 respectively).

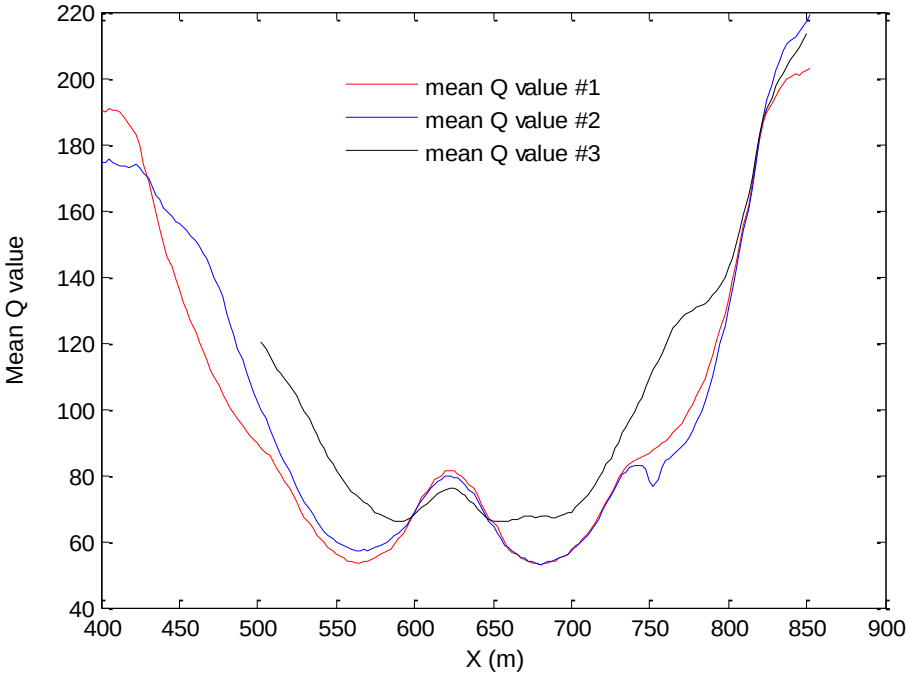

Figure 3.96. The variation of mean Q value with horizontal coordinates for the zoomed Q profiles (#1, #2, #3 – the zoomed Q profiles shown in Figure 3.92, 3.93, and 3.94 respectively).

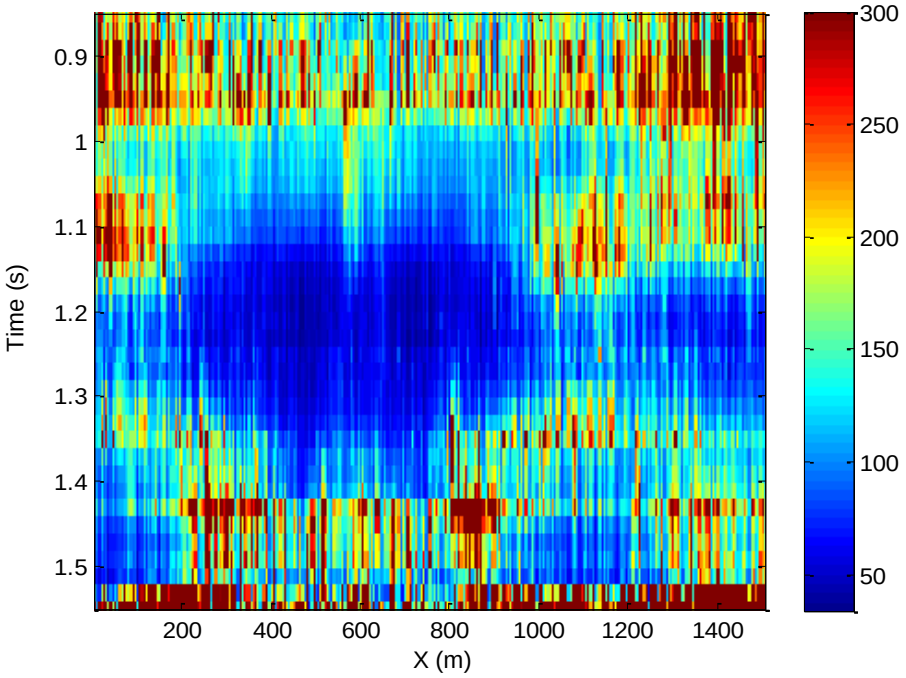

Figure 3.97. Q profile estimated by match-filter method using the NMO corrected CDP gather with noise level of $SNR = 3$ corresponding to the shot record shown in Figure 3.86.

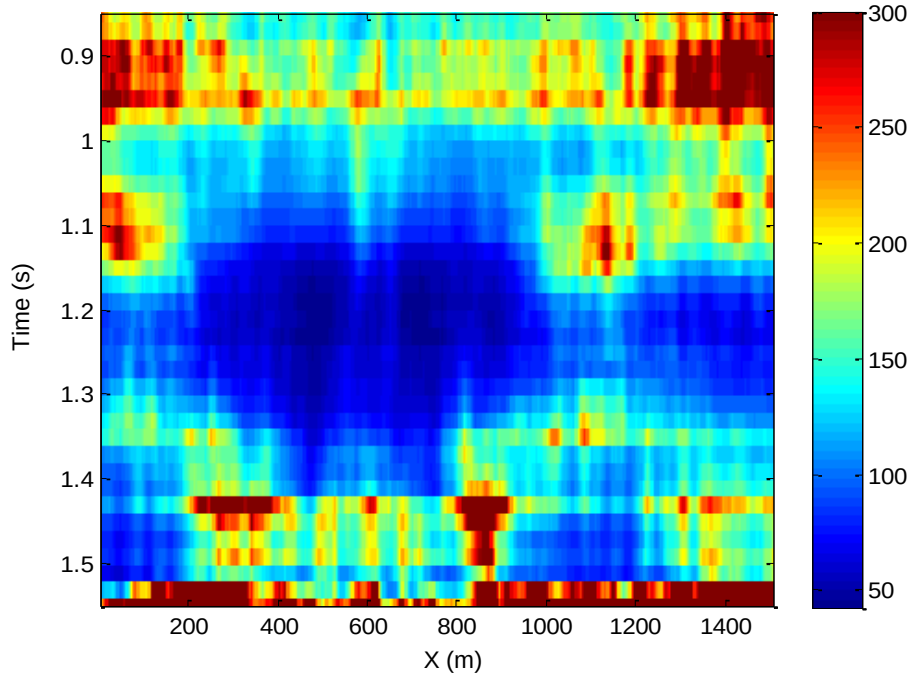

Figure 3.98. Q profile estimated by match-filter method using the NMO corrected CDP gather with noise level of $SNR = 3$ corresponding to the shot record shown in Figure 3.86 (An ensemble of neighboring traces are used for spectrum estimation).

3.5.3 2D real reflection data example for multitaper method

The 2D field data were acquired over the Blackfoot field near Strathmore, Alberta in 1995. The field data were processed using ProMAX software with a processing job flow including geometrical spreading correction, statics correction, predictive deconvolution, NMO correction, trace equalization and stacking. Considering that amplitude spectra of the near-offset traces and far-offset traces can be distorted by strong ground rolls and large NMO stretches respectively, the traces with moderate offsets are chosen to conduct the stacking. The stacked data are displayed in order of CDP bin number, as shown in Figure 3.99. For the Blackfoot line, the target zone is around $1050ms$ in two-way traveltime. In addition, there is a Well 14-09 about $200m$ away from it, which has nearly the same X coordinate with the trace CDP 36.

Q estimation by the match-filter method is conducted using the $750ms - 1050ms$ and $1300 - 1600ms$ parts of the traces CDP 25- CDP 265, which roughly gives the average Q for the time interval $900ms - 1450ms$. The variation of estimated Q values with X coordinates (CDP bin numbers) is shown in Figure 3.100, and the histogram of the estimated Q values is shown in Figure 3.101. The estimated Q values vary with the trace positions while they remain within a reasonable range. As shown in Figure 3.102, a Q profile was estimated from the CDP gather, using sliding windows with a length of $300ms$ and an interval of $100ms$. We can see that, there is measurable attenuation around $1050ms$ nearly across the entire line even a small interval time is employed for Q estimation, and the target zone of the well 14-09 locates within the low amplitude area of the estimated Q profile.

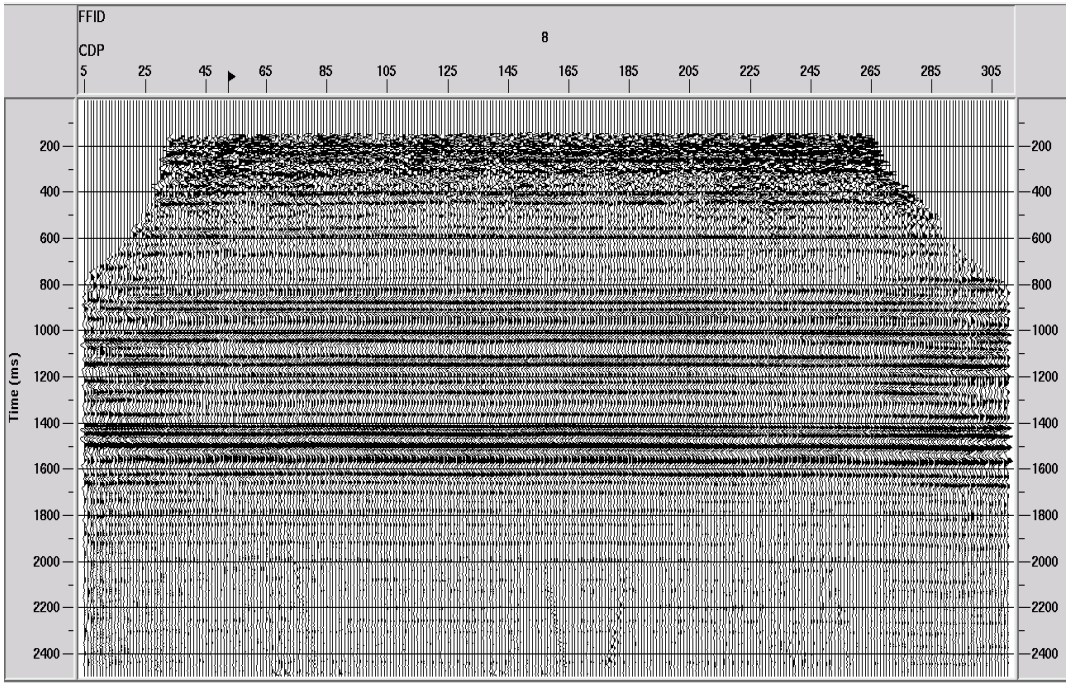

Figure 3.99 Stacked CDP gather for Blackfoot field data.

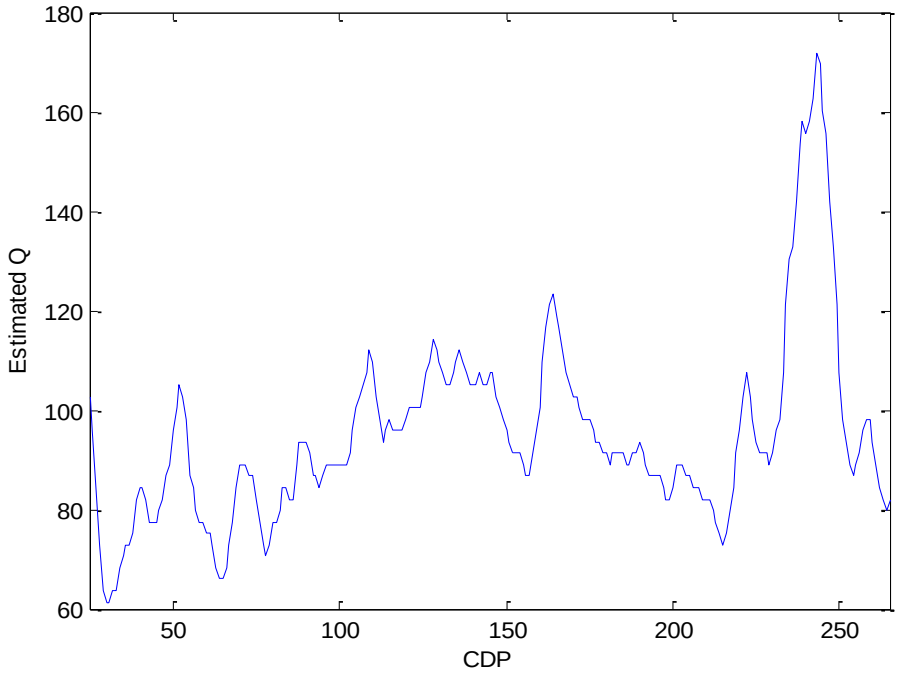

Figure 3.100. Q values estimated by the match-filter method for the traces CDP 25-265 using their $750ms - 1050ms$ and $1300ms - 1600ms$ parts.

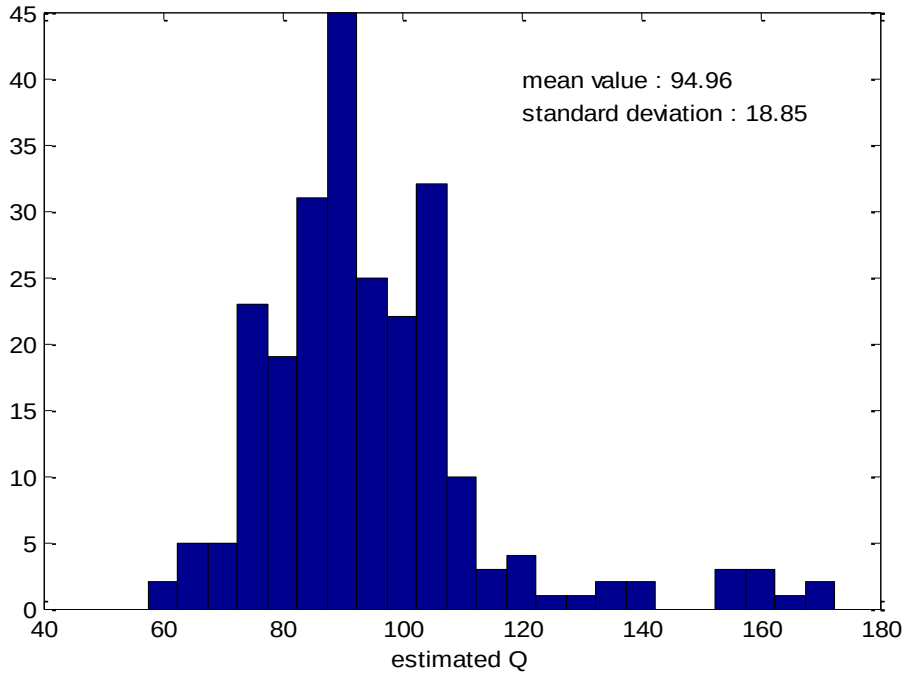

Figure 3.101. Histogram of the estimated Q values shown in Figure 3.100.

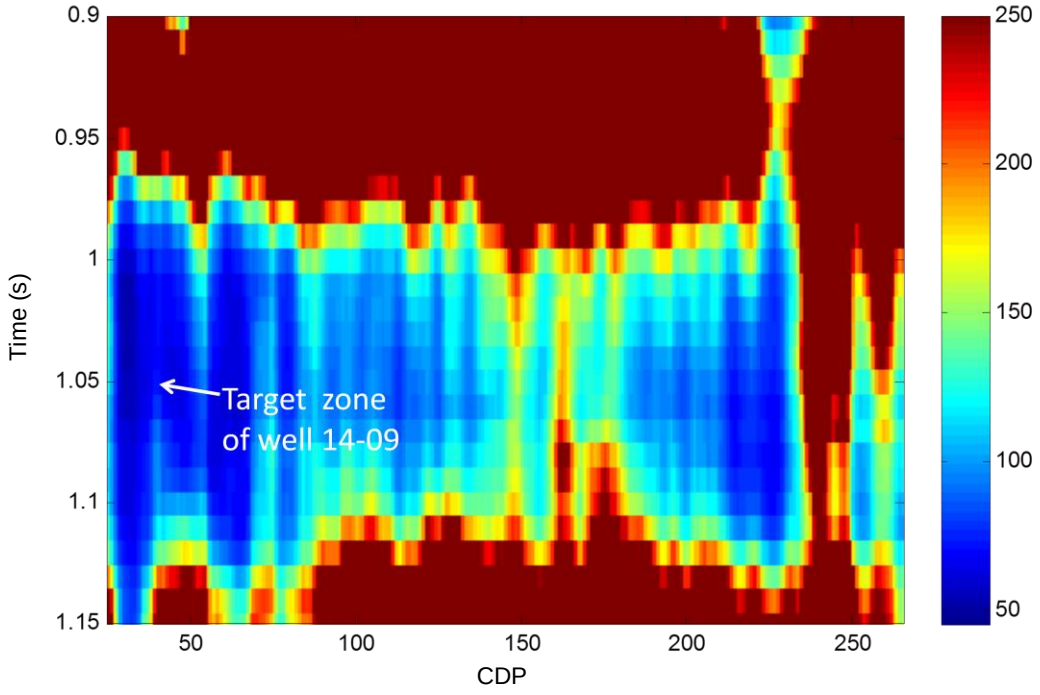

Figure 3.102. Q profile estimated by the match-filter method for CDP gather shown in Figure 3.99, using sliding windows with a length of $300ms$ and an interval of $100ms$.

3.6 Summary

The theory of various Q estimation methods is introduced in this chapter, including classic spectral-ratio method, complex spectral-ratio method, interpretive spectral-ratio methods, spectrum- modeling method, match-technique method and match-filter method.

The performance of above Q estimation methods is evaluated using synthetic and field data. Testing on synthetic VSP data shows that match-filter method and complex spectral-ratio method are more stable and robust to noise compared to other methods, while all of them can give good estimation results for VSP data with moderate noise.

The classic spectral-ratio method, the spectrum-modeling method and the match-technique method, as methods in frequency domain, can be sensitive to the distortion of amplitude spectrum caused by application of spectrum estimation or noise. For the match-filter method, appropriate spectrum smoothing can improve the estimation of embedded wavelets, and, in turn, make the estimation result more stable.

All the frequency domain methods are subject to the frequency band chosen for Q estimation. Theoretically, the result of match-filter method, as a time-domain method, can also be affected by the frequency band used to estimate the embedded wavelets. Accurate estimation results require a rough match of the frequency bands for embedded wavelets, which can be chosen based on the evaluation of their amplitude spectra of original local waves.

Testing on real VSP data shows that match-filter method and spectrum modeling method give more stable results, since no spectral division is involved in their algorithm, and all the methods can obtain similar results at most cases when VSP data with high SNR is used for Q estimation.

Complex spectral-ratio method is subject to the reference frequency chosen for modeling phase difference as well. Inaccurate reference frequency can distort the estimation. To apply the complex spectral-ratio method to real data, minimum phase equivalent wavelet transformation are necessary before Q estimation, and the chosen of reference frequency can be chosen with the calibration of other methods.

When applied to reflection data, the classic spectral-ratio method, spectrum-modeling method and match-technique method fail. The interpretive spectral-ratio method significantly improves the performance of classic spectral-ratio method, while the estimation results still have large standard deviation value. In contrast, match-filter method gives quite accurate estimations, and is insensitive to noise. This may indicate that the spectrum estimation of local wavelets by multitaper method is mainly affected by the tuning effect of local reflectors instead of noise. Testing results show that Q estimation can be conducted with reflection data either before or after stationary deconvolution.

When conducting Q estimation for a 2D gather, a small ensemble of neighbouring traces can be employed to give the final spectrum estimation for a single trace. This approach can help to obtain a better smoothed spectrum and stabilize the Q estimation. Numerical tests using the 2D synthetic data and field data demonstrate that the match filter has the potential to identify the localized low Q zone of the subsurface from surface reflection data.

Chapter Four: Gabor deconvolution and the color correction to white-reflectivity assumption

4.1 Introduction

Deconvolution is an essential part of seismic data processing. The deconvolution algorithm is derived from the corresponding convolution model. Conventional deconvolution methods are developed based on the stationary convolution model, such as Wiener spiking deconvolution. However, the seismic trace is nonstationary due to attenuation during the propagation for various reasons such as Q attenuation and geometric spreading. Deconvolution algorithms usually assume that the reflectivity is a random series, meaning that reflectivity has a white amplitude spectrum. In practice, the reflectivity is colored, i.e., the magnitude of its Fourier amplitude spectrum demonstrates obvious frequency dependency. The white reflectivity assumption can lead to distortion of reflectivity estimation. In addition, the color feature of the true reflectivity is nonstationary (Cheng and Margarve, 2009a).

The nonstationary characteristic of both seismic trace and true reflectivity can be corrected in a nonstationary way. This chapter gives a basic introduction to Gabor deconvolution, and presents the color correction method to white-reflectivity assumption for Gabor deconvolution. The influence of the time-variant reflectivity color is analyzed in detail, and synthetic data and field data are used to evaluate the color correction method.

4.2 Gabor deconvolution

4.2.1 The Gabor transform

Gabor transform (GT) provides a manner of time-frequency decomposition of a signal. In this section, we will follow Margrave and Lamoureux (2001), Margrave et al (2011) to give a

brief introduction to the GT. The continuous GT of a signal $s(t)$ can be defined as (Mertins, 1999)

$$S_G(\tau, f) = \int_{-\infty}^{\infty} s(t)\vartheta(t-\tau)e^{-j2\pi ft}\,dt, \tag{4.1}$$

where $\vartheta(t)$ is the Gabor analysis window, and τ denotes the center of the analysis window. We can see that the continuous GT gives local spectrum of the signal by weighting the signal with a window function before the Fourier transform. By sliding the analysis window along the signal, GT produces a collection of local spectra. So, a time-frequency decomposition of the signal is obtained. Even if signal $s(t)$ is nonstationary for the whole time range, $s(t)$ can still be regarded to be approximately stationary within a specified time window. From this point of view, GT can give a better characterization of nonstationary signal compared with Fourier transform. Given $S_G(\tau, f)$, the signal $s(t)$ can be reconstructed as

$$s(t) = \iint_{-\infty}^{\infty} S_G(\tau, f)\,\gamma(t-\tau)e^{-j2\pi ft}df dt, \tag{4.2}$$

where $\gamma(t)$ is the Gabor synthesis window. To achieve a perfect reconstruction, the analysis window and synthesis window should satisfy the following condition

$$\int_{-\infty}^{\infty} \gamma(t)\vartheta(t)\,dt = 1. \tag{4.3}$$

When $\vartheta(t) = 1$ and $\gamma(t) = \delta(t)$, Gabor transform reduces to Fourier transform. So, Fourier transform can be viewed as a particular case of Gabor transform.

For practical implementation, a discrete form of Gabor transform should be employed. Given a time spacing of $\Delta\tau$ and frequency spacing of Δf, the discrete Gabor transform is given by

$$S_G(m, n) = \int_{-\infty}^{\infty} s(t)\vartheta_{m,n}(t)\,dt, \tag{4.4}$$

where $\vartheta_{m,n}(t)$ is the Gabor frame defined as

$$\vartheta_{m,n}(t) = \vartheta(t - m\Delta\tau)e^{-i2\pi n\Delta f}. \quad (4.5)$$

If the Gabor frames are orthonormal to each other, the signal can be recovered from the Gabor frame operator defined by

$$V_G(s(t)) = \sum_{m,n\in Z} S_G(m,n)\,\vartheta_{m,n}(t). \quad (4.6)$$

However, the Gabor frames in equation (4.5) do not form an orthonormal basis. For the DGT, the reconstruction of signal should involve the inversion of the Gabor frame operator. So, the recovery of $s(t)$ can be formulated as

$$s(t) = \sum_{m,n\in Z} S_G(m,n)\,{V_G}^{-1}\vartheta_{m,n}(t) = \sum_{m,n\in Z} S_G(m,n)\gamma_{m,n}(t), \quad (4.7)$$

where $\gamma_{m,n}(t) = {V_G}^{-1}\vartheta_{m,n}(t)$ is the dual Gabor frame. The Gabor frames are complete in $L^2(R)$ on condition that $\Delta f\Delta\tau < 1$ (Margrave and Lamoureux, 2001). We can exactly recover the signal by (4.7). However, it is hard to get an inversion of the Gabor frame. In practice, we can choose an approximate way to implement the discrete Gabor transform.

If we can find a set of analysis window $\vartheta(t - k\Delta\tau)$ to make the following equation hold

$$s(t) \approx s(t)\sum_{k\in Z}\vartheta(t - k\Delta\tau) = \sum_{k\in Z} s_k(t), \quad (4.8)$$

where $s_k(t) = s(t)\vartheta(t - k\Delta\tau)$. Then, we apply a forward Fourier transform

$$\hat{S}(f) = \sum_{k\in Z} S_k\,(f), \quad (4.9)$$

where $S_k(f)$ is given by

$$S_k(f) = \int_{-\infty}^{\infty} s_k(t)e^{-i2\pi ft}\,dt. \quad (4.10)$$

And, we can reconstruct the signal by

$$s(t) = F^{-1}[\hat{S}(f)]. \quad (4.11)$$

Therefore, we can get the approximate forward and inverse discrete Gabor transform by (4.10) and (4.11). The requirement for equation (4.8) can be written as

$$\sum_{k\in Z} \vartheta(t - k\Delta\tau) \approx 1. \tag{4.12}$$

The Gaussians can be a good choice of the analysis window, i.e.

$$\vartheta(t - k\Delta\tau) = \frac{\Delta\tau}{\delta\sqrt{\pi}} e^{-[t-k\Delta\tau]^2\delta^{-2}}, \tag{4.13}$$

where δ is the Gaussian half-width. Margrave and Lamoureux (2001) gave a precise expression of the summation of the Gaussians, which is

$$\sum_{k\in Z} \vartheta(t - k\Delta\tau) = 1 + 2\cos\left(\frac{2\pi t}{\Delta\tau}\right) e^{-[\pi T/\Delta t]^2} + \cdots. \tag{4.14}$$

We can use the second term in (4.14) to estimate the approximate errors. So, the error can be made as small as we want by increasing the ratio $\delta/\Delta t$. For geophysical applications, the error is negligible when $\delta/\Delta t > 1.5$ (Margrave and Lamoureux, 2001).

The inherent end effect of the approximate discrete Gabor transform can be further reduced by normalization using the summation curve. The Gabor transform given in equation (4.10) can be normalized as (Margrave and Lamoureux, 2001)

$$\hat{s}_k(f) = \frac{\int_{-\infty}^{\infty} s_k(t) e^{-j2\pi f t} dt}{h(k\Delta\tau)}, \tag{4.15}$$

Where $h(k\Delta\tau) = \sum_{k\in Z} g(t - k\Delta\tau)$ is the actual summation curve of Gabor transform.

4.2.2 The Gabor deconvolution algorithm

Gabor deconvolution is based on a nonstatioanry convolution model of the seismic trace. Margrave and Lamoureux (2002) presented a seismic trace model addressing the seismic wavelet and the nonstationary effect of constant-Q attenuation. The nonstationary convolution model is introduced in chapter 1, and will be restated here for introducing Gabor deconvloution algorithm. The attenuated seismic trace can be modeled as

$$S(f) = W(f)\int_{-\infty}^{\infty} \alpha_Q(\tau, f) r(\tau) e^{-j2\pi f\tau} d\tau, \quad (4.16)$$

where $S(f)$ and $W(f)$ are the Fourier spectra of the seismic trace $s(t)$ and seismic source wavelet $w(t)$ respectively; $r(\tau)$ is the reflectivity, and $\alpha_Q(\tau, f)$ is the constant-Q transfer function given by

$$\alpha_Q(\tau, f) = e^{-\frac{\pi f\tau}{Q} + jH(\frac{\pi f\tau}{Q})}, \quad (4.17)$$

where H denotes the Hilbert transform. Then, the Gabor transform of the attenuated seismic trace can be approximated by (Margrave and Lamoureux, 2002; Margrave et al, 2011)

$$S_G(\tau, f) \approx W(f)\alpha_Q(\tau, f)R_G(\tau, f)\,, \quad (4.18)$$

where $R_G(\tau, f)$ is the Gabor transform of reflectivity.

Based on equation (4.18), $|W(f)||\alpha_Q(\tau, f)|$ can be estimated by smoothing $|S_G(\tau, f)|$ with an assumption that$|R_G(\tau, f)| \approx 1$. The simplest smoothing can be achieved by convolving $|S_G(\tau, f)|$ with a 2-D boxcar over (τ, f). Let $\overline{|S_G(\tau, f)|}$ be a proper smoothing of $|S_G(\tau, f)|$. With a minimum-phase assumption, the attenuated wavelet or propagating wavelet is estimated as

$$W(f)\alpha_Q(\tau, f) \approx \overline{|S_G(\tau, f)|}e^{j\varphi(\tau, f)}\,, \quad (4.19)$$

where the phase $\varphi(\tau, f)$ is given by the Hilbert transform (over frequency),

$$\varphi(\tau, f) = H(ln\overline{|S_G(\tau, f)|})\,. \quad (4.20)$$

Therefore, an estimation of the reflectivity can be formulated in the Gabor spectral domain as

$$R_G(\tau, f)_{est} = S_G(\tau, f)\mathrm{D}(\tau, f), \quad (4.21)$$

where $\mathrm{D}(\tau, f)$ is the deconvolution operator formulated as

$$\mathrm{D}(\tau, f) = \frac{1}{\overline{|S_G(\tau,f)|} + \mu A_{max}} e^{-j\varphi(\tau,f)}, \qquad (4.22)$$

in which μ is the stability factor, and A_{max} is the maximum value of $\overline{|S_G(\tau, f)|}$.

4.2.3 Examples

First, we will use some examples to evaluate the approximate discrete Gabor transform. Figure 4.1 shows the summation curve of a set of Gaussian with a Gaussian half-width of $\delta = 0.1s$ and a window spacing of $\Delta\tau$ =0.04s. We can see that the summation is a very good approximation to unity except at the both ends. Figure 4.2 shows a suit of summation curves with a fixed Gaussian width of $\delta = 0.1s$ and varied window spacing of $\Delta\tau = 0.02s$, $0.04s$, $0.1s$ and $0.2s$. As $\Delta\tau/\delta$ increases, the error term in equation (4.14) becomes more obvious. For the signal reconstruction using the approximate discrete Gabor transform, Figure 4.3 shows the difference between the original signal and the reconstructed signal. The deviations occur at both ends, which are the inherent error resulting from equation (4.12) and (4.14). Figure 4.4 shows the signal reconstruction using the normalized Gabor transform. We can notice that that the inherent error is reduced by the normalization.

Then, an attenuated seismic trace created according to equation (4.16) is shown in Figure 4.5. The source/embedded wavelet is a minimum-phase wave with a dominant frequency of $40Hz$. And the attenuation is predicted using the constant-Q model with a Q value of 50. We can see that the modeled seismic trace decays with time gradually. A comparison of Gabor deconvolution and stationary deconvolution (for instance, the Wiener spiking deconvolution) is illustrated by Figure 4.6. For stationary deconvolution, proceeding AGC is applied to the attenuated seismic trace. While for Gabor deconvolution, the proceeding gain correction is not necessary. We can see that Gabor deconvolution produces a good estimation of the actual

reflectivity, which is better than the result of Wiener spiking deconvolution. Figure 4.7 shows the magnitude of the Gabor spectrum of bandlimited actual reflectivity. For the frequency components within the frequency-band $0Hz - 140Hz$, their magnitude is approximately of the same level. However, the relative magnitude may vary with time. For instance, there is a local high amplitude row near $\tau = 1.2s$ corresponding to the spike near $1.2s$ of the actual reflectivity. Generally, the assumption of $|R_G(\tau, f)| \approx 1$ is reasonable when we derive the Gabor deconvolution algorithm. The magnitude of the Gabor spectrum of attenuated seismic trace is shown in Figure 4.8. We can see the amplitude decays with increasing frequency and travel-time. The magnitude of the Gabor spectra for the two deconvolution algorithms are shown in Figure 4.9 and 4.10. For the stationary deconvolution, the Gabor spectrum of the estimated reflectivity is obviously distorted compared to the one shown in Figure 4.7. For the Gabor deconvolution, the Gabor spectrum of the estimated result has magnitude of approximately the same level over all frequency (within the given frequency band) and traveltime, which is consistent with the assumption $|R_G(\tau, f)| \approx 1$ of conventional Gabor deconvolution. When this assumption violated, the estimated result might be distorted as well. For instance, the local high amplitude row near $\tau = 1.2s$ in Figure 4.7 is not addressed by conventional Gabor dencovolution, the spike near $1.2s$ of the actual is not recovered by the deconvolution. Generally, for deconvolution algorithms, how well the reflectivity is estimated depends on how well the involved assumptions address the reality.

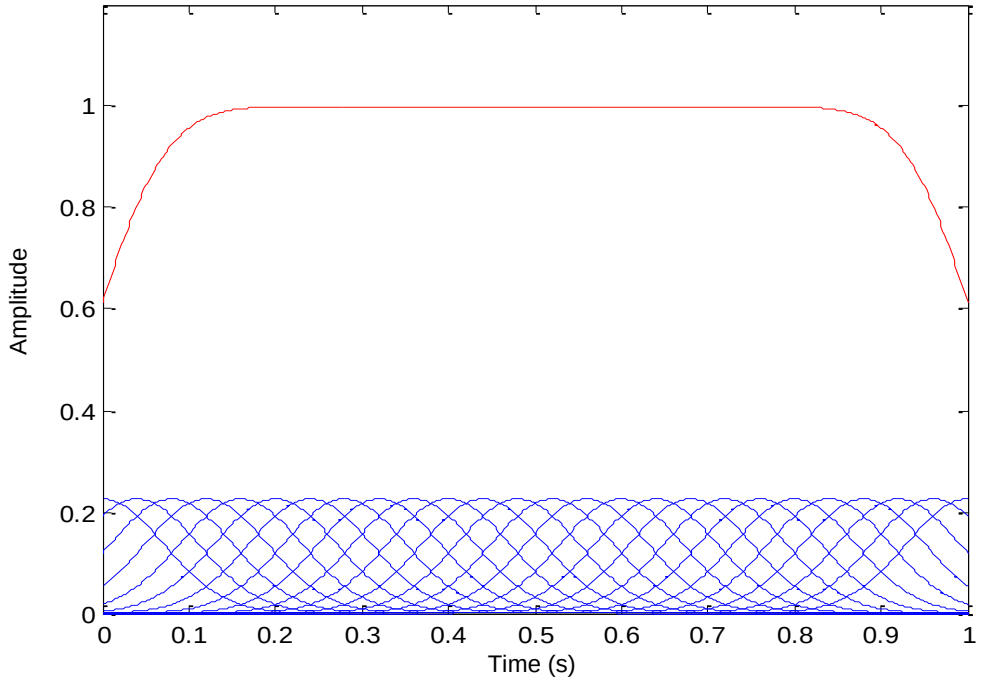

Figure 4.1. The summation curve of a set of Gaussian windows with half-with of $\delta = 0.1s$ and spacing of $\Delta\tau = 0.04s$ (red: summation curve; blue: Gaussian windows).

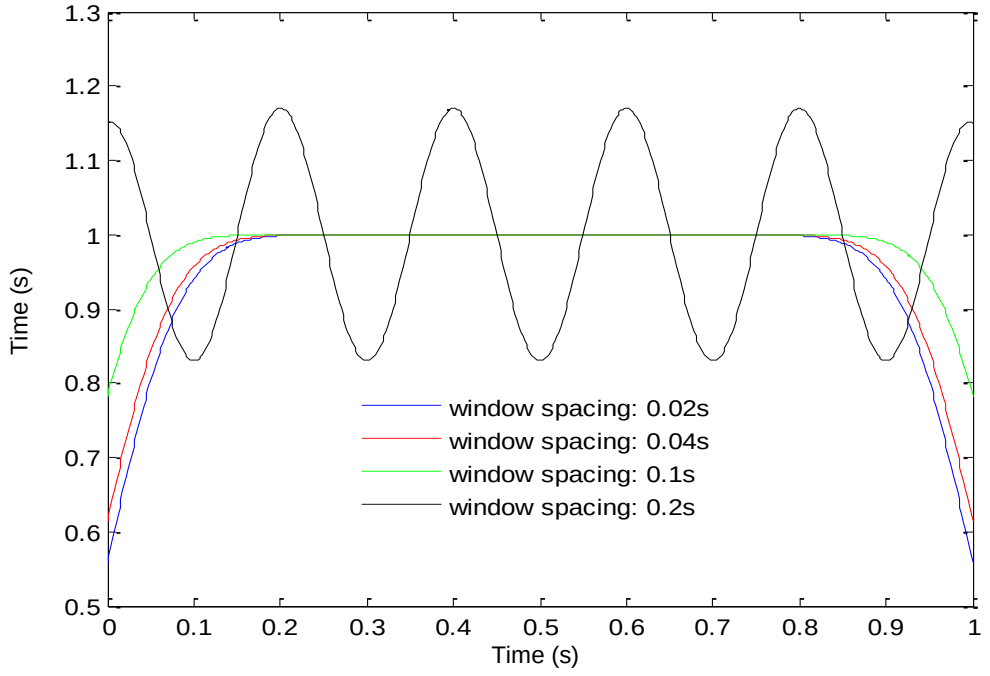

Figure 4.2. The summation curves of a set of Gaussian windows with fix Gaussian width of $0.1s$ and varied window spacing of $0.02s$, $0.04s$, $0.1s$, and $0.2s$.

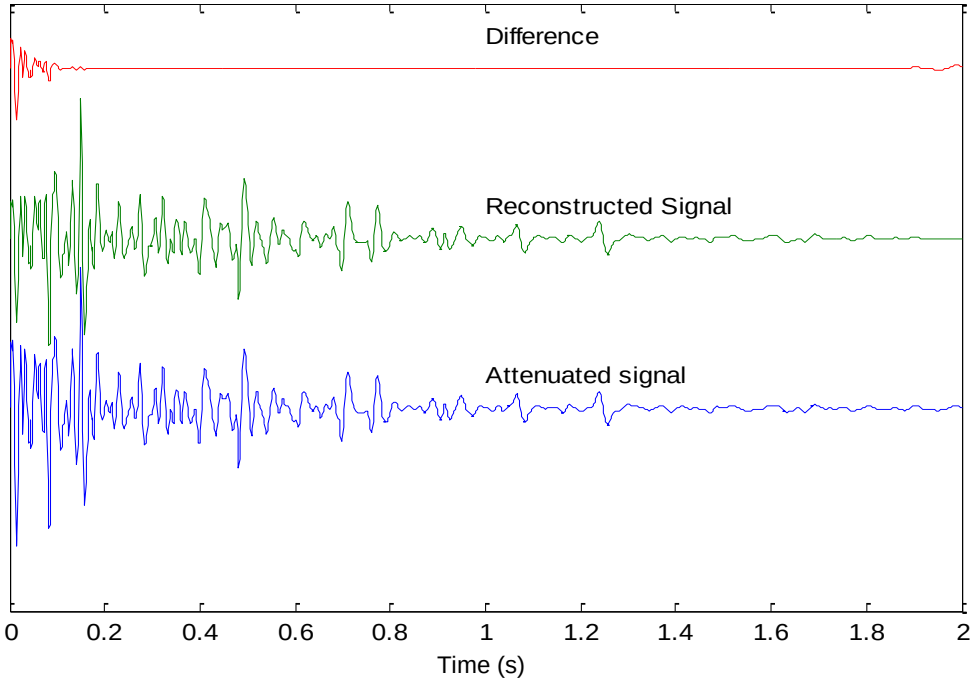

Figure 4.3. Signal reconstruction using approximate discrete Gabor transform.

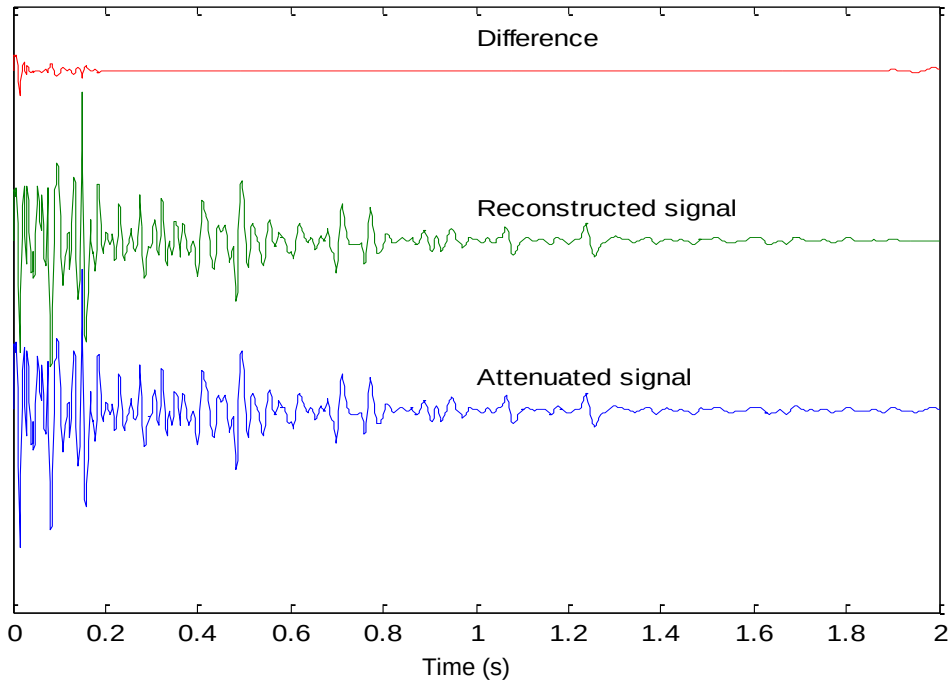

Figure 4.4. Signal reconstruction using normalized discrete Gabor transform.

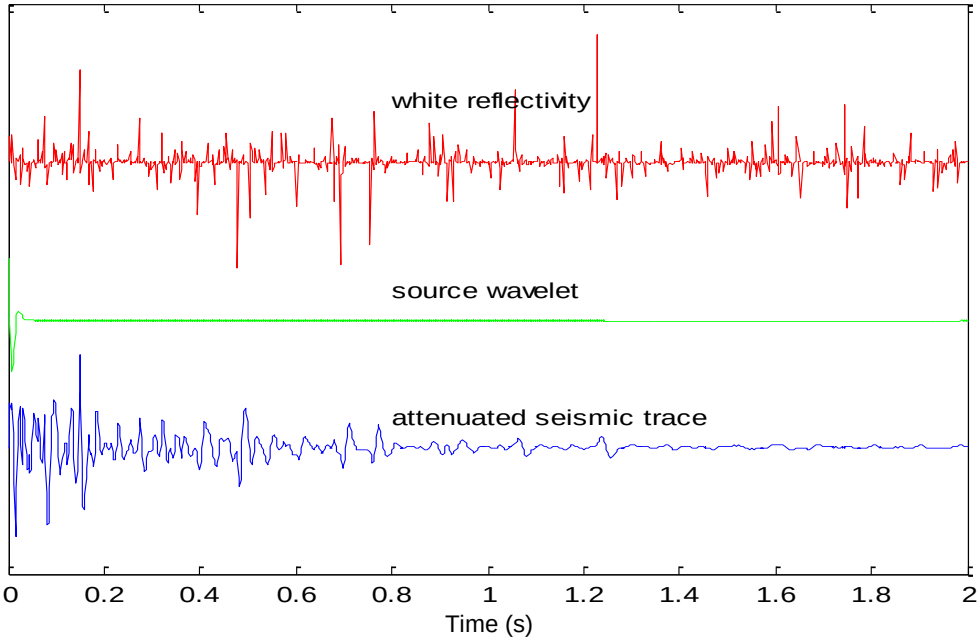

Figure 4.5. An attenuated seismic trace created from random/white reflectivity by a constant-Q model. The source wavelet is a minimum-phase wave with a dominant frequency of $40Hz$ and the Q value is 50.

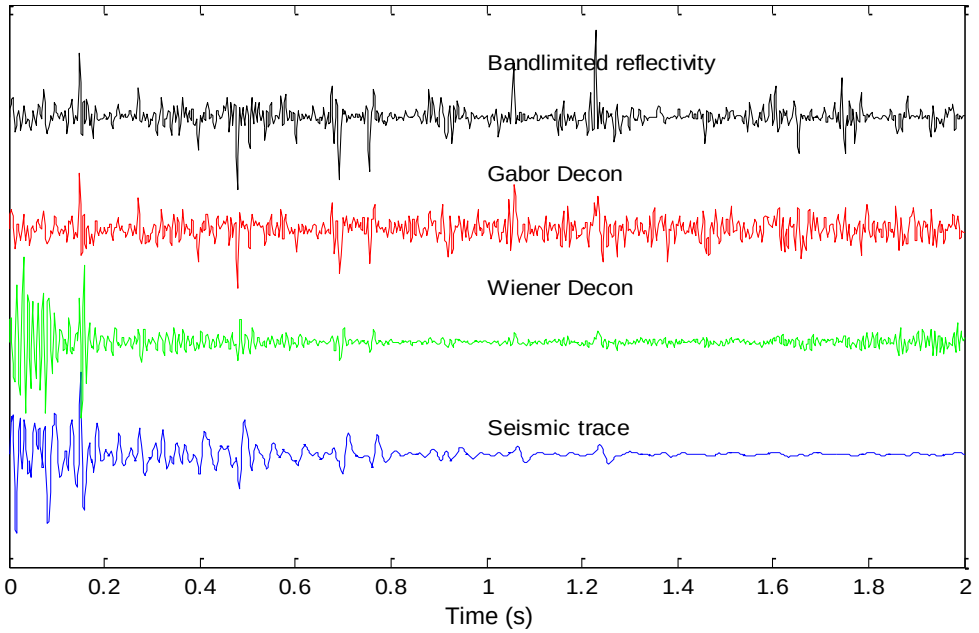

Figure 4.6. Results of the Gabor deconvolution and Wiener spiking deconvolution. (blue) The attenuated seismic trace shown in Figure 4.5. (green) The result of Winner spiking deconvolution proceeded by AGC. (red) The result of Gabor deconvolution without proceeding gain correction. (black) The bandlimited actual reflectivity.

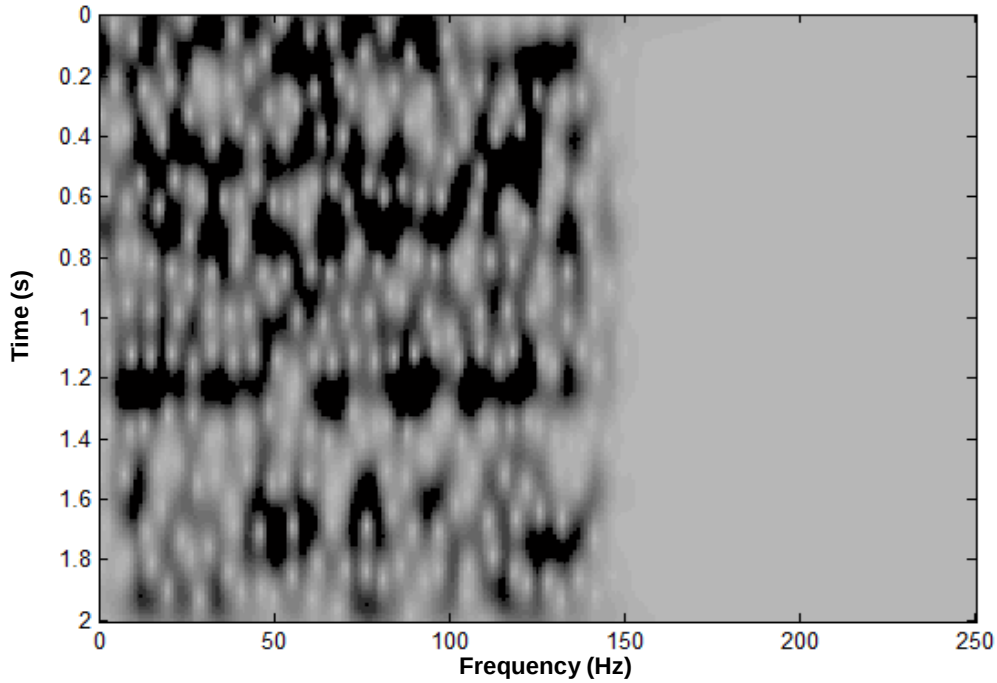

Figure 4.7. Magnitude of the Gabor transform of the band-limited actual reflectivity in Figure 4.6.

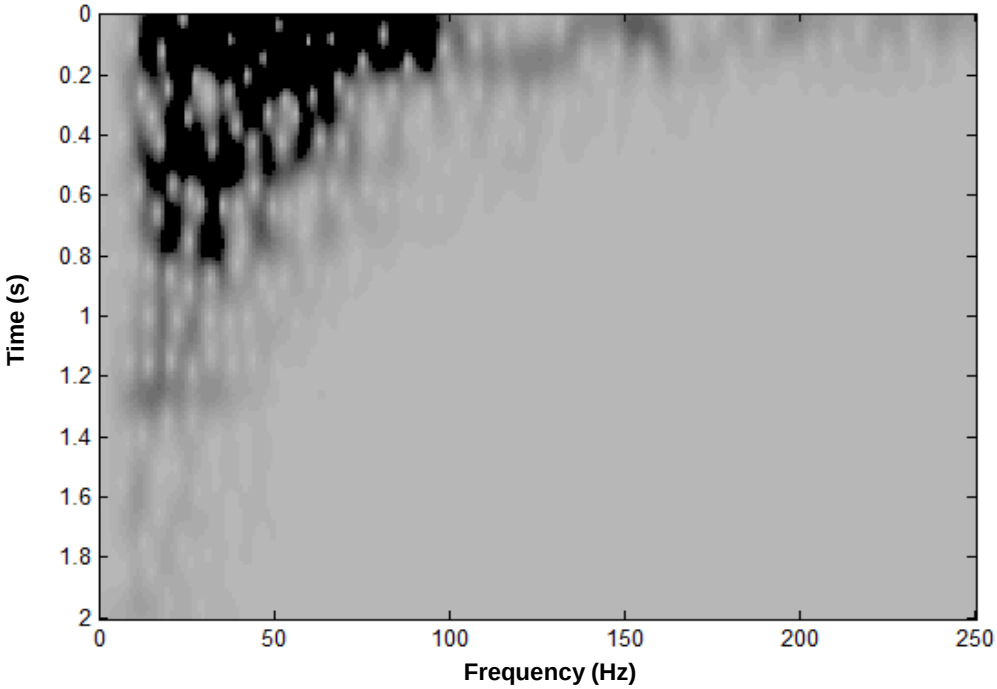

Figure 4.8. Magnitude of the Gabor transform of the attenuated seismic trace in Figure 4.6.

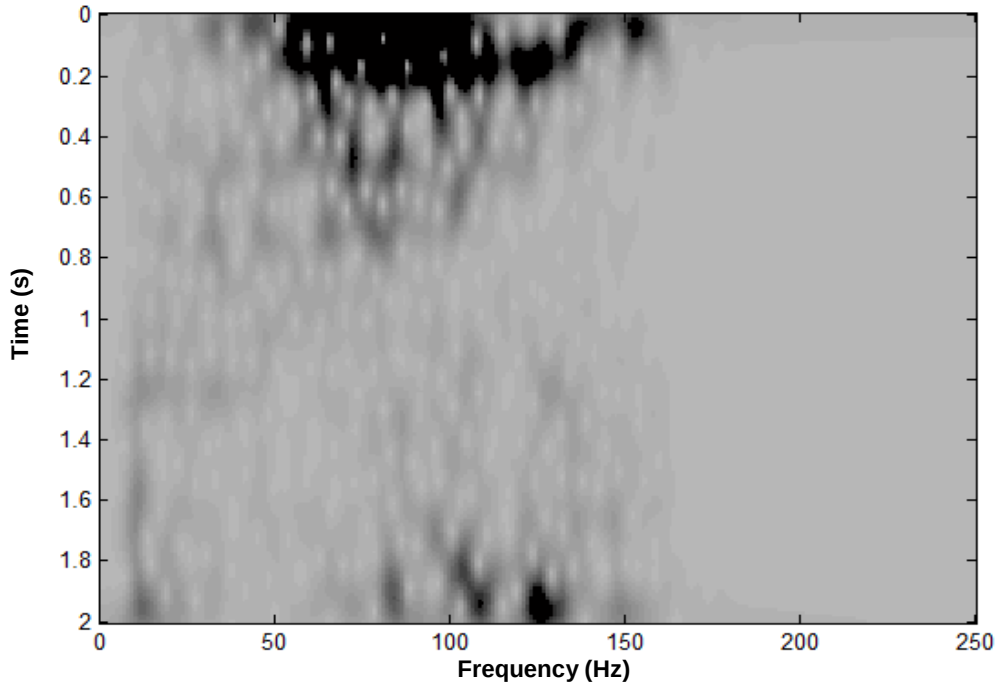

Figure 4.9. Magnitude of the Gabor transform of the estimated reflectivity by the Wiener spiking deconvolution in Figure 4.6.

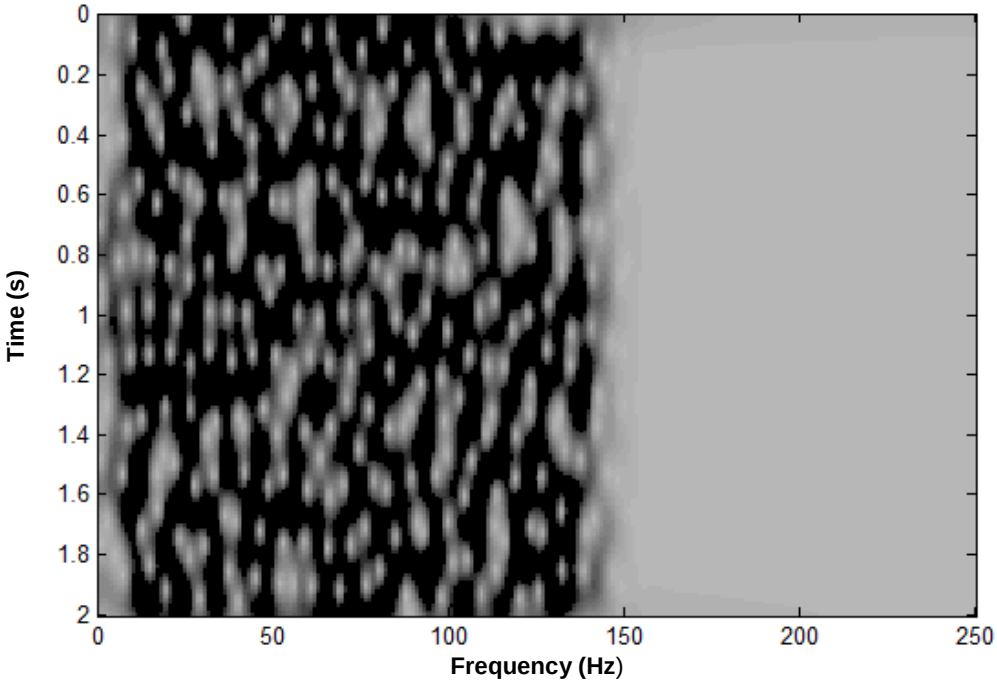

Figure 4.10. Magnitude of the Gabor transform of estimated reflectivity by Gabor deconvolution in Figure 4.6.

4.3 Color correction for Gabor deconvolution

4.3.1 Theory of the color correction method

If the assumption of white reflectivity is violated, i.e. $|R_G(\tau,f)|$ deviates from unity significantly, which is usually true in practice. Then deconvolution algorithm discussed above should modified accordingly, since it always gives estimation result with white amplitude spectrum ($|R_G(\tau,f)_{est}| \approx 1$), which may differ from the true nonwhite reflectivity apparently. If some relevant regional well log information is available, we can conduct color correction to the Gabor deconvolution.

Suppose that $R_G^{'}(\tau,f)$ is the Gabor transform of the nonwhite reflectivity $r_c(t)$ calculated from a well log, and $\overline{\left|R_G^{'}(\tau,f)\right|}$ is the corresponding smoothed amplitude spectrum. The Gabor deconvolution operator with color correction can be formulated as (Cheng and Margrave, 2009a)

$$D_c(\tau,f) = \frac{\overline{|R_G'(\tau,f)|}}{\overline{|S_G(\tau,f)|}+\mu A_{max}} e^{j\varphi_c(\tau,f)}, \tag{4.23}$$

where μ is the stability factor, A_{max} is the maximum value of $\overline{|S_G(\tau,f)|}$, and the phase $\varphi_c(\tau,f)$ is given by the Hilbert transform (over frequency),

$$\varphi_c(\tau,f) = H(\ln|\frac{\overline{|R_G'(\tau,f)|}}{\overline{|S_G(\tau,f)|}+\mu A_{max}}|). \tag{4.24}$$

The estimation of nonwhite reflectivity can be expressed in Gabor domain as

$$R'_G(\tau,f)_{est} = \frac{S_G(\tau,f)\overline{|R_G'(\tau,f)|}}{\overline{|S_G(\tau,f)|}+\mu A_{max}} e^{j\varphi(\tau,f)}. \tag{4.25}$$

While equation (4.25) uses well log information to estimate the non-white reflectivity, what we need is only a smoothed Gabor amplitude spectrum. Neither detail nor phase information is needed. It is quite likely that this required well information is a very slowly

changing function of position so that wells that are quite distant can still be used for color correction to conventional Gabor deconvolution.

The estimated result with the white reflectivity assumption can be viewed as a special case where $\overline{|R_G'(\tau,f)|}$ is nearly constant. When the real $\overline{|R_G'(\tau,f)|}$ has obvious amplitude fluctuations, a white-reflectivity estimation tends to enlarge some particular parts of reflectivity series, which correspond to the low amplitude areas of $\overline{|R_G'(\tau,f)|}$. In addition, the effect of color correction depends on how much $\overline{|R_G'(\tau,f)|}$ departs from unity or a constant and how reliable the employed $\overline{|R_G'(\tau,f)|}$ is, which, in turn, is subject to the available frequency band and completeness of well log information.

The key point of the correction method is that how to obtain an appropriate $\overline{|R_G'(\tau,f)|}$. If sufficient well log information is available, $r_c(t)$ and $s(t)$ nearly have the same length in time, which can be denoted by a time interval $[0, t_{max}]$. $\overline{|R_G'(\tau,f)|}$ can be directly obtained from the Gabor spectrum of $r_c(t)$. For this case, color correction can improve the reflectivity estimation effectively.

4.3.2 Practical consideration for the color correction method

In practice, the well log is usually incomplete and limited to some depth range, which corresponds to only a part of the whole seismic trace recorded at the surface. On this occasion, we need to use the limited well log to estimate a complete $\overline{|R_G'(\tau,f)|}$, which should be of the same size with $S_G(\tau,f)$ in time-frequency domain as indicated by equation (4.25). There may be different ways to achieve this. One way assumes that the color feature of nonwhite reflectivity is temporally stationary, i.e. $\overline{|R_G'(\tau,f)|}$ only changes with frequency f. Suppose that $r_c'(t)$ is the

incomplete reflectivity series with a time interval $[t_1, t_2]$ ($0 < t_1 < t_2 < t_{max}$), and its' Fourier spectrum is $\acute{R}_c(f)$. Then, $\overline{|R_G^{'}(\tau, f)|}$ can be approximated by a smoothed version of $\acute{R}_c(f)$. There are various ways to do the smoothing. In this chapter, we use a polynomial approximation approach. The order of the polynomial can be chosen manually as an input parameter for the correction method, and we use the polynomial approximation with highest order of 2 as example to introduce the approach. So, the spectrum of well-log reflectivity $\acute{R}_c(f)$ can be approximated as

$$|\acute{R}_c(f)| \approx a_0 + a_1 f + a_2 f^2, \tag{4.26}$$

where a_0, a_1 and a_2 are constants determined using a least-squares algorithm. So, $\overline{|R_G^{'}(\tau, f)|}$ can be modeled as

$$\overline{|R_G^{'}(\tau, f)|} = a_0 + a_1 f + a_2 f^2. \tag{4.27}$$

As an alternative, another way derives $\overline{|R_G^{'}(\tau, f)|}$ from the Gabor spectrum, $\acute{R}_G(\tau, f)$ of the incomplete reflectivity $\acute{r_c}(t)$, based on an assumption that the color feature of nonwhite reflectivity is slowly time-variant. First, $\acute{R}_G(\tau, f)$ is smoothed as

$$|\acute{R}_G(\tau, f)| \approx a_0'(\tau) + a_1'(\tau) f + a_2'(\tau) f^2, \ \tau \in [t_1, t_2] \tag{4.28}$$

where $a_i'(\tau)$, $i = 1, 2, 3$, is a coefficient curve and limited to the interval $[t_1, t_2]$ because of the incompleteness of $\acute{r_c}(t)$. Then, $\overline{|R_G^{'}(\tau, f)|}$ can be expressed as

$$\overline{|R_G'(\tau, f)|} = a_0(\tau) + a_1(\tau) f + a_2(\tau) f^2, \ \tau \in [0, t_{max}], \tag{4.29}$$

where $a_i(\tau)$, $i = 1, 2, 3$, can be obtained as

$$a_i(\tau) = \begin{cases} a_i'(t_1), & 0 \le \tau \le t_1 \\ a_i'(\tau), & t_1 < \tau < t_2 \\ a_i'(t_2), & t_2 \le \tau \le t_{max} \end{cases} . \qquad (4.30)$$

When multiple well logs of the same region are available, we can take full advantage of all available information. First, the Gabor spectra of well-log reflectivities are smoothed using equation (4.28). So, we can get a set of coefficient curves. Then, $\overline{|R_G'(\tau, f)|}$ is still modeled by equation (4.29), while $a_i(\tau)$ is calculated by combining all the coefficient curves of each well log through interpolation and extrapolation. Through this approach, we can approximate the true $\overline{|R_G'(\tau, f)|}$ very well if the well logs are well distributed in time and the color feature of nonwhite reflectivity is not drastically time-variant.

4.3.3 Examples

A 0.85s long reflectivity series, calculated from a well log 14-09, is used to test the color correction method. Figure 4.11 shows the reflectivity series and its amplitude spectrum. There is an obvious roll-off in the amplitude spectrum from $0\,Hz$ to $100Hz$, which indicates that the reflectivity is not white. The Gabor amplitude spectrum of the reflectivity series is shown in Figure 4.12. The low amplitude zone around $0.5s$ is apparent, which demonstrates that the color feature of the nonwhite reflectivity is time-variant.

According to equation (4.16), a synthetic attenuated seismic trace was created by applying a forward Q filter to the nonwhite reflectivity, and then convolving the result with a source wavelet. For the examples in this section, the Q value is 50, and the source wavelet is a minimum phase wavelet with a dominant frequency of $40Hz$. Supposing that a complete well log is available and the effective frequency band for deconvolution is $10 - 150Hz$, a testing on color correction method, directly conducted according to equation (4.25), is shown in Figure

4.13. We can see that conventional Gabor deconvolution, with white reflectivity assumption, gave an obviously enlarged estimation from $0.5s$ to $0.8s$ compared to the true reflectivity series, which corresponds to the low magnitude area of the Gabor spectrum shown in Figure 4.12. With color correction, the estimated result is very close to the true reflectivity. With sufficient well log information and wide frequency band for deconvolution, such a case is ideal for applying color correction.

However, the available frequency band may be limited by the quality of seismic data in practice. Figure 4.14 and 4.15 show the results of the Gabor deconvolution with a frequency band of $10-100Hz$ and $10-60Hz$ respectively. As demonstrated by Figure 4.13, 4.14, and 4.15, the color correction method, even with complete well log information, gradually loses its advantage over conventional deconvolution method when the frequency band becomes increasingly limited.

In addition, the actual well log is usually recorded within some depth range and is incomplete compared with the seismic trace. Figure 4.16 shows a truncated part of the nonwhite reflectivity shown in Figure 4.11, its amplitude spectrum and the polynomial approximation of amplitude spectrum. Assuming the color feature of nonwhite reflectivity is stable, color correction was conducted using equation (4.25) and (4.27). The result is shown in Figure 4.17. For this case, color correction improved the estimation by addressing the nonwhite Fourier spectrum shown in Figure 4.16, for example, the estimated reflectivity series is obviously more accurate around 0.19s and 0.36s, but it still gives an enlarged estimation around 0.5s because the time-variant color feature is not honored. Taking the time-variant color feature of nonwhite reflectivity into account, the Gabor spectrum can be smoothed using equation (4.28). For the complete nonwhite reflectivity series, the coefficient curves for the polynomial approximation

with highest order of 2 are shown in Figure 4.18, in which the smooth curves indicate the color feature of nonwhite reflectivity is slowly time-variant. For the incomplete reflectivity series shown in Figure 4.16, the coefficient curves can be created using equation (4.30). The color correction method was applied using equation (4.25) and (4.29). Figure 4.19 shows the deconvolved results. We can see that the reflectivity series around 0.5s is estimated with better relative amplitudes compared with the result in Figure 4.17, which is due to the partially addressing of the time-variant color feature.

When multiple incomplete well logs of the same area are available, the coefficient curves can be obtained through interpolation and extrapolation. An example for this case is illustrated by Figure 4.20. The coefficient values for time interval $0.2s - 0.4s$ and $0.6s - 0.8s$ are obtained from two well logs using equation (4.28) respectively. Then, the coefficient values for other time intervals are obtained through interpolation and constant extrapolation. After modeling the Gabor spectrum of the nonwhite reflectivity, the color correction is applied according to equation (4.25), whose results are shown in Figure 4.21. We can see that the deconvolved trace with color correction matches the true reflectivity well, because the time-variant feature of the nonwhite reflectivity is addressed with sufficient accuracy.

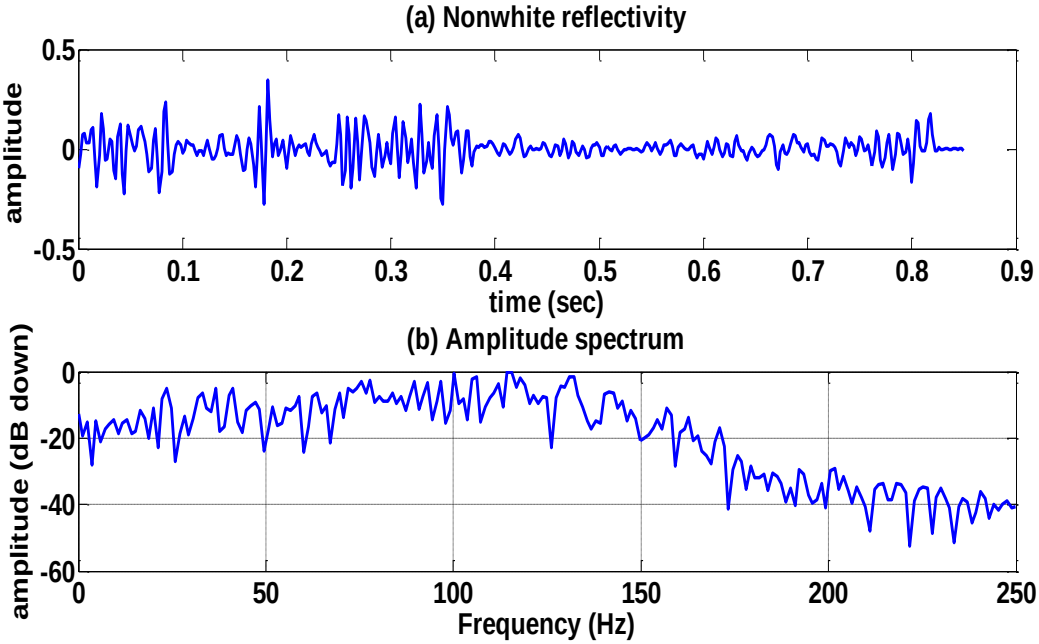

Figure 4.11. (a) Nonwhite reflectivity calculated from well log 14-09. (b) The amplitude Fourier spectrum of nonwhite reflectivity.

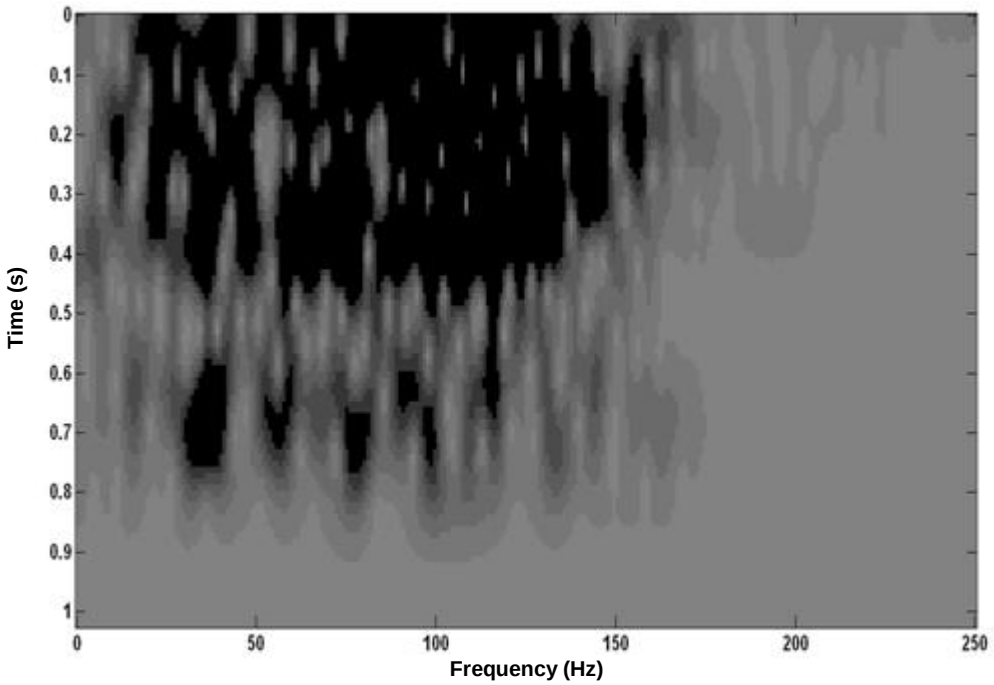

Figure 4.12. Amplitude Gabor spectrum of the nonwhite reflectivity shown in Figure 4.11.

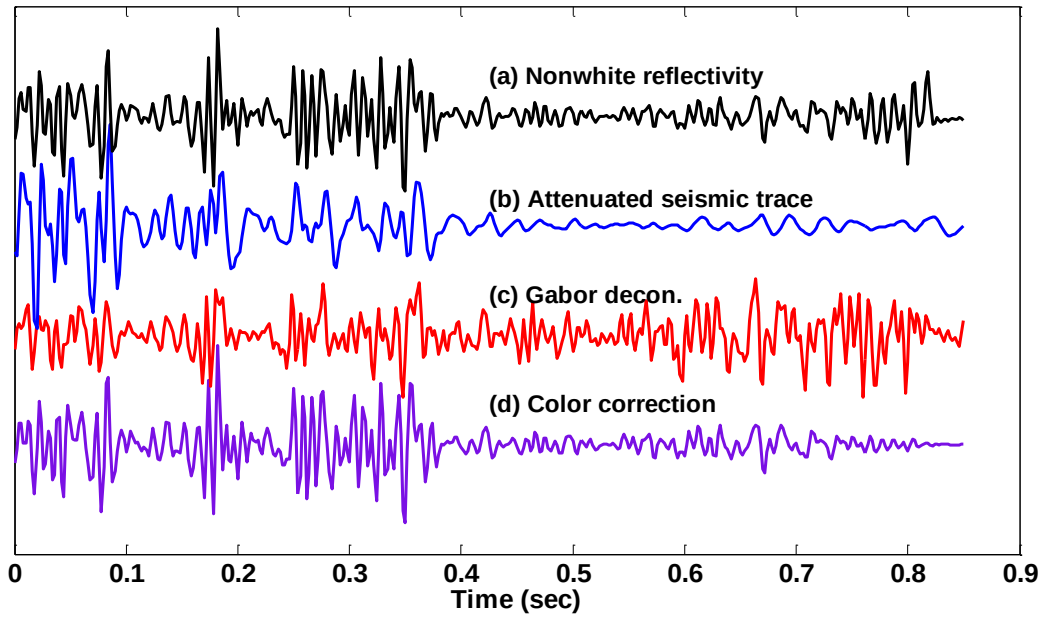

Figure 4.13. Gabor deconvolution with a frequency band of $10Hz - 150Hz$. (a) Non-white reflectivity. (b) Synthetic attenuated trace. (c) Gabor deconvolved trace without color correction. (d) Gabor deconvolved trace with color correction using a complete reference well log.

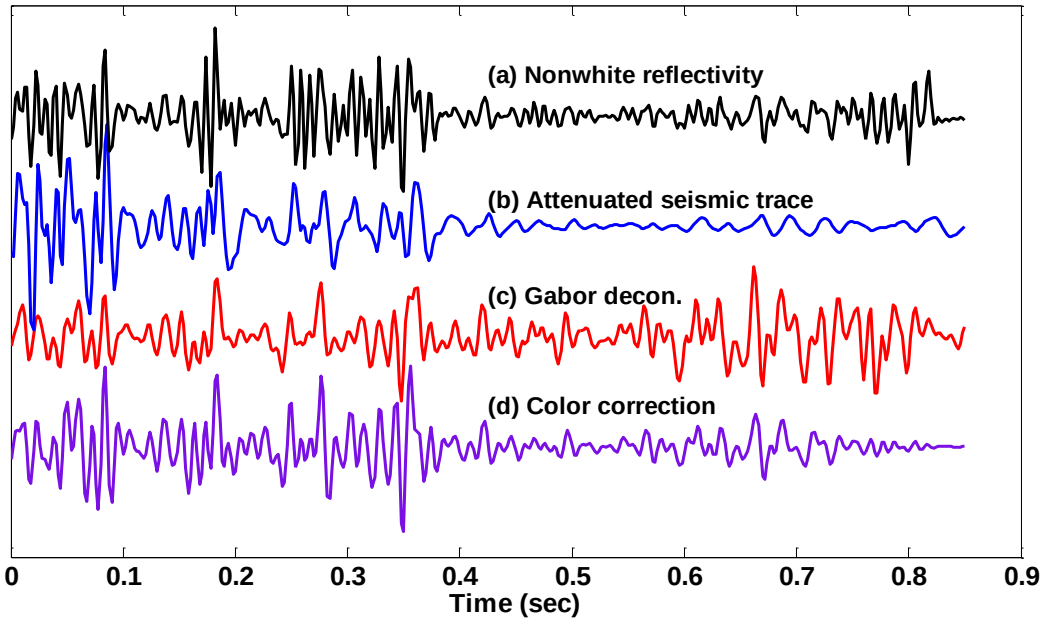

Figure 4.14. Gabor deconvolution with a frequency band of $10Hz - 100Hz$. (a) Nonwhite reflectivity. (b) Synthetic attenuated trace. (c) Gabor deconvolved trace without color correction. (d) Gabor deconvolved trace with color correction using a complete reference well log.

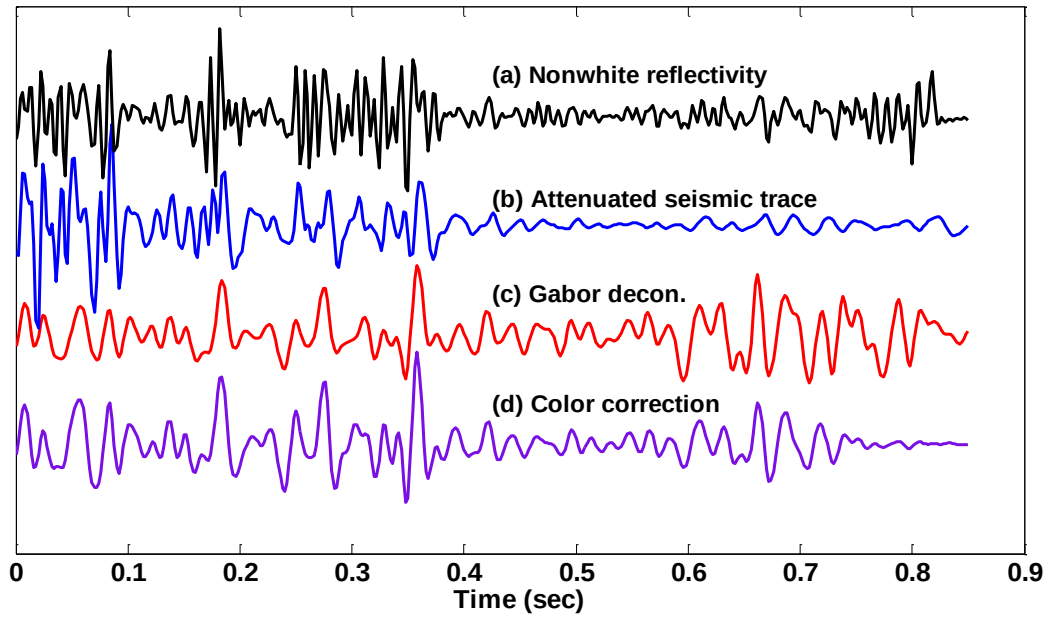

Figure 4.15. Gabor deconvolution with a frequency band of $10Hz - 60Hz$. (a) Nonwhite reflectivity. (b) Synthetic attenuated trace. (c) Gabor deconvolved trace without color correction. (d) Gabor deconvolved trace with color correction using a complete well log.

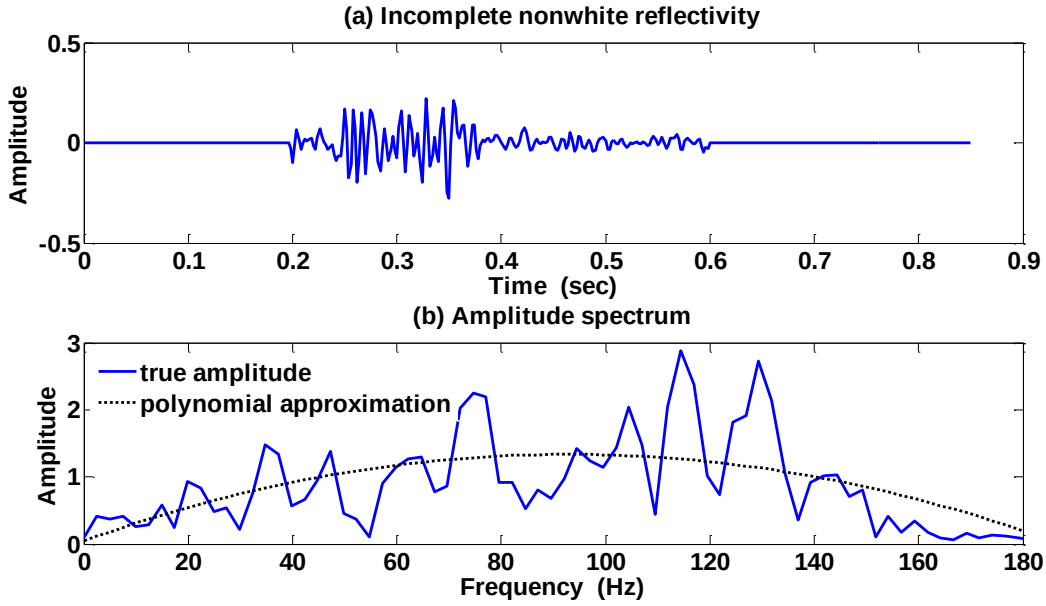

Figure 4.16. (a) Incomplete nonwhite reflectivity: the $0.2s - 0.6s$ part of the reflectivity series shown in Figure 4.11. (b) The amplitude spectrum of the incomplete reflectivity and its polynomial approximation with highest order of 2.

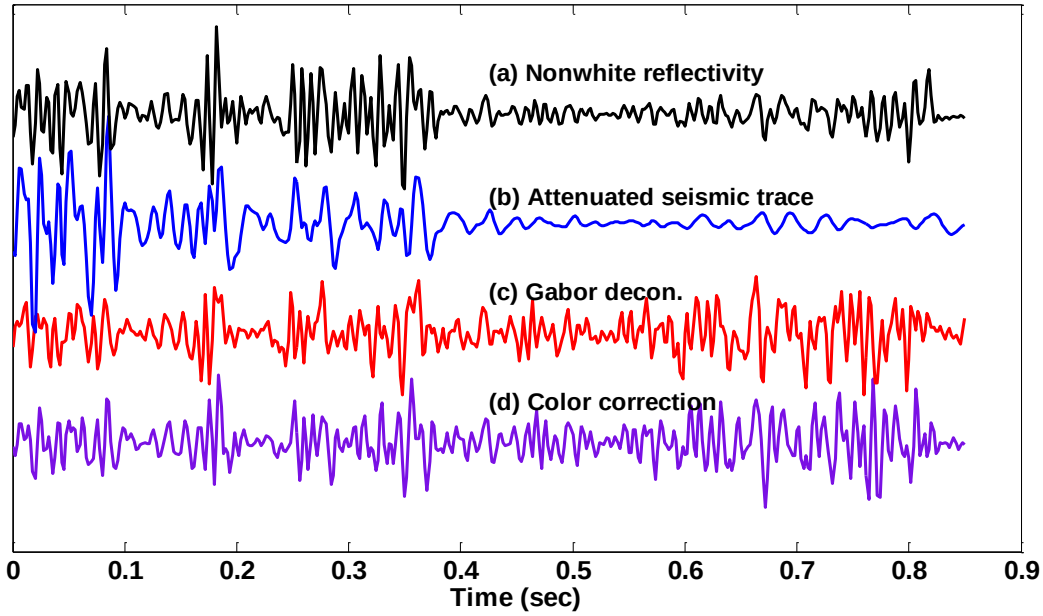

Figure 4.17. Color correction using single incomplete well log shown in Figure 4.16. (a) Nonwhite reflectivity. (b) Synthetic attenuated trace. (c) Gabor deconvolved trace. (d) Gabor deconvolved trace with color correction using equation (4.25) and (4.27).

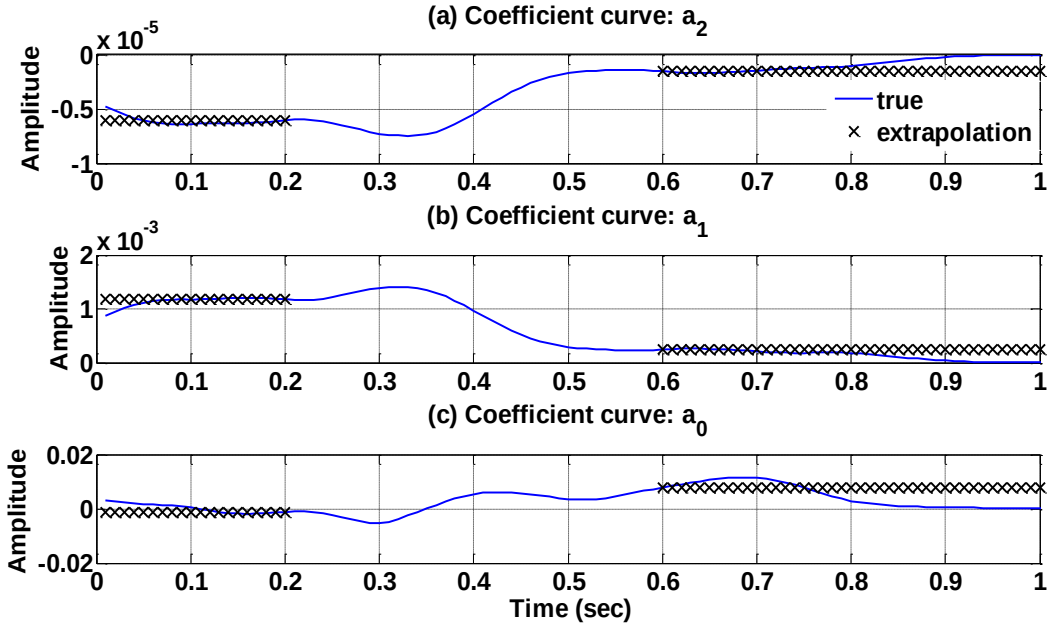

Figure 4.18. Coefficient curves for polynomial approximation of Gabor spectrum of the nonwhite reflectivity. (a) Coefficient curve $a_2(\tau)$. (b) Coefficient curve $a_1(\tau)$. (c) Coefficient curve $a_0(\tau)$.

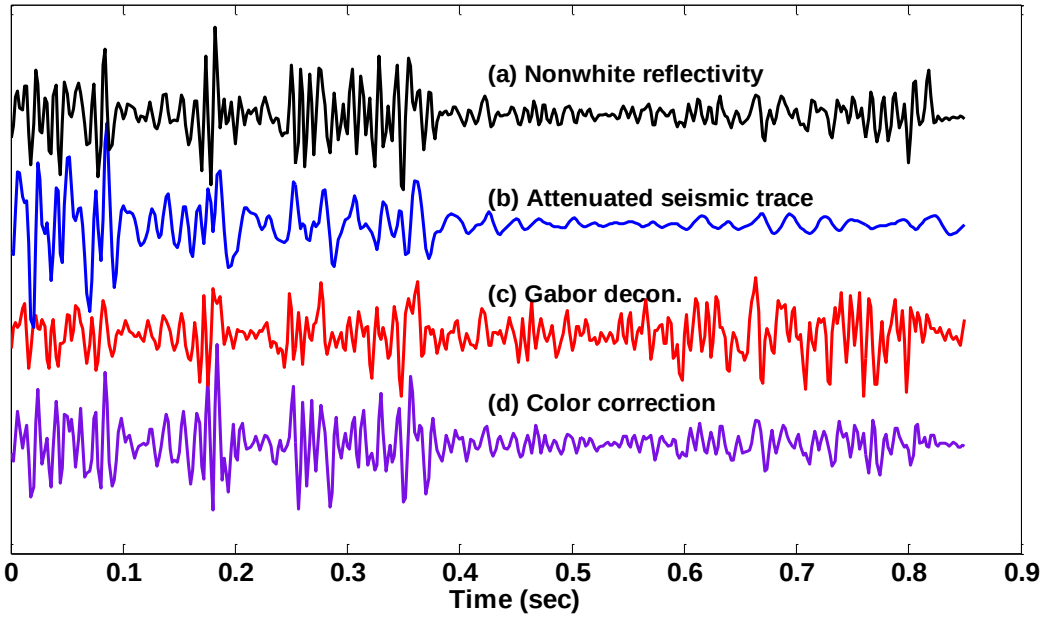

Figure 4.19. Color correction using single incomplete well log shown in Figure 4.16. (a) Nonwhite reflectivity. (b) Synthetic attenuated trace. (c) Gabor deconvolved trace without color correction. (d) Gabor deconvolved trace with color correction based equation (4.25) and (4.30).

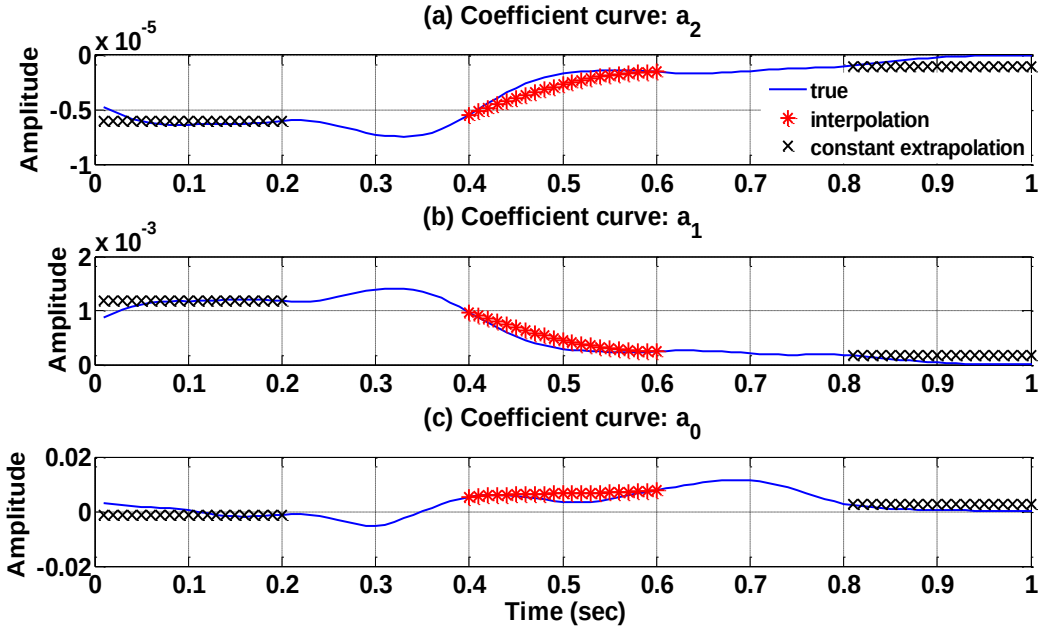

Figure 4.20. Calculation of coefficient curves for polynomial approximation of the Gabor spectrum of the nonwhite reflectivity using two incomplete reflectivity series (One is from 0.2s to 0.4s, the other is from 0.6s to 0.8s) (a) Coefficient curve $a_2(\tau)$. (b) Coefficient curve $a_1(\tau)$. (c) Coefficient curve $a_0(\tau)$.

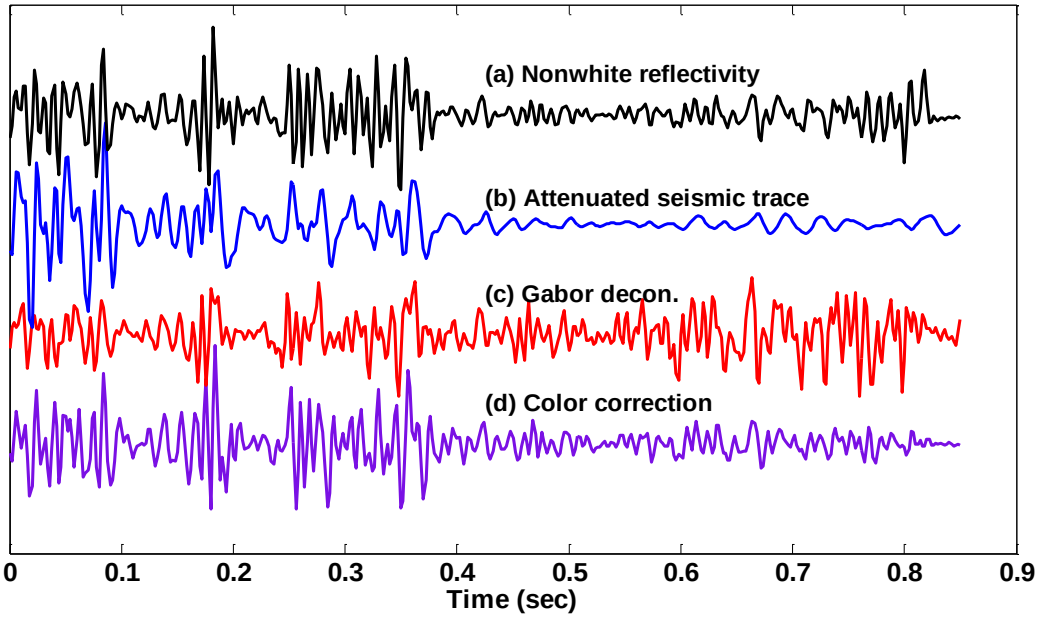

Figure 4.21. Color correction using multiple well logs. (a) Nonwhite reflectivity. (b) Synthetic attenuated trace. (c) Gabor deconvolved trace without color correction. (d) Gabor deconvolved trace with color correction; The coefficient curves shown in Figure 4.20 are used to build the Gabor spectrum of nonwhite reflectivity according to equation (4.30).

4.4 The influence of reflectivity color

4.4.1 Amplitude distortion and phase rotation

When the real $\overline{|R_G(\tau,f)|}$ demonstrates obvious spectral or temporal color feature, a white reflectivity estimation tends to have distorted relative amplitude and large phase rotation compared with true reflectivity. The relative amplitude can be revealed by comparing the envelopes of the estimated reflectivity and the true reflectivity calculated from well log. A simple way to roughly estimate the envelope of a signal $s(t)$ is formulated as

$$s_E(t) = \sqrt{s(t)^2 + s_H(t)^2}, \tag{4.31}$$

where $s_H(t)$ is the Hilbert transform of $s(t)$.

A definition of the nonstationary phase rotation was proposed by Cheng and Margrave (2009a) as following

$$s_\theta(t) = s(t)\cos(\theta(t)) + s_{\pi/2}(t)\sin(\theta(t)), \qquad (4.32)$$

where $\theta(t)$ is the time-variant phase rotation, $s_{\pi/2}(t)$ is the 90 degree phase rotated version of $s(t)$, and $s_\theta(t)$ is the nonstationary phase rotated version of $s(t)$. The time-variant phase rotation between two signal $s_1(t)$ and $s_2(t)$ can be measured through least-square analysis

$$\theta(t_i) = min \left\| \{\epsilon(\tau - t_i)s_1(\tau)\}_\theta - \epsilon(\tau - t_i)s_2(\tau) \right\|, \quad i = 1, 2, ..., \qquad (4.33)$$

where $\epsilon(\tau - t_i)$ is a window function center at t_i, $\{\epsilon(\tau - t_i)s_1(\tau)\}_\theta$ is a rotated version of $\epsilon(\tau - t_i)s_1(\tau)$ by a constant phase θ. Then, the nonstationary phase rotation can be removed based on equation (4.32). It should be pointed out that the phase rotation in equation (4.33) is measured with some time interval, which is usually larger than sampling rate. Then, to apply the phase rotation by equation (4.32), the phase term $\theta(t)$ for each sampling time can be obtained from $\theta(t_i)$ by interpolation.

The distortion of deconvolution result can be evaluated in term of amplitude distortion and phase rotation. The color feature of real reflectivity can be decomposed into temporal color and spectral color. Cheng and Margrave (2010) investigated the influence of reflectivity color on Gabor deconvolution. We will use some examples to reveal the relation between the color features and the distortion of reflectivity estimation.

4.4.2 Examples

The true reflectivity in Figure 4.11 was rotated by 60 degree, and the result is shown in Figure 4.22. Use these two reflectivity series to test the method of measuring nonstationary phased rotation as formulated by equation (4.33). The measured phase rotation is shown in Figure 4.23. We can see that the measurement is accurate with a relative error less than 1%.

The nonstationary phase rotation between the estimated reflectivity and true reflectivity is shown in Figure 4.24, which is measured in Gabor (Gaussian) windows using the reflectivity

series shown in Figure 4.13. The result of color correction has much smaller phase rotation compared with that of conventional Gabor deconvolution. To evaluate the definition of nonstationary phase rotation as equation (4.32), phase correction is applied to the estimated reflectivity in Gabor windows (method 1) and based on equation (4.32) (method 2) respectively. And then the remaining phase rotation with respect to true reflectivity is re-measured, which is shown in Figure 4.25. For the estimated results of deconvolution, phase correction can obtain better result for the case with color correction than those of conventional Gabor deconvolution, which may indicate that phase correction can achieve better results when the amplitude spectra of signals are close to each other. In addition, for phase correction, method 2 obtains a slightly better result compared with method 1, which means that the definition of nonstationary phase rotation as equation (4.32) is, to some degree, practical.

Figure 4.26 shows the envelopes of the estimated reflectivity and the true reflectivity. We can see that conventional Gabor deconvolution gives result with obviously distorted relative amplitude. With the application of color correction, amplitude distortion is mitigated.

To distinguish the influence of spectral color and temporal color on Gabor deconvolution, we separated these two color feature from the Gabor spectrum of the reflectivity. Figure 4.27 and 4.28 show the temporal color retrieved version and spectral color retrieved version of Figure 4.12 respectively. Color correction was applied using the spectral color and temporal color separately. The results are shown in Figure 4.29. The spectral color addressed estimation has similar waveform but distorted amplitude compared to the true reflectivity. The temporal color addressed estimation demonstrates close amplitude but different waveform compared to the true reflectivity. A comparison of the envelopes of the estimated reflectivity is shown in Figure 4.30 and Figure 4.31 displays the nonstationary phase rotation between the estimated reflectivity and

the true reflectivity. The results demonstrate that the spectral color is connected to large phase rotation while the temporal color is connected with amplitude distribution.

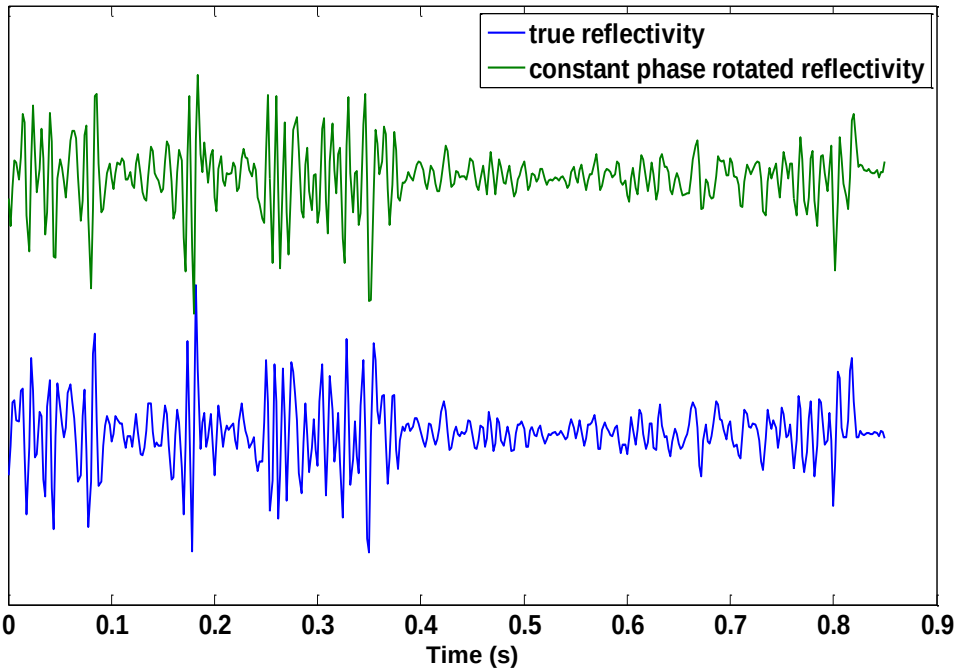

Figure 4.22. The true reflectivity series in Figure 4.11 and its 60 degree rotated version

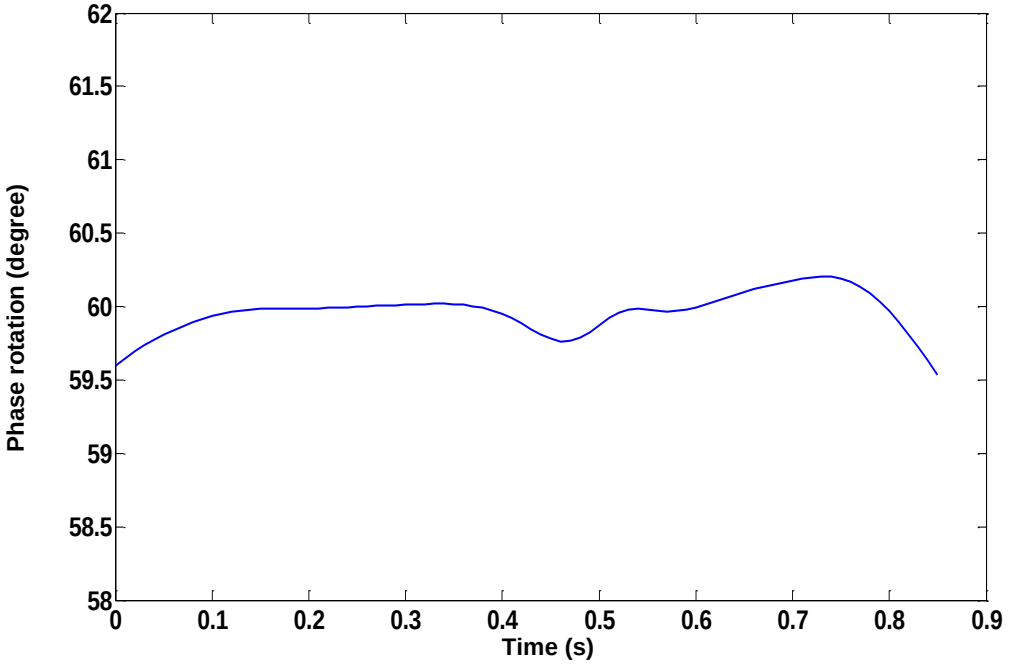

Figure 4.23. Phase rotation measurement for the two reflectivity series shown in Figure 4.22.

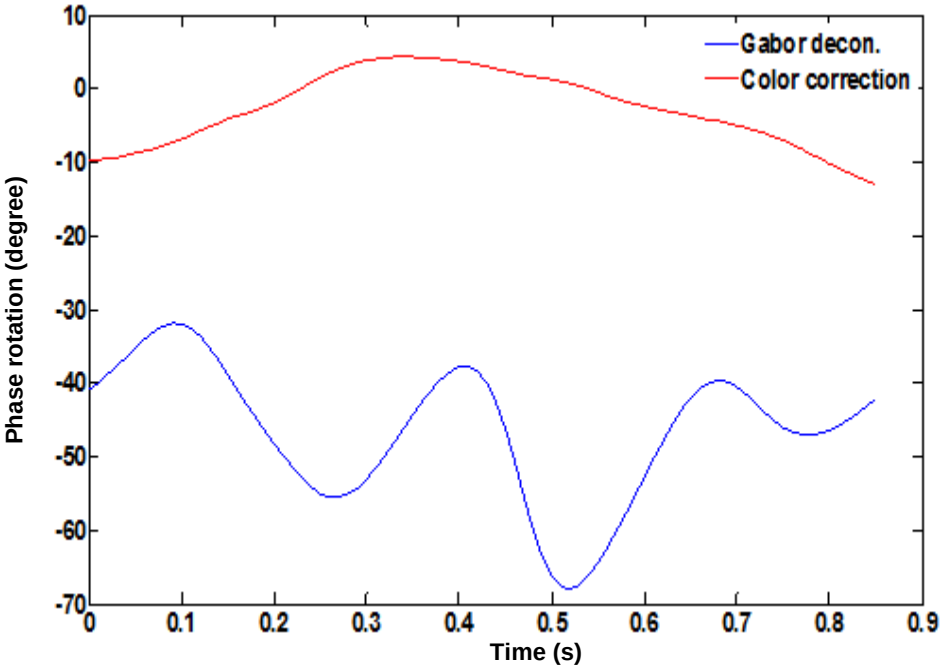

Figure 4.24. Nonstationary phase rotation of estimated reflectivity in Figure 4.13.

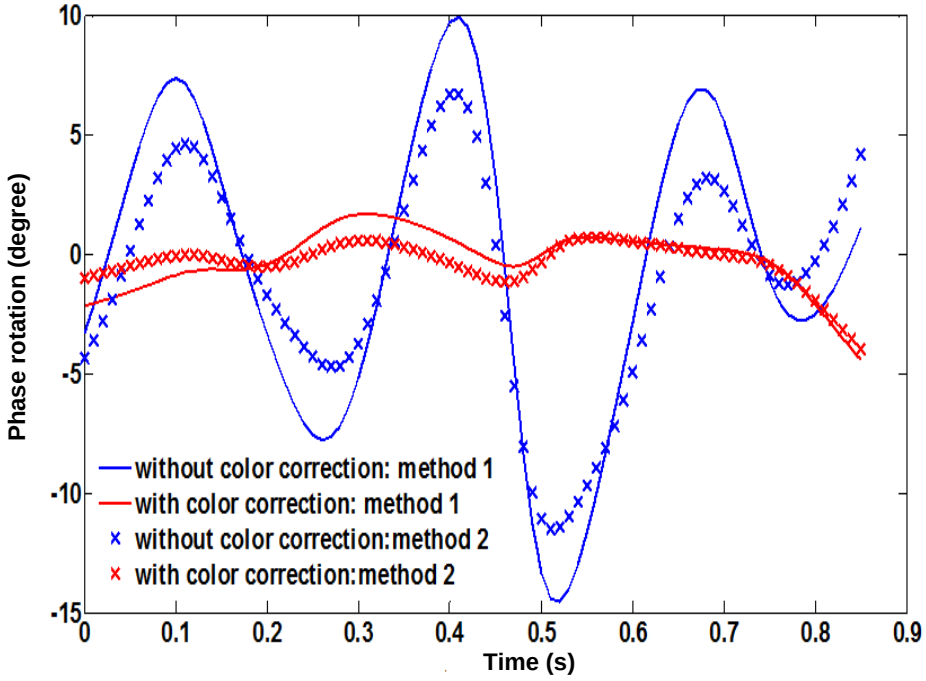

Figure 4.25. Remaining phase rotation after phase correction for the deconvolved results shown in Figure 4.13.

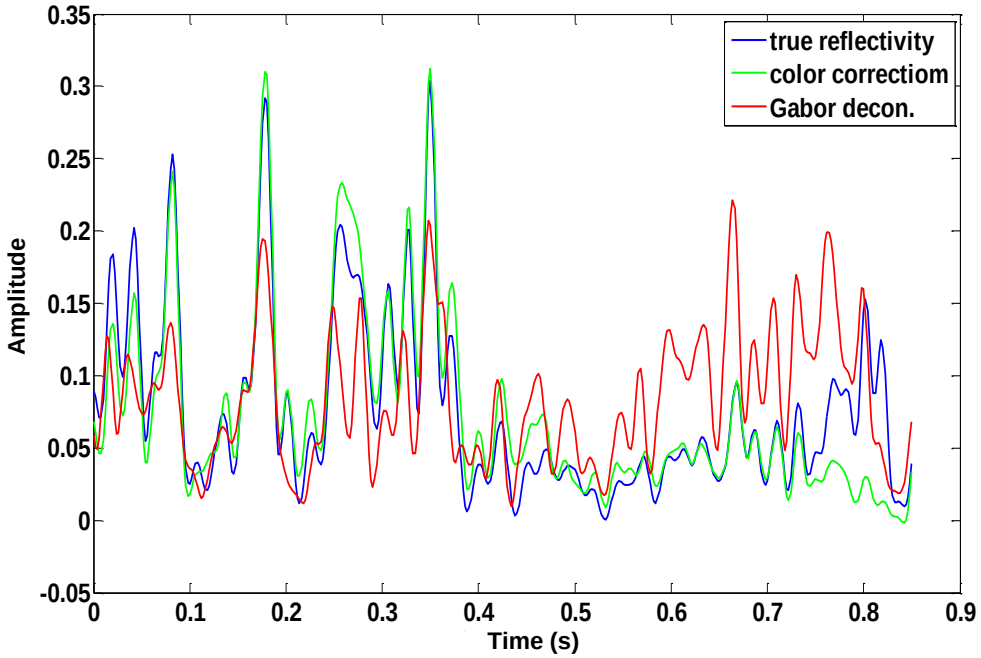

Figure 4.26. Envelopes of the reflectivity series shown in Figure 4.13.

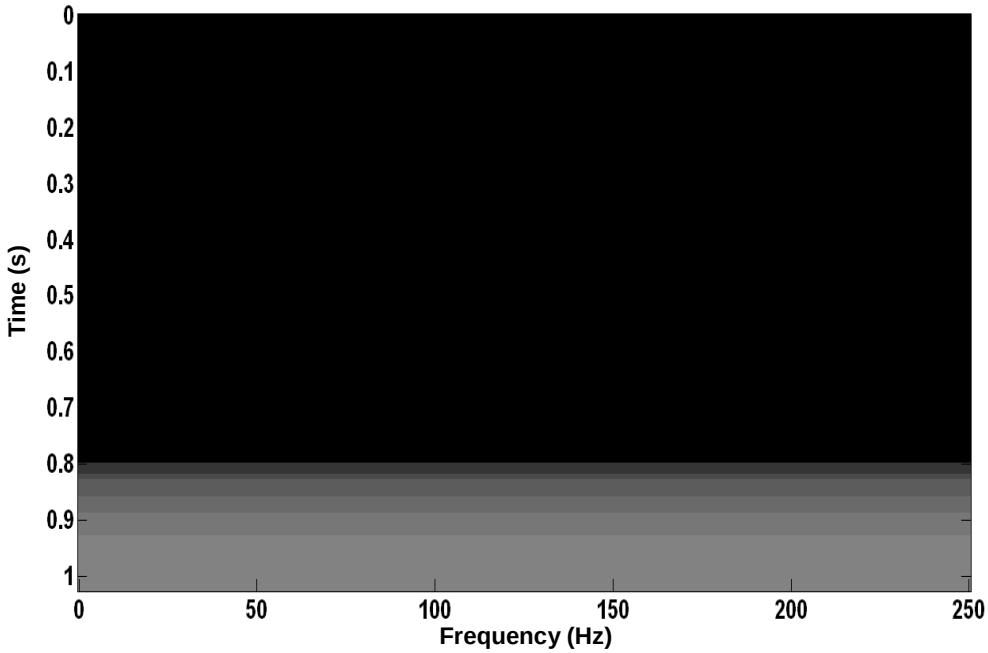

Figure 4.27. Temporal color of the Gabor spectrum shown in Figure 4.12.

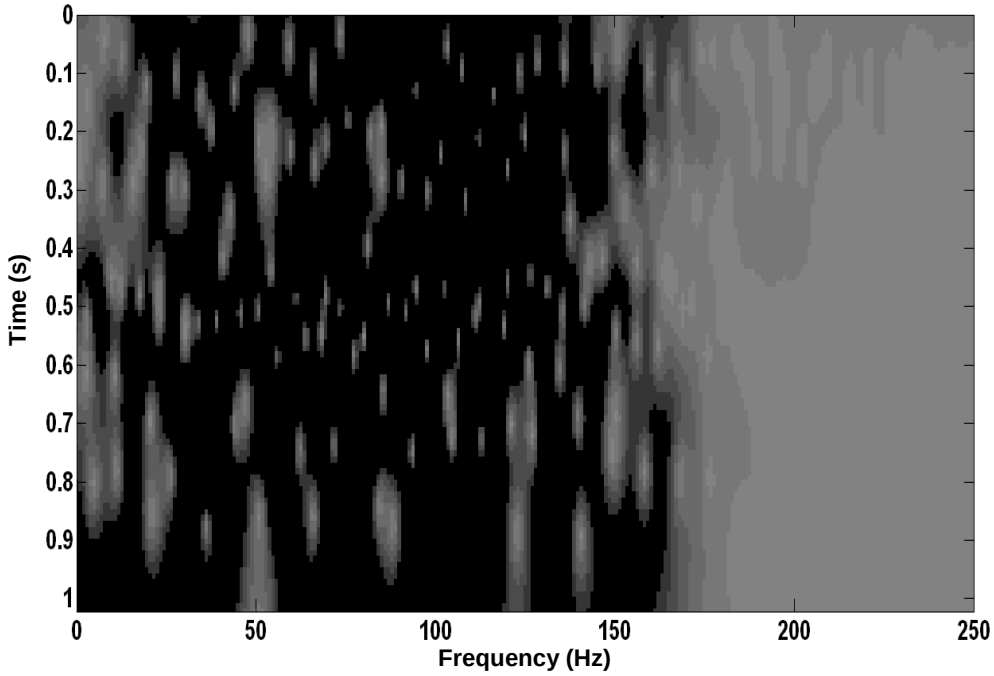

Figure. 4.28. Spectral color of the Gabor spectrum shown in Figure 4.12.

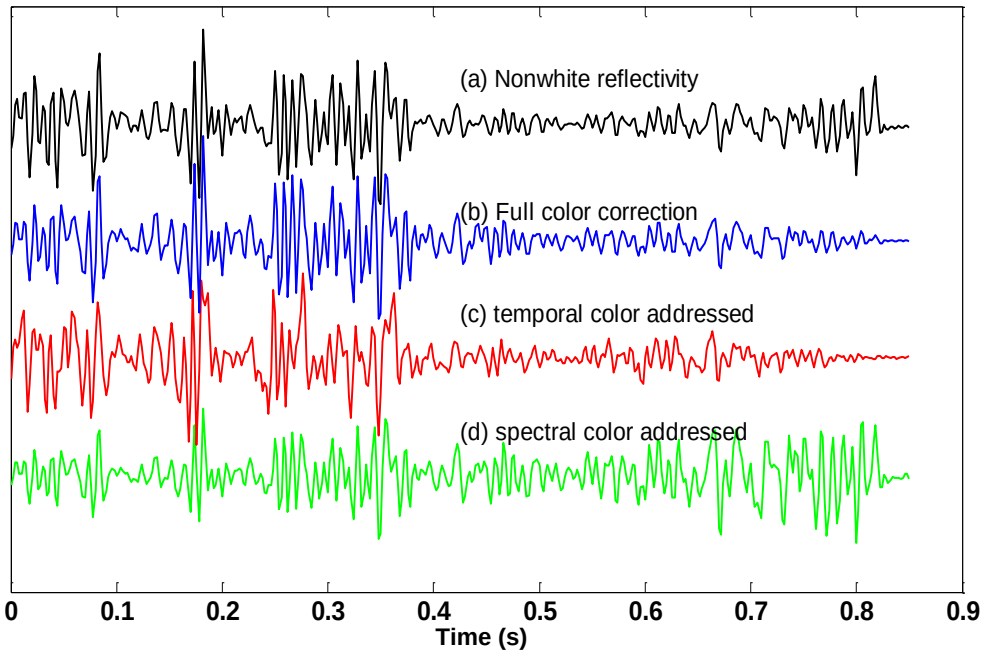

Figure 4.29. Reflectivity estimations: (a) true reflectivity; (b) full color correction estimation; (c) temporal color addressed estimation; (d) spectral color addressed estimation.

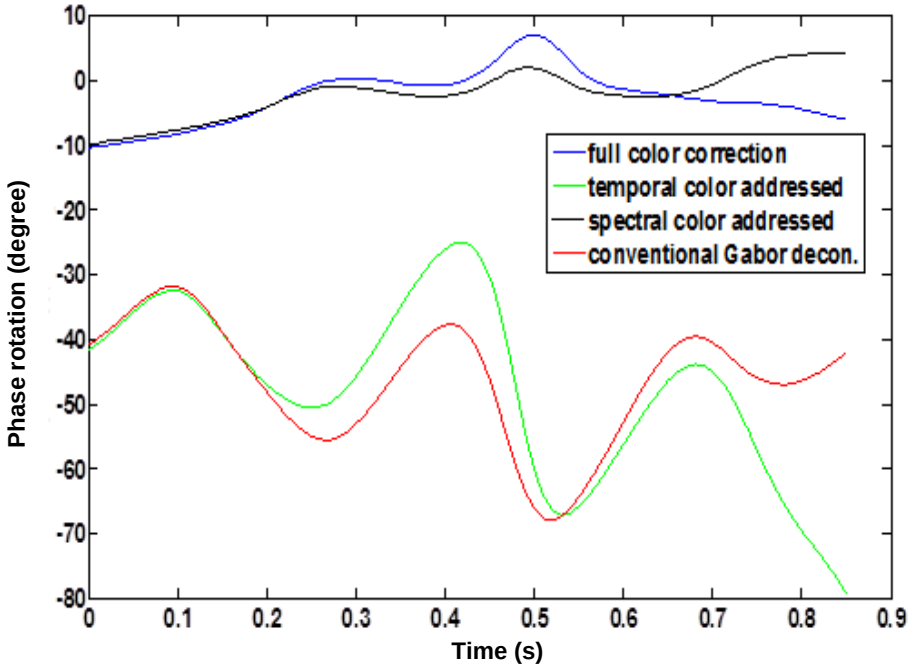

Figure 4.30. Phase rotation of reflectivity estimations shown in Figure 4.29.

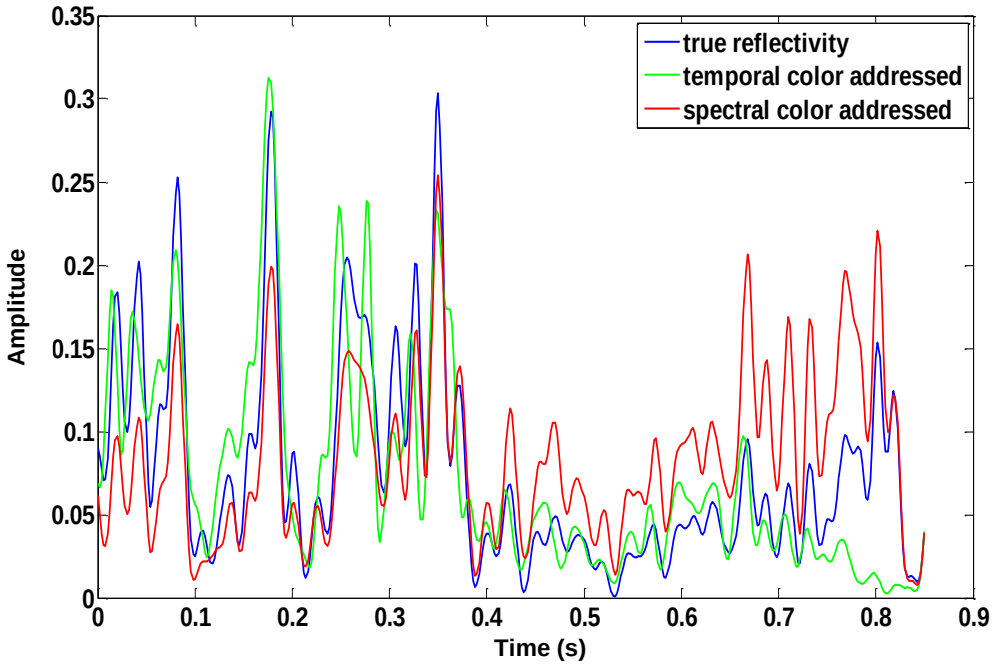

Figure 4.31. Envelopes of the reflectivity series shown in Figure 4.29.

4.5 Application of the color correction method to field data

The field data used to test our color correction method is a 2D seismic line with 159 shots and 151 receiver stations, which was acquired over Blackfoot field near Strathmore, Alberta in 1995. The reference well log is well 14-09 with a recorded depth range from $218m$ to about $1700m$, and which is about $600m$ away from the seismic line and can be projected to the seismic line using the X-Y coordinates.

The density log, P wave velocity log, computed reflectivity and synthetic seismic trace of well 14-09 are shown in Figure 4.32. Figure 4.33 shows the Gabor spectrum of the nonwhite reflectivity, whose amplitude depends on both time and frequency. Here an initial time shift of 210 was employed to align well log data to the field data, which was estimated based on the depth data, velocity data and correlation between synthetic seismic trace and the field data. In general, the true reflectivity calculated from well 14-09 has obvious spectral color and temporal color. As shown in Figure 4.34, the spectral color can be visualized on a normalized version with respect to time of the true Gabor spectrum. The temporal color roughly tells how the magnitude of localized reflectivity changes with time, as illustrated by Figure 4.35.

The spectral color correction is probably more of our interest from the point view of deconvolution due to its connection with phase rotation of the estimation result. The spectral color can be regarded as normalized color correction. Since the spectral color is not sensitive to the alignment error of well log to field data, spectral color correction may be preferable for prestack deconvolution. The spectral and temporal color correction can be a choice for poststack deconvolution. Henley et al (2010) gave a detailed description about the implementation of color correction to field data using ProMAX.

The Blackfoot seismic data was processed using ProMAX with a flow of static correction, geometric spreading correction, prestack Gabor decon (with or without color correction), NMO, stacking, poststack Gabor decon (with or without color correction), and Kirchhoff time migration. To align the well log roughly with the field data, an initial time of $210ms$, as mentioned previously, was applied to the well log data. For Gabor deconvolution case, both prestack and poststack deconvolution were conducted using conventional Gabor deconvolution. For spectral color correction case, both prestack and poststack deconvolution were conducted using Gabor deconvolution with spectral color correction. For the full color correction case, Gabor deconvolution with spectral color correction and Gabor deconvolution with full color correction were used for prestack deconvolution and poststack deconvolution respectively. The migrated seismic data for these three cases are shown as Figure 4.36, 4.37 and 4.38. To compare the above results, some zoomed parts are shown from Figure 4.39 to Figure 4.41. From Figure 4.40, we can observe the separated events at $820\ ms$ and $960ms$, which are not clear in Figure 4.39. Compared with Figure 4.40, there is a lower amplitude zone around $700ms$ in Figure 4.41, which corresponds to the low amplitude zone around 0.7s in Figure 4.35. A spectral analysis was conducted using the seismic data shown in Figure 4.36, 4.37 and 4.38. The average amplitude spectrum of the traces with CDP number from 50 to 250 and time range from $500ms$ to $1500ms$ was calculated, as shown in Figure 4.42. The seismic data with color correction applied has higher amplitude for those frequency components over $30Hz$. From the above comparison in time domain and frequency domain, we can see that spectral color correction strengthen the high frequency components of seismic data. Compared to spectral color correction, full color correction modifies the amplitude of the seismic trace according to well log information as well. To track the variation of frequency band of seismic data during the

data processing, using the spectral color correction case as an example, average amplitude spectra were calculated from seismic data after the implementation of prestack deconvolution, stacking, poststack deconvolution and migration. As shown in Figure 4.43, deconvolution whitens the seismic data to recover high frequency components, while stacking significantly de-whiten the spectrum of seismic data when it attenuates the noise. Kirchhoff migration, which can be regarded as stacking along the diffraction curves, slightly de-whitens the seismic data as well.

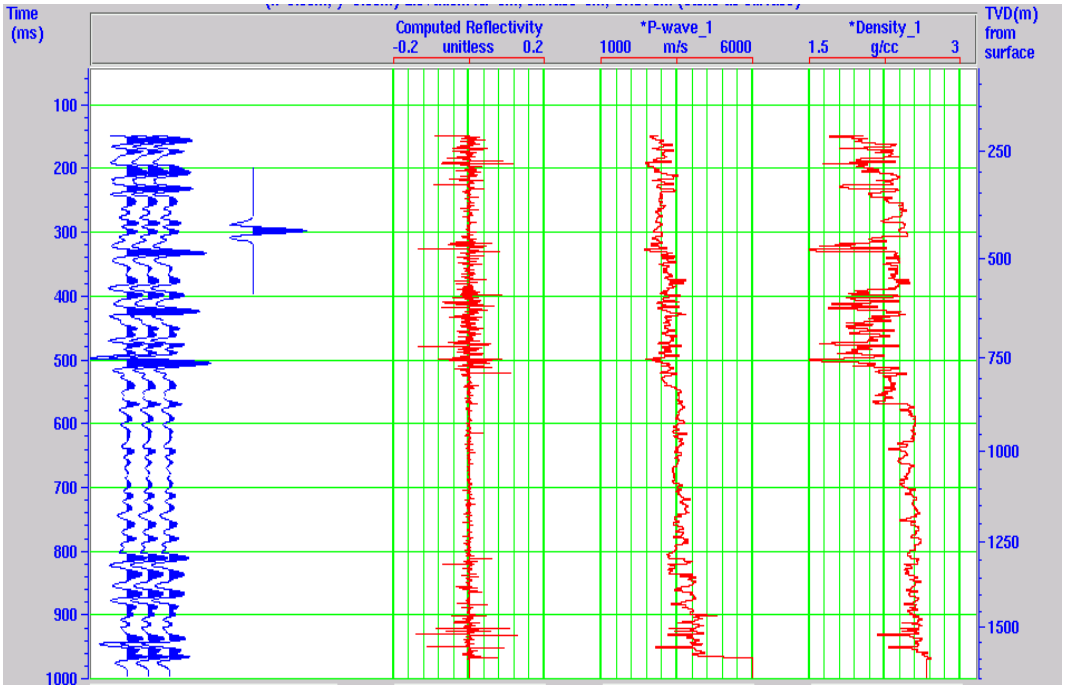

Figure 4.32. Well log 1409. From left to right: synthetic seismic trace, Ricker wavelet with a dominant frequency of $40Hz$, computed reflectivity, P wave velocity and density.

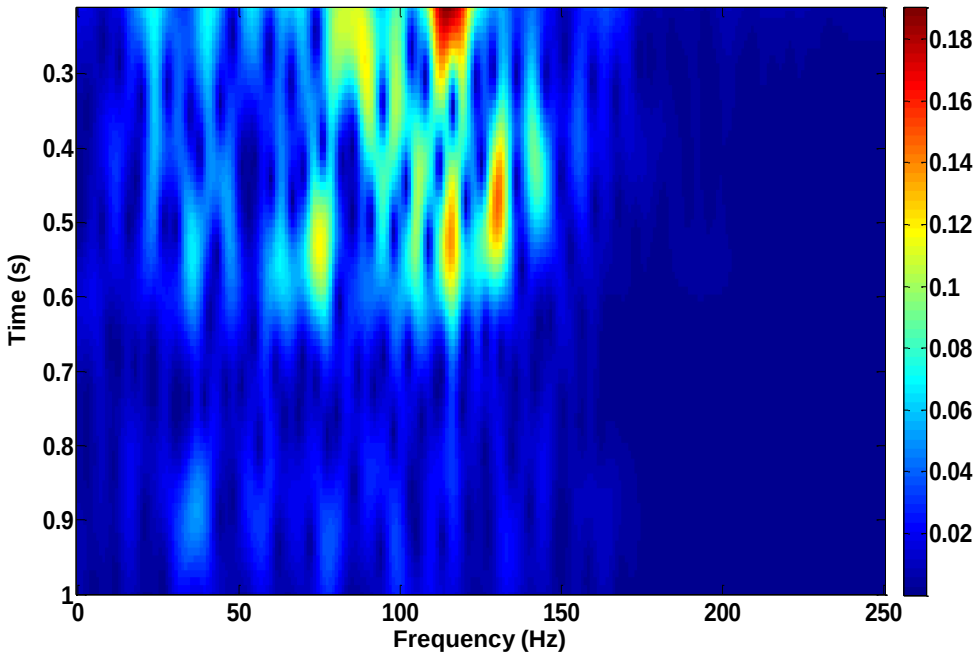

Figure 4.33. Gabor amplitude spectrum of the nonwhite reflectivity shown in Figure 4.32.

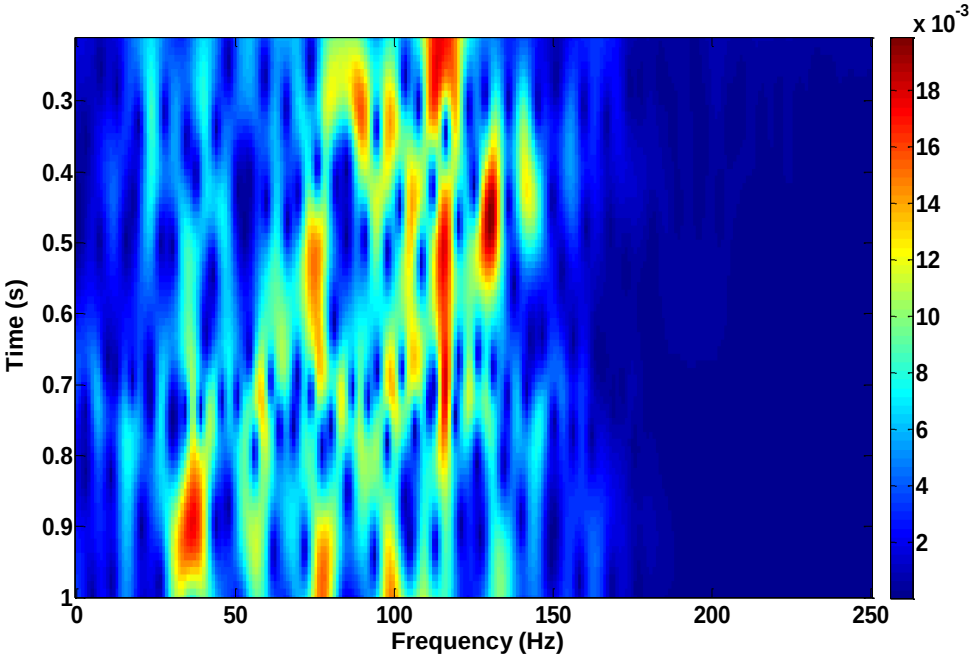

Figure 4.34. Similar to Figure 4.33 except that each constant-time row of the Gabor amplitude spectrum has been independently normalized to remove the temporal variation. This emphasizes the spectral color of the nonwhite reflectivity shown in Figure 4.32.

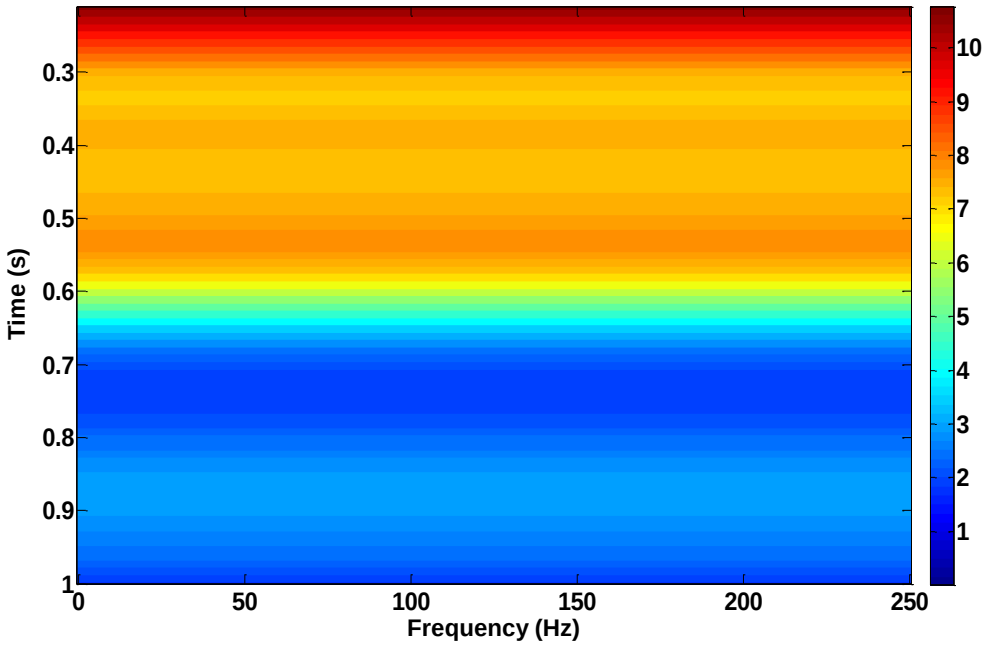

Figure 4.35. The temporal variation of the Gabor spectrum shown in Figure 4.33. This emphasizes the temporal color of the nonwhite reflectivity shown in Figure 4.32.

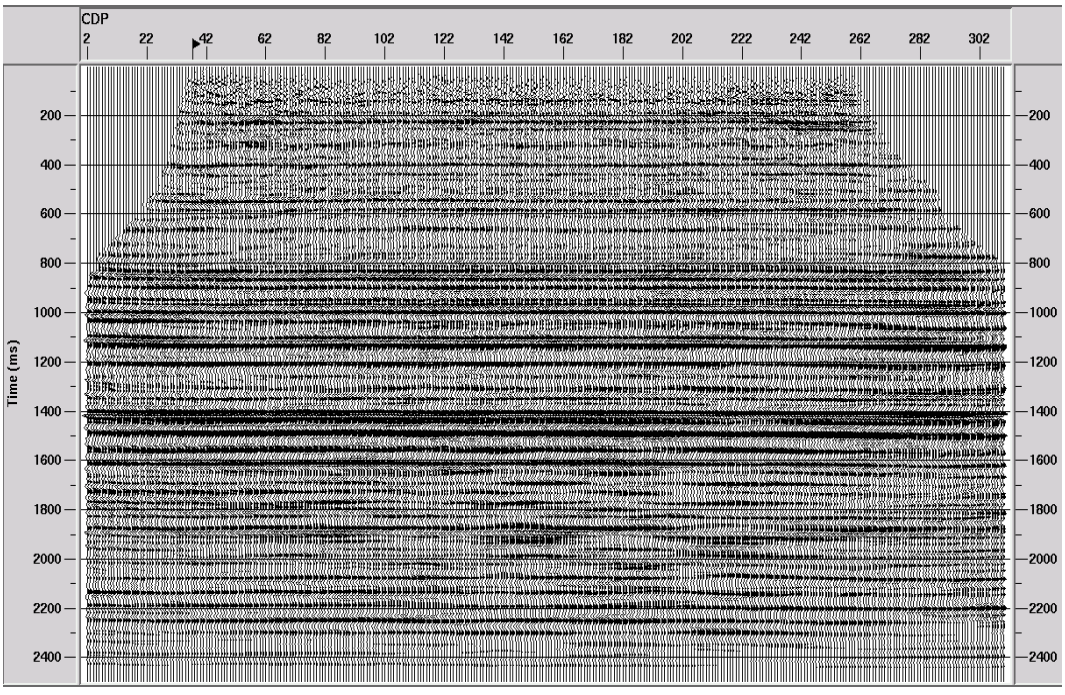

Figure 4.36. Migrated seismic data with Gabor deconvolution applied.

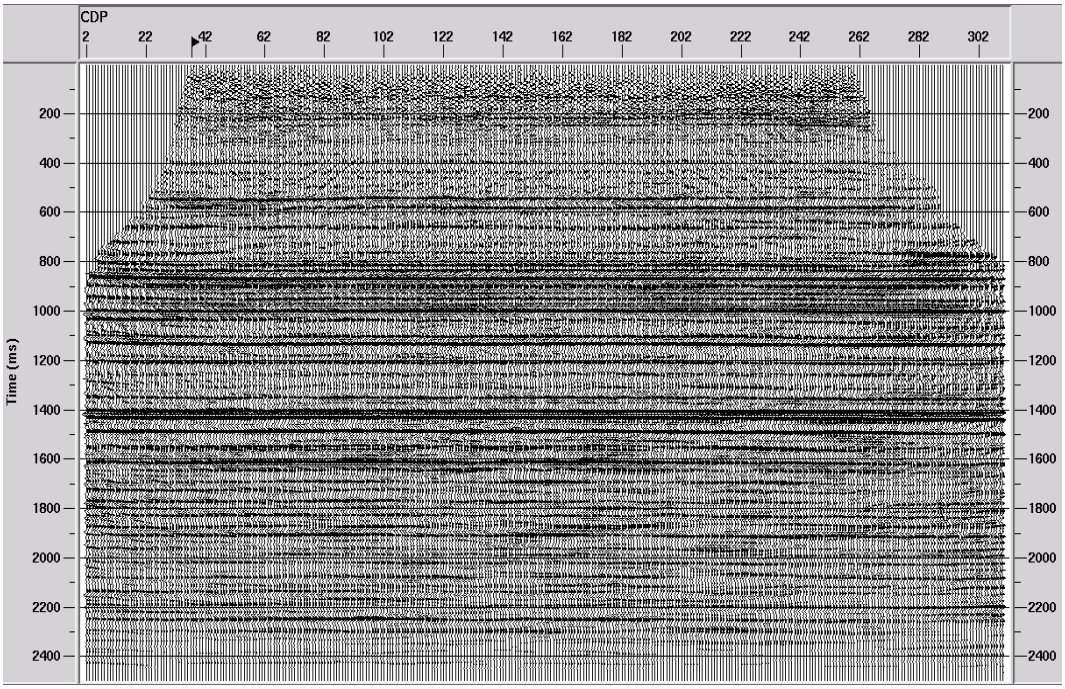

Figure 4.37. Migrated seismic data with spectral color correction applied.

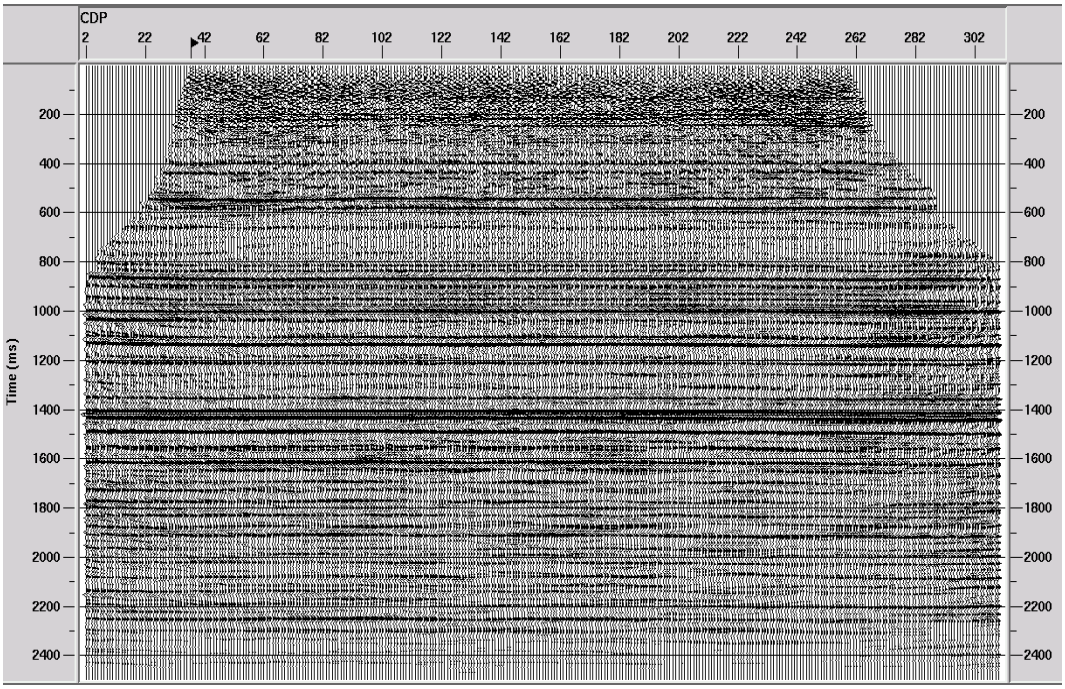

Figure 4.38. Migrated seismic section with full color correction applied.

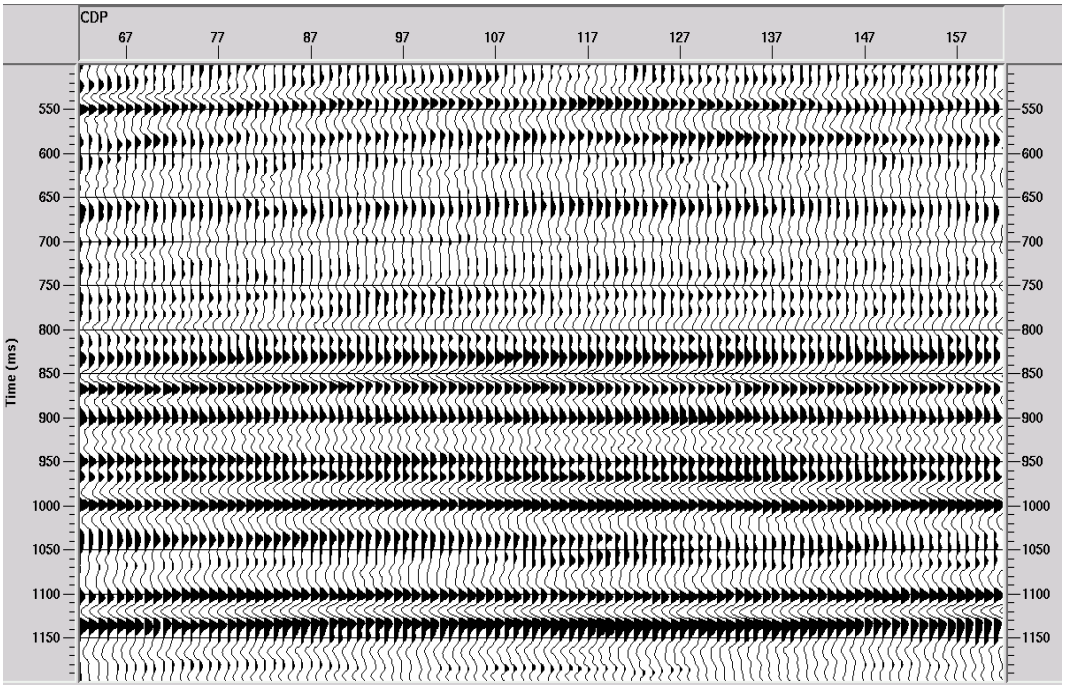

Figure 4.39. A zoomed part of the seismic data shown in Figure 4.36.

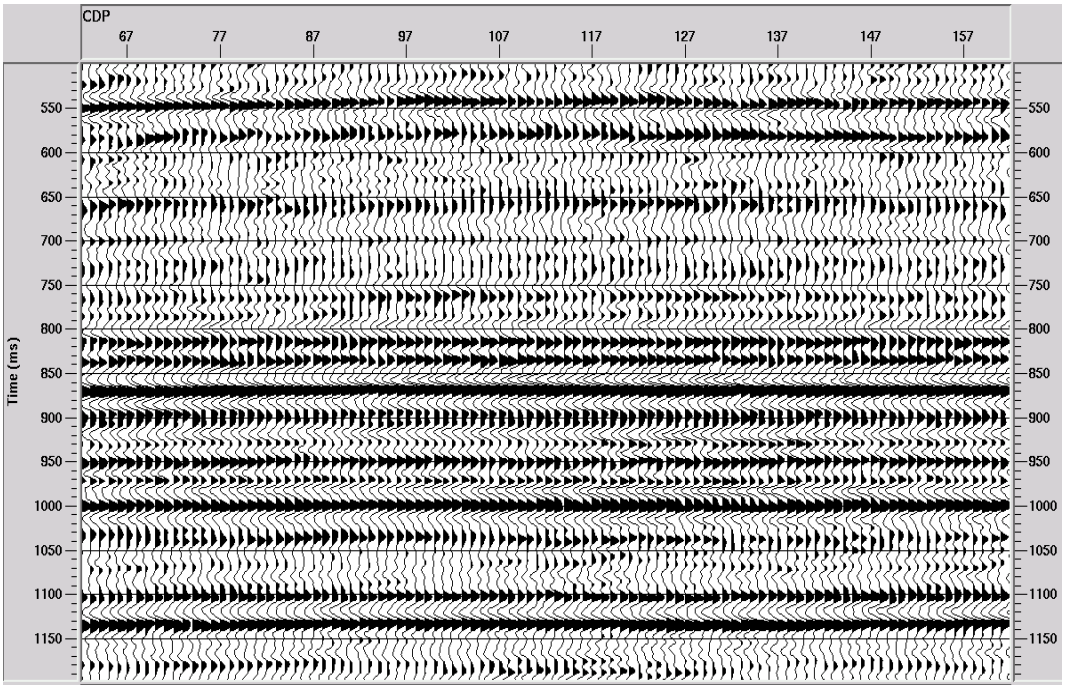

Figure 4.40. A zoomed part of the seismic data shown in Figure 4.37.

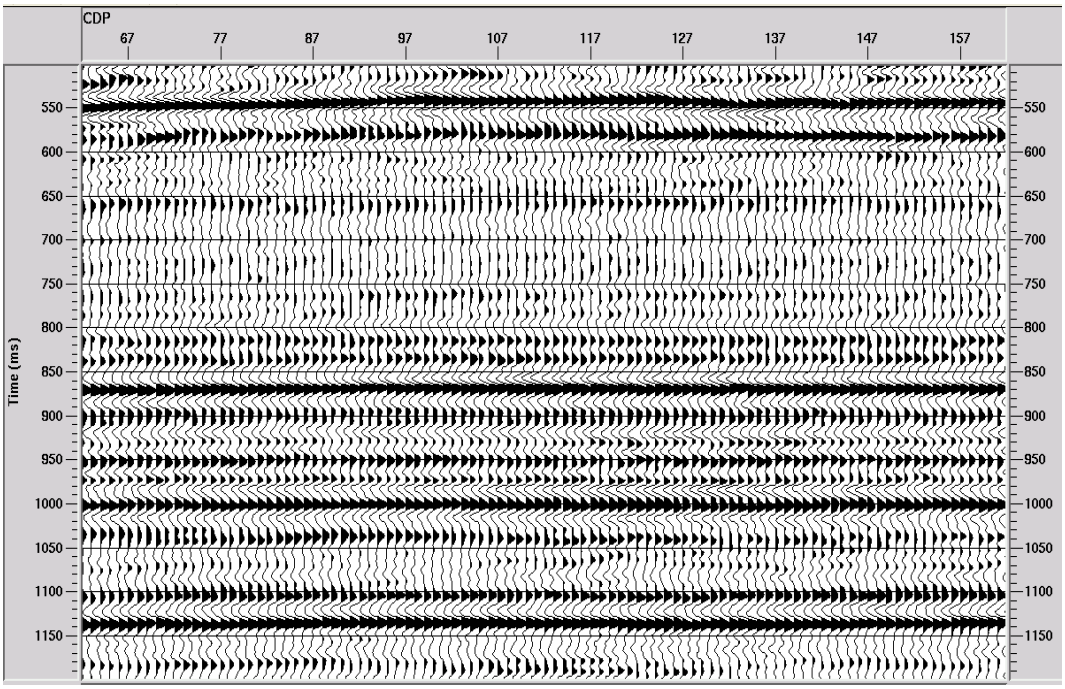

Figure 4.41. A zoomed part of the seismic data shown in Figure 4.38.

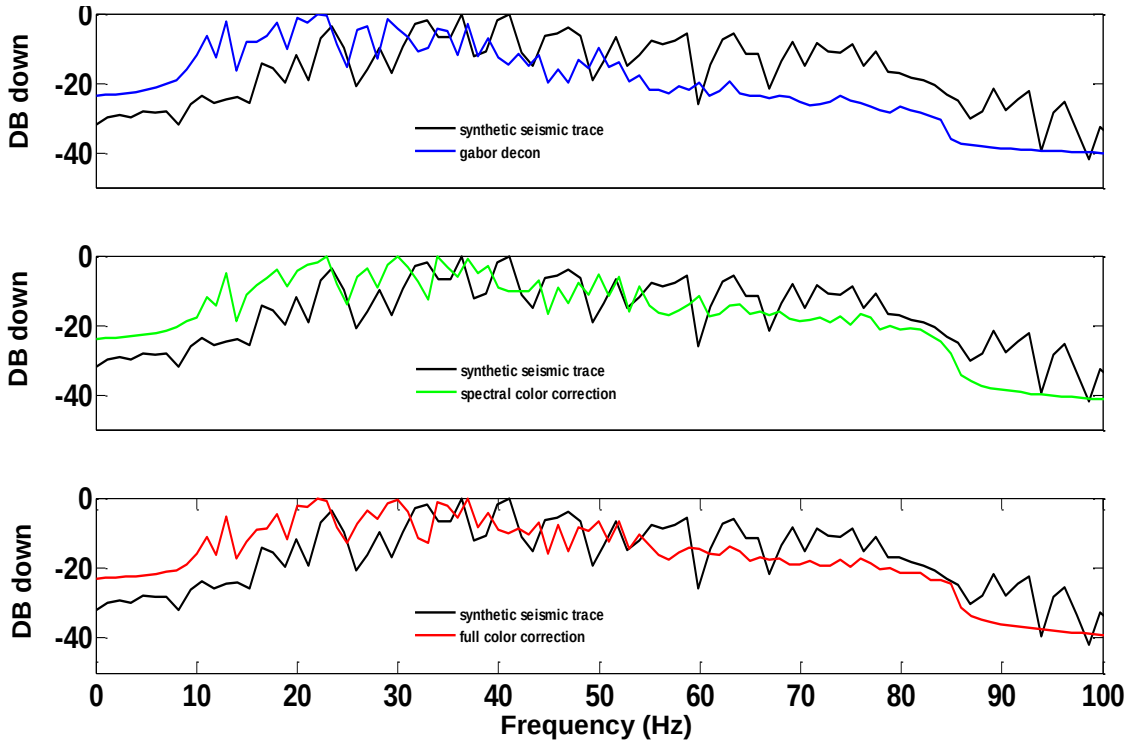

Figure 4.42. The average amplitude spectra of the seismic data (CDP 50-250, time: $500ms - 1500ms$) shown in Figure 4.36, 4.37 and 4.38 and the amplitude spectrum of synthetic seismic trace shown in Figure 4.32.

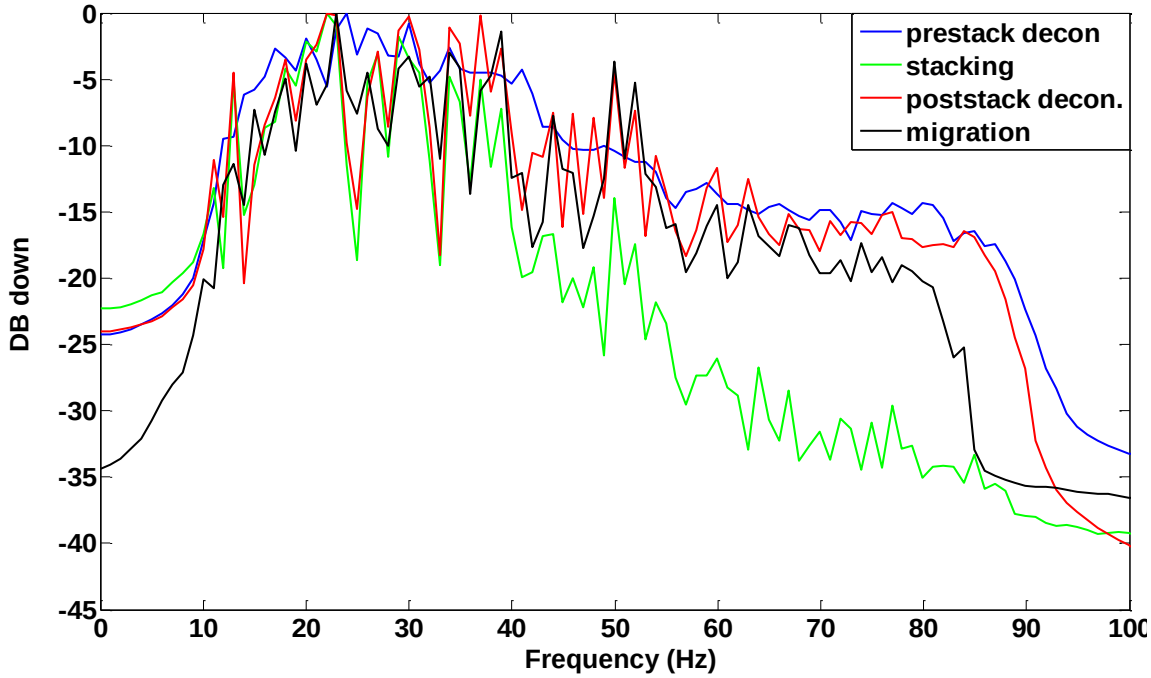

Figure 4.43. The average amplitude spectral of seismic data at different stage of data processing flow for the spectral color correction case. Blue: after prestack decon. (FFID: 7, CHAN 21-71, time: $800ms - 1800ms$); Green: after stacking (CDP 150-200, time: $500ms - 1500ms$); Red: after poststack decon. (CDP 150-200, time: $500ms - 1500ms$); Black: after Kirchhoff time migration (CDP 150-200, time: $500ms - 1500ms$).

Color correction enriches the high frequency components of seismic data. To verify whether such an effect enhances the data or boosts the noise, it is necessary to tie the migrated data to well log data. The target zone for the Blackfoot seismic data is around $1050ms$, which corresponds to the end the well log. Considering the near surface part the seismic data is highly contaminated by noise, we use the lower part of the well log to tie the seismic data. The lower part of the well log is shown as Figure 4.44. The synthetic seismic trace was created using Ricker wave with a dominant frequency of $40Hz$. In Figure 4.44, the last event of the synthetic seismic trace is generated by the single spike of the P wave velocity at the very end of well log, which usually is not real. So, we use the events from $750ms$ to $950ms$ to correlate with the migrated data. According to the X-Y coordinates of the well log location, the well log is mapped to the

seismic trace of CDP 37 that has nearly the same X coordinate. The correlation of the synthetic trace to the migrated seismic data is shown as Figure 4.45, 4.46 and 4.47. We can see that the spectral color correction and full color correction have similar results. With color correction applied, the seismic data has higher frequency components for the events around $920ms$ and $950ms$, all of which roughly match the synthetic seismic trace. For the correlation time range from $800ms$ to $1000ms$, the phase rotation between the migrated seismic traces and synthetic seismic trace was measured and shown in Figure 4.48. The phase rotation for the spectral color correction case and full color correction case is similar and comparable to the conventional Gabor deconvolution case. So, with color correction applied, seismic data has more high frequency components and roughly tie better to the well log data. In other words, color correction can improve the resolution of seismic data.

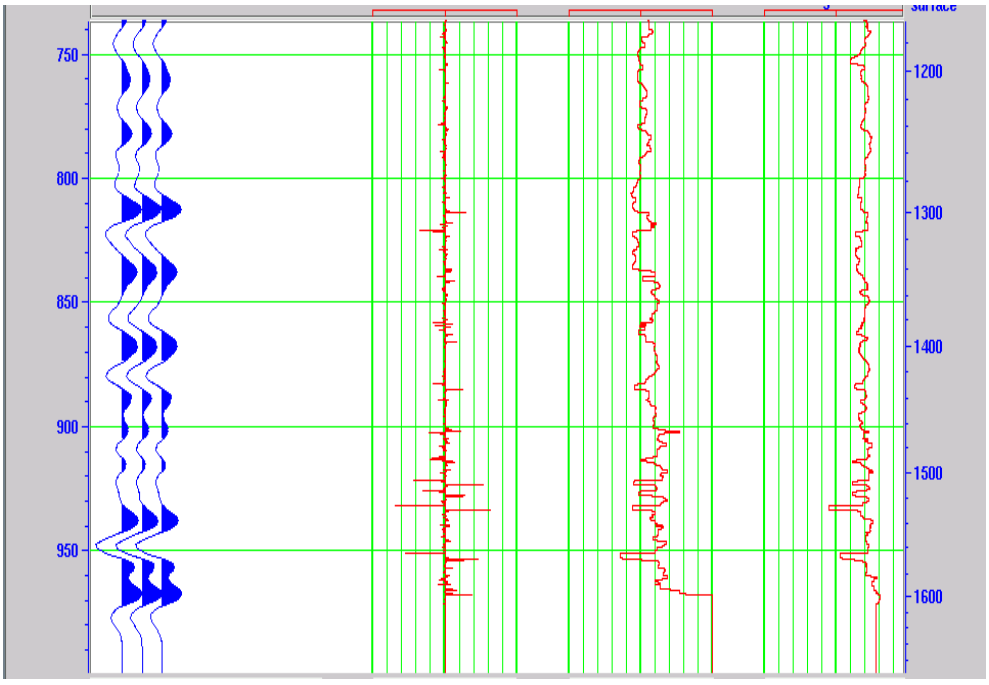

Figure 4.44. Lower part the well 14-09. From left to right: synthetic seismic trace, computed reflectivity, P wave velocity and density.

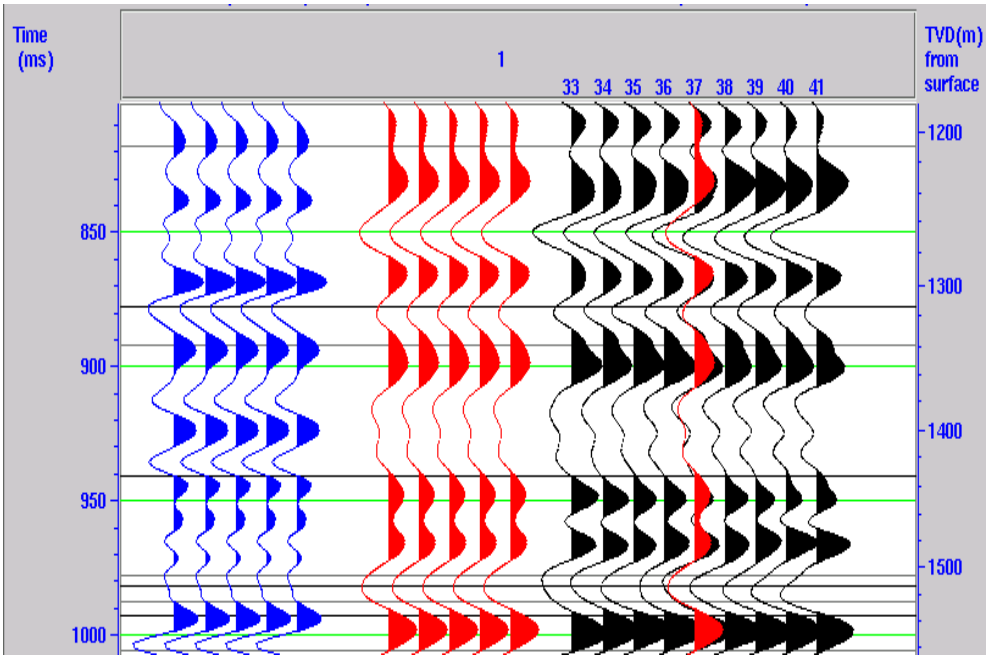

Figure 4.45. Correlation of synthetic seismic trace and migrated seismic data with Gabor decon. Blue: synthetic seismic trace; Red: migrated seismic trace with CDP 37; Black: migrated seismic traces around CDP 37.

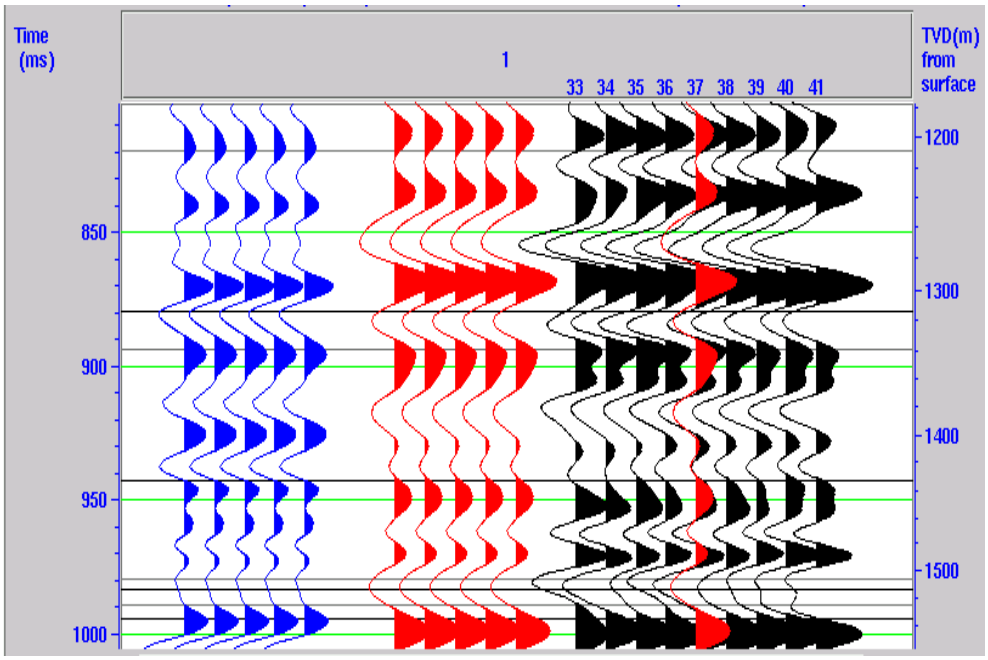

Figure 4.46. Correlation of synthetic seismic trace and migrated seismic data with spectral color correction. Blue: synthetic seismic trace; Red: migrated seismic trace with CDP 37; Black: migrated seismic traces around CDP 37.

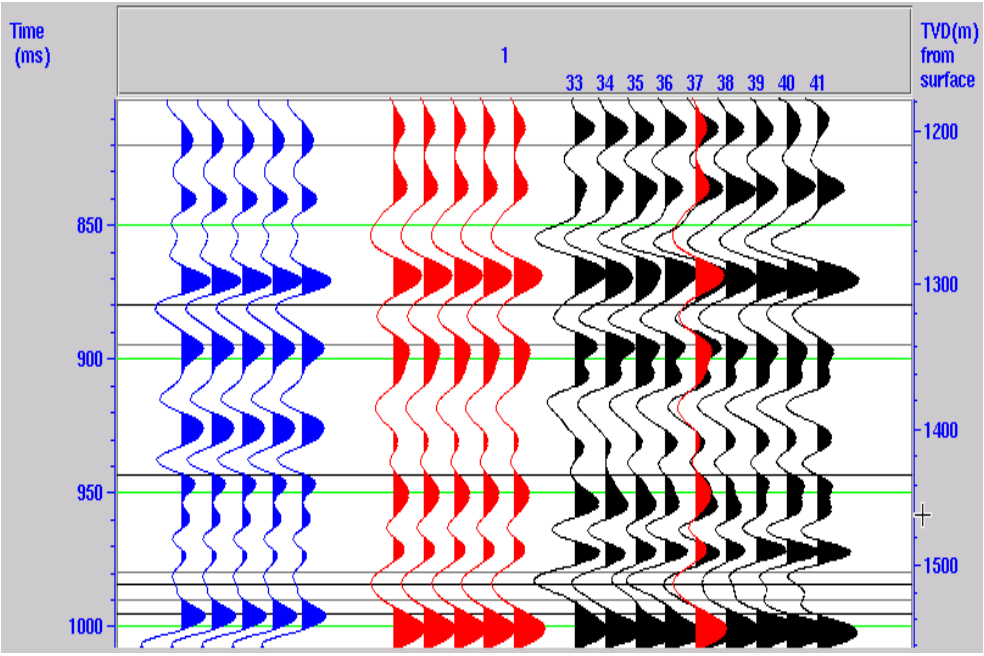

Figure 4.47. Correlation of synthetic seismic trace and migrated seismic data with full color correction. Blue: synthetic seismic trace; Red: migrated seismic trace with CDP 37; Black: migrated seismic traces around CDP 37.

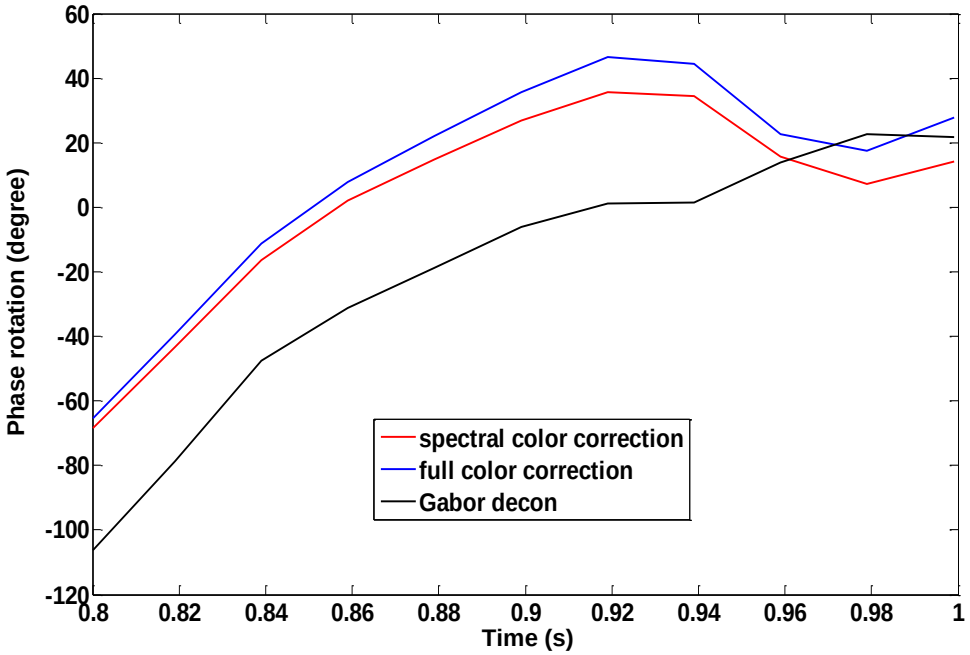

Figure 4.48. Phase rotation between synthetic seismic trace and migrated seismic trace of CDP 37 from $0.8s$ to $1s$.

4.6 Summary

The Gabor transform decomposes a signal into time-frequency domain by windowing the signal with a set of windows and then doing the Fourier transform, which provide a local spectrum of a signal. By this localization processing, Gabor transform can extend the Fourier transform to the nonstationary realm. The discrete Gabor transform can be easily realized using an approximate way, whose error can be well controlled by properly choosing of parameters.

The Gabor deconvolution algorithm is developed based on a nonstationary convolution model. It can estimate the attenuated propagating wavelet, which can address the constant-Q attenuation inherently and is equivalent to applying an inverse-Q compensation to seismic trace when conducting the deconvolution. Therefore, Gabor deconvolution can be regarded as a combination of stationary deconvolution, inverse-Q filtering and gain correction. Testing on synthetic data shows that Gabor deconvolution can provide better estimation of reflectivity than conventional Wiener spiking deconvolution.

In practice, the reflectivity is usually nonwhite and the color feature is time-variant, which needs to be corrected in a nonstationary way. A color correction method is presented in this chapter. If relevant well-log information is available, color correction can be incorporated into Gabor deconvolution in a nonstationary way. To make the correction method practical, the time-variant reflectivity color can be approximated by a low-order polynomial fitting over frequency with time-variant coefficients. This approach addresses the nonstatioanry reflectivity color appropriately, and it also deals with incomplete well-log or multi-well log information conveniently.

The distortion of reflectivity estimation can be divided into relative amplitude distortion and phase rotation. Color correction can significantly improve the reflectivity estimation with

smaller relative distortion and phase rotation. The effect of color correction depends on the frequency band available. When frequency band becomes narrow, color correction may lose its effect gradually. In addition, a practical way to measure and remove the nonstationary phase rotation between two associated signals is proposed, which can be used to remove the phase rotation of estimated reflectivity.

The time-variant reflectivity color can be decomposed into spectral color and reflectivity color. Testing with synthetic data and field data both reveal that the temporal color and spectral color are responsible for amplitude distortion and phase rotation respectively.

The color correction method is applied to a field 2D line. Testing results, to some degree, indicate that color correction can improve the resolution of seismic data and obtain a better tie to the well-log data.

In addition, data processing result of the field 2D line shows that deconvolution can whiten the spectrum of seismic data to recover high frequency components, while stacking and Kirchhoff time migration, at different levels, de-whiten the spectrum of seismic data.

Chapter Five: Conclusions

5.1 Modeling of seismic attenuation

A nonstationary convolution model, the reflectivity method, and a finite-difference technique for viscoelastic modeling are reviewed. All of them can incorporate the attenuation into their modeling results with sufficient accuracy. Depending on the circumstance and our needs, we can choose these methods to produce realistic results for absorptive media.

For the implementation of the nonstationary convolution model, the key issue is to incorporate the impulse response representing attenuation accurately. In the matrix-vector production form of the nonstationary model, truncation of the original impulse response is necessary. The amplitude spectrum of the truncated impulse response is distorted if a direct truncation is made, which makes the incorporation of Q attenuation inaccurate. A bandlimited version or a circle-shifted version of the original impulse response can be adopted to preserve its amplitude spectrum, which can incorporate constant-Q attenuation accurately.

The reflectivity method is very useful and widely used for the seismic modeling of stratified media. We implement this method for stratified anelastic media. It can model all kinds of waves and address the geometric spreading and Q attenuation properly. This makes the modeling result realistic and gives sufficient information for layered earth model. In addition, testing results show that the amplitudes of reflection events are consistent with the result given by Zoeppritz equation. Another advantage of the reflectivity method is its flexibility, which is demonstrated by our implementation as well.

The finite-difference technique is a powerful tool for viscoelastic seismic modeling, which can deal with 2D or 3D heterogeneous media and arbitrary distribution of quality factors.

Synthetic seismograms obtained from the Tiger software show that finite difference technique can produce very realistic results.

5.2 Measurement of seismic attenuation

To develop a Q-estimation method that is robust to noise and suitable for application to reflection data, three new methods are presented for Q estimation in this thesis, including complex spectral-ratio method, interpretive spectral-ratio method, and match-filter method. In contrast to the classic spectral ratio method, the complex spectral-ratio method takes full use of both amplitude spectra and phase spectra. It adopts an inversion approach to estimation of Q. In addition, it can give different weights to amplitude spectra information and phase information to give final estimation. Therefore, the classic spectral-ratio method is a special case of complex spectral-ratio method. For the interpretive spectral-ratio method, it simulates the case that Q is estimated by classic spectral-ratio method with a manual picking of frequency band. By obtaining local slopes of the calculated spectral ratios through polynomial fitting, a piecewise linear-line fitting scheme is approximated. Then it automatically chooses a local and optimal piece to give the final estimation. When the order of polynomial fitting is one, it reduces to the classic spectral-ratio method. For the match-filter method, it only employs the amplitude spectra information, and can be regarded as, to some degree, matching the amplitude spectra in time domain to avoid the spectral division. The spectrum smoothing before the minimum-phase wavelet calculation is helpful for two reasons. First, smoothed amplitude spectrum can lead to a smooth minimum-phase wavelet. The matching between two smooth wavelets can be stable, since both of them are of minimum-phase and they have similar waveforms. Second, the spectrum smoothing can help to mitigate the influence of local reflectors. The ideal case is that the amplitude spectra of local reflectors cancel with each other, such as the VSP data case.

Reflectivity is assumed to be random series, which has similar smoothed amplitude spectrum. Therefore, smoothing can help to reduce the influence of local reflectivities when we conduct Q estimation using reflection data.

Theoretically, the three proposed methods have connection with the spectral-ratio method, the spectrum-modeling method and the match-technique method. Among all these methods, the match-filter method is a time-domain method while other methods are frequency-domain methods. The spectrum division is involved for the spectral ratio methods and match technique method, and is absent in spectrum-modeling method. The match-technique method can be regarded as a sophisticated spectral-ratio method with spectral-ratio estimation, and match-filter method can be regarded as a sophisticated wavelet modeling method with wavelet estimation. The match-filter method, to some degree, can be regarded as the counterpart of spectrum-modeling method in time domain.

The performance of above Q-estimation methods is evaluated using synthetic and field VSP data. Testing on synthetic VSP data shows that match-filter method and complex spectral-ratio method are more stable and robust to noise compared to other methods while all of them can give good estimation results for VSP data with moderate noise. Testing on real VSP data shows that the match-filter method and the spectrum-modeling method give more stable results, since no spectral division is involved in their algorithm, and all the methods can obtain similar results at most cases when VSP data with high SNR is used for Q estimation.

For the effect of spectrum smoothing, classic spectral-ratio method, spectrum-modeling method and match-technique method, as methods in frequency domain, are sensitive to the distortion of amplitude spectrum caused by application of spectrum estimation, which is shown by the testing results using synthetic VSP data. Therefore, for these three methods, spectrum

smoothing should be optional for application to VSP data depending on the SNR level. For the match-filter method, appropriate spectrum smoothing can improve the estimation of embedded wavelets, and, in turn, make the estimation result more stable. Testing results show that spectrum smoothing can improve the performance for all cases. Therefore, spectrum smoothing can be an integrated part of the match-filter method.

All the frequency domain methods are directly subject to the frequency band chosen for Q estimation. Theoretically, the result of the match-filter method can be affected by the frequency band used to estimate the embedded wavelets. Accurate estimation of Q requires a rough match of the frequency bands for embedded wavelets, which can be chosen based on the evaluation of their amplitude spectra of original local waves.

For the complex spectral ratio-method, testing results with synthetic VSP data show that Q estimation is dominated by the phase information when the misfits from amplitude spectra and phase difference are equally weighted, which might indicate that we can obtain better estimation result using phase information than using amplitude spectra information. In addition, complex spectral-ratio method is subject to the reference frequency chosen for modeling phase difference as well. Inaccurate reference frequency can distort the estimation. To address this problem, the calibration of other methods can be used to choose reference frequency, with the expectation that they should obtain similar results. An alternative approach can be that the reference frequency is determined by minimizing the mismatch between modeled phase difference and measured phase difference. However, these two approaches fail when we conducted Q estimation with real VSP data, which might indicate that the phase relation is not preserved as well as the amplitude spectrum relation between propagating wavelets for field VSP data. To successfully apply the complex spectral-ratio method to real VSP data, minimum-phase equivalent wavelet

transformation might be necessary before Q estimation, and the reference frequency can be chosen with the calibration of other methods. When applied properly, the complex spectral-ratio method can obtain similar results to match-filter method.

When applied to reflection data, the classic spectral-ratio method, spectrum-modeling method and match-technique method fail. The interpretive spectral-ratio method significantly improves the performance of classic spectral-ratio method, while the estimation results still have large standard deviation value. In contrast, match-filter method gives quite accurate and stable results. The estimation results of match-filter method are quite insensitive to noise, which may indicate that the spectrum estimation of local wavelets by multitaper method is mainly affected by the tuning effect of local reflectors instead of noise. Theoretical analysis shows that Q estimation can be applied to reflection data either before or after stationary deconvolution, which is verified with the test using synthetic 1D data.

When conducting Q estimation for a 2D gather, a small ensemble of neighbouring traces can be employed to give the final spectrum estimation for a single trace centered at this ensemble. This approach can help to obtain a better smoothed spectrum and stabilize the Q estimation. To identify the low Q zone of subsurface, Q profiles can be obtained from CDP gathers using match-filter method, then the low Q zone can be identified by evaluating the variation of estimated Q with respect to travel-time and horizontal coordinates. Testing with synthetic 2D reflection data and field data demonstrates that this approach has the potential to identify the localized low Q zone from reflection data for a layered media.

Generally, for all the Q-estimation methods discussed in this thesis, the match-filter is significantly superior to others in terms of accuracy and robustness to noise, and is much more suitable to be applied to reflection data.

5.3 Gabor deconvolution and the color correction to white-reflectivity assumption

Gabor deconvolution estimates the attenuated propagating wavelet and de-signature it from the seismic trace. Through this approach, Gabor deconvolution addresses the constant-Q attenuation inherently and is equivalent to make an inverse-Q compensation to seismic trace when conducting the deconvolution. Therefore, Gabor deconvolution can be regarded as a combination of stationary deconvolution, inverse-Q filtering and gain correction. Testing on synthetic data shows that Gabor deconvolution can provide better estimation of reflectivity than conventional Wiener spiking deconvolution.

In practice, the reflectivity usually does not have a white amplitude spectrum, and the reflectivity color is time-variant, which is obvious when the reflectivity is transformed into Gabor domain. The white-reflectivity assumption can lead to distortion to reflectivity estimation. To address this problem, a color correction for Gabor deconvolution is presented, in which the correction to white reflectivity assumption is incorporated into deconvolution algorithm in a non-stationary way using relevant well-log reflectivity.

To make the color correction method practical, the Gabor spectrum of well-log reflectivity is approximated by low-order polynomial fitting with time-variant coefficients. The time-variant feature of reflectivity is addressed by the time-variant coefficients. The adoption of low-order polynomial fitting means that only a rough trend of the reflectivity color is needed, which makes the color correction method insensitive to a particular well and well-log information from the same region useful.

The distortion of reflectivity estimation can be evaluated in term of distortion of relative amplitude and nonstationary phase rotation. The distortion of relative amplitudes can be evaluated by comparing the envelopes of estimated reflectivity and true reflectivity. The

nonstationary phase rotation can be measured in Gabor windows. A practical definition of nonstationary phase rotation is proposed, which can be used to remove the phase rotation of estimated reflectivity. Testing results with synthetic data show that color correction can significantly improve the reflectivity estimation with better relative amplitude and smaller phase rotation. Test with synthetic data shows that the effect of color correction is subject to the frequency band available. When the frequency band is limited, color correction will lose its effect gradually.

The time-variant reflectivity color can be decomposed into temporal color and spectral color. Testing results with synthetic data and field data both demonstrate that the temporal color and spectral color are responsible for distortion of relative amplitude and phase rotation respectively.

The color correction method is applied to a field 2D line where reference well-log information is available. Testing on field data, to some degree, indicates that color correction can restore the high frequency components of seismic data and obtain a better tie to the well log data.

The results from the data processing of a field 2D line indicate that deconvolution can whiten the spectrum of seismic data to recover high frequency components, while stacking and Kirchhoff time migration de-whiten the spectrum of seismic data at different levels.

5.4 Future work

For the Q estimation methods described in this thesis, the match-filter method has been shown to be suitable for application to reflection data and give accurate and stable results even in presence of extensive noise. The match-filter method can be further evaluated using reflection data with associated VSP data by comparing the results obtained from these two datasets. In addition, schemes to obtain reliable interval-Q structure for seismic data using VSP data or

surface reflection data need further investigation, and the match-filter can be incorporated into the schemes because of its high accuracy and stability for Q estimation.

Bibliography

Aki, K., and Richard, P. G., 1980, Quantitative Seismology, W. H. Freeman and Co., San Fransisco.

Alterman, Z. S., and Loewental, D., 1972, Computer generated seismograms, in Bolt, B., Alder, B., Fernbach, S., and Rotenberg, M., Eds., Methods in computational physics: Academic Press, 12, 1-37.

Bai, J., Yingst, D., Bloor, R., and Leveille, J., 2012, Waveform inversion with attenuation: 2012 Annual International Meeting, SEG, Expanded Abstract.

Banik .N. C., Lerche, I., and Shuey, R. T., 1985, Stratigraphic filtering, Part 1: Derivation of the O'Doherty- Anstey formula: Geophysics, 50: 2768 – 2774.

Bath, M., 1974, Spectral analysis in geophysics: Developments in Solid Earth Geophysics, Vol 7, Elsevier Science Publishing Co.

Blanch, J. O., Robertsson, J. O. A., and Symes, W. W., 1993, Viscoelastic finite-difference modeling: Tech. Rep, 93-04, Department of Computational and Applied Mathematics, Rice University.

Bouchon, M., and Aki, K., 1977, Discrete wavenumber representation of seismic-source wavefields: Bull. Seis. Soc. Am., 67, 257-277.

Carcione, J. M., 1993, Seismic modeling in viscoelastic media: Geophysics, 58, 110-120.

Carcione, J. M., Kosloff, D., and Kosloff, R., 1988a, Wave propagation simulation in a linear viscoacoustic medium: Geophys. J. Roy. Astr. Soc., 93, 393-407.

Carcione, J. M., Kosloff, D., and Kosloff, R., 1988b, Viscoacoustic wave propagation simulation in the earth: Geophysics, 53, 769-777.

Carcione, J. M., Kosloff, D., and Kosloff, R., 1988c, Wave propagation simulation in a linear viscoelastic medium: Geophys. J. Roy. Astr. Soc., 95, 597-611.

Causse, E., R. Mittet, and B. Ursin, 1999, Preconditioning of full-waveforminversion in viscoacoustic media: Geophysics, 64, 130–145.

Cheng, P., and Margrave, G. F., 2008, Complex spectral-ratio method for Q estimation: CREWES research report, 20.

Cheng, P., and Margrave, G. F., 2009a, Color correction for Gabor deconvolution and nonstationary phase rotation: 2009 CSPG CSEG CWLS convention, abstract.

Cheng, P., and Margrave, G. F., 2009b, Q analysis using synthetic viscoacoustic seismic data: CREWES research report, 21.

Cheng, P., and Margrave, G. F., 2010, The influence of reflectivity color on Gabor deconvolution : 2010 CSPG CSEG CWLS convention, abstract.

Cheng, P., and Margrave, G. F., 2011a, Reflectivity modeling for stratified anelastic media: CREWES research report, 23

Cheng, P., and Margrave, G. F., 2011b, A match-filter method for Q estimation: CREWES research report, 23.

Cheng, P., and Margrave, G. F., 2011c, Color correction for Gabor deconvolution: a test with field data: 2011 CSPG CSEG CWLS convention, abstract.

Cheng, P., and Margrave, G. F., 2012, A match-filter method for Q estimation: 2012 Annual International, SEG, Expanded Abstract.

Cheng, P., and Margrave, G. F., 2013, Estimation of Q: a comparison of different computational methods: 2013 GeoCanada convention, abstract.

Christensen, R. M., 1982, Theory of viscoelasticity – An introduction: Academic Press, Inc.

Clark, G. K. C., 1968, Time-varying deconvolution filters: Geophysics, 33, 936-944.

Dasgupta, R., and Clark, R. A., 1998, Estimation of Q from surface seismic reflection data: Geophysics, 63, 2120-2128.

Day, S. M., and Minster, J. B., 1984, Numerical simulation of attenuated wavefield in using a Padé approximation method: Geophys. J. Roy. Astr. Soc., 78, 105-118.

Dong, Z., and McMechan, G. A., 1995, 3-D viscoelastic anisotropic modeling of data from a multicomponent, multi-azimuth experiment in northeast Texas: Geophysics, 60, 1128-1138.

Emmerich, H., and Korn, M., 1987, Incorporation of attenuation into time-domain computation of seismic wavefield: Geophysics, 52, 1252-1264.

Engelhard, L., 1996, Determination of the seismic wave attenuation by complex trace analysis: Geophysical Journal International, 125, 608-622.

Frazer, L. N., 1978, Synthesis of shear-coupled PL: Ph.D thesis, Princeton University.

Frazer, L. N., and Gettrust, J. F., 1984, On a generalization of Filon's method and the computation of oscillatory integrals of seismology: Geophys. J. Roy. Astr. Soc., 72, 193-211.

Fryer, G. J., 1981, A slowness approach to the reflectivity method of seismogram synthetics: Geophys. J. R. astr. Soc., 63, 747-758.

Fuchs, K., and Müller, G., 1971, Computation of synthetic seismograms with the reflectivity method and comparison with observations: Gephys. J. R. astr. Soc., 23, 417-433.

Futterman, W. I., 1962, Dispersive body waves: J. Geohys. Res., 67, 5279-5291.

Griffiths, L. J., F. R. Smolka, and L. D. Trembly, 1977, Adaptive deconvolution: A new technique for processing time-varying seismic data: Geophysics, 42, 742-759.

Hackert, C. L., and Parra, J. O., 2004, Improving Q estimates from seismic reflection data using well-log-based localized spectral correction: Geophysics, 69, 1521-1529.

Hargreaves, N. D., and Calvert, A. J., 1991, Inverse Q filtering by Fourier transform: Geophysics, 56, 519-527.

Hauge, P. S., 1981, Measurements of attenuation from vertical seismic profiles: Geophysics, 46, 1548-1558.

Henley, D. C., Cheng, P. and Margrave, G. F., Earthtones: nonstationary color correction in ProMAX, CREWES 2010 research report, 22.

Innanen, K. A., and J. E. Lira, 2010, Direct nonlinear Q-compensation of seismic primaries reflecting from a stratified, two-parameter absorptive medium: Geophysics, 75, no. 2, V13–V23.

Jannsen, D., Voss, J., and Theilen, F., 1985, Comparison of methods to determine Q in shallow marine sediments from vertical reflection seismograms: Geophysical Prospecting, 33, 479-497, 1985.

Kelly, K. R., Ward, R. W., Treitel, S., and Alford, R. M., 1976, Synthetic seismograms: A finite-difference approach: Geophysics, 41, 2-27.

Kennett, B. L. N., 1975, The effect of attenuation on seismograms: Bull. Seis. Soc. of Am., 43, 17-34.

Kennett, B. L. N., 1979, Theoretical reflection seismograms for an elastic medium: Geophys. Prosp., 27, 301-321.

Kennett, B. L. N., 1980, Seismic waves in a stratified half-space II – Theoretical seismograms: Geophys. J.Roy. Astr. Soc., 61, 1-10.

Kennett, B. L.N., and Clarke, T. J., 1983, Seismic waves in stratified half-space IV P-SV wave decoupling and surface wave dispersion: Geophys. J. Roy. Astr. Soc., 72, 633-645.

Kennett, B. L.N., and Illingworth, M. R., 1981, Seismic waves in a stratified half-space III – Piecewise smooth models: Geophys. J. Roy. Astr. Soc., 66, 633-675.

Kennett, B. L.N., and Kerry, N. J., 1979, Seismic waves in a stratified half-space: Geophys. J. Roy. Astr. Soc., 57, 557-583.

Kind, R., 1976, Computation of reflection coefficients for layered media: J. Geophys., 42, 425-446.

Knopoff, L., and G. J. F. MacDonald, 1958, Attenuation of small amplitude stress waves in solid: Revs. Modern Phys., 30, 1178-1192.

Knopoff, L., 1964, Q: Rev. Geophys. Space Phys., 2, 625-660.

Koehler, F., and M. T. Taner, 1985, The use of the conjugate-gradient algorithm in the computation of predictive deconvolution operators: Geophysics, 50, 2752-2758.

Krebes, E. S., and Quiroga-Goode, G., 1994, A standard finite-difference scheme for the time-domain computation of anelastic wavefields: Geophysics, 59, 290-296.

Levander, A. R., 1988, Fourth-order finite -difference P-SV seismograms: Geophysics, 53, 1425-1436.

Liao, Q., and G. A. McMechan, 1996, Multifrequency viscoaccoustic modeling and inversion: Geophysics, 61, 1371-1378.

Liu, H, P., D. L. Anderson, and H. Kanamori, 1976, Velocity dispersion due to anelasticity; Implications for seismology and mantle composition: Geophys. J. Roy. Astron. Soc., 47, 41-58.

Lomnitz, C., 1957, Linear dissipation in solids: J. Geol., 64, 473-479.

Ma, Y. W., Loures, L., and Margrave, G. F., 2004, Seismic modeling with the reflectivity method: CREWES research report, 16.

McDonal F. J., F. A. Angona, R. L. Mills, R. L. Sengbush, R. G. Van Nostrand, and J. E. White, 1958, Attenuation of shear and compressional waves in Pierre shale: Geophysics, 23, 421-439.

Mallick, S., and Frazer, L. N., 1987, Practical aspects of reflectivity modeling: Geophysics, 52, 1355-1364.

Margarve G. F., 1998, Theory of nonstationary linear filtering in the Fourier domain with application to time-variant filtering: Geophysics, 63, 244-259.

Margrave, G. F., P. C. Gibson, J. P. Grossman, D. C. Henley, V. Iliescu, and M. P. Lamoureux, 2004, The Gabor transform, Pseudodifferential operators, and seismic deconvolution: Integrated computer-aided Engineering, 9, 1-13.

Margrave, G. F. and M. P. Lamoureux, 2001, Gabor deconvolution: CREWES Research Report, 13, 241-276.

Margrave, G. F., M. P. Lamoureux, P. C. Gibson, J. P. Grossman, and V. Iliescu, 2002, Gabor deconvolution of seismic data for source waveform and Q correction: 72nd Annual International Meeting, SEG, Expanded Abstract, 2190-2193.

Margrave, G. F. and Lamoureux, M. P., 2002, Gabor deconvolution: CREWES Annual Research Report, 13.

Margrave, G. F., M. P. Lamoureux, and D. C. Henley, 2011, Gabor deconvolution: Estimating reflectivity by nonstationary deconvolution of seismic data: Geophysics, 76, W15- W30.

Mateeva, A., Hart, D., and MacKay, S., 2002, Apparent attenuation from short-period multiples and intrinsic absorption in the seismic wavelet model: 72nd Annual International Meeting, SEG, Expanded Abstract.

Mittet, R., Sollie, R., and Hokstak, K., 1995, Prestack depth migration with compensation for absorption and dispersion: Geophysics, 60, 1485-1494.

Montana, C. A., and G.F. Margrave, 2006, Surface consistent Gabor deconvolution: 76th Annual International Meeting, SEG, Expanded Abstracts, 2812-2816.

Müller, G., 1985, The reflectivity method: a tutorial: J. Geophys., 58, 153-174.

Murchy, W. F. III, 1982, Effects of partial saturation on attenuation in Massilon sandstone and Vycor porous glass: J. Acoust. Soc. Am., 71, 1458-1468.

Neep, J. P., Sams, M. S., Worthington, M. H., and O'Hara-Dhand, K. A., 1996, Measurement of seismic attenuation from high-resolution crosshole data: Geophysics, 61, 1175-1188.

Nowroozi, A. A., 1968, Measurement of Q values form free oscillations of the earth: J. Geoph. Res., 73, 1407-1415.

O' Connell, E. J., and B. Budiansky, 1978, Measures of dissipation in viscoelastic media: Geophys. Res. Lett., 5, 5-8.

O'Doherty , R. F., and N. A. Anstey, 1971, Reflections on amplitudes: Geophysical prospecting, 19, no. 3, 430 – 458.

O'Neill, M. E., and Hill, D. P., 1979, Causal absorption: its effect on synthetic seismograms computed by the reflectivity method: Bull., Seis. Soc, Am., 69, 17-26.

Park, J., Lindberg, C. R., and Vernon III, F. L., 1987, Multitaper spectral analysis of high frequency seismograms: J. Geoph. Res., 92, 12675-12684.

Patton, S. W., 1988, Robust and least-squares estimation of acoustic attenuation from well-log data: Geophysics, 53, 1225-1232.

Phinney, R. A., 1965, Theoretical calculations of the spectra of first arrivals in layered elastic mediums: J. Geophys. Res., 70, 5107-5123.

Pipkin, A. C., 1986, Lectures on Viscoelasticity theory: Springer Verlag, New York, Inc.

Pratt, R. G., and Worthington, M. H., 1990, Inversion theory applied to multisource crosshole tomography. Part I: Acoustic wave-equation method: Geophys. Prosp., 38, 287-310.

Quan, Y., and Harris, J. M., 1997, Seismic attenuation tomography using the frequency shift method: Geophysics, 62, 895-905.

Raikes, S. A., and R. E. White, 1984, Measurements of earth attenuation from downhole and surface seismic recordings: Geophysical Prospecting, 32, 892-919.

Robertsson, J. O. A., Blanch, J. O., and Symes, W. W., 1994, Viscoelastic finite-difference modeling: Geophysics, 59, 1444-1456.

Samec, P., and Blangy, J. P., 1992, Viscoelastic attenuation, anisotropy, and AVO: Geophysics:, 57, 441-450.

Sheriff, R. E., and L. P. Geldart, 1995, Exploration seismology, 2nd ed.: Cambridge University Press.

Sipkin, S. A., Orcutt, J. A., and Jordan, T. H., 1978, An examination of ScS travel times with causal Q reflectivity algorithm for SH polarized waves (abstract): EOS, Trans., Am. Geophys. Union, 59, 324.

Slepian, D., 1978, Prolate spheroidal wave function, Fourier analysis, and uncertainty – V: The Discrete case: Bell Syst. Tech. J., 57, 1371- 1429.

Song, S., and K. A.Innanen, 2002, Multiresolution modeling and wavefield reconstruction in attenuating media: Geophysics, 67, 1192–1201.

Spencer, J. W. Jr., 1981, Stress relaxation at low frequencies in fluid-saturated rocks: Attenuation and modulus dispersion: J. Geophys. Res., 86, 1803-1812.

Spencer, T. W., Sonnad, J. R., and Butler, T. M., 1982, Seismic Q – stratigraphy or dissipation: Geophysics, 47, 16-24.

Spudich, P., and Ascher, U., 1983, Calculation of complete theoretical seismograms in vertically varying media using collocation methods: Geophys. J. Roy. Astr. Soc., 75, 101-24.

Strick, E., 1967, The determination of Q, dynamic viscosity and creep curves from wave propagation measurements: Geophys. J. Roy. Astron. Soc., 13, 197-218.

Sun, X., X. Tang, C. H. Cheng, and L. N. Frazer, 2000, P- and S- wave attenuation logs from monopole sonic data: Geophysics, 65, 755-765.

Tal-Ezer, H., Carcione, J. M., and Kosloff, D., 1990, An accurate and efficient scheme for wave propagation in a linear viscoelastic medium: Geophysics, 55, 1366-1379.

Thomson, D. J., 1982, Spectrum estimation and harmonic analysis: Proc. IEEE, 70, 1055-1096.

Tonn, R., 1991, The determination of seismic quality factor Q from VSP data: A comparison of different computational methods: Geophys. Prosp., 39, 1-27.

Walden, A. T., and Hosken, J. W. J., 1985, An investigation of the spectral properties of primary reflection coefficients: Geophys. Prosp., 33, 400-435.

Wang, Y., 2002, A stable and efficient approach of inverse Q filtering: Geophysics, 67, 657-663

Wang, Y., 2008, Inverse-Q filtered migration: Geophysics, 73, no. 1, S1-S6.

White, J. E., 1966, Static friction as a source of seismic attenuation: Geophysics, 31, 333-339.

White, R. E., 1992, The accuracy of estimating Q from seismic data: Geophysics, 57, 1508-1511.

Xu, T., and McMechan, G. A., 1995, Composite memeory variables for viscoelastic synthetic seismograms: Geophys. J. Int., 121, 634-639.

Zhang, J., and K. Wapenaar, 2002, Wavefield extrapolation and prestack depth migration in anelastic inhomogeneous media: Geophys. Prosp., 50, 629-643.